US 20240191365A1

(19) **United States**

(12) **Patent Application Publication**

(10) **Pub. No.: US 2024/0191365 A1**

(43) **Pub. Date: Jun. 13, 2024**

Jin et al.

(54) **METAL COMPOUND BASED CATALYSTS FOR ELECTROSYNTHESIS OF HYDROGEN PEROXIDE AND LINEAR PAIRED ELECTROCHEMICAL VALORIZATION OF BIOMASS-DERIVED FEEDSTOCKS**

(71) Applicant: **Wisconsin Alumni Research Foundation**, Madison, WI (US)

(72) Inventors: **Song Jin**, Madison, WI (US); **Jordan Schmidt**, Fitchburg, WI (US); **Hongyuan Sheng**, Los Angeles, CA (US); **Kwanpyung Lee**, Madison, WI (US); **Richard Ross**, Madison, WI (US); **Aurora Janes**, Philadelphia, PA (US)

(21) Appl. No.: **18/532,418**

(22) Filed: **Dec. 7, 2023**

Related U.S. Application Data

(60) Provisional application No. 63/430,933, filed on Dec. 7, 2022.

Publication Classification

(51) **Int. Cl.**

C25B 1/30	(2006.01)
C25B 11/053	(2006.01)
C25B 11/081	(2006.01)
C25B 15/08	(2006.01)

(52) **U.S. Cl.**

CPC ***C25B 1/30*** (2013.01); ***C25B 11/053*** (2021.01); ***C25B 11/081*** (2021.01); ***C25B 15/087*** (2021.01)

(57) **ABSTRACT**

Disclosed herein is an electrochemical cell comprising an electrolyte and a cathode immersed in the electrolyte, wherein the cathode comprises a two-electron oxygen reduction reaction ($2e^-$ ORR) electrocatalyst composed of a metal chalcogenide. Also disclosed are methods for production of hydrogen peroxide or preparing oxidation products of a biomass-derived feedstock with the electrochemical cells described herein.

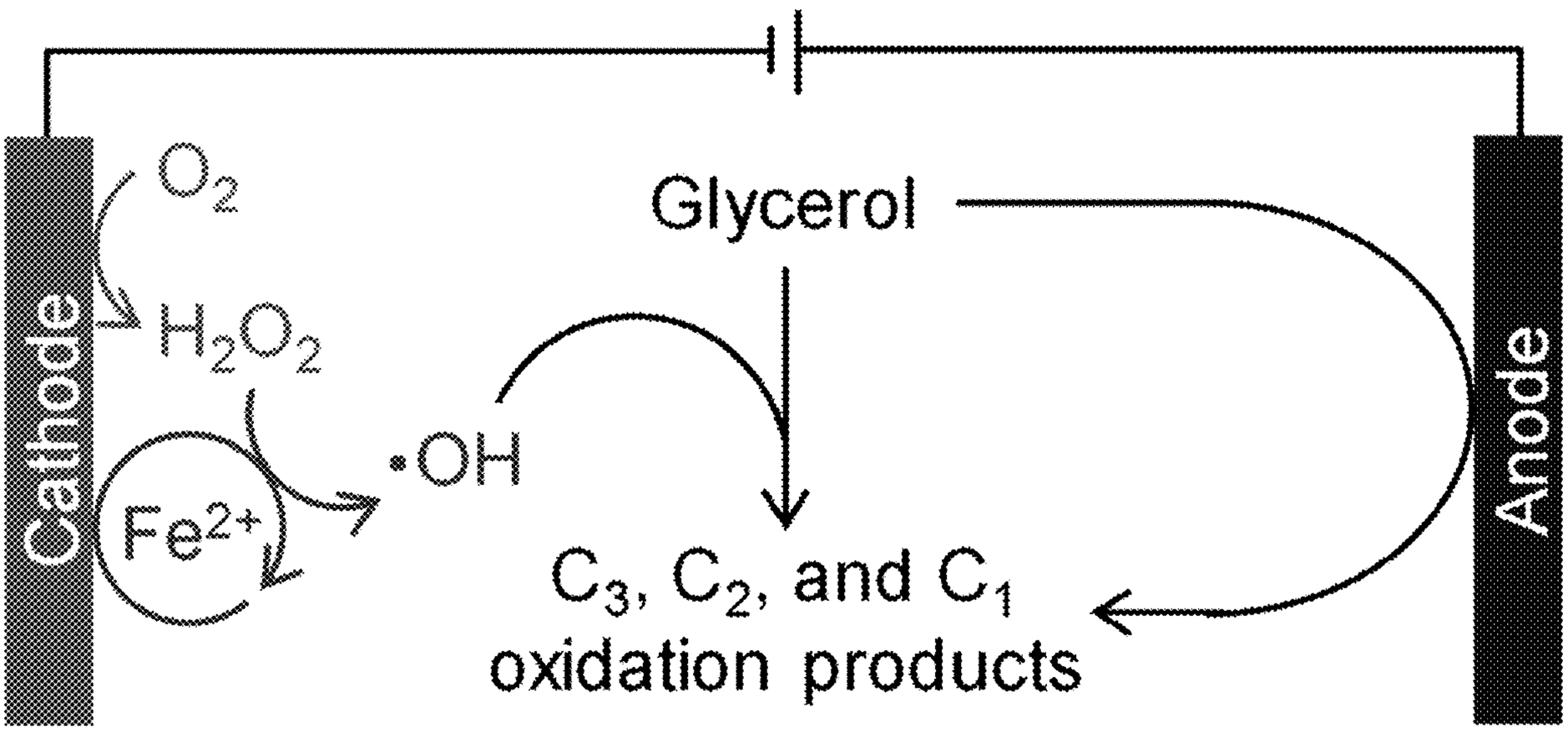

FIG. 1

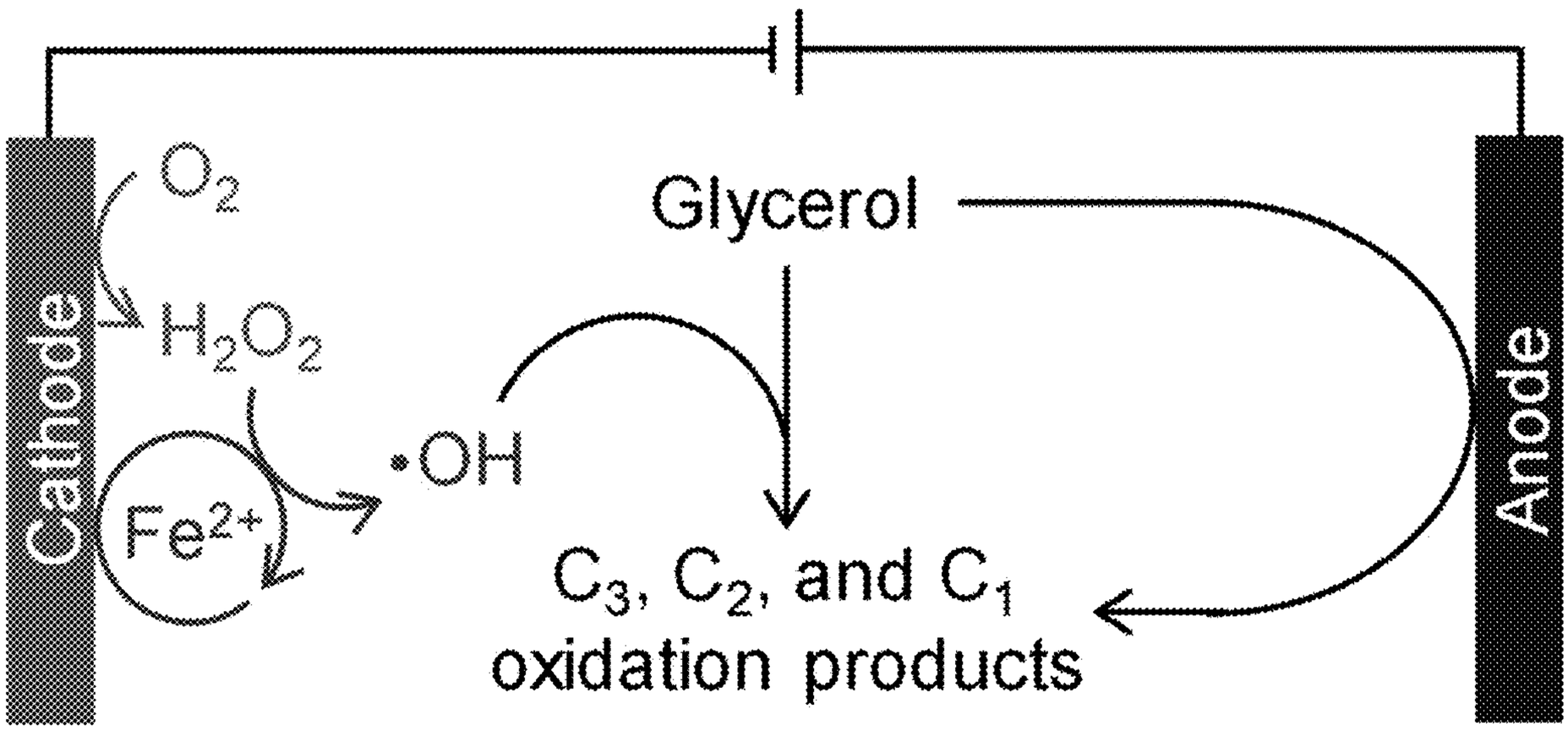
Cathode
Anode
O_2
H_2O_2
Fe^{2+}
•OH
Glycerol
C_3, C_2, and C_1
oxidation products

FIG. 2

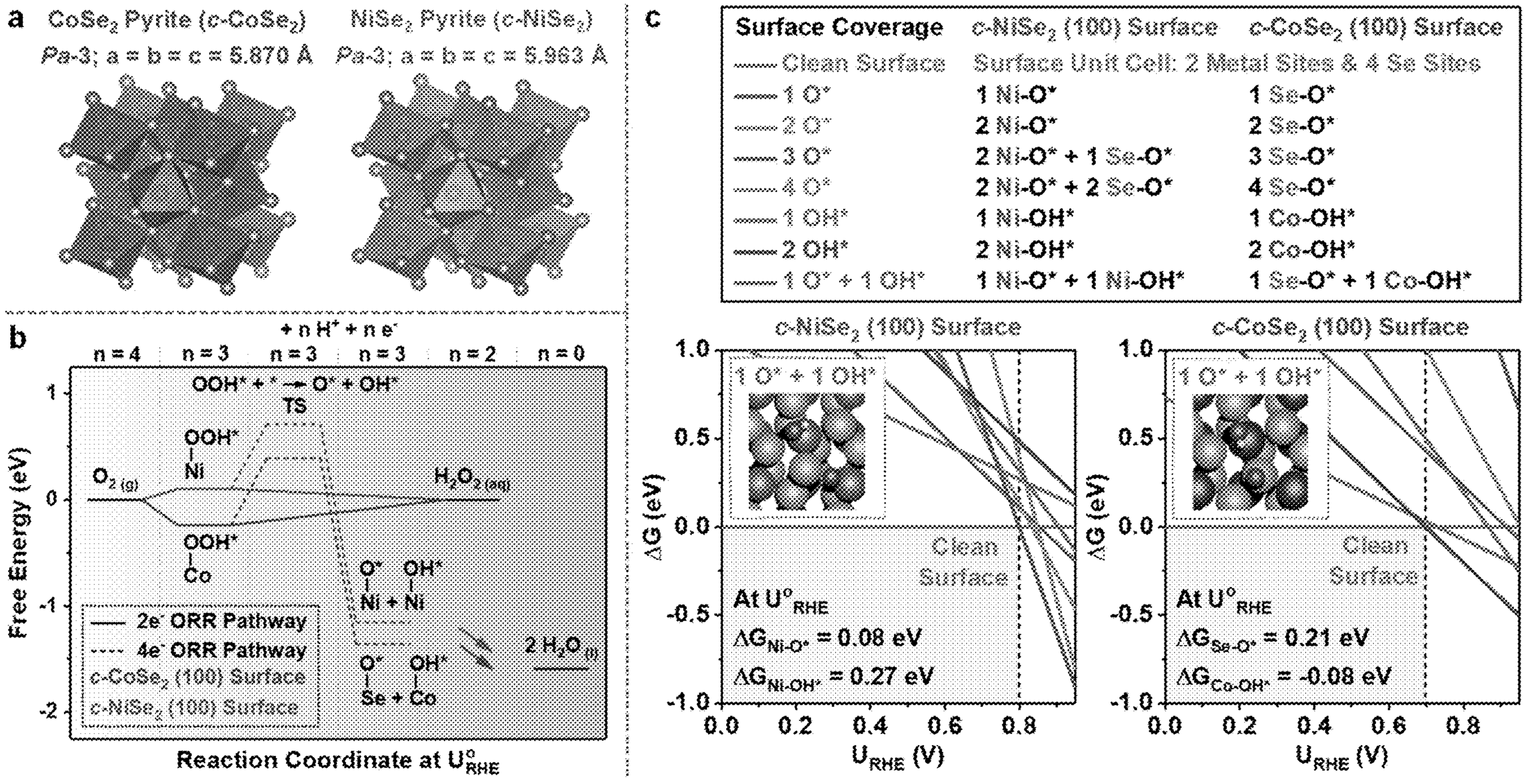
a
$CoSe_2$ Pyrite (c-$CoSe_2$)
Pa-3; a = b = c = 5.870 Å
$NiSe_2$ Pyrite (c-$NiSe_2$)
Pa-3; a = b = c = 5.963 Å
b
+ n H+ + n e-
n = 4
n = 3
n = 3
n = 3
n = 2
n = 0
OOH* + * → O* + OH*
TS
OOH*
Ni
$O_{2\,(g)}$
$H_2O_{2\,(aq)}$
OOH*
Co
O* OH*
Ni + Ni
O* OH*
Se + Co
$2\,H_2O_{(l)}$
2e- ORR Pathway
4e- ORR Pathway
c-$CoSe_2$ (100) Surface
c-$NiSe_2$ (100) Surface
Free Energy (eV)
Reaction Coordinate at U^{o}_{RHE}
c
Surface Coverage
c-$NiSe_2$ (100) Surface
c-$CoSe_2$ (100) Surface
Clean Surface
Surface Unit Cell: 2 Metal Sites & 4 Se Sites
1 O*
1 Ni-O*
1 Se-O*
2 O*
2 Ni-O*
2 Se-O*
3 O*
2 Ni-O* + 1 Se-O*
3 Se-O*
4 O*
2 Ni-O* + 2 Se-O*
4 Se-O*
1 OH*
1 Ni-OH*
1 Co-OH*
2 OH*
2 Ni-OH*
2 Co-OH*
1 O* + 1 OH*
1 Ni-O* + 1 Ni-OH*
1 Se-O* + 1 Co-OH*
c-$NiSe_2$ (100) Surface
c-$CoSe_2$ (100) Surface
1 O* + 1 OH*
Clean Surface
At U^{o}_{RHE}
$\Delta G_{Ni\text{-}O^*}$ = 0.08 eV
$\Delta G_{Ni\text{-}OH^*}$ = 0.27 eV
$\Delta G_{Se\text{-}O^*}$ = 0.21 eV
$\Delta G_{Co\text{-}OH^*}$ = -0.08 eV
ΔG (eV)
U_{RHE} (V)

FIG. 3

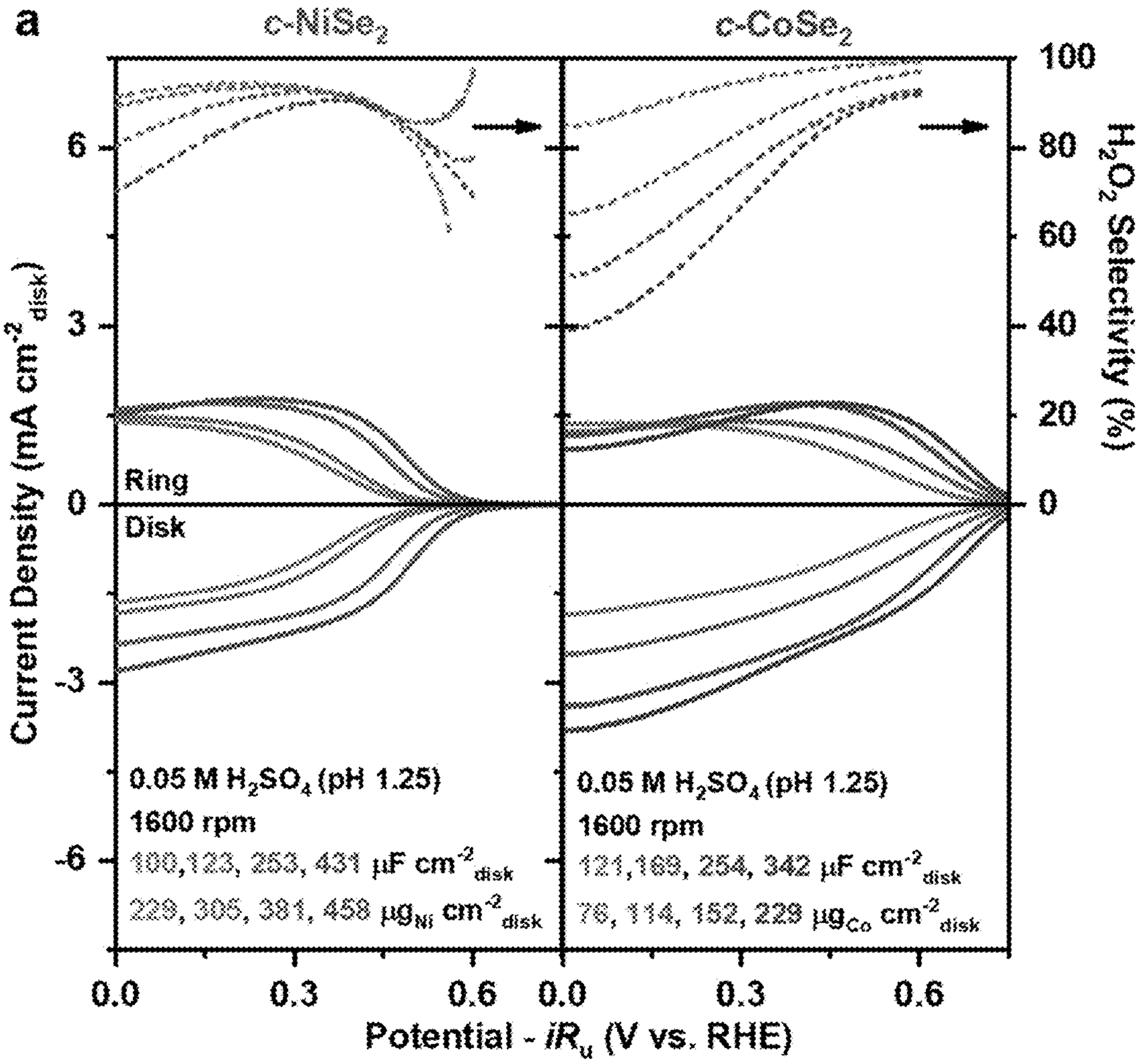
a
c-NiSe2
c-CoSe2
Current Density (mA cm-2disk)
H2O2 Selectivity (%)
Ring
Disk
0.05 M H2SO4 (pH 1.25)
1600 rpm
100,123, 253, 431 μF cm-2disk
229, 305, 381, 458 μgNi cm-2disk
121,169, 254, 342 μF cm-2disk
76, 114, 152, 229 μgCo cm-2disk
Potential - iRu (V vs. RHE)
b
c-NiSe2
c-CoSe2
H2O2
(μgNi cm-2disk)
(μgCo cm-2disk)
Selectivity (%)
Cdl (μF cm-2disk)
305
76
Potential - iRu (V vs. RHE)

FIG. 3 Continued

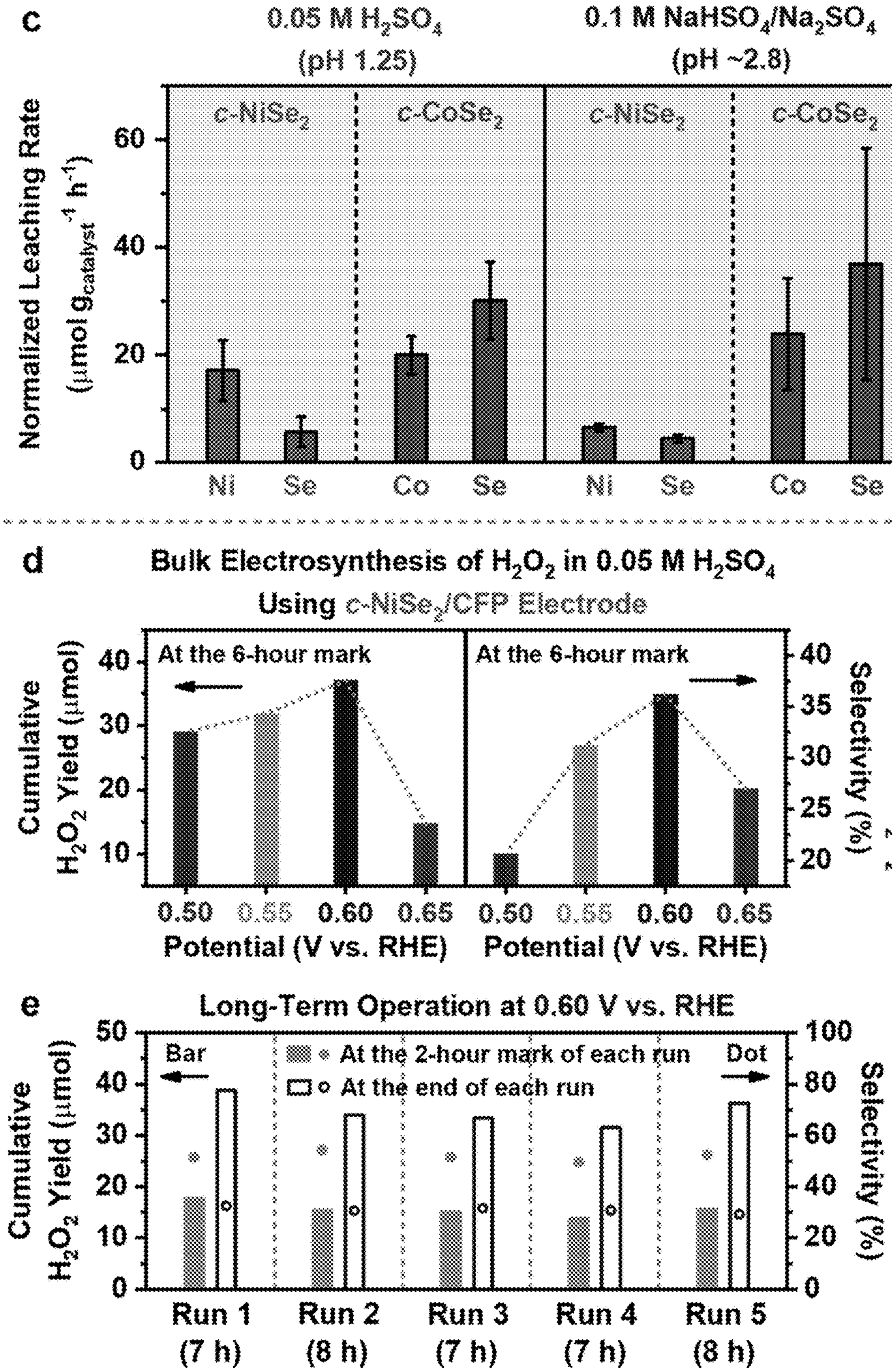

FIG. 4

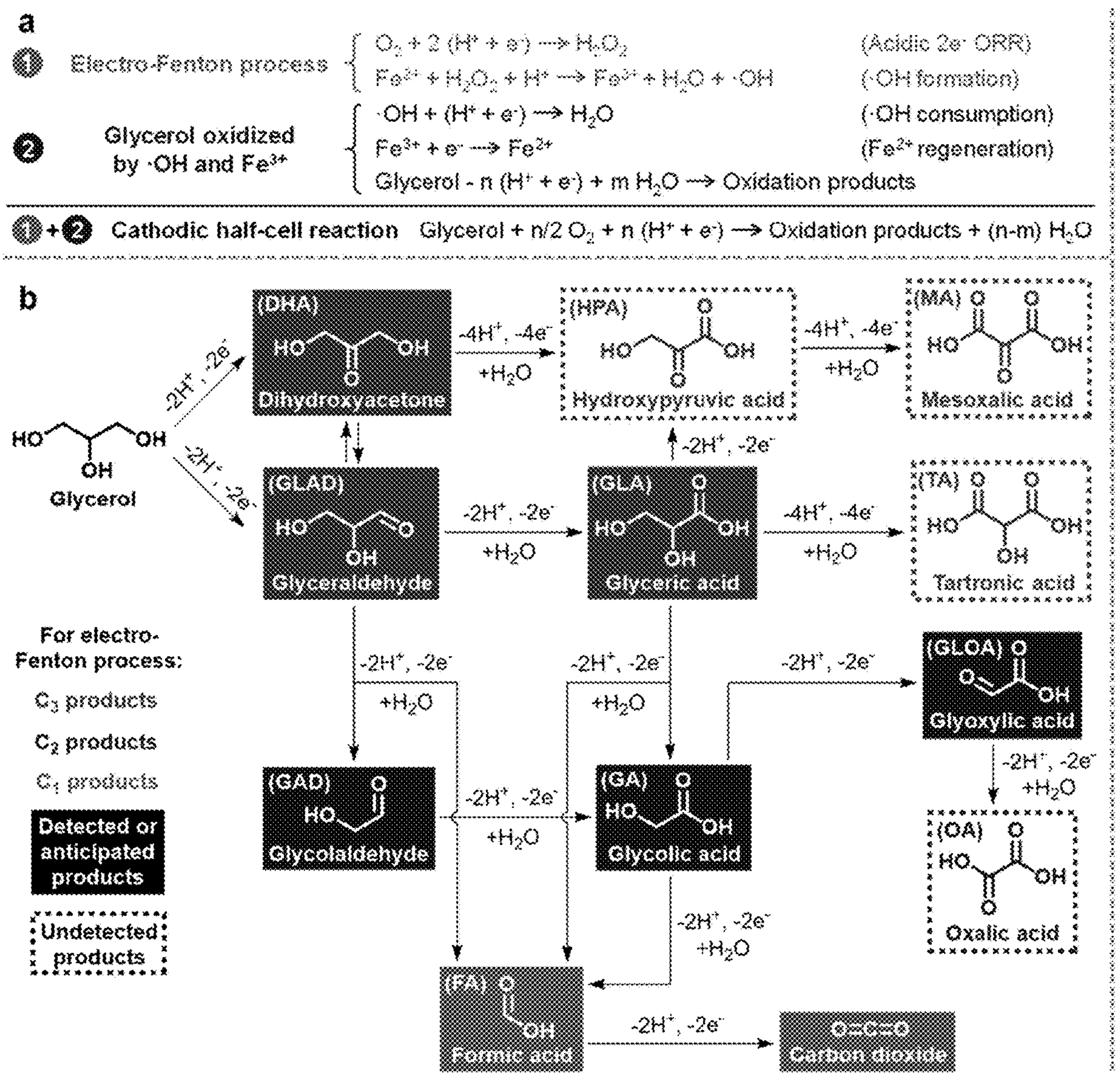
a
Electro-Fenton process
$O_2 + 2(H^+ + e^-) \rightarrow H_2O_2$ (Acidic 2e⁻ ORR)
$Fe^{2+} + H_2O_2 + H^+ \rightarrow Fe^{3+} + H_2O + \cdot OH$ (·OH formation)
Glycerol oxidized by ·OH and Fe^{3+}
$\cdot OH + (H^+ + e^-) \rightarrow H_2O$ (·OH consumption)
$Fe^{3+} + e^- \rightarrow Fe^{2+}$ (Fe^{2+} regeneration)
Glycerol - n $(H^+ + e^-)$ + m H_2O → Oxidation products
Cathodic half-cell reaction
Glycerol + n/2 O_2 + n $(H^+ + e^-)$ → Oxidation products + (n-m) H_2O
b
Glycerol
(DHA) Dihydroxyacetone
(HPA) Hydroxypyruvic acid
(MA) Mesoxalic acid
(GLAD) Glyceraldehyde
(GLA) Glyceric acid
(TA) Tartronic acid
(GLOA) Glyoxylic acid
(GAD) Glycolaldehyde
(GA) Glycolic acid
(OA) Oxalic acid
(FA) Formic acid
O=C=O Carbon dioxide
$-2H^+, -2e^-$
$-4H^+, -4e^-$
$+H_2O$
For electro-Fenton process:
C_3 products
C_2 products
C_1 products
Detected or anticipated products
Undetected products

FIG. 4 Continued

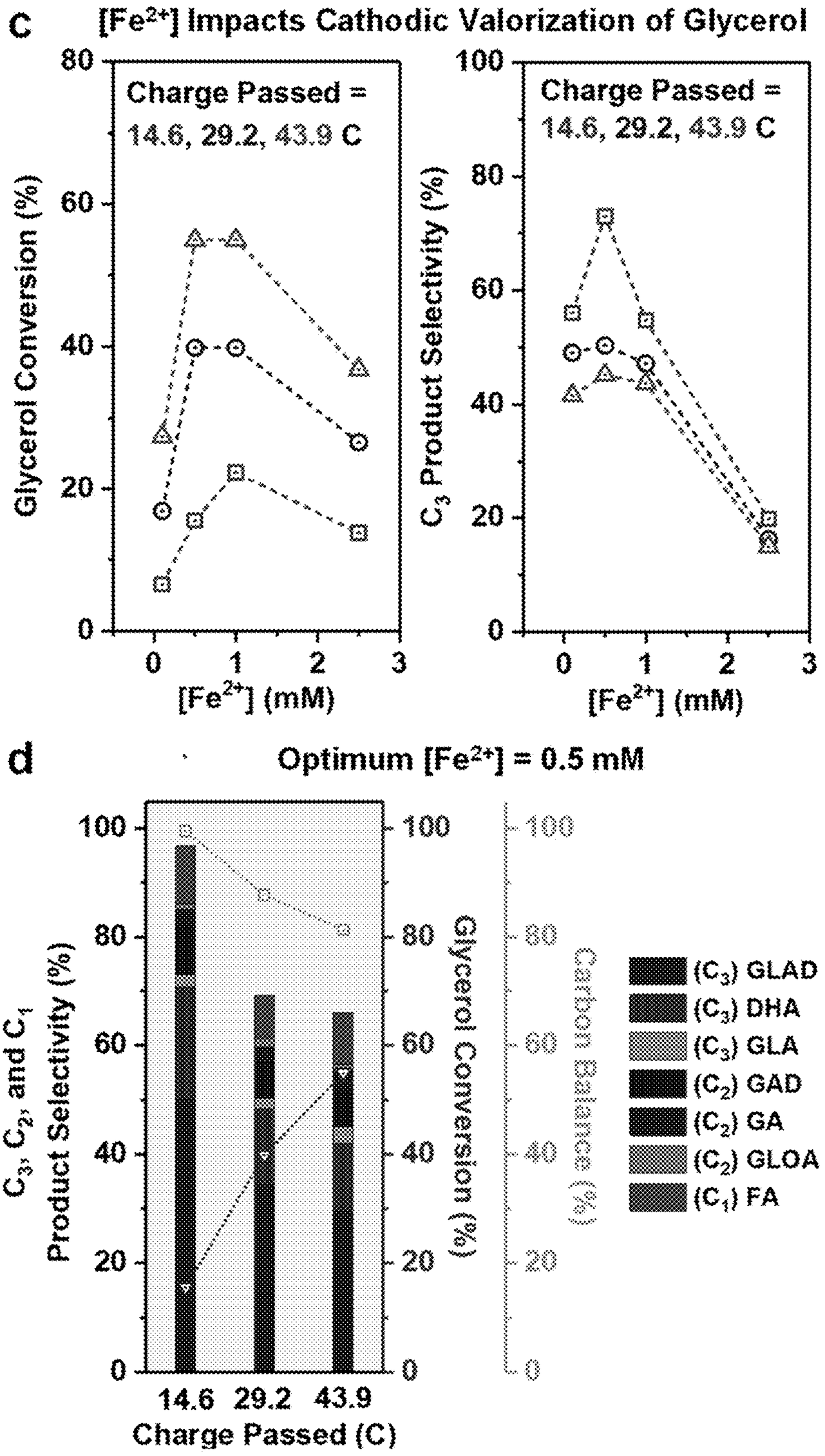

FIG. 5

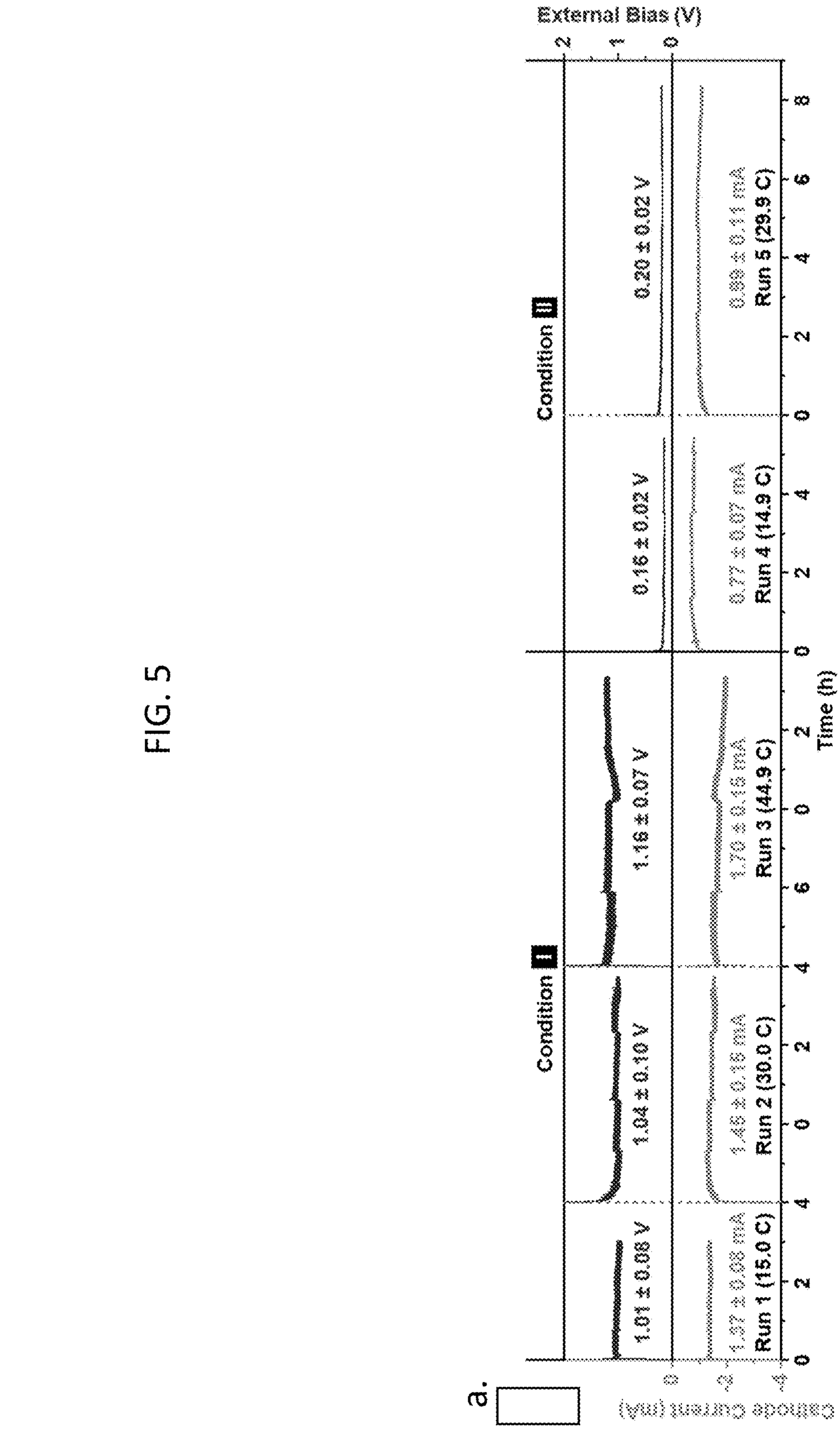
a.
Condition III
Condition II
Condition I
External Bias (V)
2
1
0
0.20 ± 0.02 V
0.80 ± 0.11 mA
Run 5 (29.9 C)
0.16 ± 0.02 V
0.77 ± 0.07 mA
Run 4 (14.9 C)
1.16 ± 0.07 V
1.70 ± 0.16 mA
Run 3 (44.9 C)
1.04 ± 0.10 V
1.48 ± 0.16 mA
Run 2 (30.0 C)
1.01 ± 0.08 V
1.57 ± 0.08 mA
Run 1 (15.0 C)
Time (h)
cathode current (mA)
0
-2
-4
0
2
4
6
8

FIG. 5 continued

b.

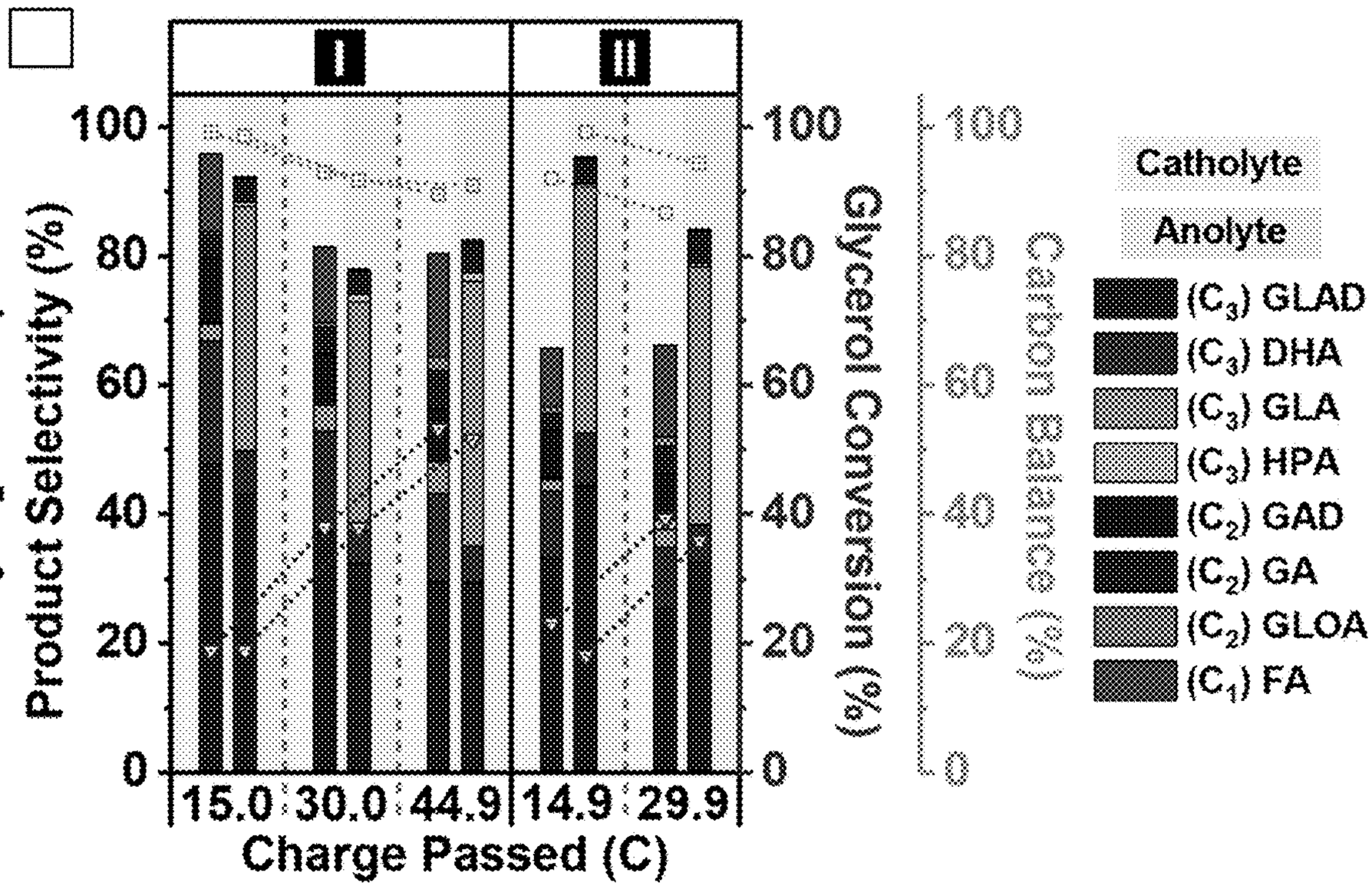

FIG. 6

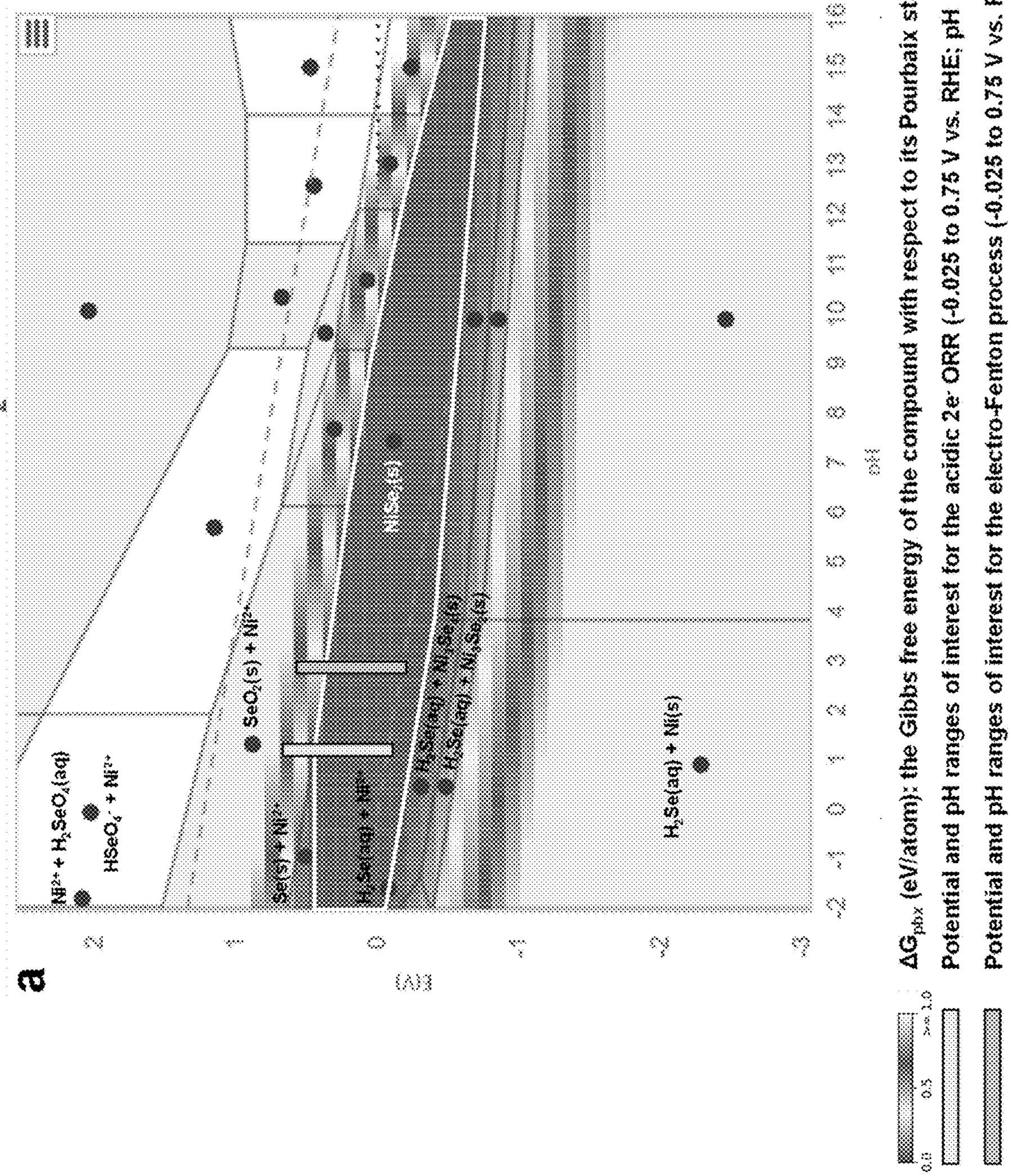
a
E(V)
pH
c-NiSe2
Ni2+ + H2SeO4(aq)
HSeO4- + Ni2+
SeO2(s) + Ni2+
Se(s) + Ni2+
H2Se(aq) + Ni2+
H2Se(aq)
NiSe(s)
Ni(s) + H2Se(aq)
H2Se(aq) + Ni(s)
ΔGpbx (eV/atom): the Gibbs free energy of the compound with respect to its Pourbaix stable phase
Potential and pH ranges of interest for the acidic 2e- ORR (-0.025 to 0.75 V vs. RHE; pH 1.25 for 0.05 M H2SO4)
Potential and pH ranges of interest for the electro-Fenton process (-0.025 to 0.75 V vs. RHE; pH 2.8 to 3.0)

FIG. 6 Continued

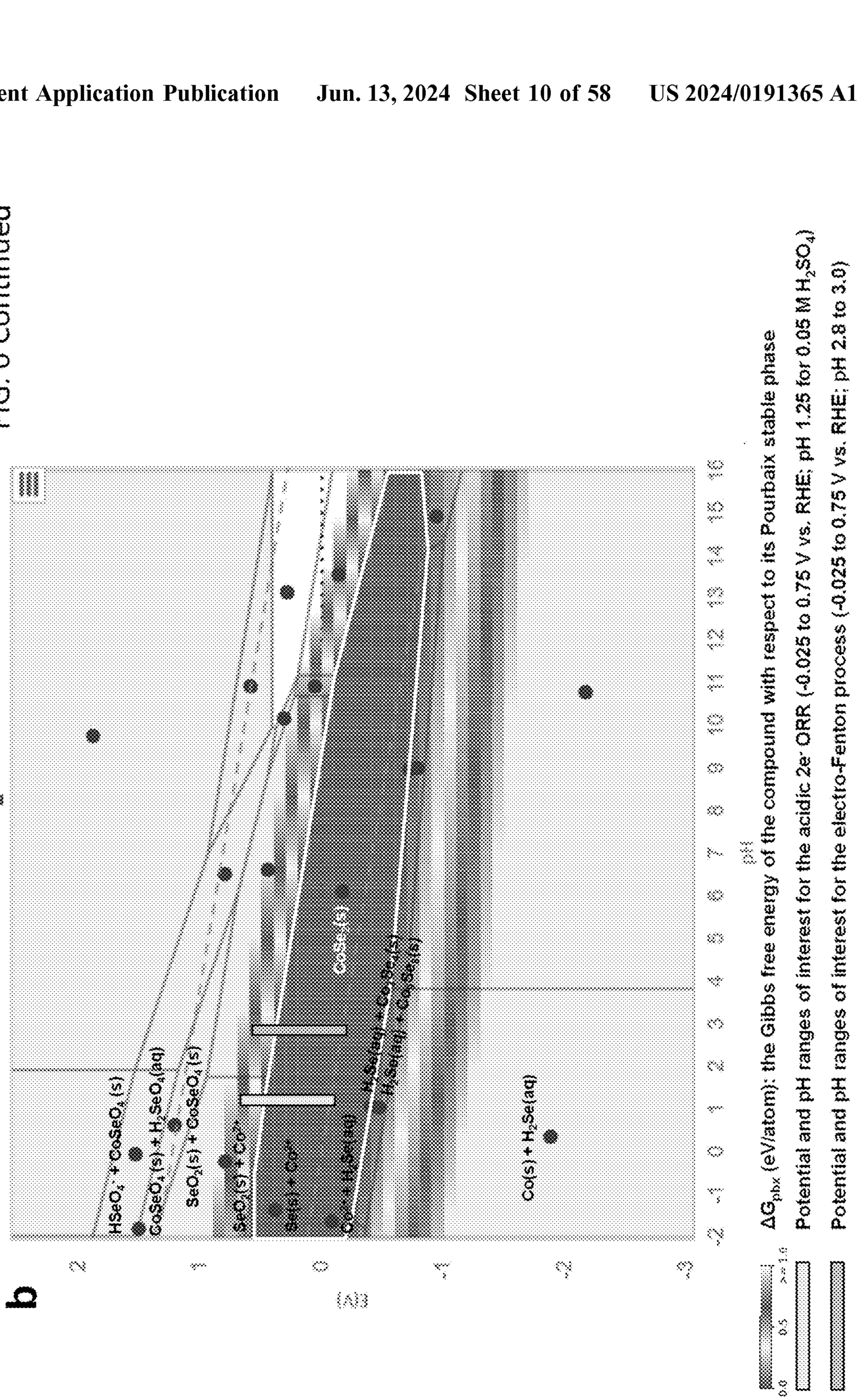

FIG. 7

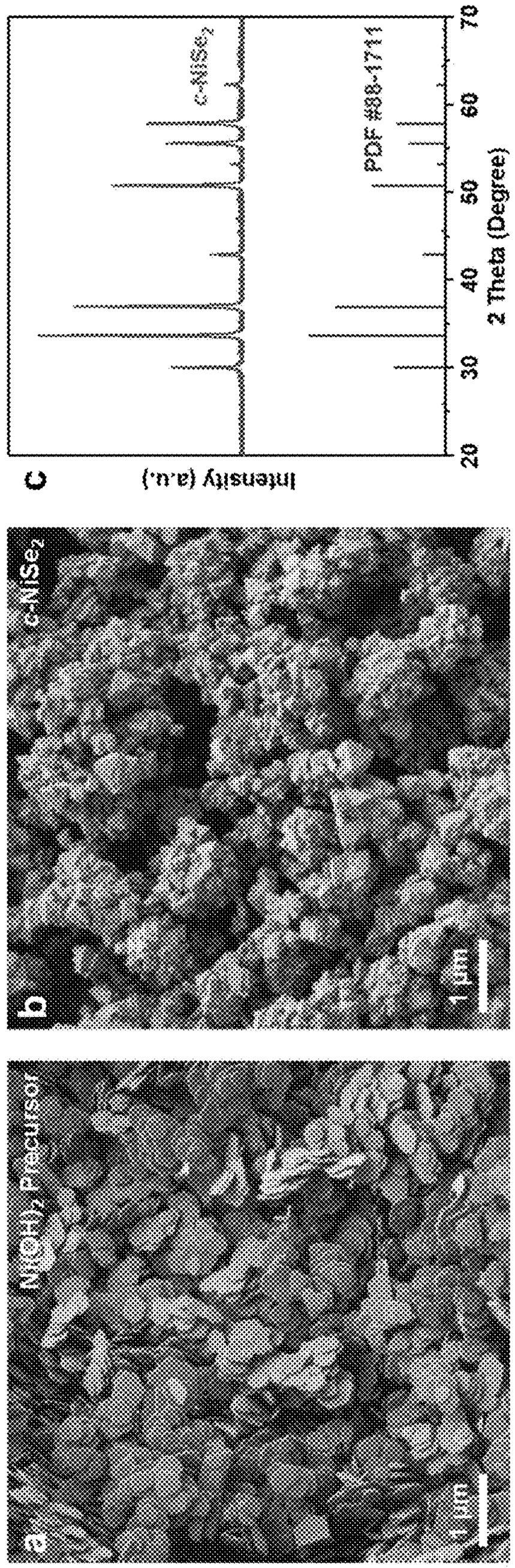
a
Ni(OH)2 Precursor
1 μm
b
c-NiSe2
1 μm
c
c-NiSe2
PDF #88-1711
Intensity (a.u.)
2 Theta (Degree)
20
30
40
50
60
70
d
A1g
T2g
T2g Eg
c-NiSe2
Intensity (a.u.)
Raman Shift (cm-1)
100
150
200
250
300
350
400
e
Ni 2p
2p3/2
2p1/2
c-NiSe2
Intensity (a.u.)
Binding Energy (eV)
890
880
870
860
850
f
Se 3d
3d5/2
3d3/2
c-NiSe2
Intensity (a.u.)
Binding Energy (eV)
65
60
55
50

FIG. 8

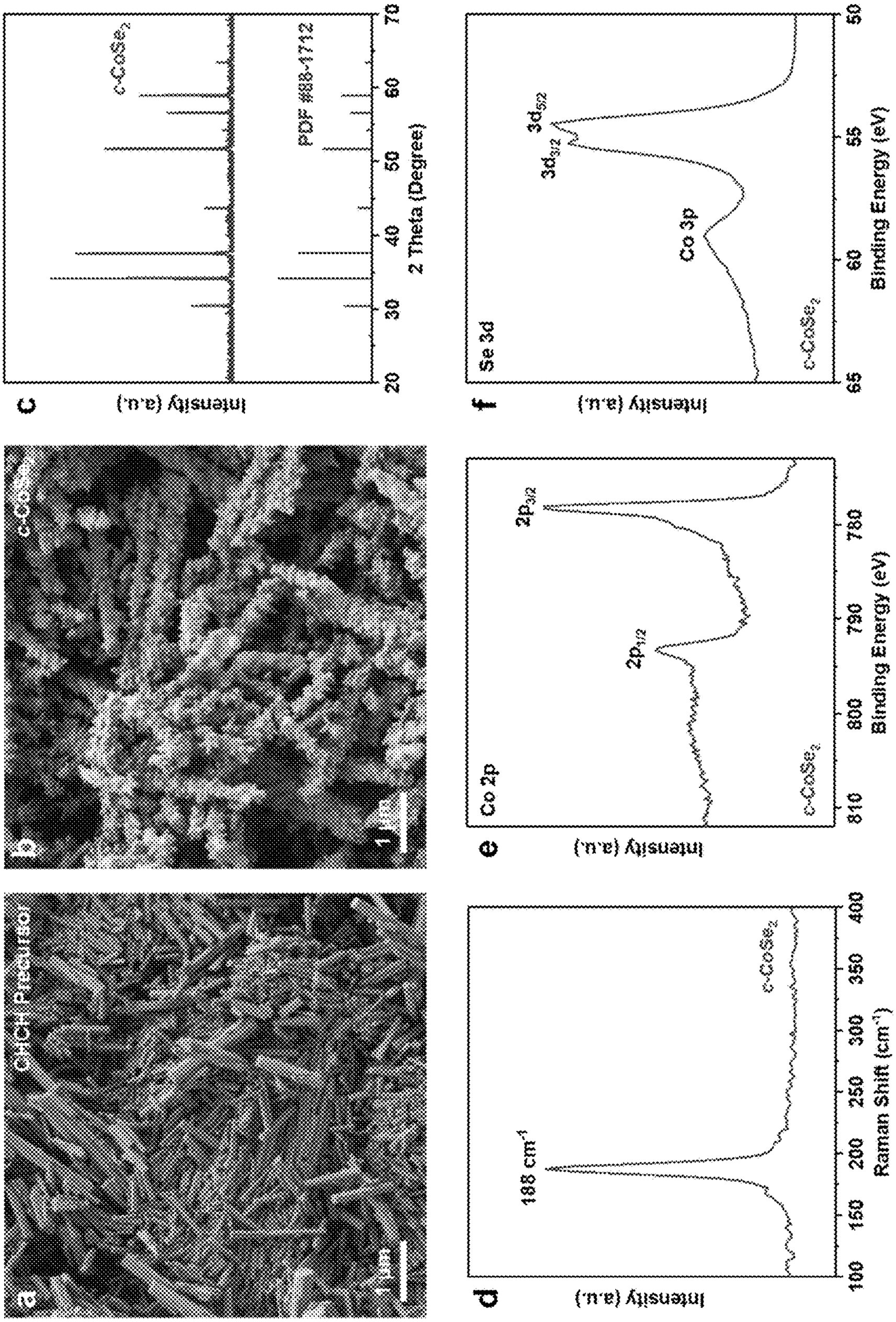
a
CHCH Precursor
1 μm
b
c-CoSe2
1 μm
c
c-CoSe2
PDF #88-1712
Intensity (a.u.)
2 Theta (Degree)
20
30
40
50
60
70
d
188 cm-1
c-CoSe2
Intensity (a.u.)
Raman Shift (cm-1)
100
150
200
250
300
350
400
e
Co 2p
2p3/2
2p1/2
c-CoSe2
Intensity (a.u.)
Binding Energy (eV)
810
800
790
780
f
Se 3d
3d3/2
3d5/2
Co 3p
c-CoSe2
Intensity (a.u.)
Binding Energy (eV)
65
60
55
50

FIG. 9

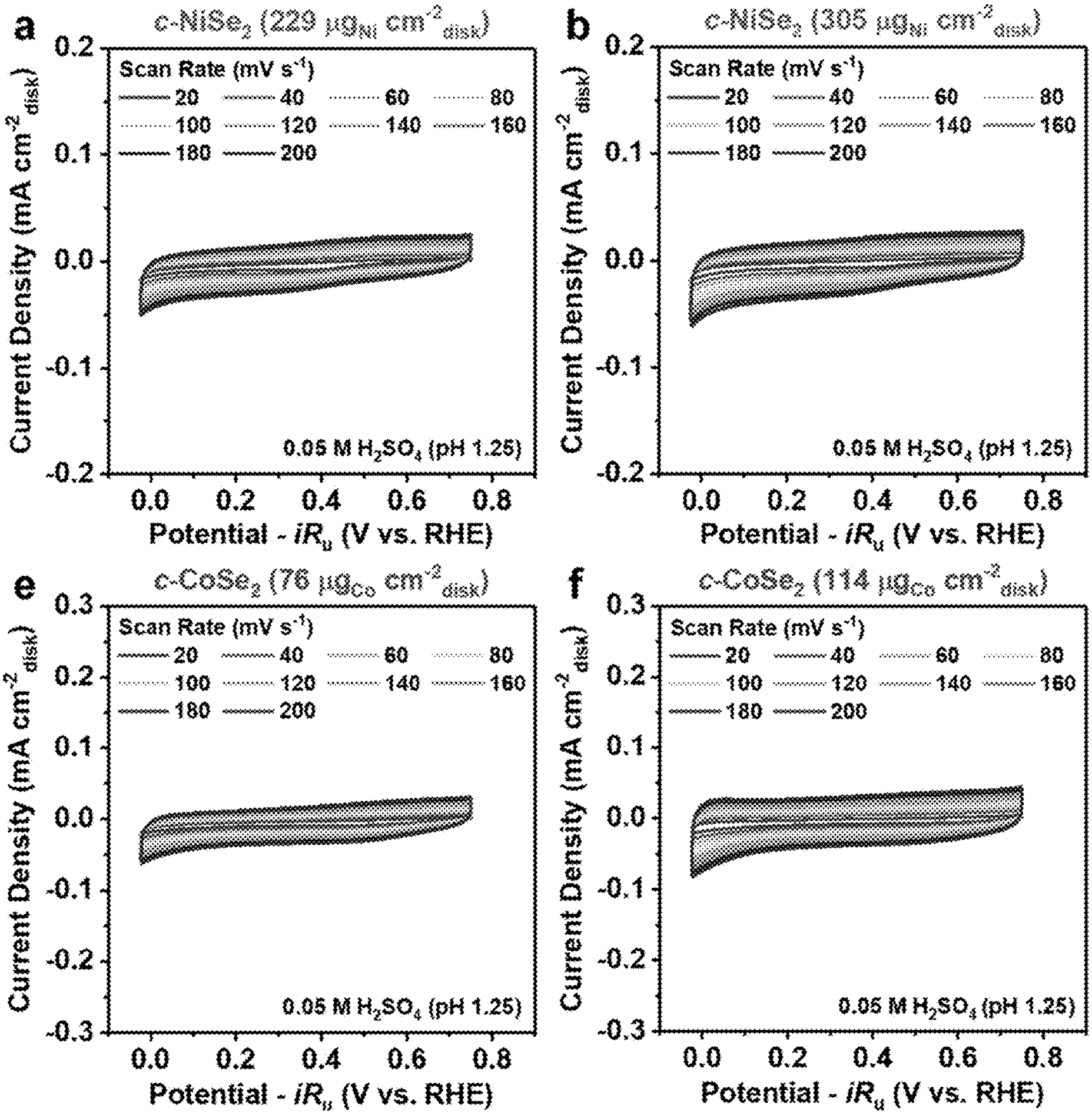
a
c-NiSe2 (229 μgNi cm-2disk)
b
c-NiSe2 (305 μgNi cm-2disk)
e
c-CoSe2 (76 μgCo cm-2disk)
f
c-CoSe2 (114 μgCo cm-2disk)
Scan Rate (mV s-1)
20
40
60
80
100
120
140
160
180
200
0.05 M H2SO4 (pH 1.25)
Current Density (mA cm-2disk)
Potential - iRu (V vs. RHE)

FIG. 9 continued

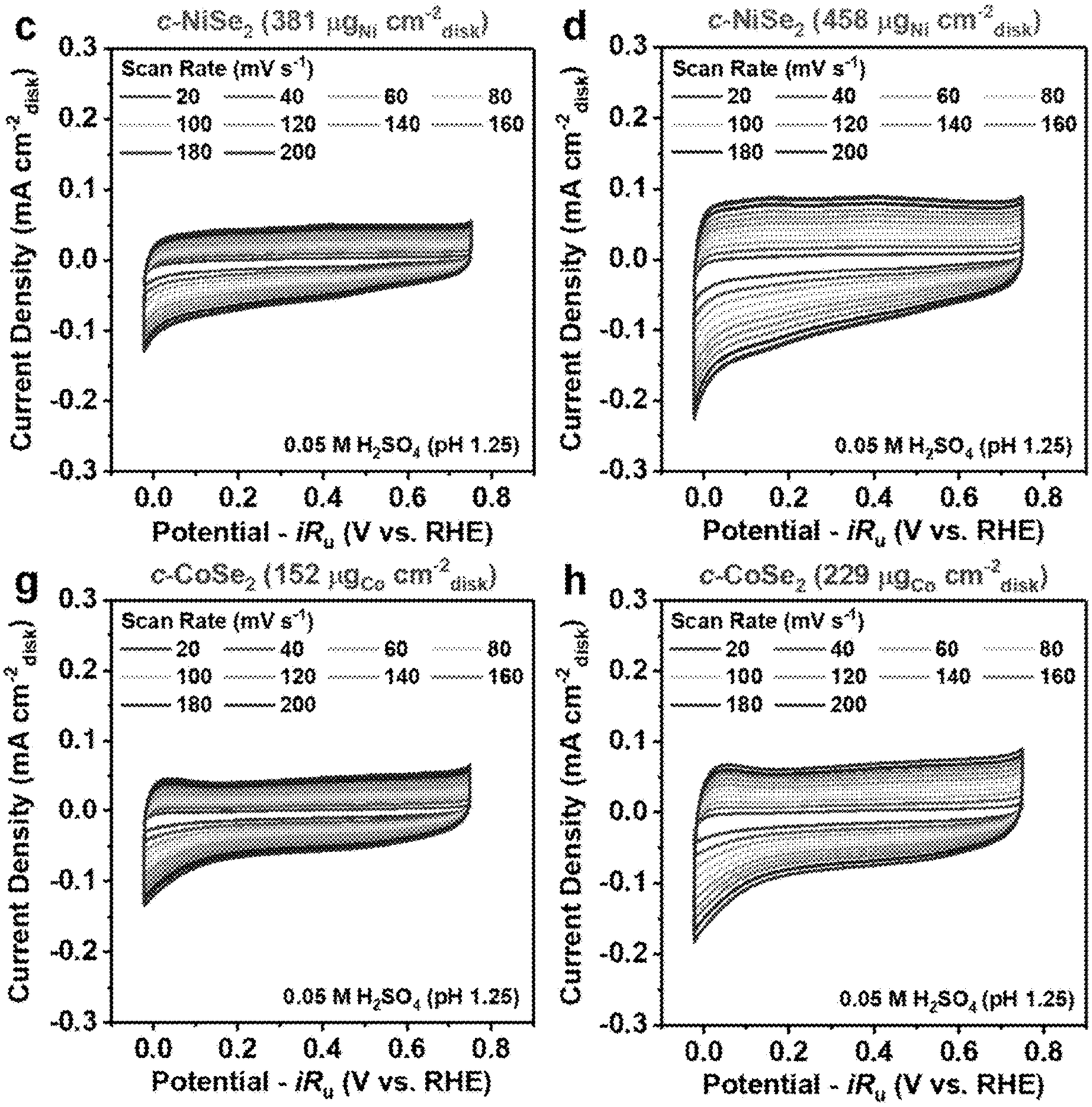

FIG. 9 continued

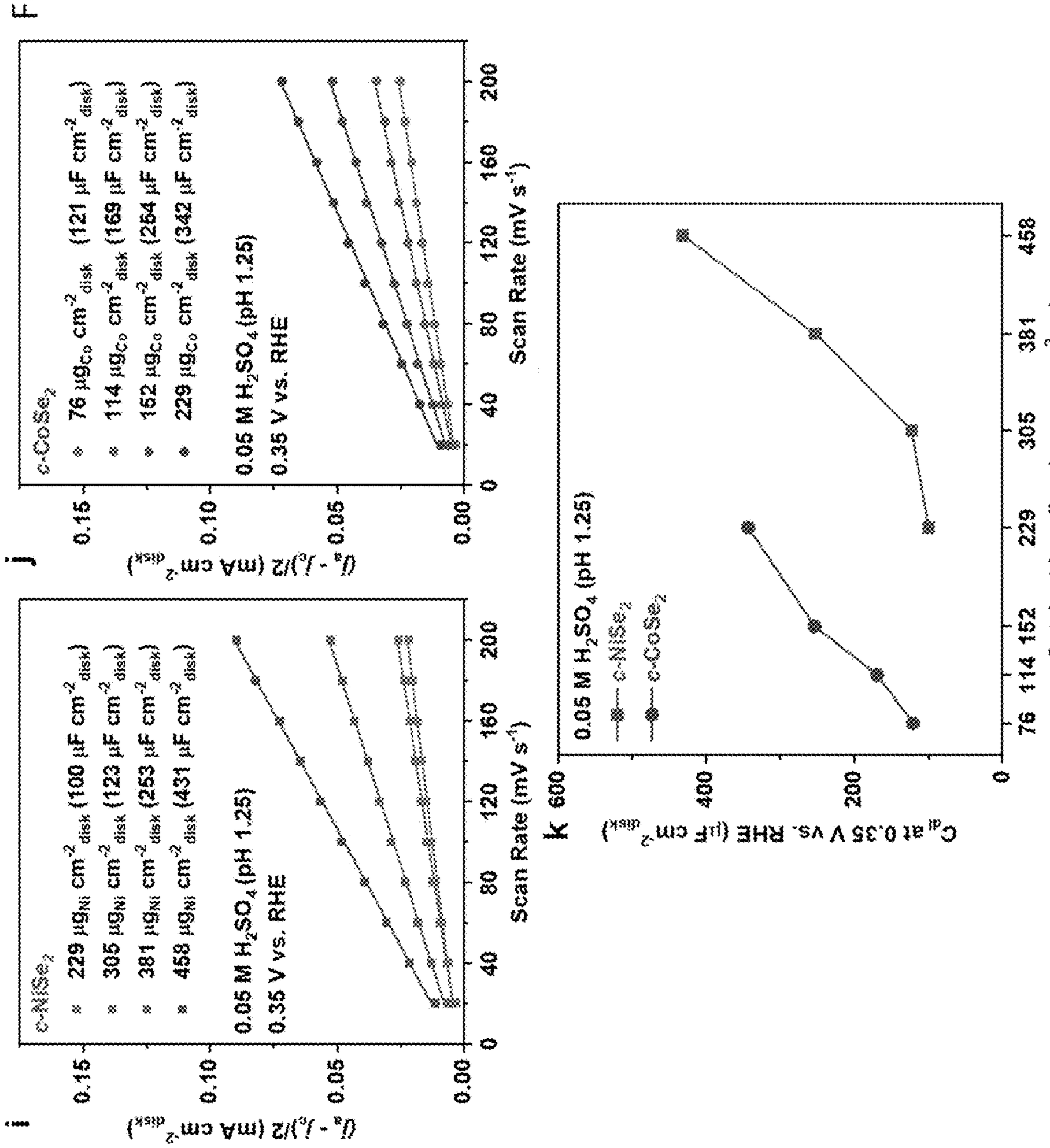

FIG. 10

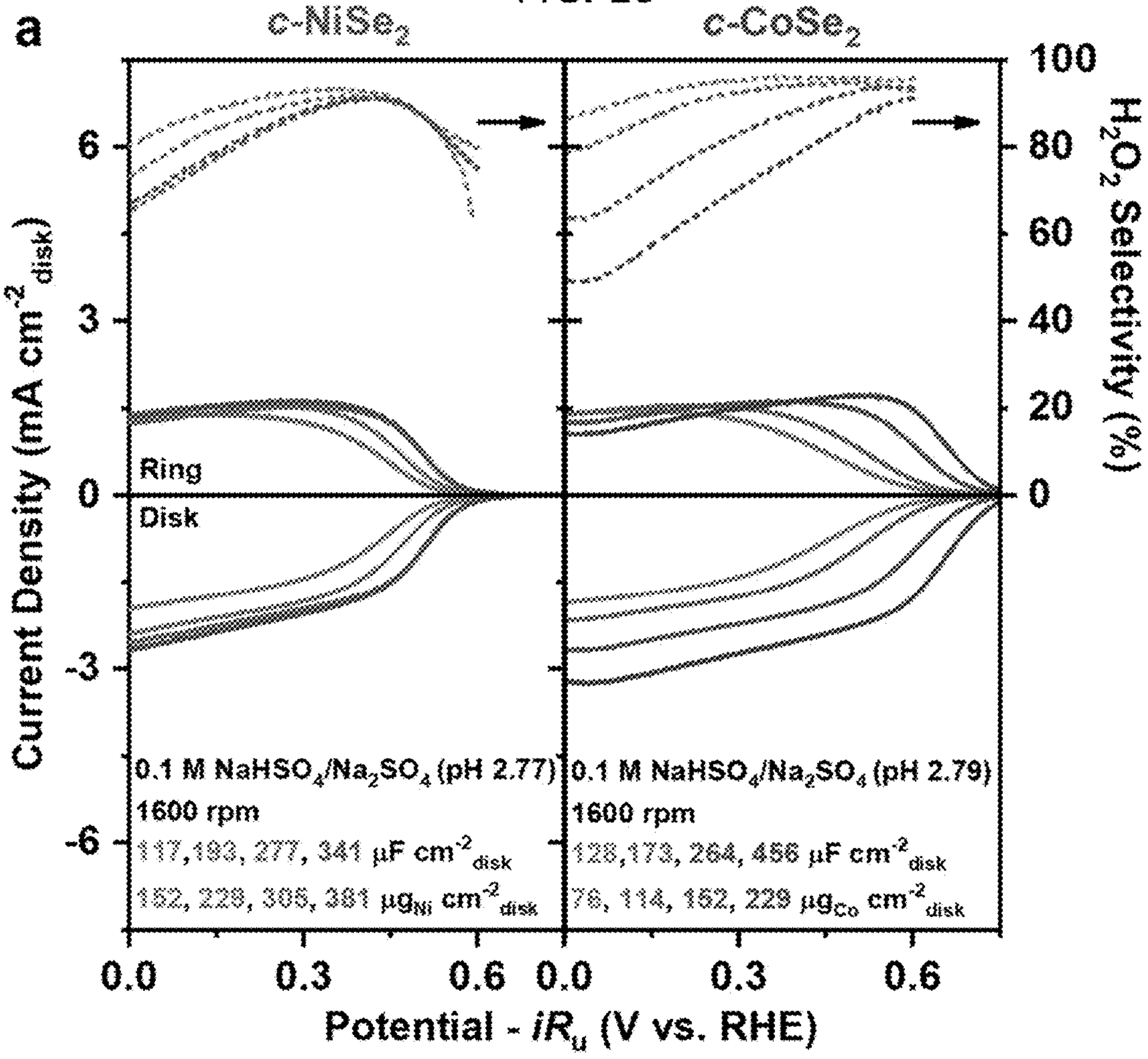
a
c-NiSe2
c-CoSe2
Ring
Disk
0.1 M NaHSO4/Na2SO4 (pH 2.77)
1600 rpm
117, 193, 277, 341 μF cm-2 disk
152, 229, 305, 381 μgNi cm-2 disk
0.1 M NaHSO4/Na2SO4 (pH 2.79)
1600 rpm
128, 173, 264, 456 μF cm-2 disk
76, 114, 152, 229 μgCo cm-2 disk
Current Density (mA cm-2 disk)
H2O2 Selectivity (%)
Potential - iRu (V vs. RHE)

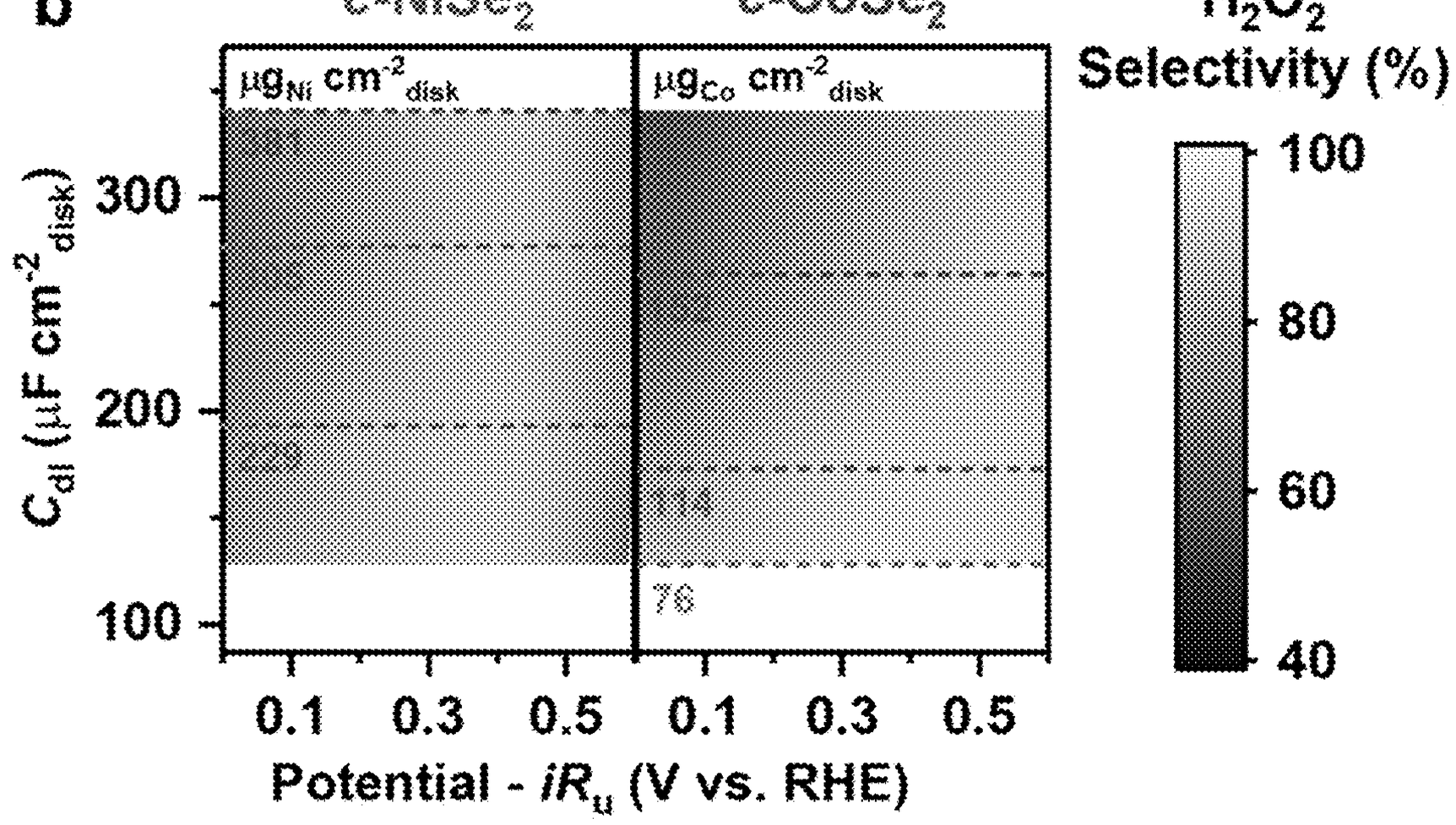
b
c-NiSe2
c-CoSe2
H2O2
μgNi cm-2 disk
μgCo cm-2 disk
76
Cdl (μF cm-2 disk)
Potential - iRu (V vs. RHE)
Selectivity (%)

FIG. 11

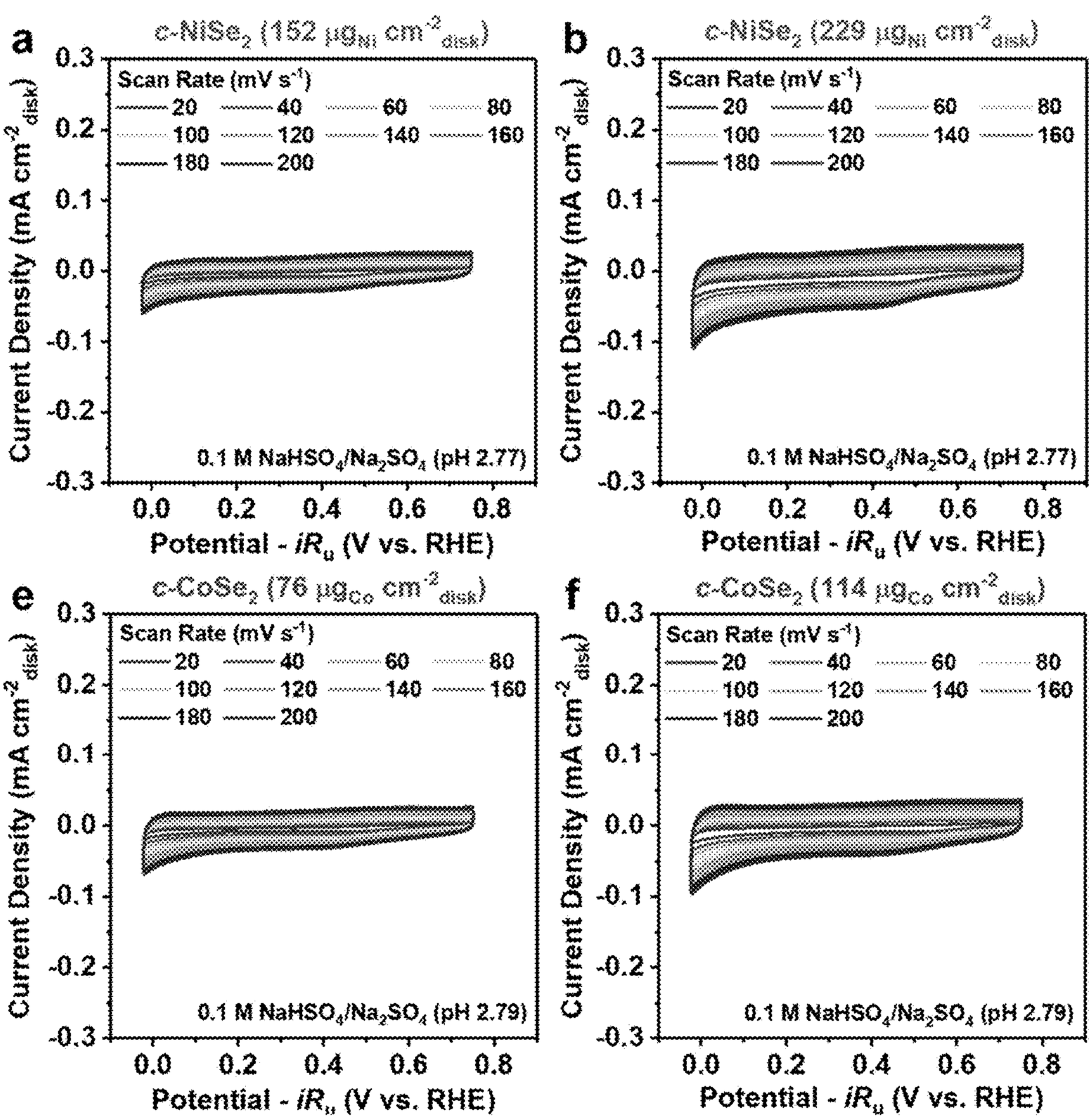
a
c-NiSe2 (152 μgNi cm-2disk)
b
c-NiSe2 (229 μgNi cm-2disk)
e
c-CoSe2 (76 μgCo cm-2disk)
f
c-CoSe2 (114 μgCo cm-2disk)
Scan Rate (mV s-1)
20 40 60 80
100 120 140 160
180 200
0.1 M NaHSO4/Na2SO4 (pH 2.77)
0.1 M NaHSO4/Na2SO4 (pH 2.79)
Current Density (mA cm-2disk)
Potential - iRu (V vs. RHE)
0.3
0.2
0.1
0.0
-0.1
-0.2
-0.3
0.0 0.2 0.4 0.6 0.8

FIG. 11 continued

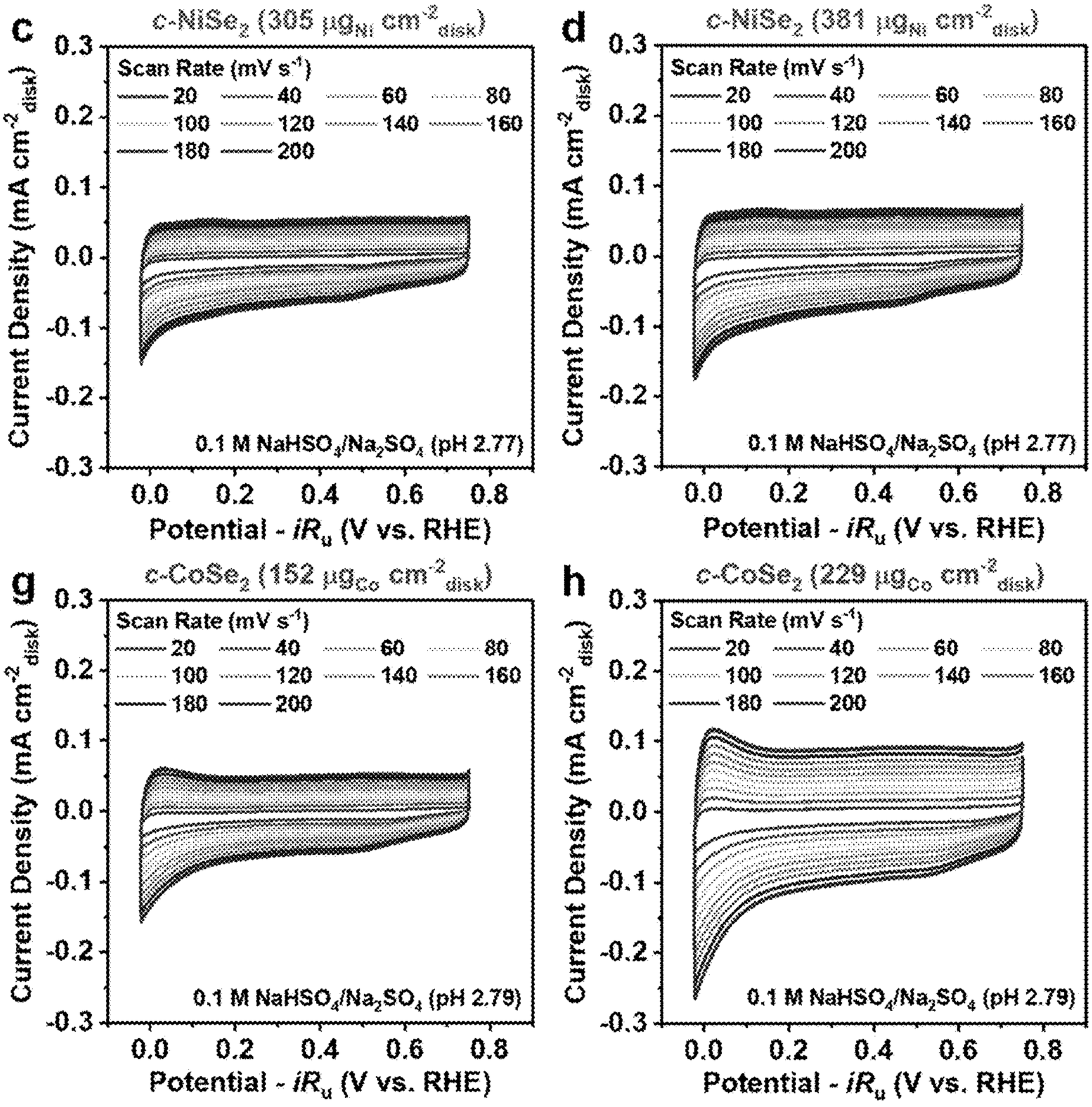

FIG. 11 continued

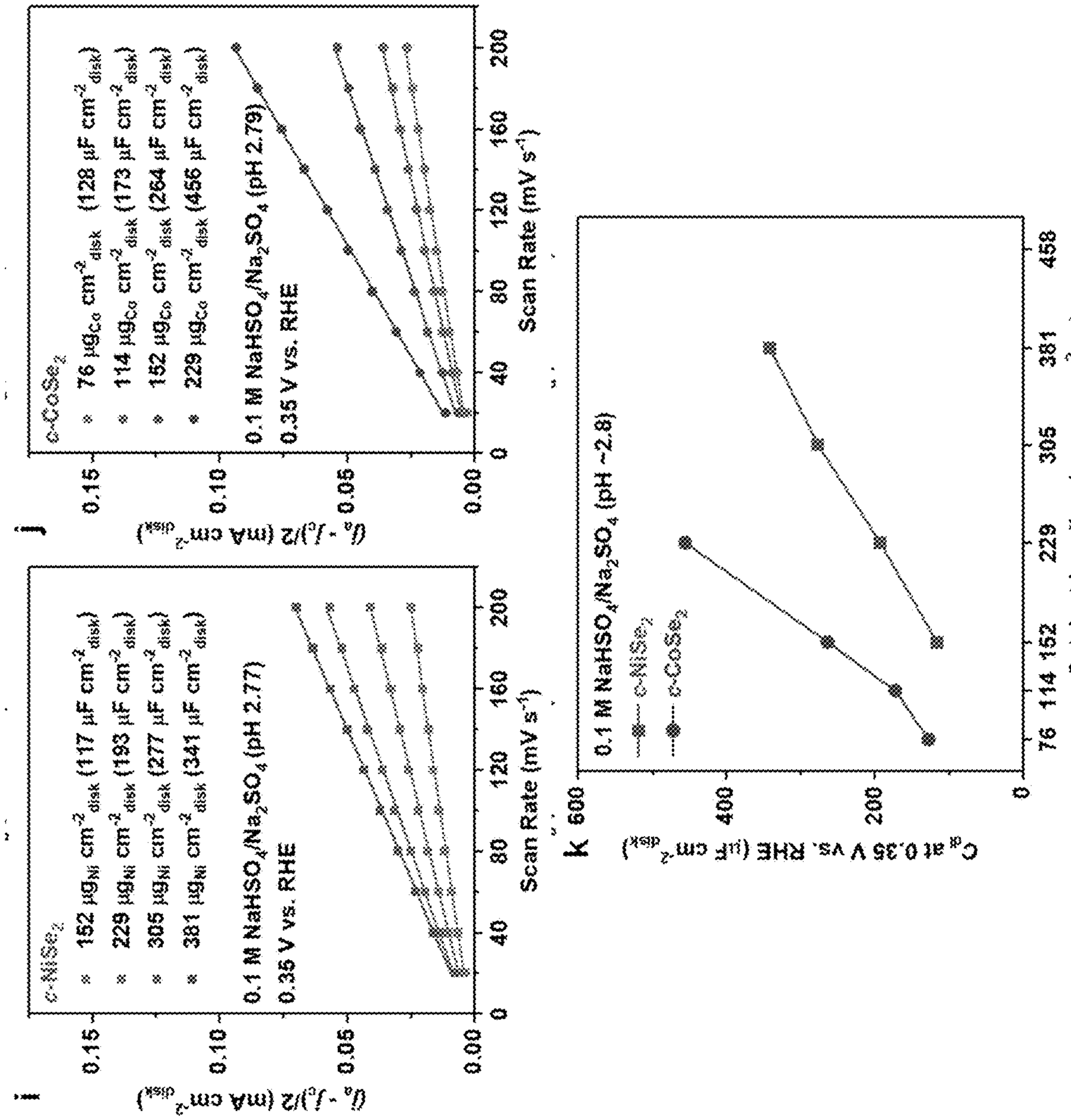

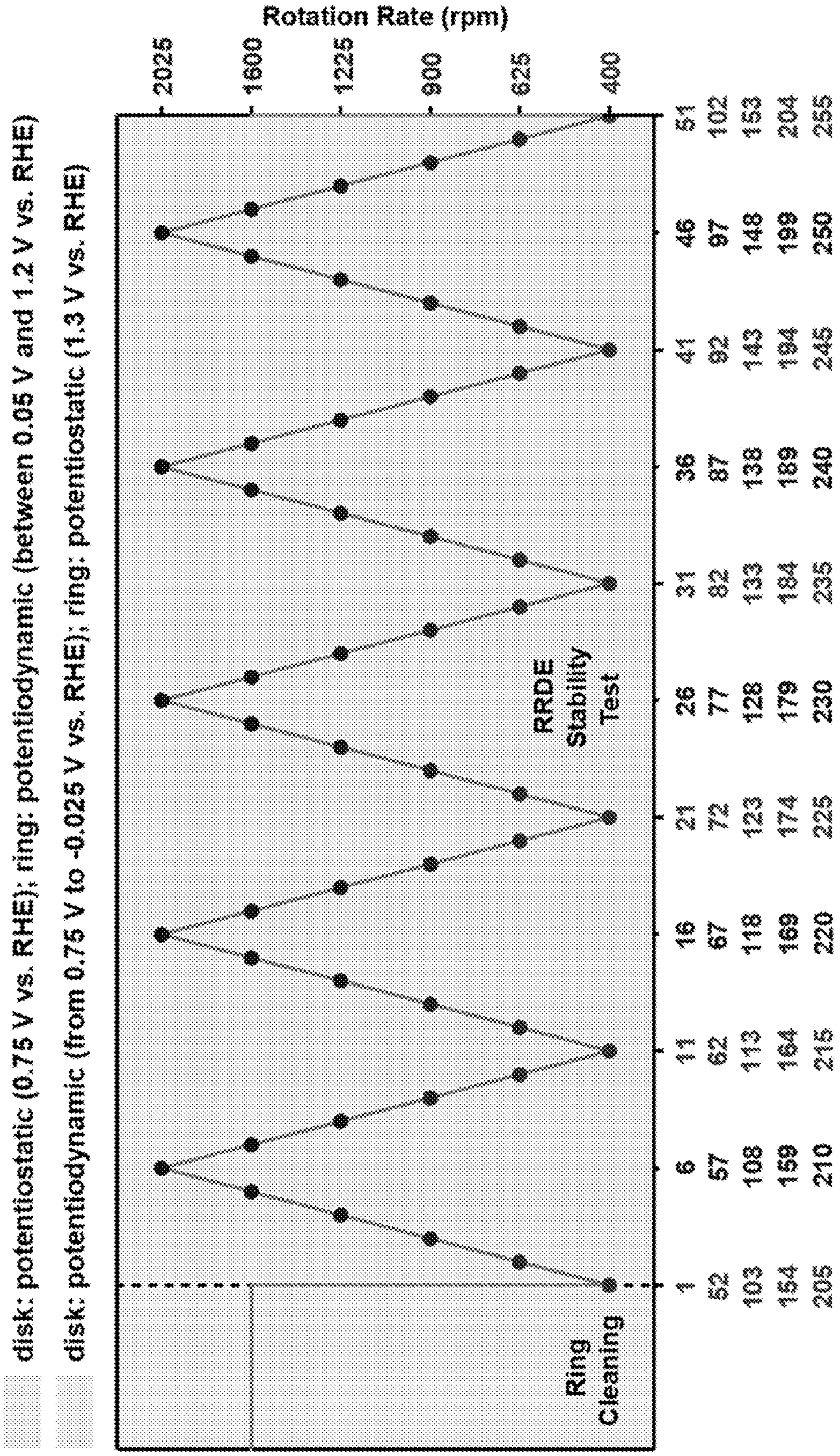
Rotation Rate (rpm)
2025
1600
1225
900
625
400
disk: potentiostatic (0.75 V vs. RHE); ring: potentiodynamic (between 0.05 V and 1.2 V vs. RHE)
disk: potentiodynamic (from 0.75 V to -0.025 V vs. RHE); ring: potentiostatic (1.3 V vs. RHE)
Ring Cleaning
RRDE Stability Test
Scan Number
1
52
103
154
205
6
57
108
159
210
11
62
113
164
215
16
67
118
169
220
21
72
123
174
225
26
77
128
179
230
31
82
133
184
235
36
87
138
189
240
41
92
143
194
245
46
97
148
199
250
51
102
153
204
255

FIG. 12

FIG. 13

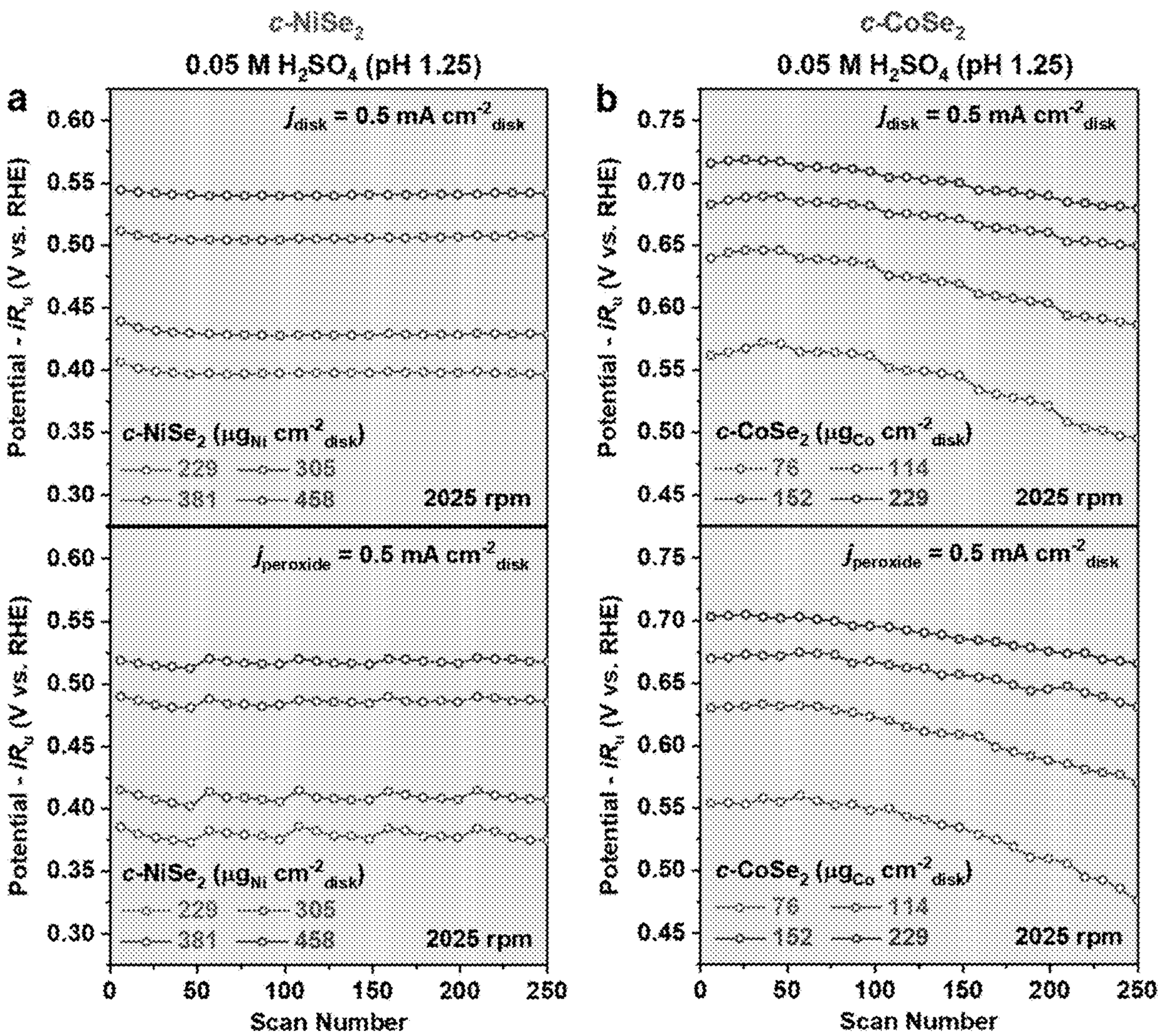
a
c-NiSe2
0.05 M H2SO4 (pH 1.25)
jdisk = 0.5 mA cm-2 disk
jperoxide = 0.5 mA cm-2 disk
Potential - iRu (V vs. RHE)
c-NiSe2 (μgNi cm-2 disk)
229
305
381
458
2025 rpm
b
c-CoSe2
0.05 M H2SO4 (pH 1.25)
jdisk = 0.5 mA cm-2 disk
jperoxide = 0.5 mA cm-2 disk
Potential - iRu (V vs. RHE)
c-CoSe2 (μgCo cm-2 disk)
76
114
152
229
2025 rpm
Scan Number

FIG. 14

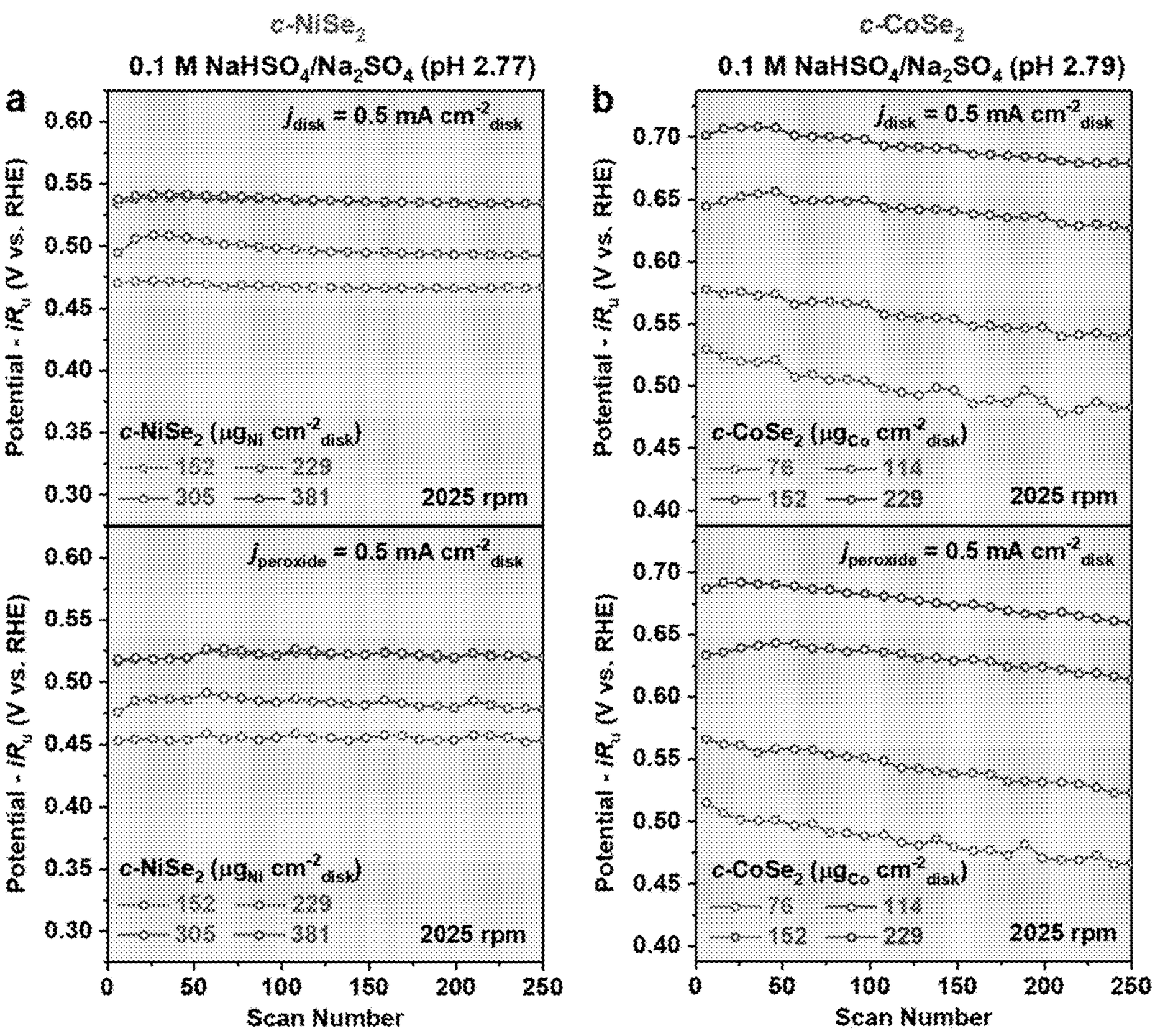
a
c-NiSe2
0.1 M NaHSO4/Na2SO4 (pH 2.77)
jdisk = 0.5 mA cm-2 disk
jperoxide = 0.5 mA cm-2 disk
c-NiSe2 (μgNi cm-2 disk)
152
229
305
381
2025 rpm
b
c-CoSe2
0.1 M NaHSO4/Na2SO4 (pH 2.79)
c-CoSe2 (μgCo cm-2 disk)
76
114
Potential - iRu (V vs. RHE)
Scan Number

FIG. 15

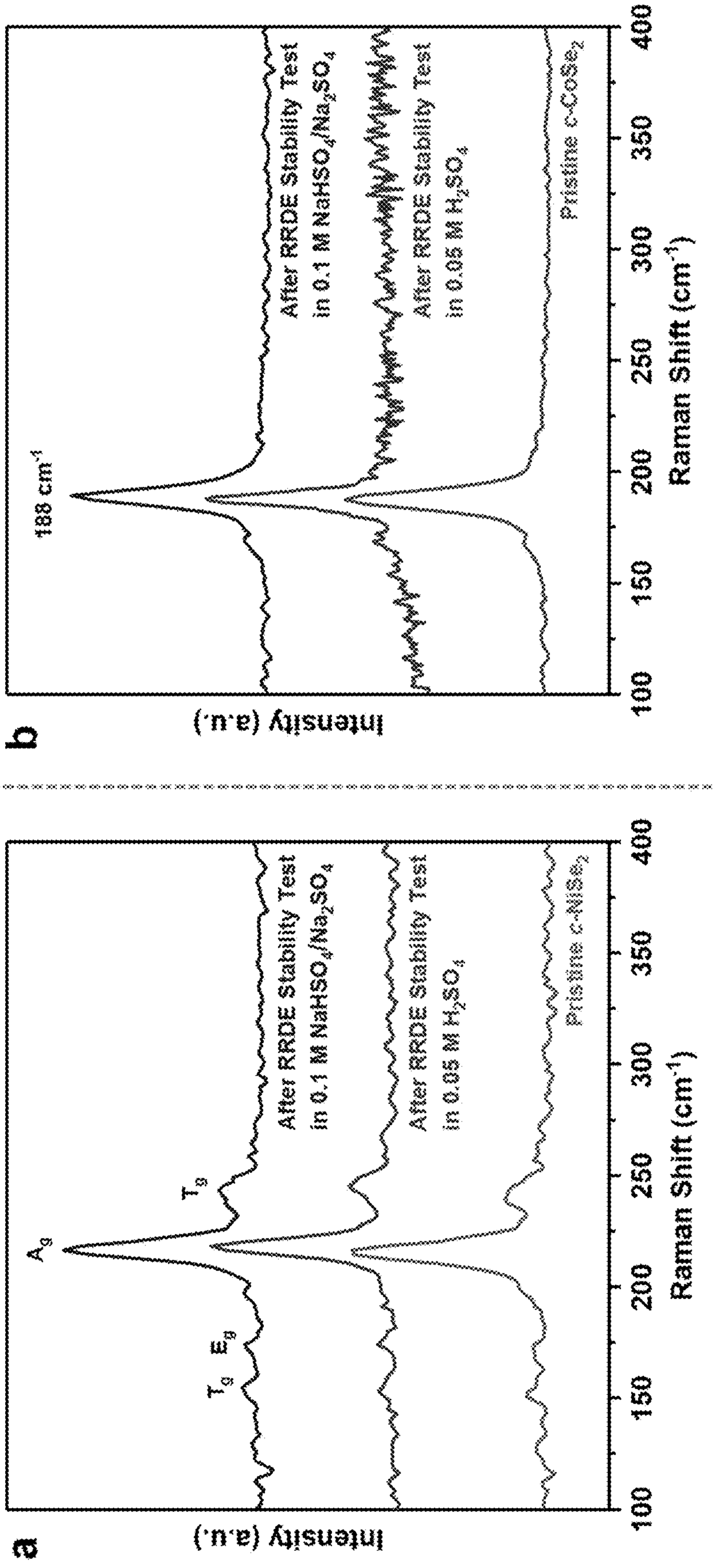
b
Intensity (a.u.)
188 cm-1
After RRDE Stability Test
in 0.1 M NaHSO4/Na2SO4
After RRDE Stability Test
in 0.05 M H2SO4
Pristine c-CoSe2
100
150
200
250
300
350
400
Raman Shift (cm-1)
a
Intensity (a.u.)
Ag
Tg
Tg Eg
After RRDE Stability Test
in 0.1 M NaHSO4/Na2SO4
After RRDE Stability Test
in 0.05 M H2SO4
Pristine c-NiSe2
100
150
200
250
300
350
400
Raman Shift (cm-1)

FIG. 15 Continued

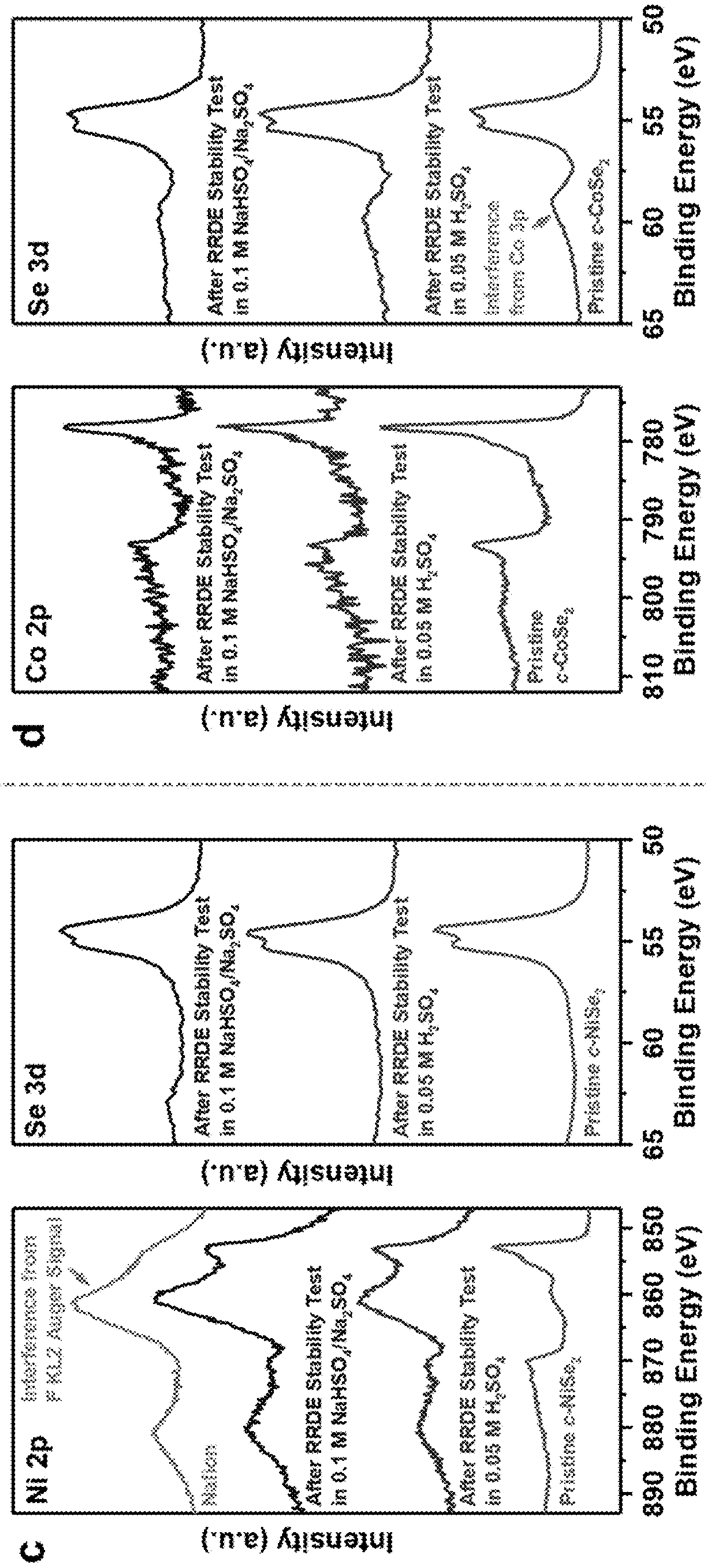

FIG. 16

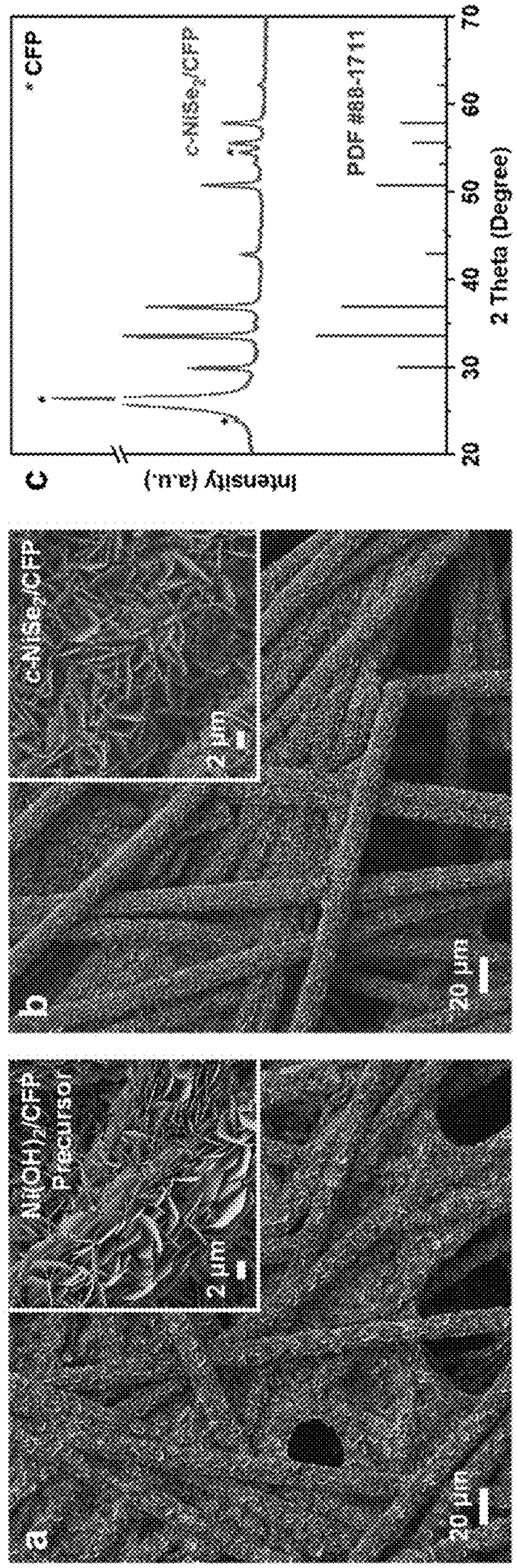
a
Ni(OH)2/CFP Precursor
2 μm
20 μm
b
c-NiSe2/CFP
2 μm
20 μm
c
* CFP
c-NiSe2/CFP
PDF #88-1711
2 Theta (Degree)
Intensity (a.u.)
d
A1g
T2g
T2g Eg
c-NiSe2/CFP
Raman Shift (cm-1)
Intensity (a.u.)
e
Ni 2p
2p3/2
2p1/2
c-NiSe2/CFP
Binding Energy (eV)
Intensity (a.u.)
f
Se 3d
3d5/2
3d3/2
c-NiSe2/CFP
Binding Energy (eV)
Intensity (a.u.)

FIG. 17

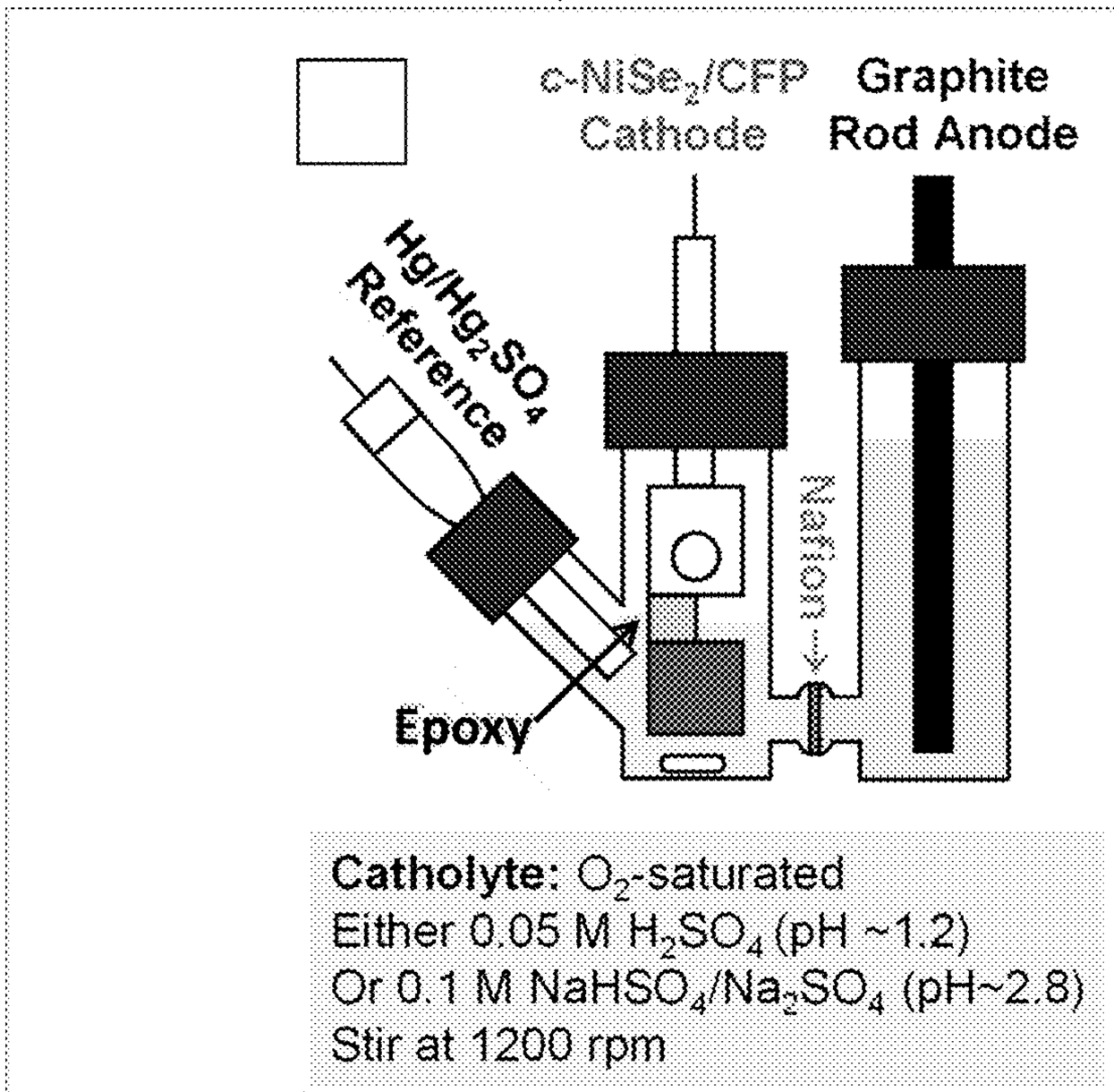
Two-Compartment Three-Electrode H-Cell for Bulk Electrosynthesis of H_2O_2 in Acidic Solution
c-$NiSe_2$/CFP Cathode
Graphite Rod Anode
Hg/Hg_2SO_4 Reference
Nafion
Epoxy
Catholyte: O_2-saturated
Either 0.05 M H_2SO_4 (pH ~1.2)
Or 0.1 M $NaHSO_4/Na_2SO_4$ (pH~2.8)
Stir at 1200 rpm
Anolyte:
0.05 M H_2SO_4 (pH ~1.2)
c-$NiSe_2$/CFP Cathode:
0.60 V vs. RHE

FIG. 18

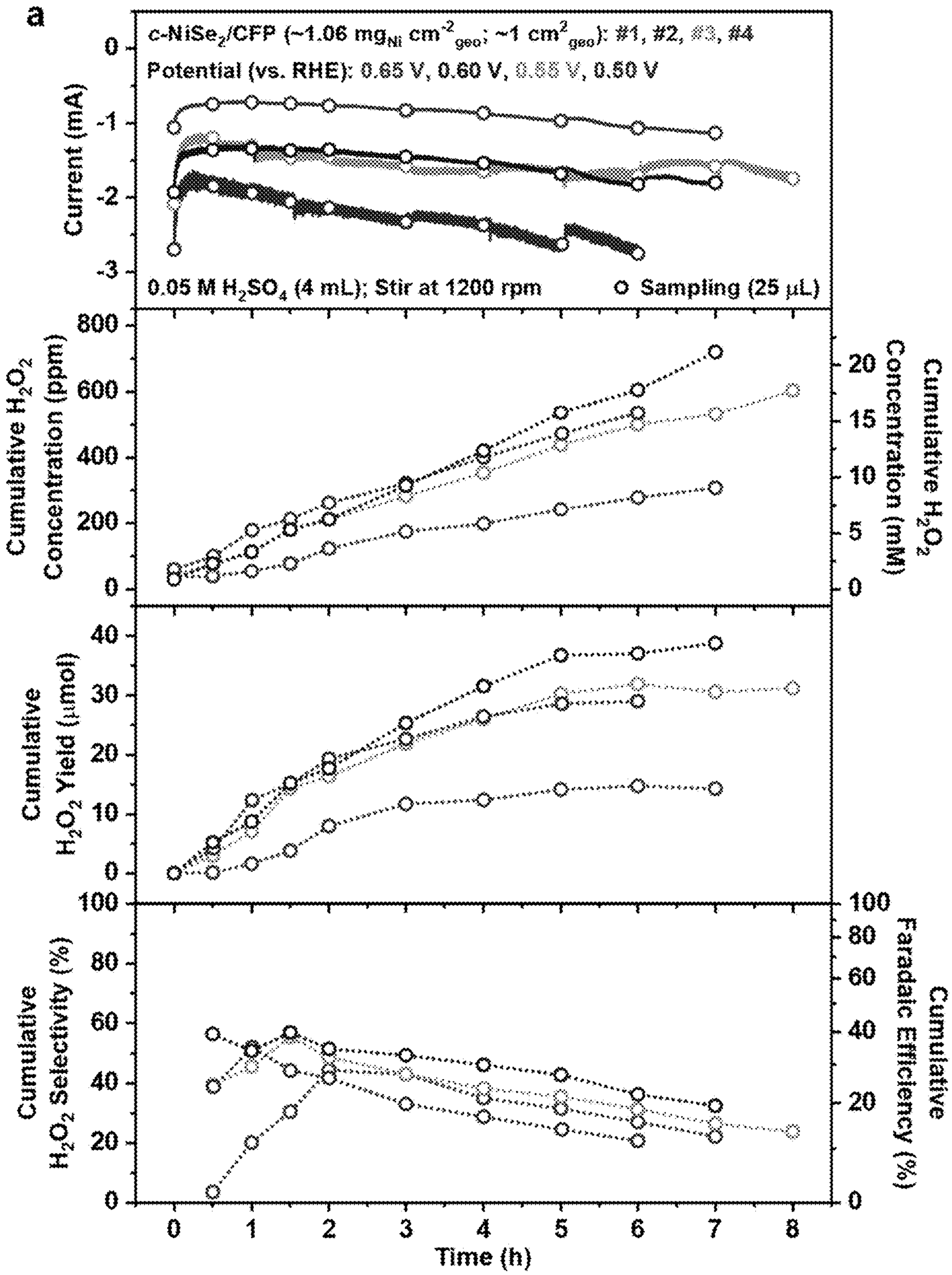
a
c-NiSe2/CFP (~1.06 mgNi cm-2geo; ~1 cm2geo): #1, #2, #3, #4
Potential (vs. RHE): 0.65 V, 0.60 V, 0.55 V, 0.50 V
0.05 M H2SO4 (4 mL); Stir at 1200 rpm
Sampling (25 μL)
Current (mA)
Cumulative H2O2 Concentration (ppm)
Cumulative H2O2 Concentration (mM)
Cumulative H2O2 Yield (μmol)
Cumulative H2O2 Selectivity (%)
Cumulative Faradaic Efficiency (%)
Time (h)

FIG. 18 Continued

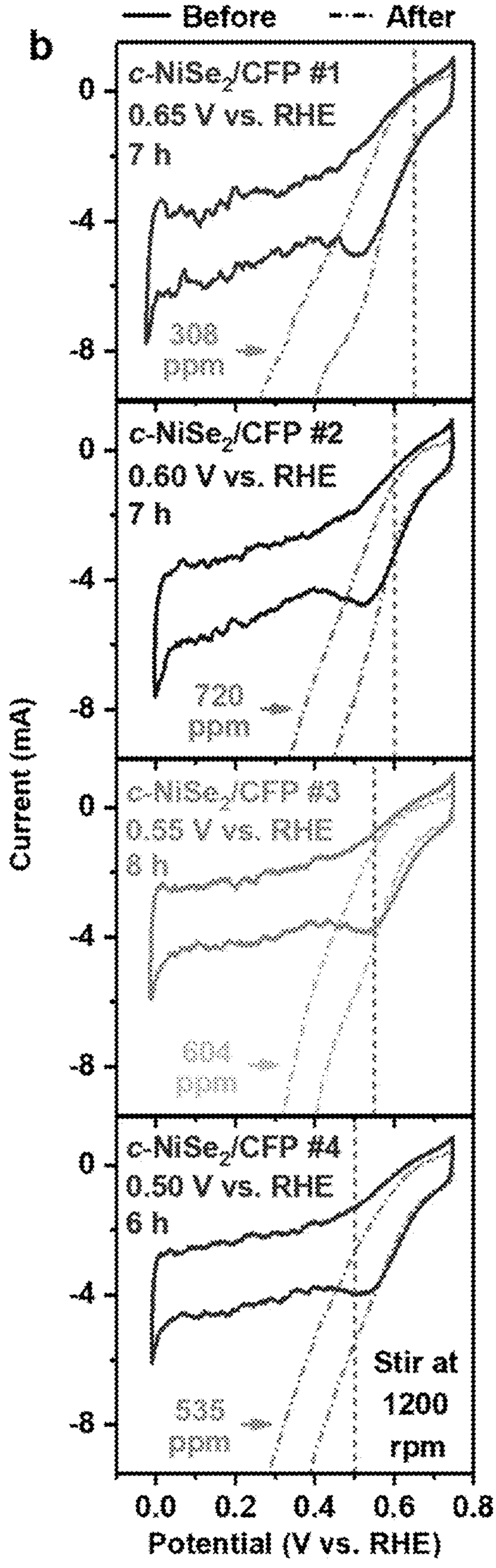

FIG. 19

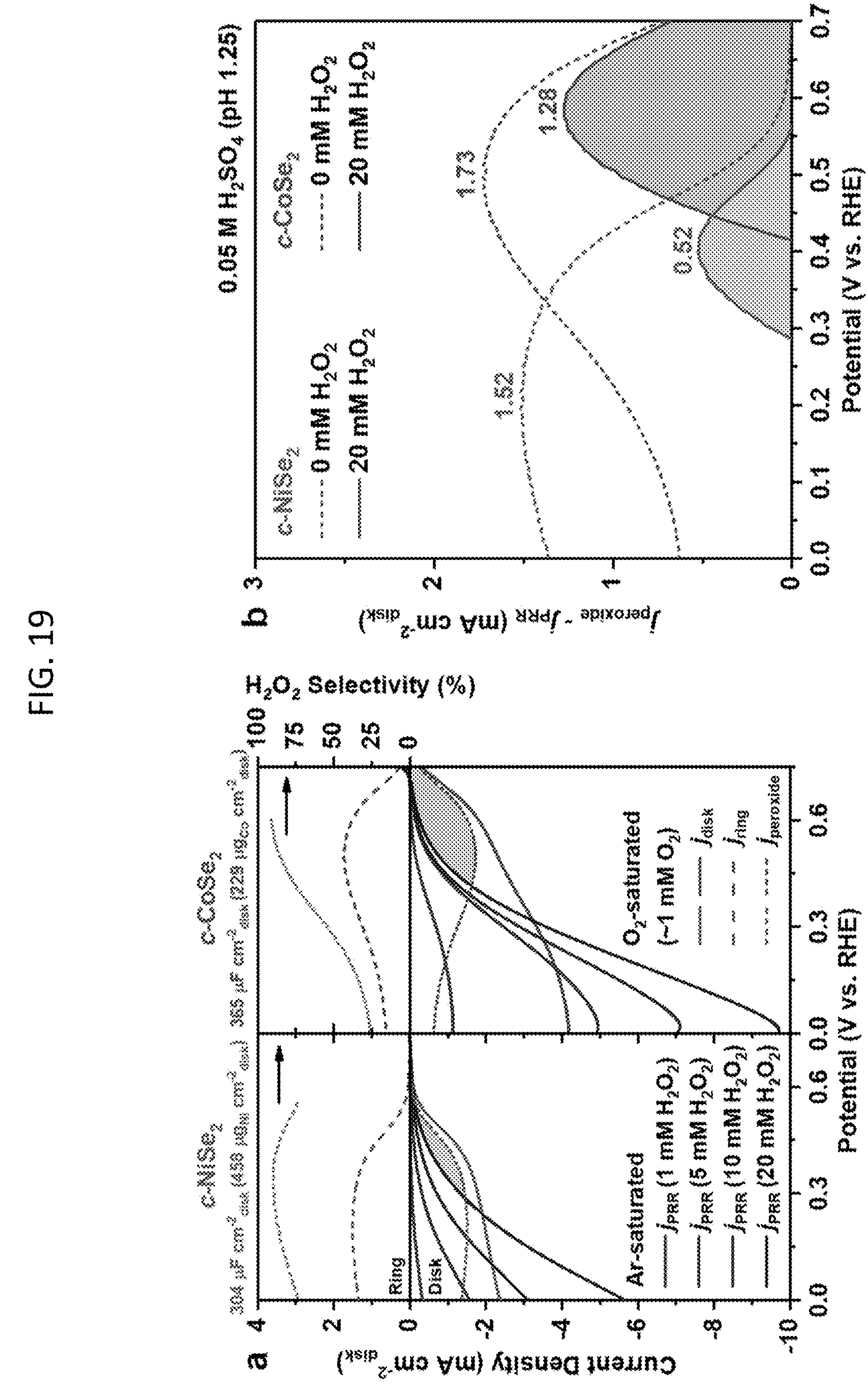
0.05 M H_2SO_4 (pH 1.25)
c-$CoSe_2$
0 mM H_2O_2
20 mM H_2O_2
1.73
1.28
1.52
0.52
$j_{peroxide}$ ~ j_{PRR} (mA cm^{-2}_{disk})
Potential (V vs. RHE)
c-$NiSe_2$
0 mM H_2O_2
20 mM H_2O_2
b
H_2O_2 Selectivity (%)
c-$CoSe_2$
O2-saturated
(~1 mM O_2)
j_{disk}
j_{ring}
$j_{peroxide}$
c-$NiSe_2$
Ring
Disk
Ar-saturated
j_{PRR} (1 mM H_2O_2)
j_{PRR} (5 mM H_2O_2)
j_{PRR} (10 mM H_2O_2)
j_{PRR} (20 mM H_2O_2)
Current Density (mA cm^{-2}_{disk})
a
Potential (V vs. RHE)

FIG. 20

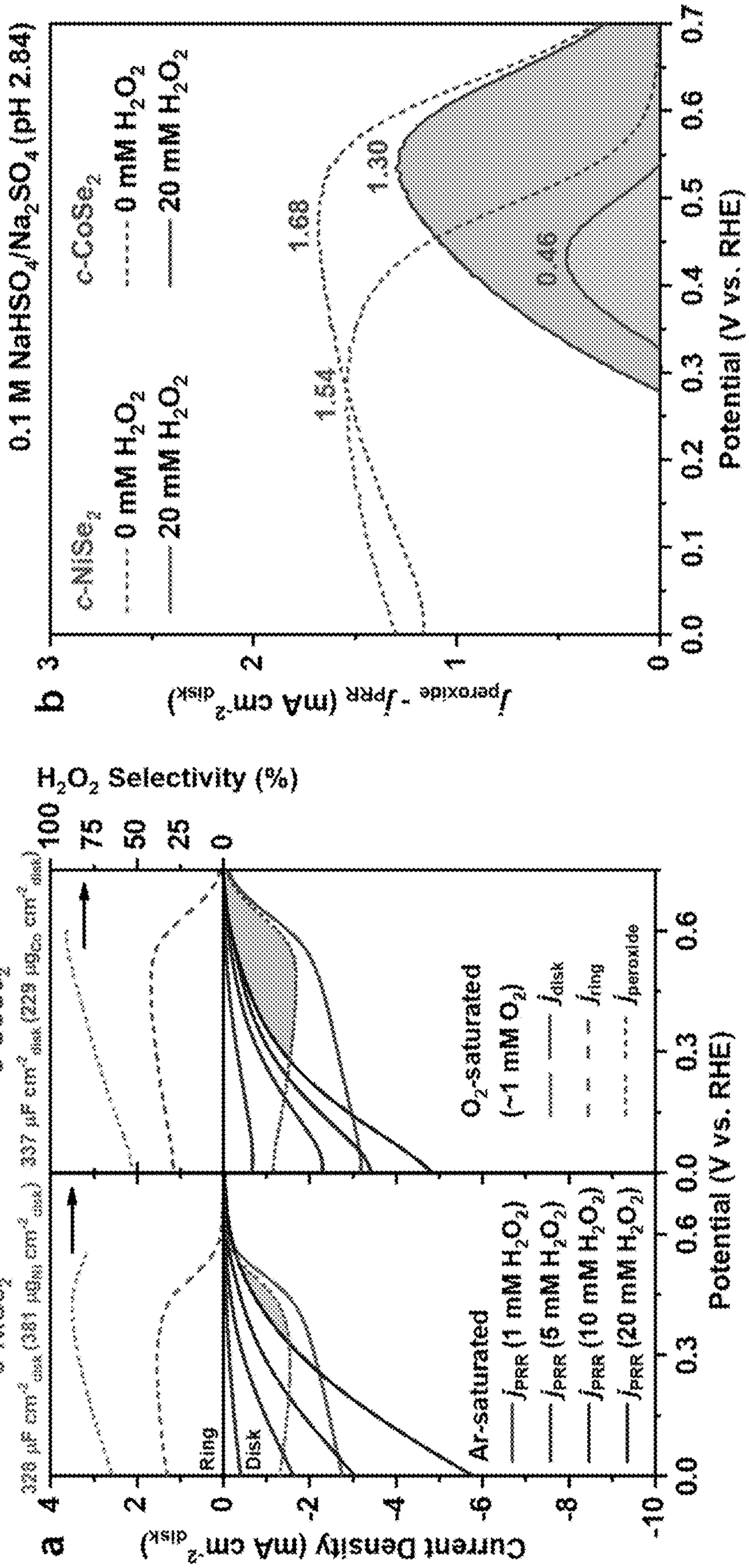
0.1 M NaHSO4/Na2SO4 (pH 2.84)
c-CoSe2
0 mM H2O2
20 mM H2O2
1.68
1.54
1.30
0.46
Potential (V vs. RHE)
b
Jperoxide - JPRR (mA cm-2disk)
c-NiSe2
H2O2 Selectivity (%)
O2-saturated
(~1 mM O2)
Jdisk
Jring
Jperoxide
a
Current Density (mA cm-2disk)
Ring
Disk
Ar-saturated
JPRR (1 mM H2O2)
JPRR (5 mM H2O2)
JPRR (10 mM H2O2)
JPRR (20 mM H2O2)

FIG. 21

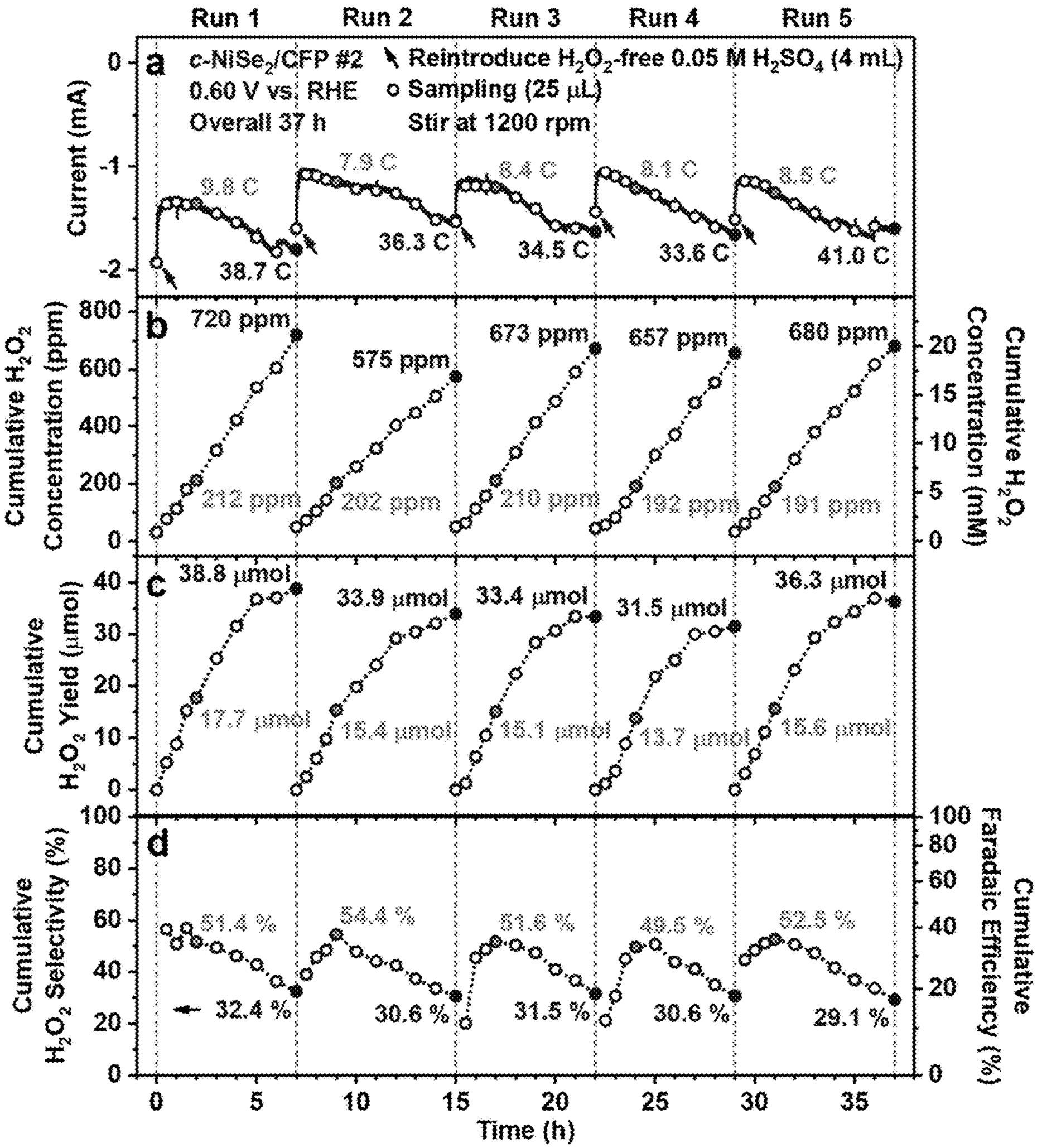
Run 1
Run 2
Run 3
Run 4
Run 5
a
c-NiSe2/CFP #2
0.60 V vs. RHE
Overall 37 h
Reintroduce H2O2-free 0.05 M H2SO4 (4 mL)
Sampling (25 μL)
Stir at 1200 rpm
Current (mA)
9.8 C
38.7 C
7.9 C
36.3 C
8.4 C
34.5 C
8.1 C
33.6 C
8.5 C
41.0 C
b
720 ppm
575 ppm
673 ppm
657 ppm
680 ppm
212 ppm
202 ppm
210 ppm
192 ppm
191 ppm
Cumulative H2O2 Concentration (ppm)
Cumulative H2O2 Concentration (mM)
c
38.8 μmol
33.9 μmol
33.4 μmol
31.5 μmol
36.3 μmol
17.7 μmol
16.4 μmol
15.1 μmol
13.7 μmol
15.6 μmol
Cumulative H2O2 Yield (μmol)
d
51.4 %
54.4 %
51.8 %
49.6 %
52.5 %
32.4 %
30.6 %
31.5 %
30.6 %
29.1 %
Cumulative H2O2 Selectivity (%)
Cumulative Faradaic Efficiency (%)
Time (h)

FIG. 22

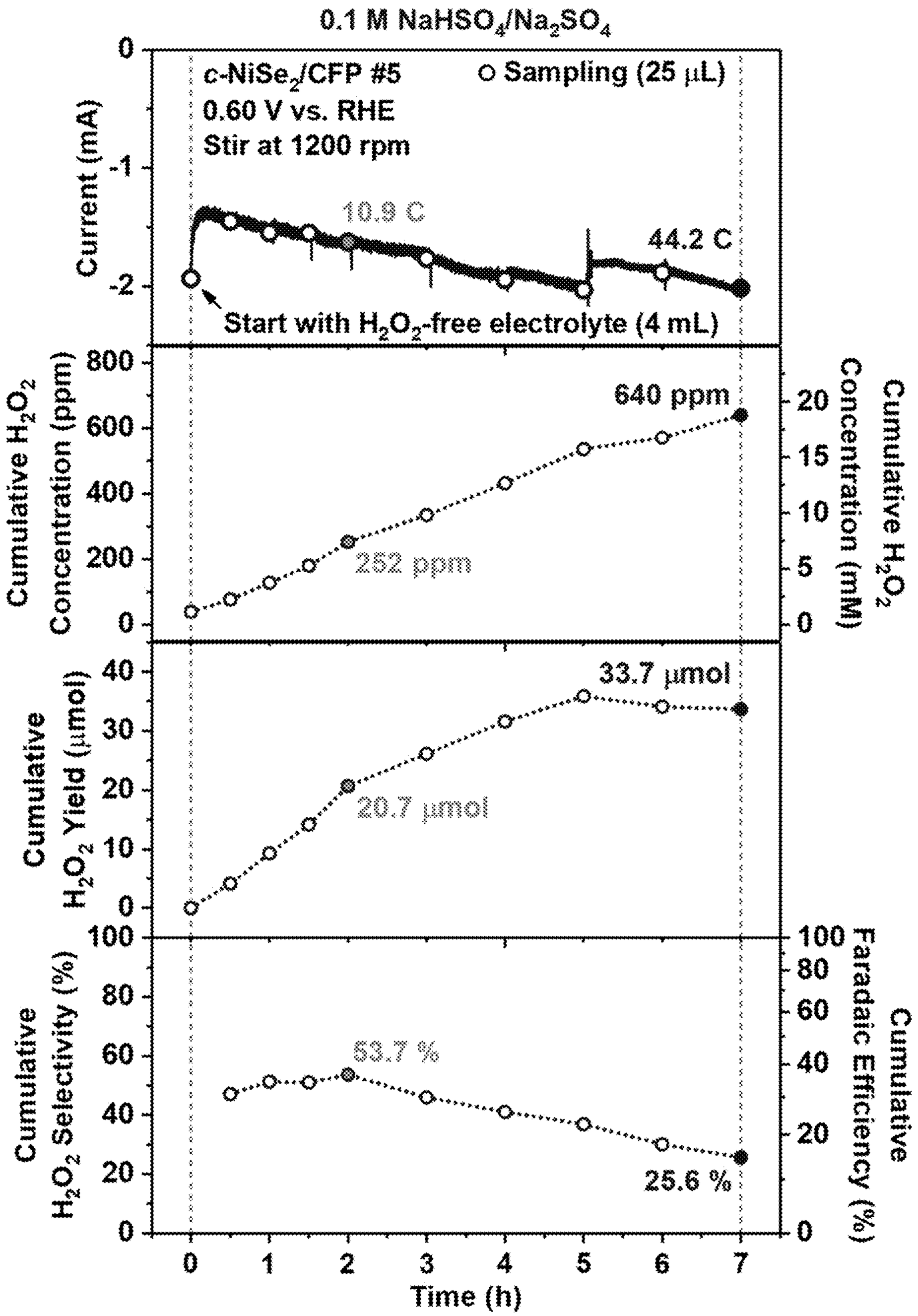
0.1 M NaHSO4/Na2SO4
c-NiSe2/CFP #5
0.60 V vs. RHE
Stir at 1200 rpm
Sampling (25 μL)
10.9 C
44.2 C
Start with H2O2-free electrolyte (4 mL)
Current (mA)
Cumulative H2O2 Concentration (ppm)
640 ppm
252 ppm
Cumulative H2O2 Concentration (mM)
Cumulative H2O2 Yield (μmol)
33.7 μmol
20.7 μmol
Cumulative H2O2 Selectivity (%)
63.7 %
25.6 %
Cumulative Faradaic Efficiency (%)
Time (h)

FIG. 23

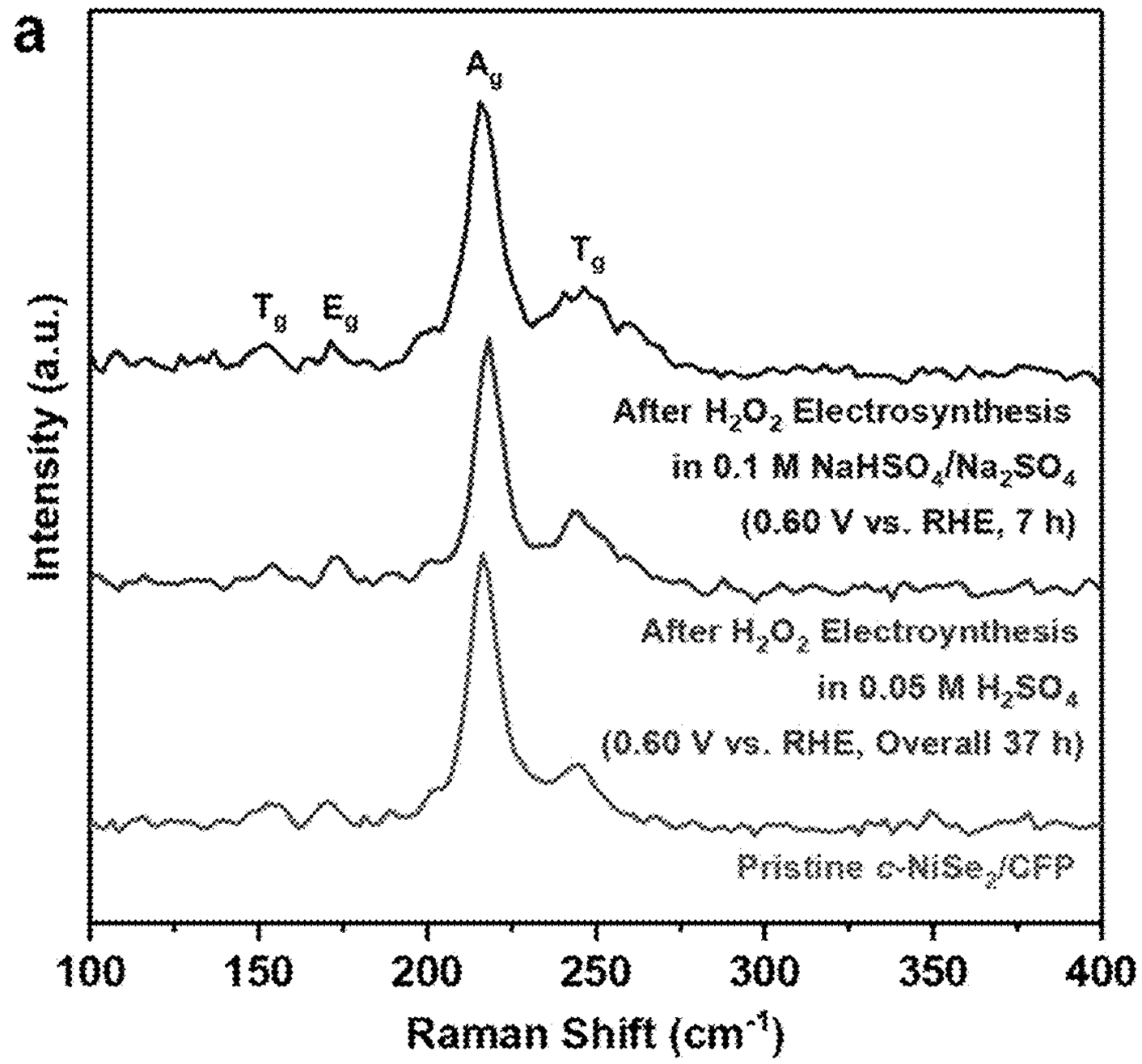
a
Intensity (a.u.)
A_g
T_g
T_g
E_g
After H_2O_2 Electrosynthesis in 0.1 M $NaHSO_4/Na_2SO_4$ (0.60 V vs. RHE, 7 h)
After H_2O_2 Electroynthesis in 0.05 M H_2SO_4 (0.60 V vs. RHE, Overall 37 h)
Pristine c-$NiSe_2$/CFP
100
150
200
250
300
350
400
Raman Shift (cm^{-1})

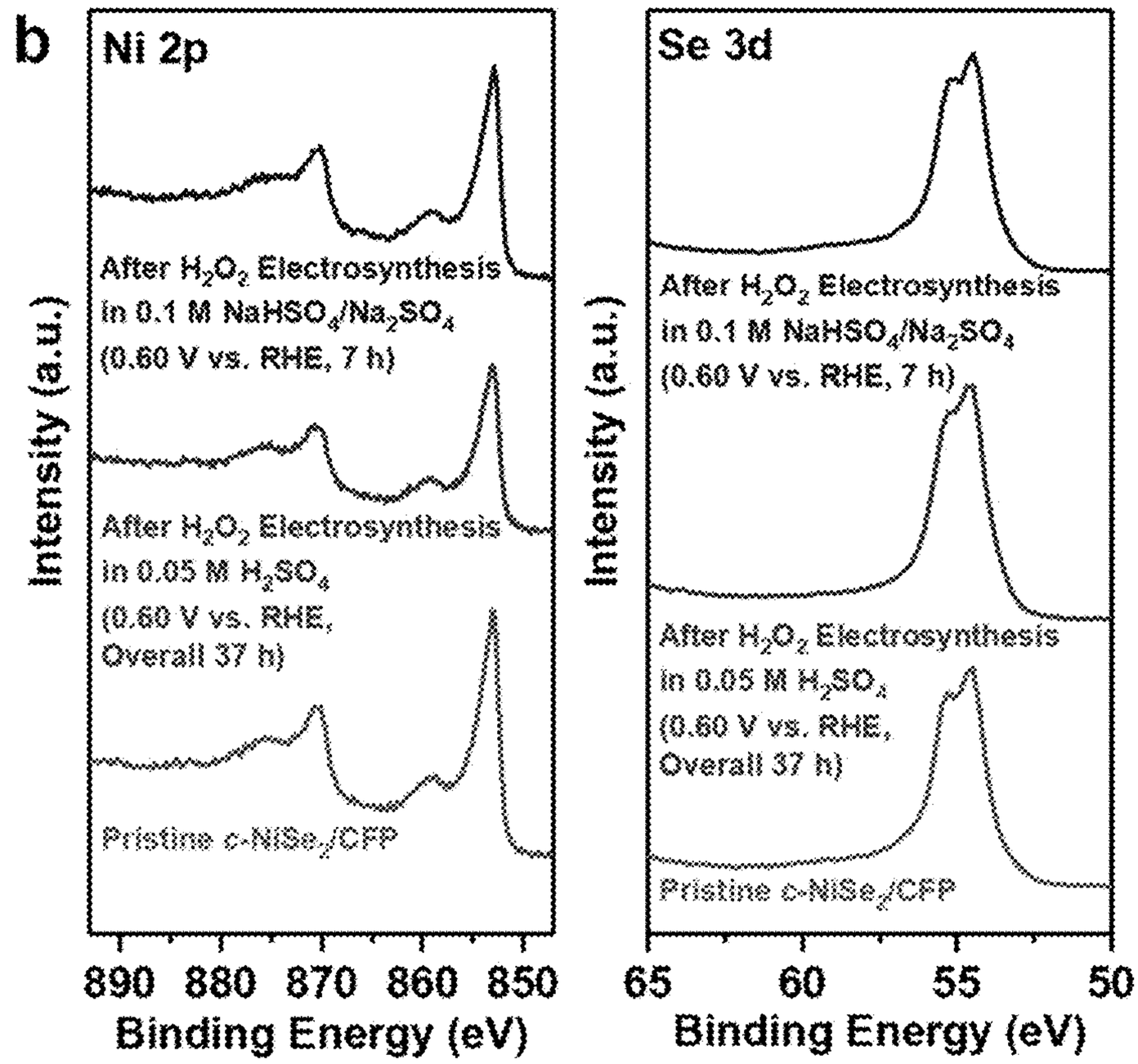
b
Ni 2p
Se 3d
Intensity (a.u.)
After H_2O_2 Electrosynthesis in 0.1 M $NaHSO_4/Na_2SO_4$ (0.60 V vs. RHE, 7 h)
After H_2O_2 Electrosynthesis in 0.05 M H_2SO_4 (0.60 V vs. RHE, Overall 37 h)
Pristine c-$NiSe_2$/CFP
890
880
870
860
850
65
60
55
50
Binding Energy (eV)

FIG. 23 continued

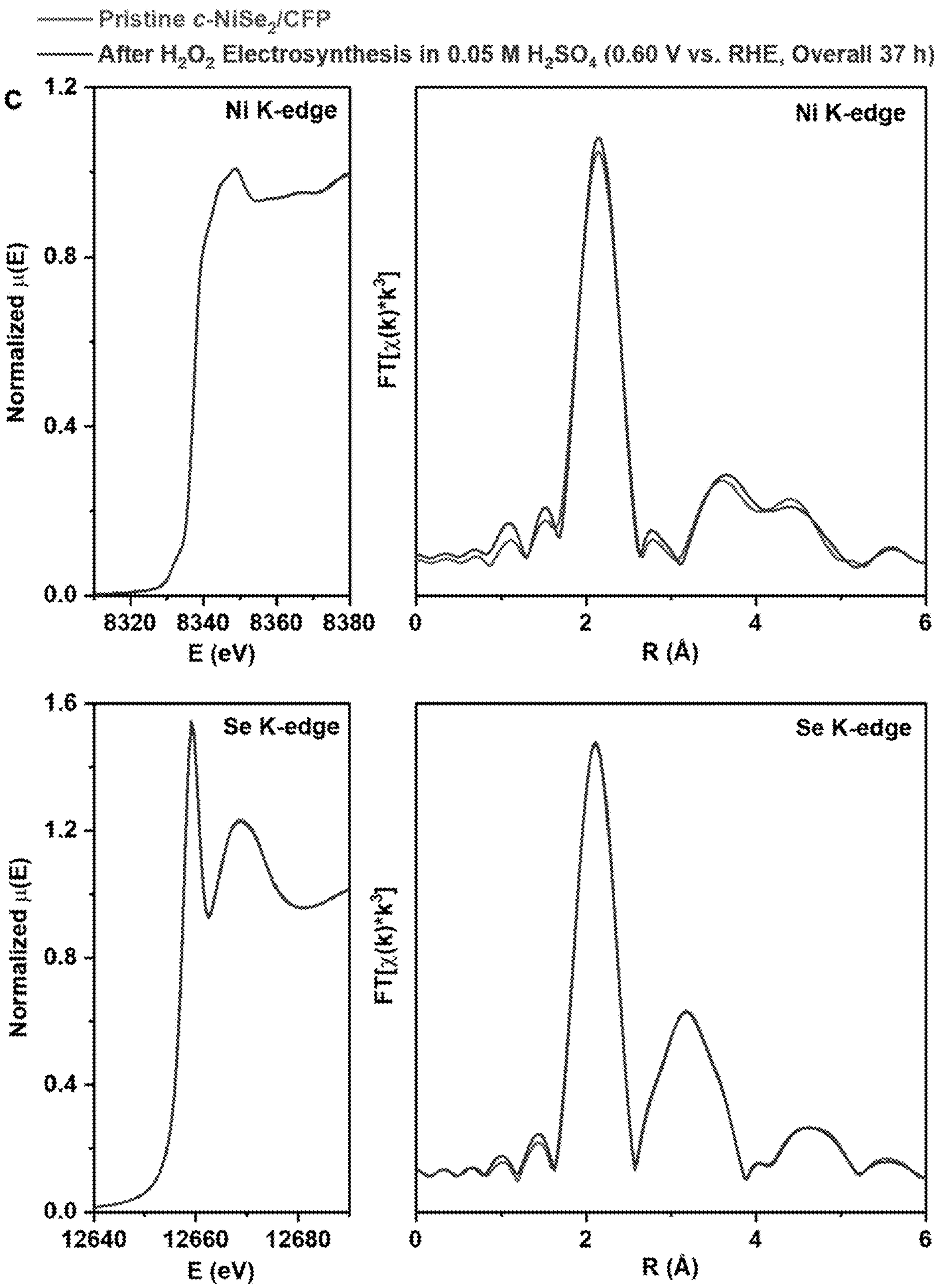

FIG. 23 continued

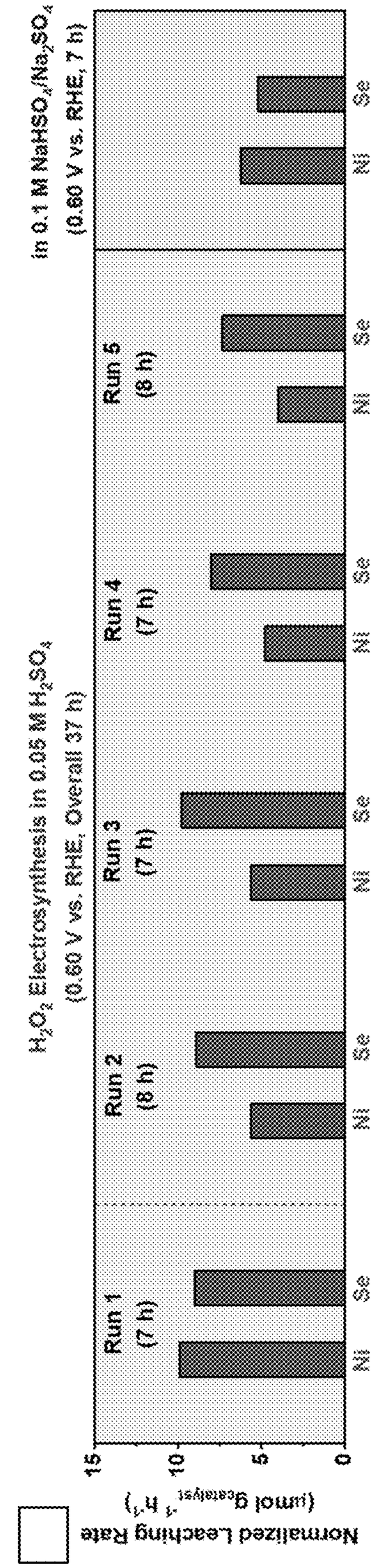

FIG. 24

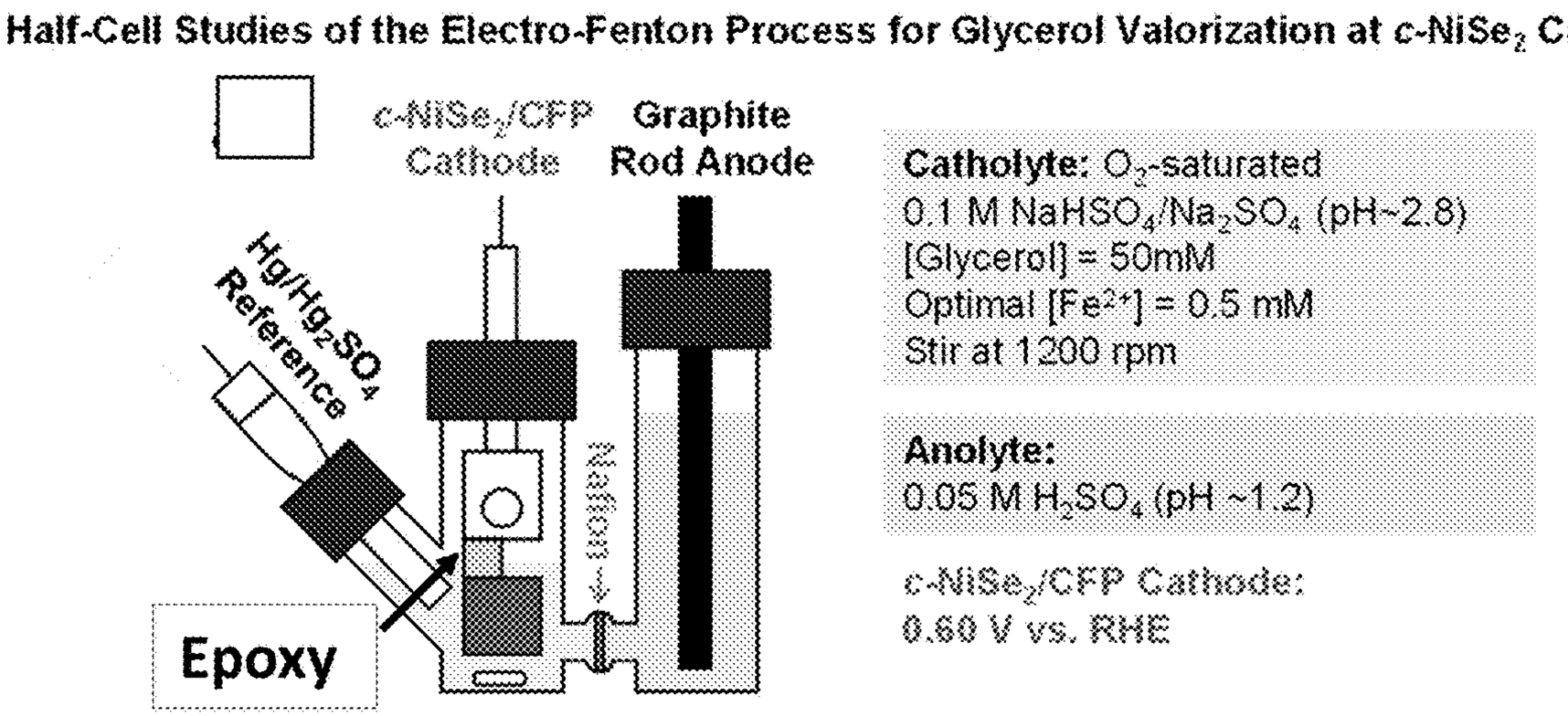
Half-Cell Studies of the Electro-Fenton Process for Glycerol Valorization at c-NiSe2 Cathode
c-NiSe2/CFP Cathode
Graphite Rod Anode
Hg/Hg2SO4 Reference
Nafion
Epoxy
Catholyte: O2-saturated
0.1 M NaHSO4/Na2SO4 (pH~2.8)
[Glycerol] = 50mM
Optimal [Fe2+] = 0.5 mM
Stir at 1200 rpm
Anolyte:
0.05 M H2SO4 (pH ~1.2)
c-NiSe2/CFP Cathode:
0.60 V vs. RHE

FIG. 25

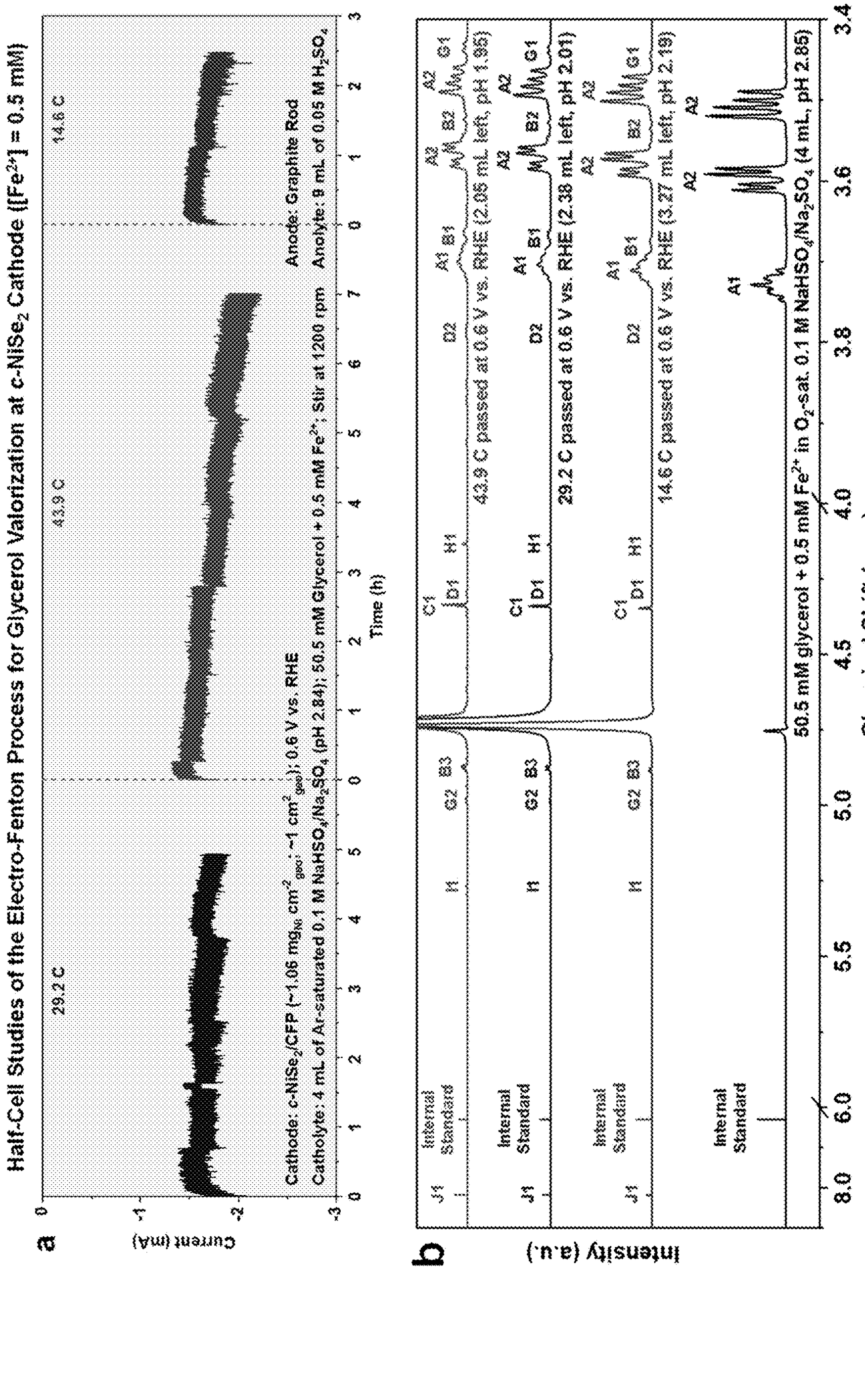
Half-Cell Studies of the Electro-Fenton Process for Glycerol Valorization at c-NiSe2 Cathode ([Fe2+] = 0.5 mM)
a
Current (mA)
Time (h)
29.2 C
43.9 C
14.6 C
Cathode: c-NiSe2/CFP (~1.05 mgNi cm-2geo; ~1 cm2geo); 0.6 V vs. RHE
Catholyte: 4 mL of Ar-saturated 0.1 M NaHSO4/Na2SO4 (pH 2.84); 50.5 mM Glycerol + 0.5 mM Fe2+; Stir at 1200 rpm
Anode: Graphite Rod
Analyte: 8 mL of 0.05 M H2SO4
b
Intensity (a.u.)
Chemical Shift (ppm)
50.5 mM glycerol + 0.5 mM Fe2+ in O2-sat. 0.1 M NaHSO4/Na2SO4 (4 mL, pH 2.85)
14.6 C passed at 0.6 V vs. RHE (3.27 mL left, pH 2.19)
29.2 C passed at 0.6 V vs. RHE (2.38 mL left, pH 2.01)
43.9 C passed at 0.6 V vs. RHE (2.05 mL left, pH 1.95)
Internal Standard
A1
A2
B1
B2
B3
C1
D1
D2
G1
G2
H1
H2

FIG. 25 continued

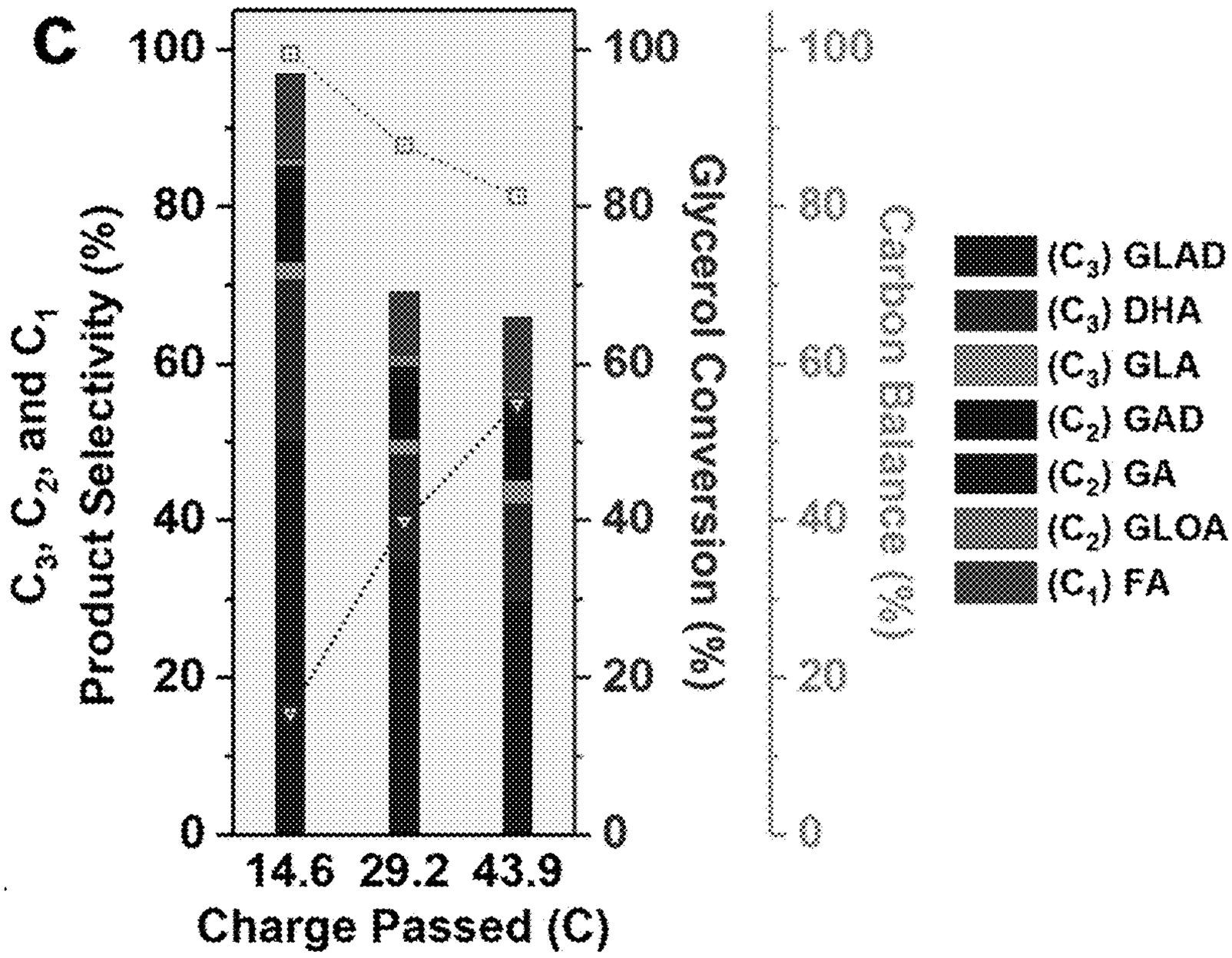

FIG. 26

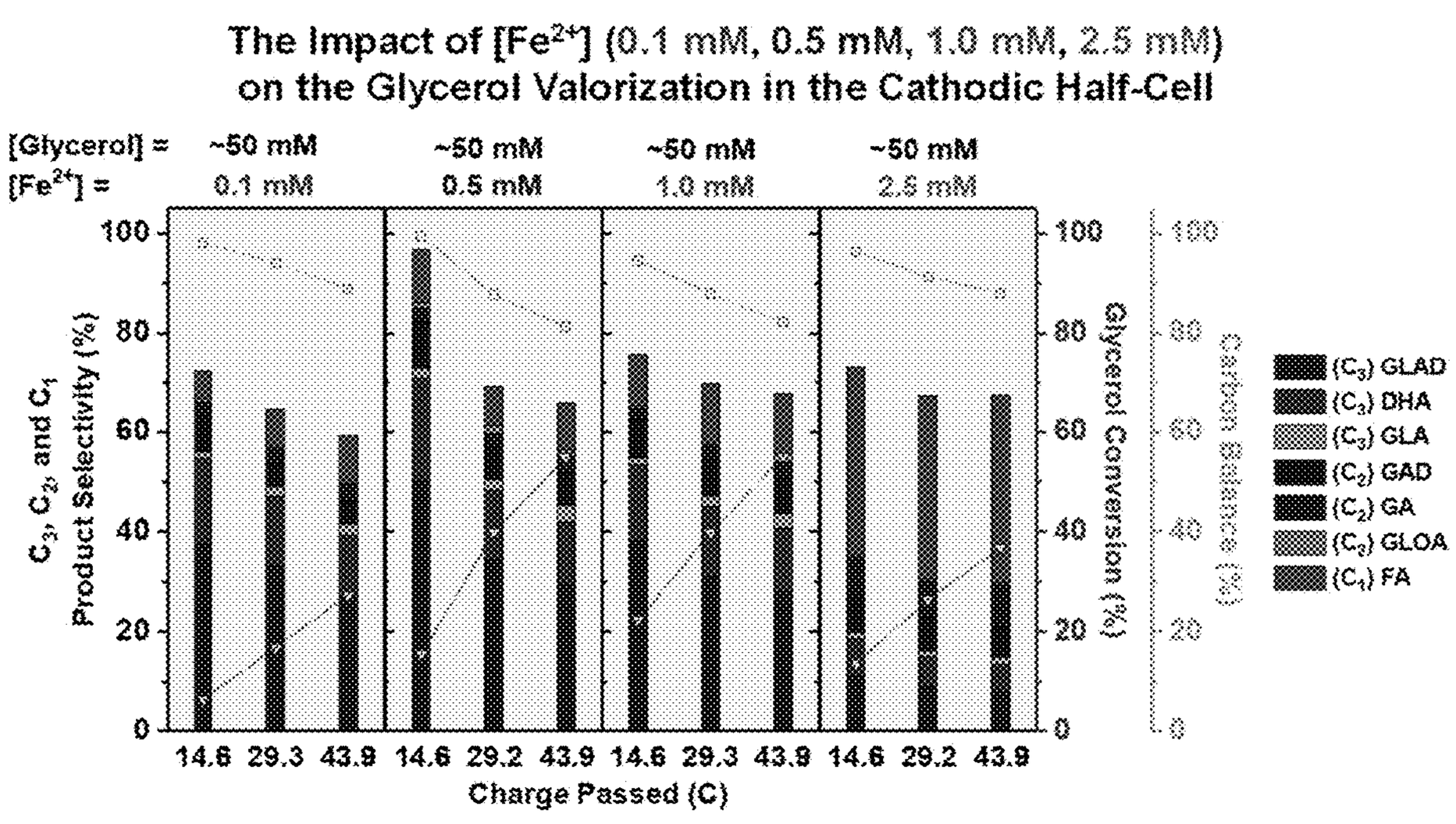

FIG. 27

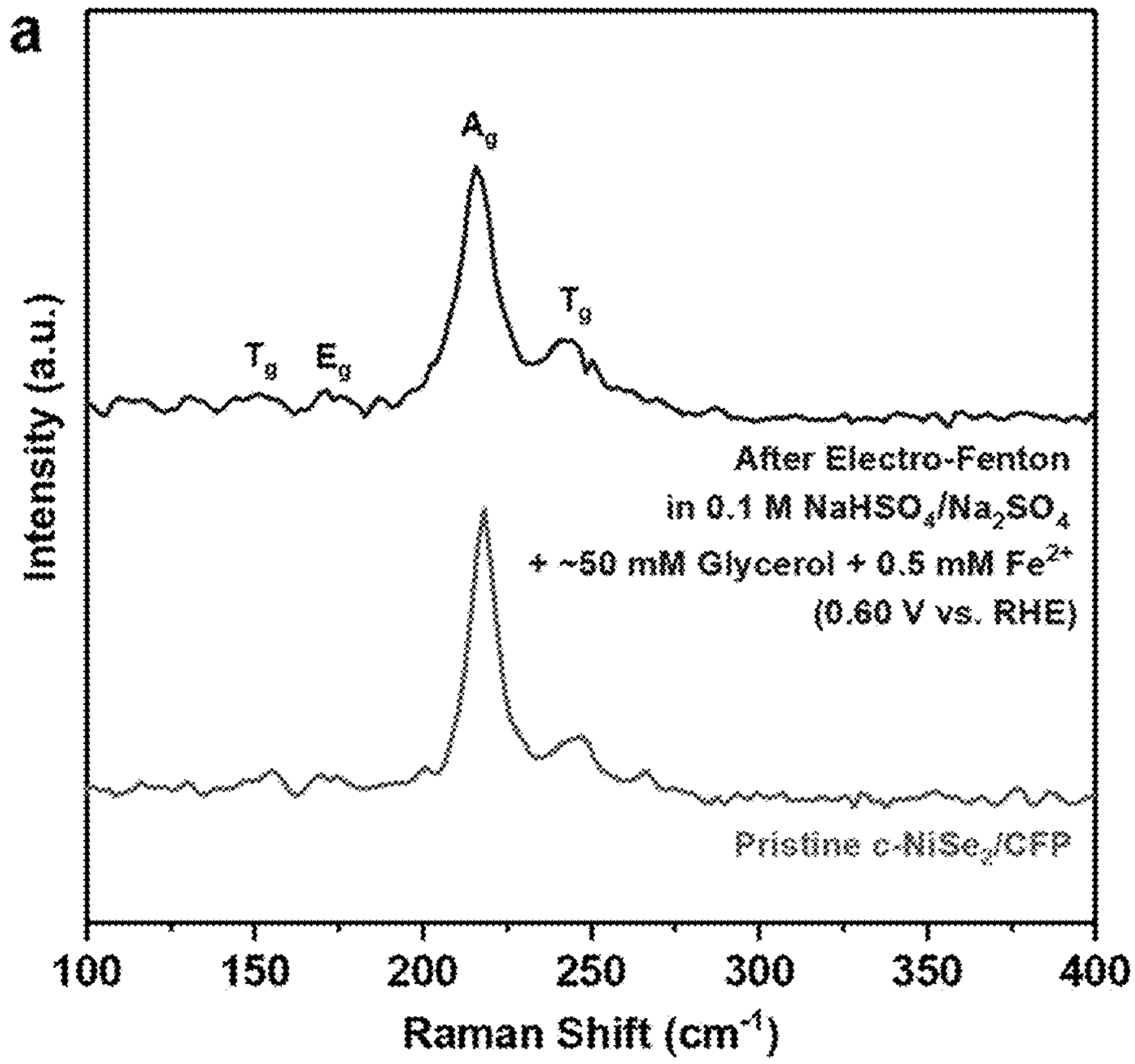
a
Intensity (a.u.)
A_g
T_g
T_g
E_g
After Electro-Fenton
in 0.1 M $NaHSO_4/Na_2SO_4$
+ ~50 mM Glycerol + 0.5 mM Fe^{2+}
(0.60 V vs. RHE)
Pristine c-$NiSe_2$/CFP
100
150
200
250
300
350
400
Raman Shift (cm^{-1})

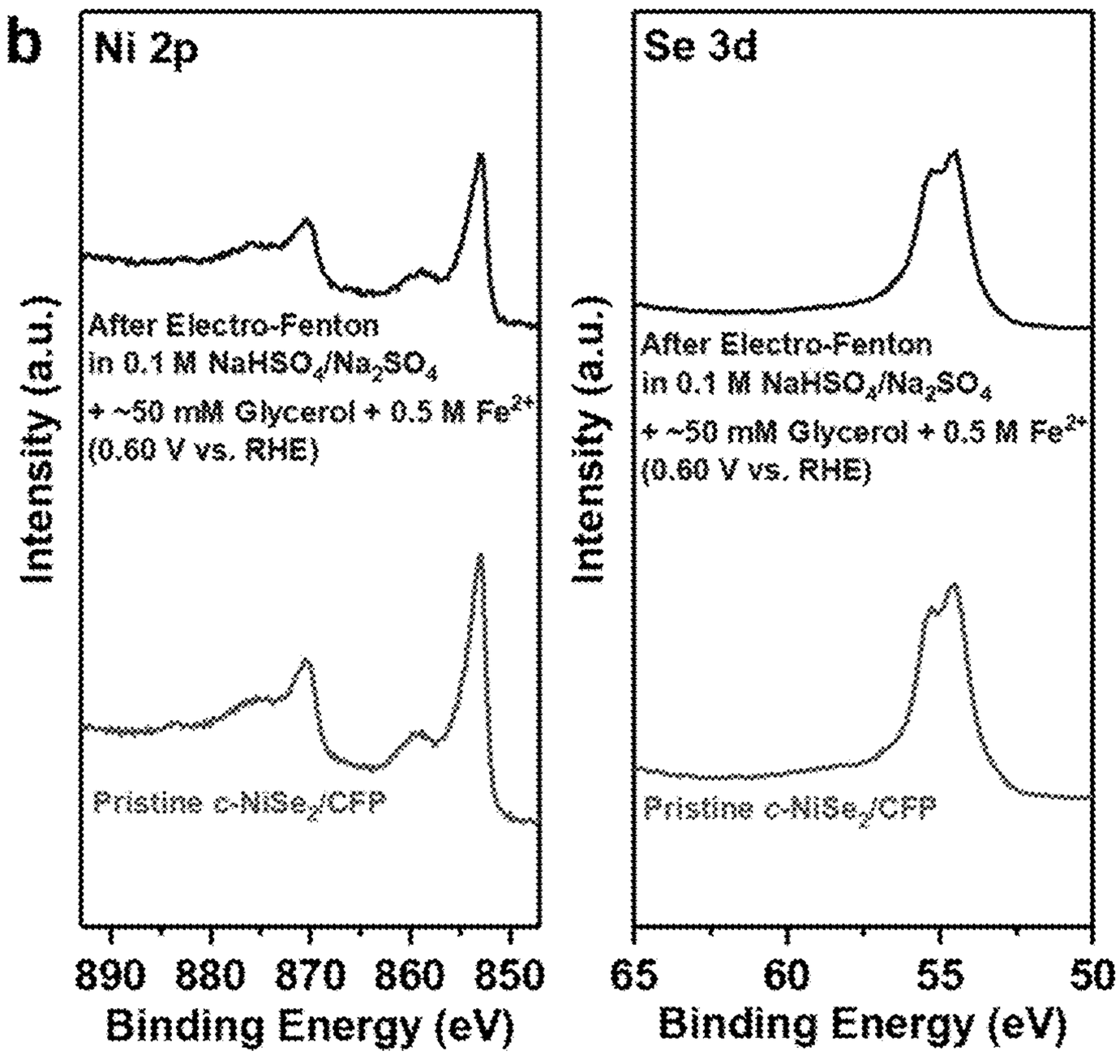
b
Ni 2p
Intensity (a.u.)
After Electro-Fenton
in 0.1 M $NaHSO_4/Na_2SO_4$
+ ~50 mM Glycerol + 0.5 M Fe^{2+}
(0.60 V vs. RHE)
Pristine c-$NiSe_2$/CFP
890
880
870
860
850
Binding Energy (eV)
Se 3d
Intensity (a.u.)
After Electro-Fenton
in 0.1 M $NaHSO_4/Na_2SO_4$
+ ~50 mM Glycerol + 0.5 M Fe^{2+}
(0.60 V vs. RHE)
Pristine c-$NiSe_2$/CFP
65
60
55
50
Binding Energy (eV)

FIG. 28

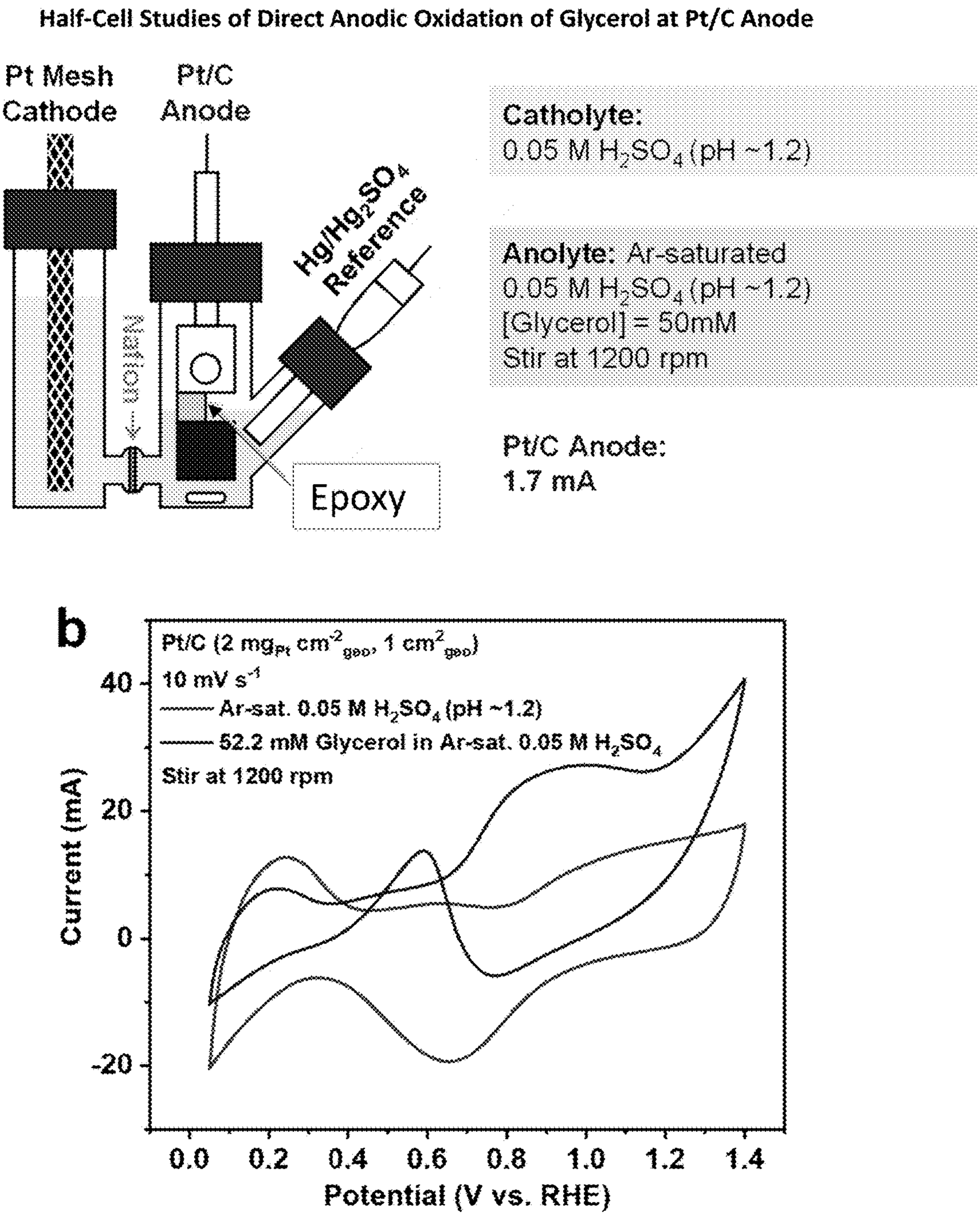
Half-Cell Studies of Direct Anodic Oxidation of Glycerol at Pt/C Anode
a
Pt Mesh Cathode
Pt/C Anode
Hg/Hg2SO4 Reference
Nafion
Epoxy
Catholyte:
0.05 M H2SO4 (pH ~1.2)
Anolyte: Ar-saturated
0.05 M H2SO4 (pH ~1.2)
[Glycerol] = 50mM
Stir at 1200 rpm
Pt/C Anode:
1.7 mA
b
Pt/C (2 mgPt cm-2geo, 1 cm2geo)
10 mV s-1
Ar-sat. 0.05 M H2SO4 (pH ~1.2)
52.2 mM Glycerol in Ar-sat. 0.05 M H2SO4
Stir at 1200 rpm
Current (mA)
40
20
0
-20
0.0
0.2
0.4
0.6
0.8
1.0
1.2
1.4
Potential (V vs. RHE)

FIG. 28 continued

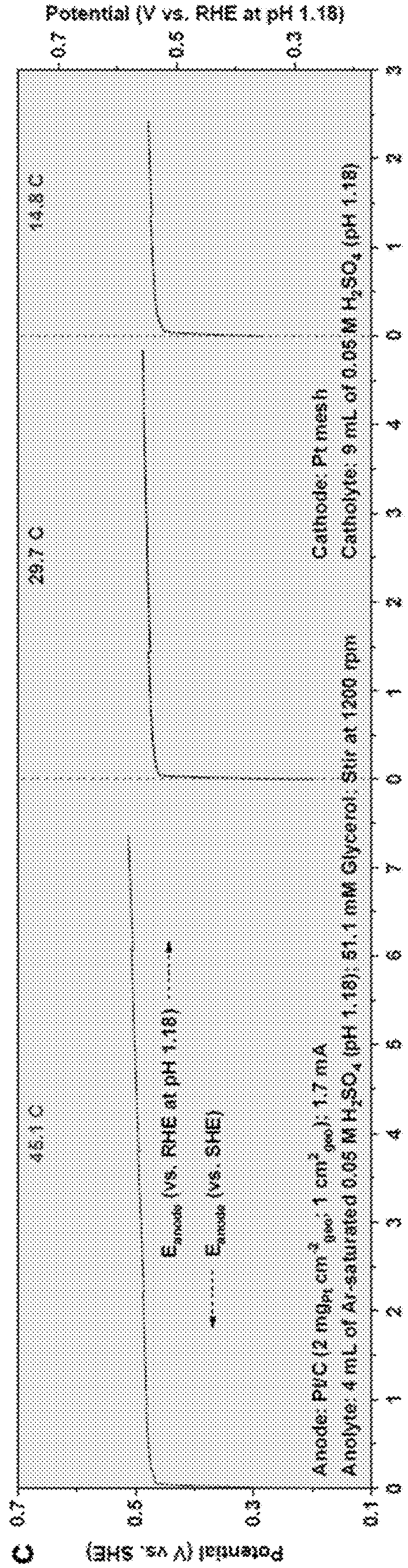

FIG. 28 continued

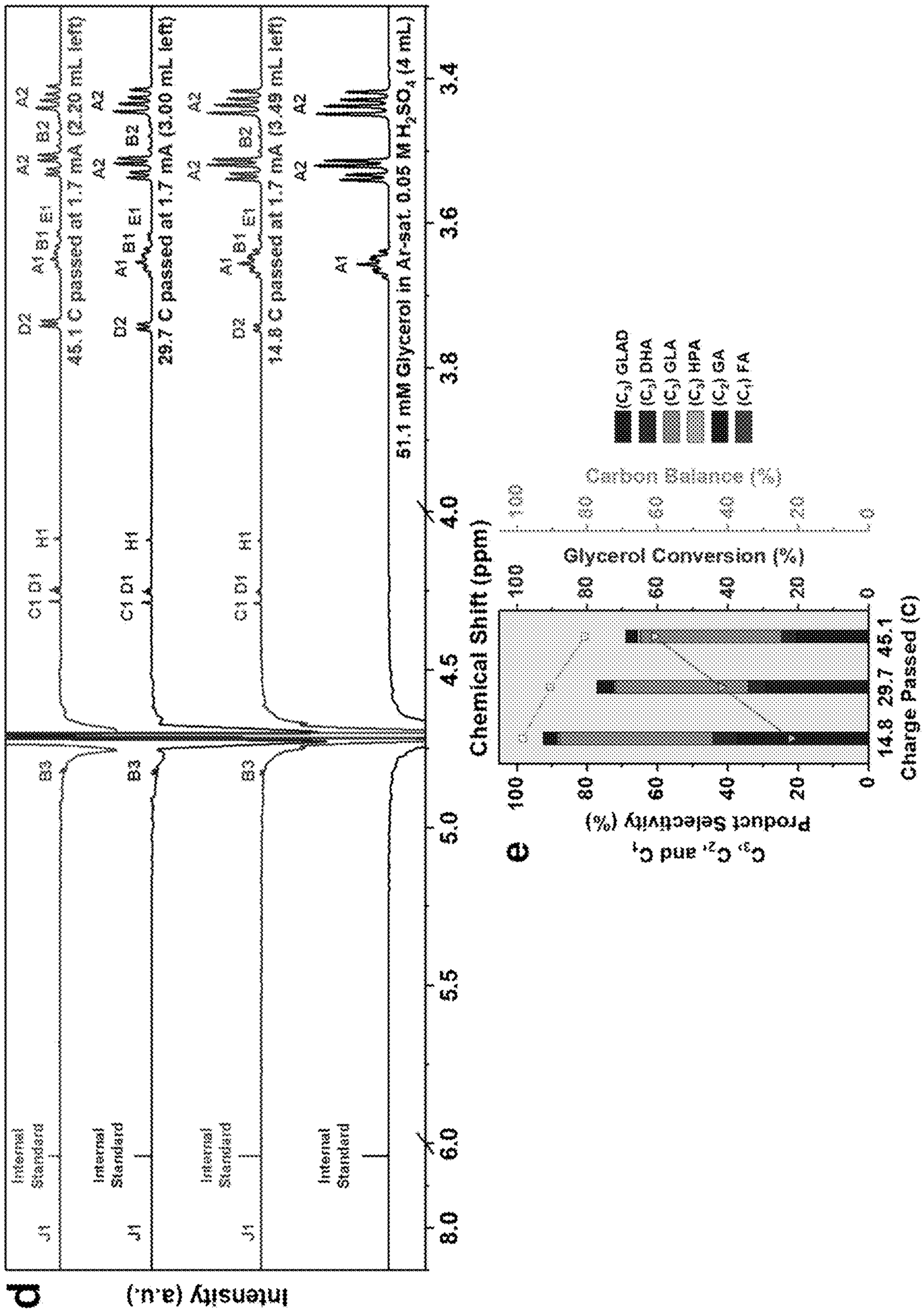

FIG. 29

Two-Compartment Three-Electrode H-Cell for Linear Paired Electrochemical Valorization of Glycerol at *c*-$NiSe_2$ Cathode and Pt/C Anode

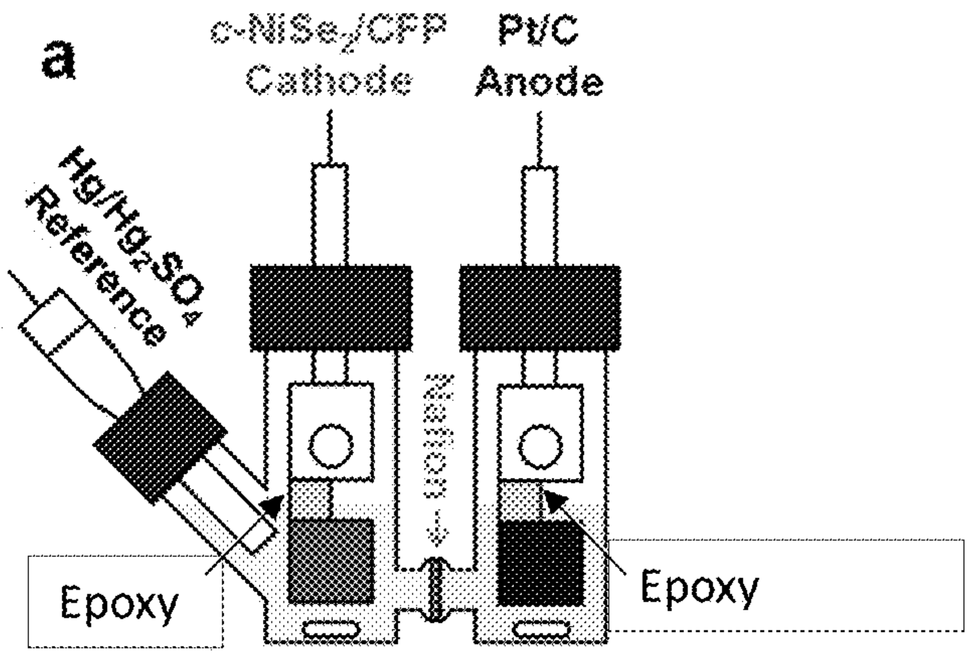

Catholyte: O_2-saturated
0.1 M or 0.5 M $NaHSO_4/Na_2SO_4$ (pH~2.8)
[Glycerol] = 50mM
Optimum $[Fe^{2+}]$ = 0.5 mM
Stir at 1200 rpm

Anolyte: Ar-saturated
0.05 M or 0.5 M H_2SO_4
[Glycerol] = 50 mM
Stir at 1200 rpm

c-$NiSe_2$/CFP Cathode:
0.60 V vs. RHE (Chronoamperometry)

Pt/C Anode:
Current Match (Chronopotentiometry)

FIG. 30

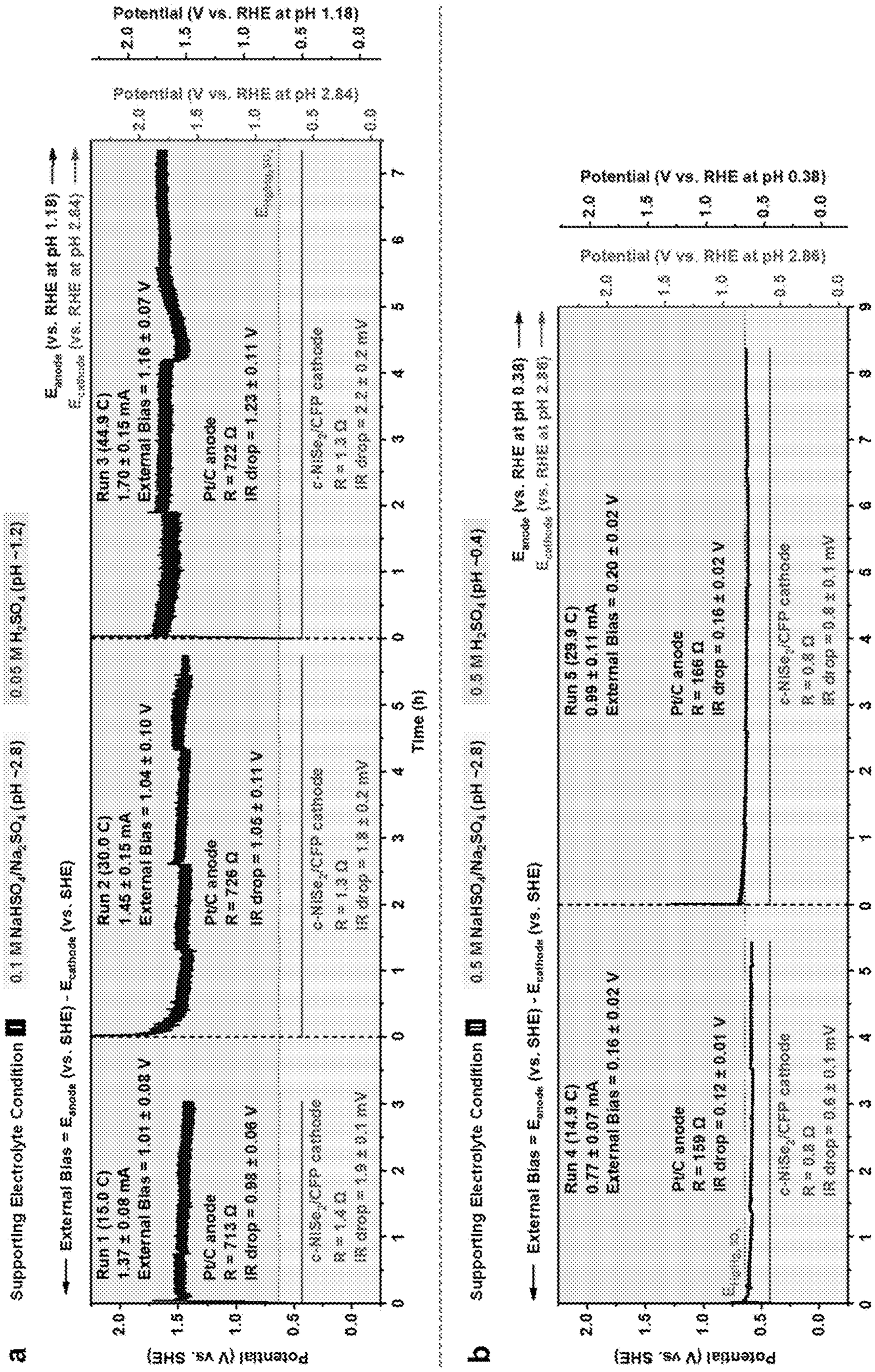
a
Supporting Electrolyte Condition II
0.1 M NaHSO4/Na2SO4 (pH ~2.8)
0.05 M H2SO4 (pH ~1.2)
Eanode (vs. RHE at pH 1.18)
Ecathode (vs. RHE at pH 2.84)
Potential (V vs. RHE at pH 1.18)
Potential (V vs. RHE at pH 2.84)
Run 2 (30.0 C)
1.45 ± 0.15 mA
External Bias = 1.04 ± 0.10 V
Run 3 (44.9 C)
1.70 ± 0.15 mA
External Bias = 1.16 ± 0.07 V
Pt/C anode
R = 726 Ω
IR drop = 1.05 ± 0.11 V
Pt/C anode
R = 722 Ω
IR drop = 1.23 ± 0.11 V
c-NiSex/CFP cathode
R = 1.3 Ω
IR drop = 1.8 ± 0.2 mV
c-NiSex/CFP cathode
R = 1.3 Ω
IR drop = 2.2 ± 0.2 mV
Time (h)
Potential (V vs. SHE)
b
Supporting Electrolyte Condition III
0.5 M NaHSO4/Na2SO4 (pH ~2.8)
0.5 M H2SO4 (pH ~0.4)
Eanode (vs. RHE at pH 0.38)
Ecathode (vs. RHE at pH 2.86)
Potential (V vs. RHE at pH 0.38)
Potential (V vs. RHE at pH 2.86)
Run 5 (29.9 C)
0.99 ± 0.11 mA
External Bias = 0.20 ± 0.02 V
Pt/C anode
R = 166 Ω
IR drop = 0.16 ± 0.02 V
c-NiSex/CFP cathode
R = 0.8 Ω
IR drop = 0.8 ± 0.1 mV
Run 1 (15.0 C)
1.37 ± 0.08 mA
External Bias = 1.01 ± 0.08 V
Run 4 (14.9 C)
0.77 ± 0.07 mA
External Bias = 0.16 ± 0.02 V
Pt/C anode
R = 713 Ω
IR drop = 0.98 ± 0.06 V
Pt/C anode
R = 159 Ω
IR drop = 0.12 ± 0.01 V
c-NiSex/CFP cathode
R = 1.4 Ω
IR drop = 1.9 ± 0.1 mV
c-NiSex/CFP cathode
R = 0.8 Ω
IR drop = 0.6 ± 0.1 mV
Time (h)
Potential (V vs. SHE)

FIG. 31

a

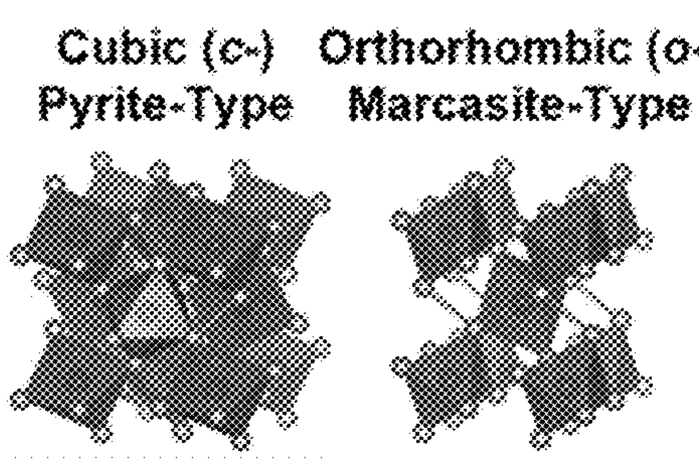

b

Surface	O* Adsorption (ΔG at $U°_{RHE}$)	OH* Adsorption (ΔG at $U°_{RHE}$)
c-CoS_2 (100)	S-O* (-0.38 eV)	Co-OH* (-0.09 eV)
c-$CoSe_2$ (100)	Se-O* (+0.21 eV)	Co-OH* (-0.08 eV)
o-$CoSe_2$ (101)	Se-O* (+0.21 eV)	Co-OH* (-0.15 eV)
c-$NiSe_2$ (100)	Ni-O* (+0.08 eV)	Ni-OH* (+0.27 eV)

DFT-Predicted Surface Stability: *c*-$NiSe_2$ > (*c*-$CoSe_2$ ≈ *o*-$CoSe_2$) > *c*-CoS_2

c

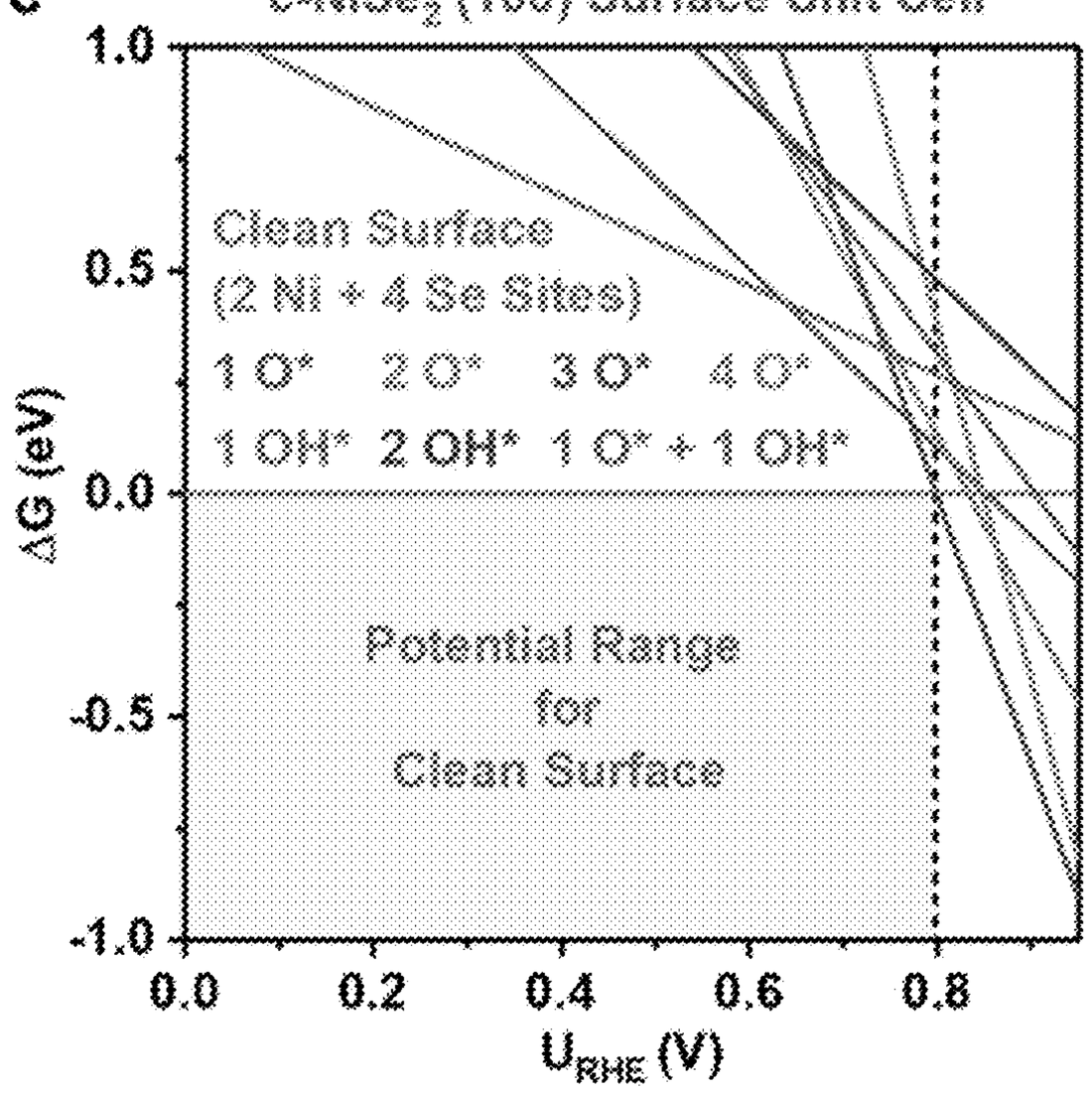

d

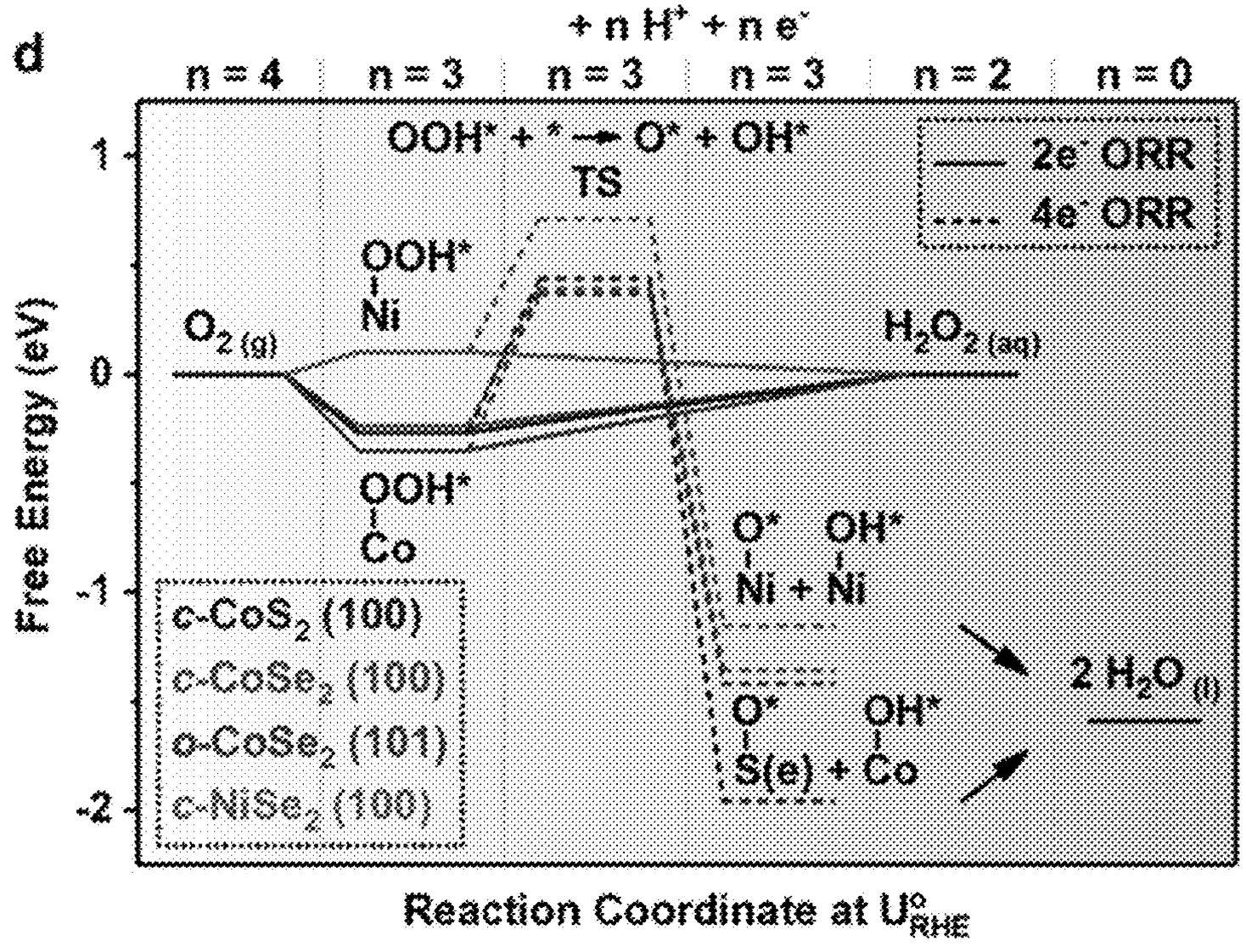

FIG. 32

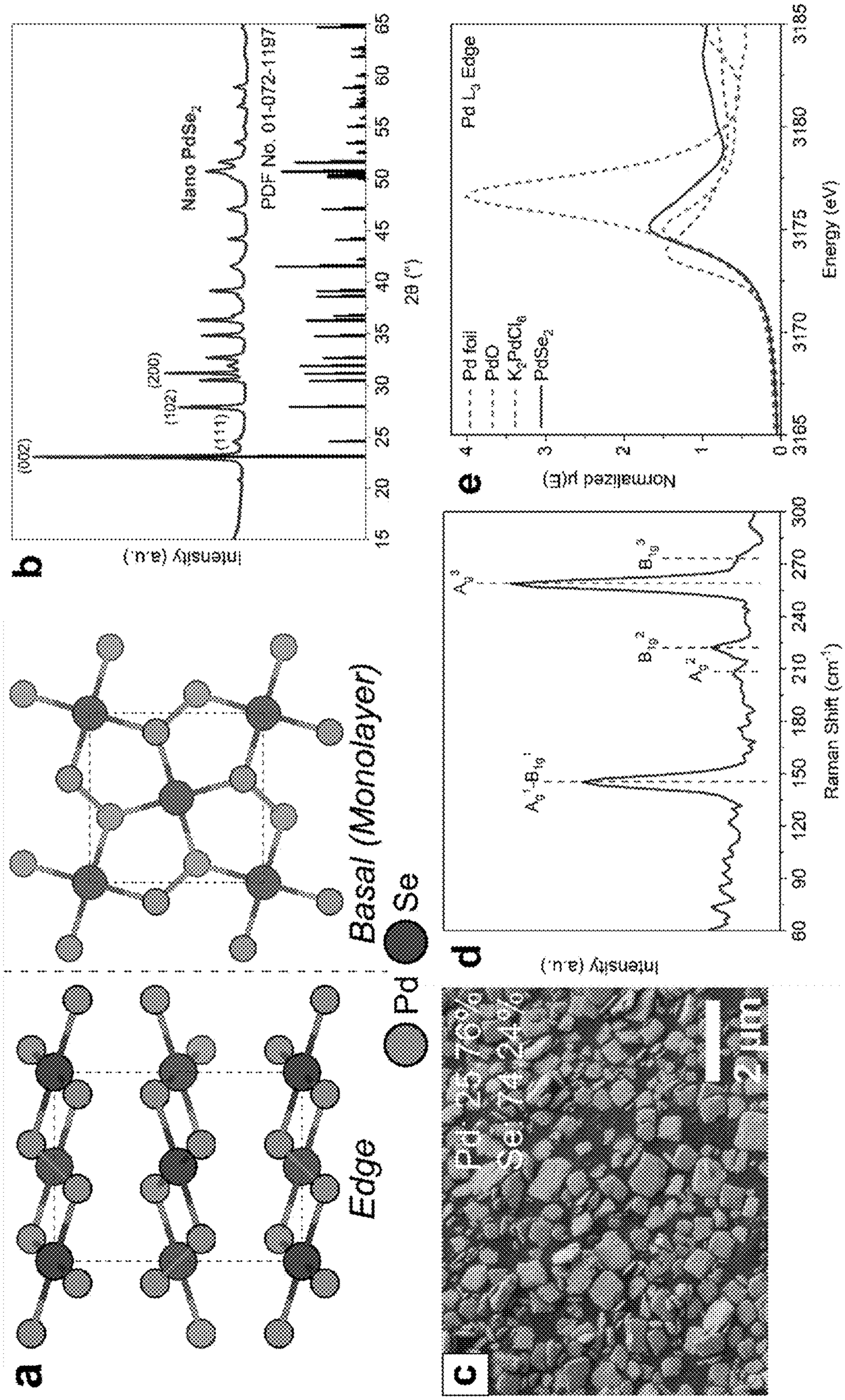
a
Edge
Pd
Se
b
Nano $PdSe_2$
PDF No. 01-072-1197
(002)
(111)
(102)
(200)
Intensity (a.u.)
2θ (°)
c
Pd: 25.76%
Se: 74.24%
2 μm
d
A_g^1-B_{1g}^1
B_{1g}^2
A_g^2
A_g^3
B_{1g}^3
Intensity (a.u.)
Raman Shift (cm^{-1})
e
Pd foil
PdO
K_2PdCl_6
$PdSe_2$
Normalized μ(E)
Energy (eV)

FIG. 33

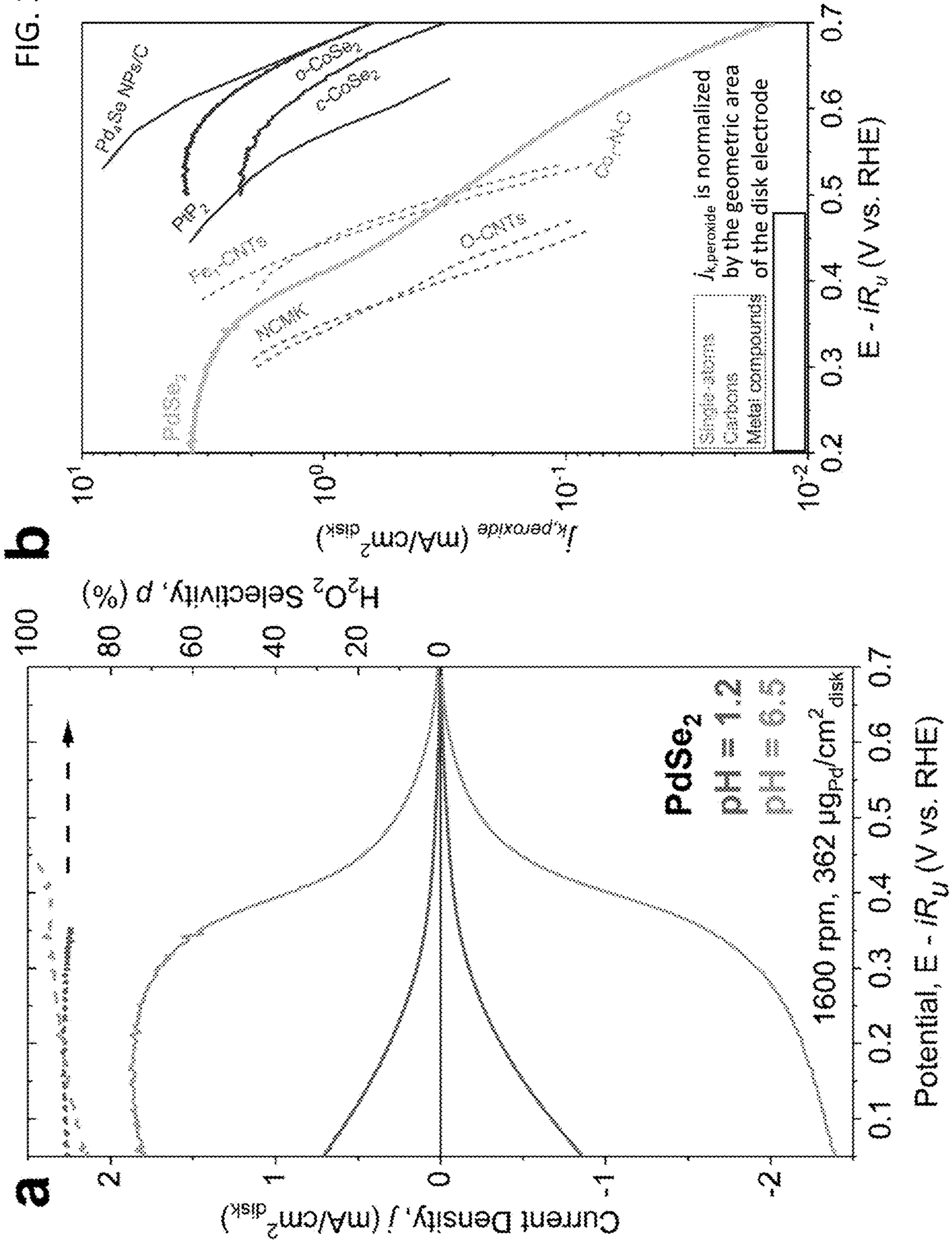
b
$j_{k,peroxide}$ (mA/cm$^2_{disk}$)
10^{1}
10^{0}
10^{-1}
10^{-2}
0.2 0.3 0.4 0.5 0.6 0.7
E - iR_u (V vs. RHE)
$j_{k,peroxide}$ is normalized by the geometric area of the disk electrode
Simple-atoms
Carbons
Metal compounds
Pd$_x$Se NPs/C
c-CoSe$_2$
o-CoSe$_2$
PtP$_2$
Fe$_1$-CNTs
O-CNTs
Co$_1$-N-C
NCMK
Pd$_4$S/C
a
Current Density, j (mA/cm$^2_{disk}$)
2
1
0
-1
-2
H_2O_2 Selectivity, p (%)
100
80
60
40
20
0
Potential, E - iR_u (V vs. RHE)
0.1 0.2 0.3 0.4 0.5 0.6 0.7
1600 rpm, 362 μg$_{Pd}$/cm$^2_{disk}$
Pd$_4$Se
pH = 1.2
pH = 6.5
pH = 13

FIG. 33 continued

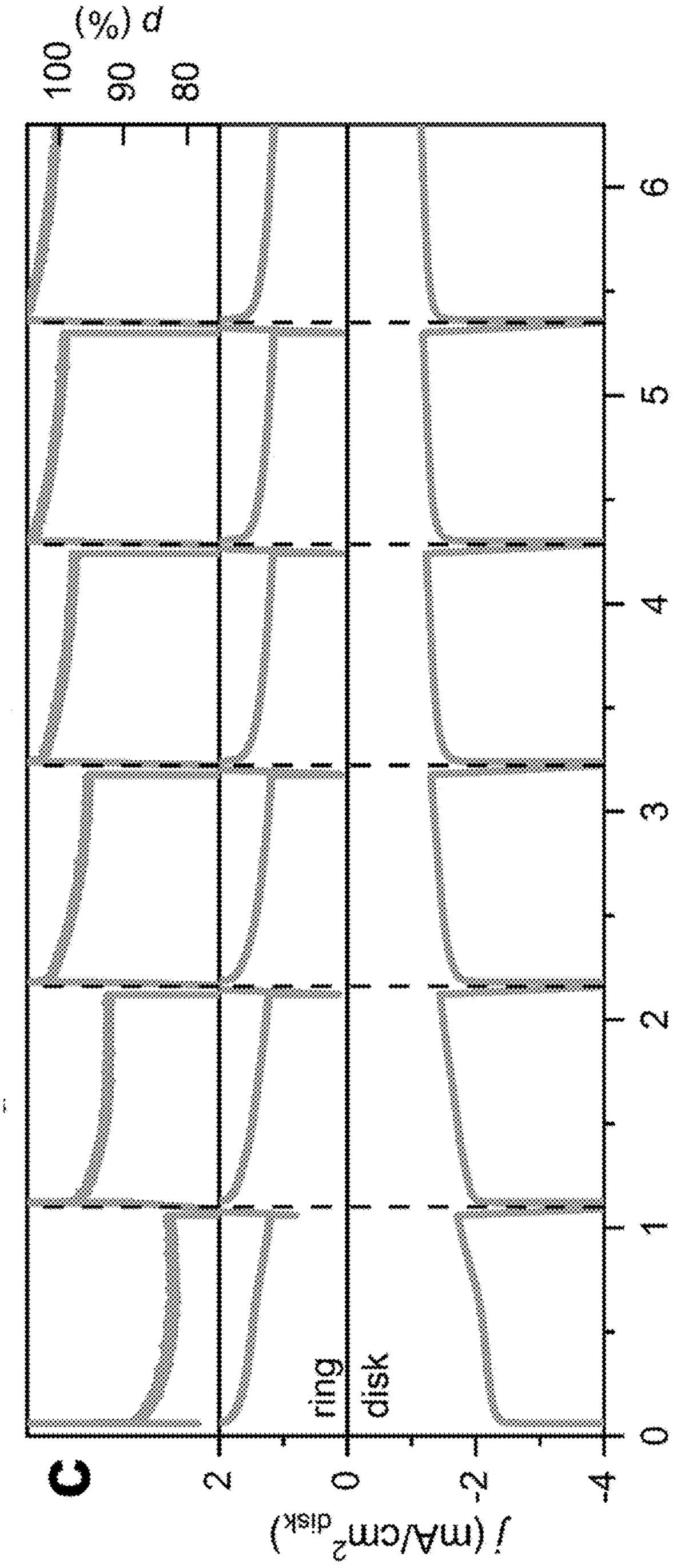

FIG. 34

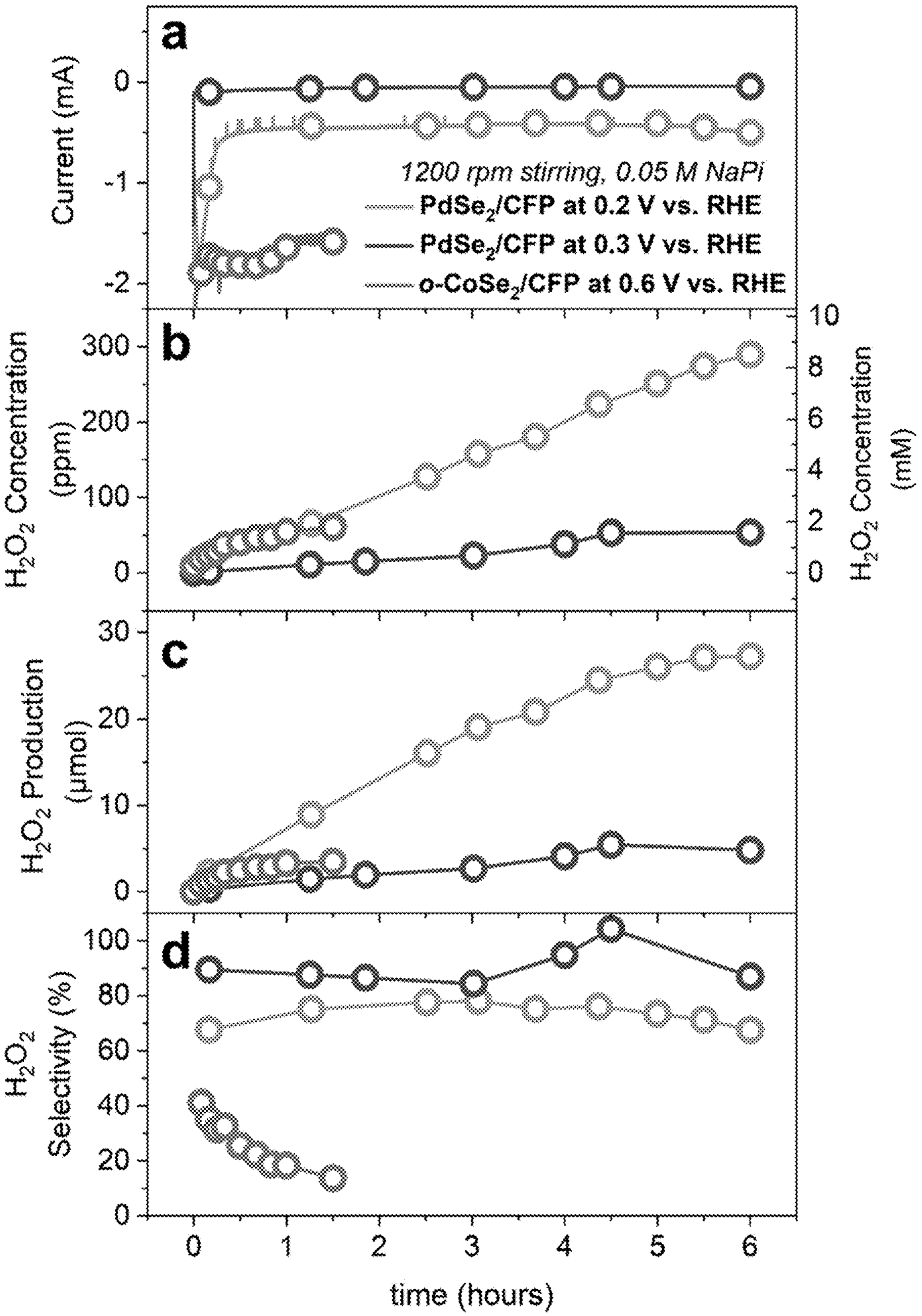
a
Current (mA)
0
-1
-2
1200 rpm stirring, 0.05 M NaPi
PdSe2/CFP at 0.2 V vs. RHE
PdSe2/CFP at 0.3 V vs. RHE
o-CoSe2/CFP at 0.6 V vs. RHE
b
H2O2 Concentration (ppm)
300
200
100
0
H2O2 Concentration (mM)
10
8
6
4
2
0
c
H2O2 Production (μmol)
30
20
10
0
d
H2O2 Selectivity (%)
100
80
60
40
20
0
0
1
2
3
4
5
6
time (hours)

FIG. 35

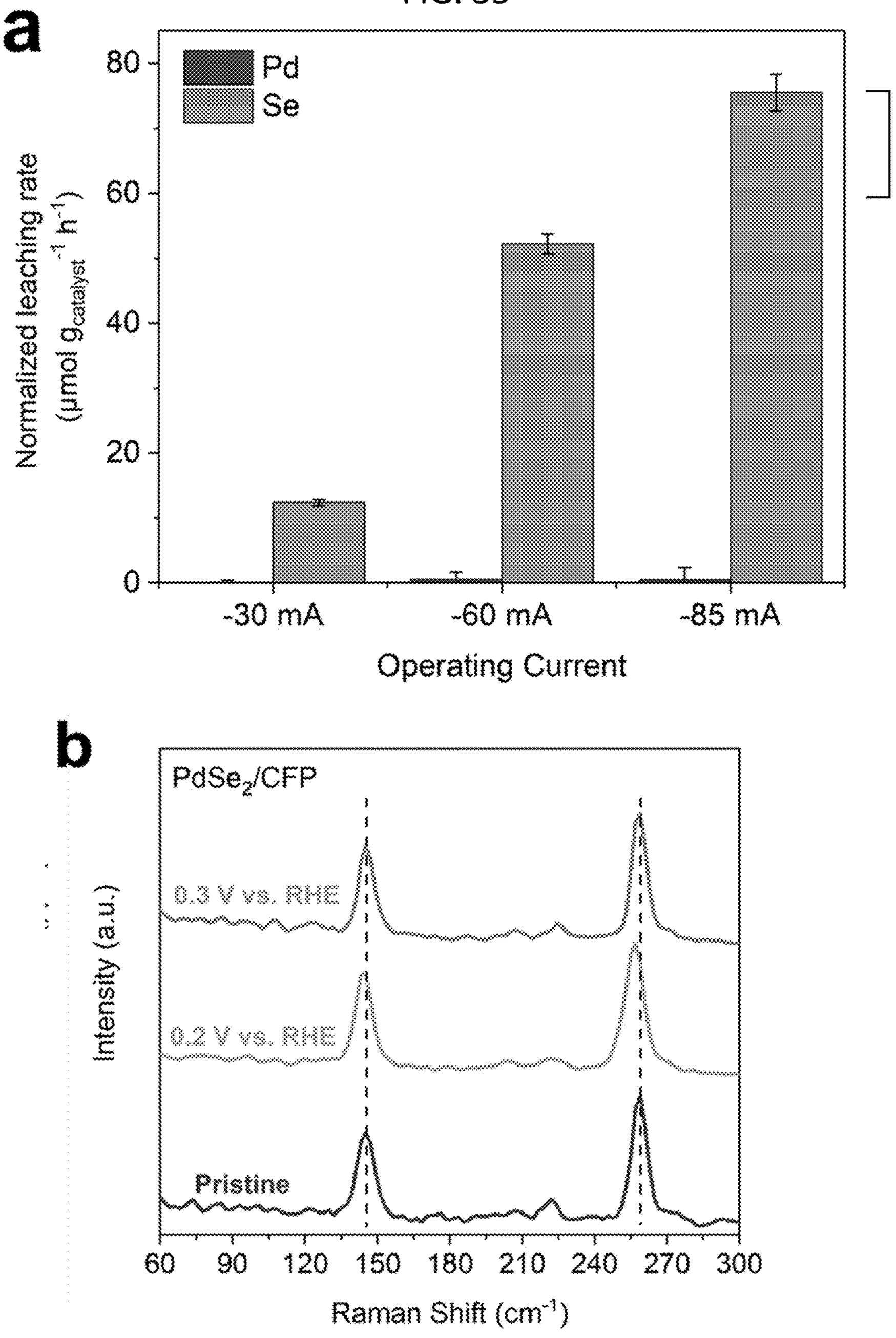
a
Pd
Se
Normalized leaching rate
(μmol $g_{catalyst}^{-1}$ h^{-1})
80
60
40
20
0
-30 mA
-60 mA
-85 mA
Operating Current
b
$PdSe_2$/CFP
0.3 V vs. RHE
0.2 V vs. RHE
Pristine
Intensity (a.u.)
60
90
120
150
180
210
240
270
300
Raman Shift (cm^{-1})

FIG. 35 Continued

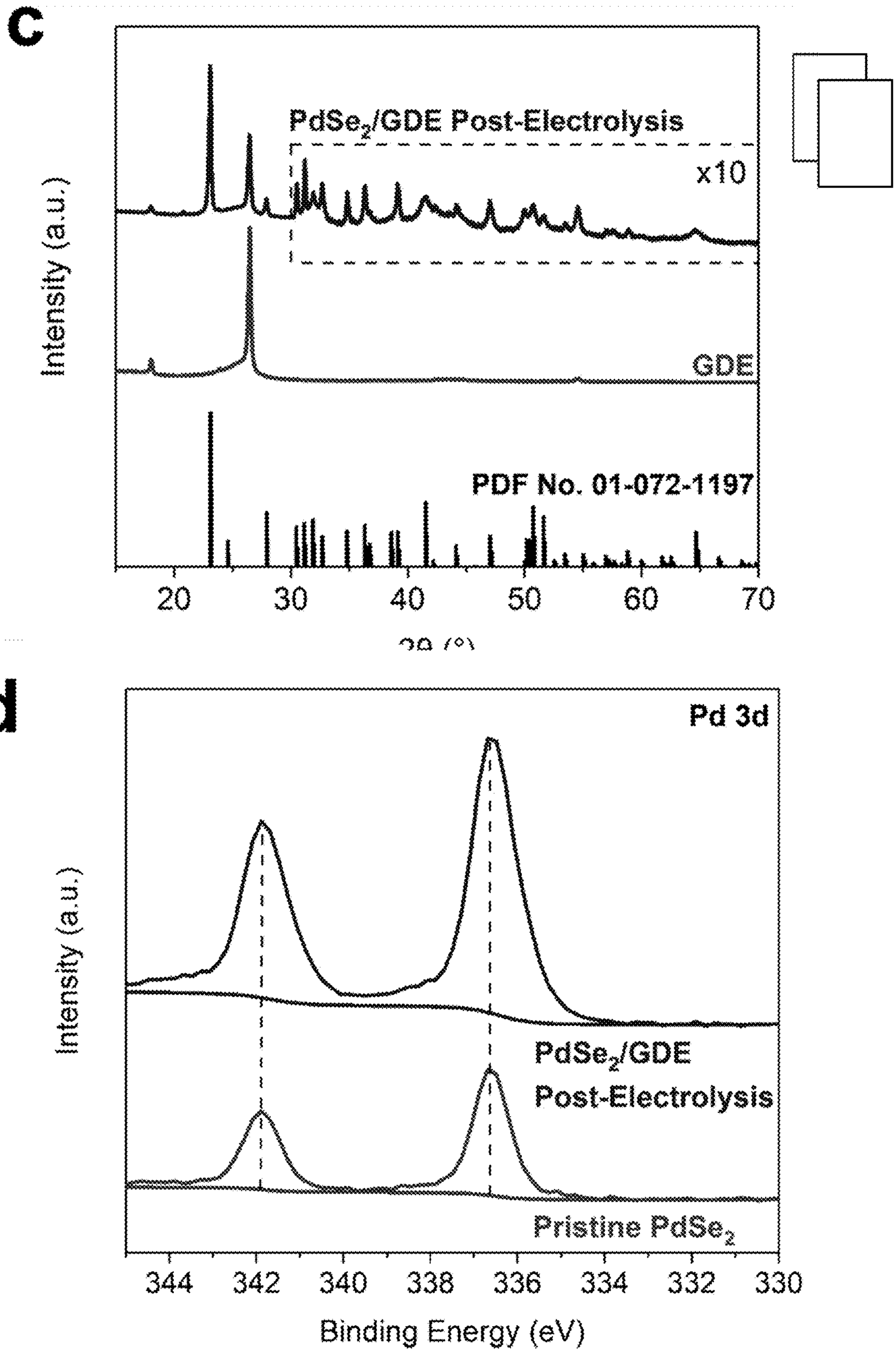

FIG. 35 Continued

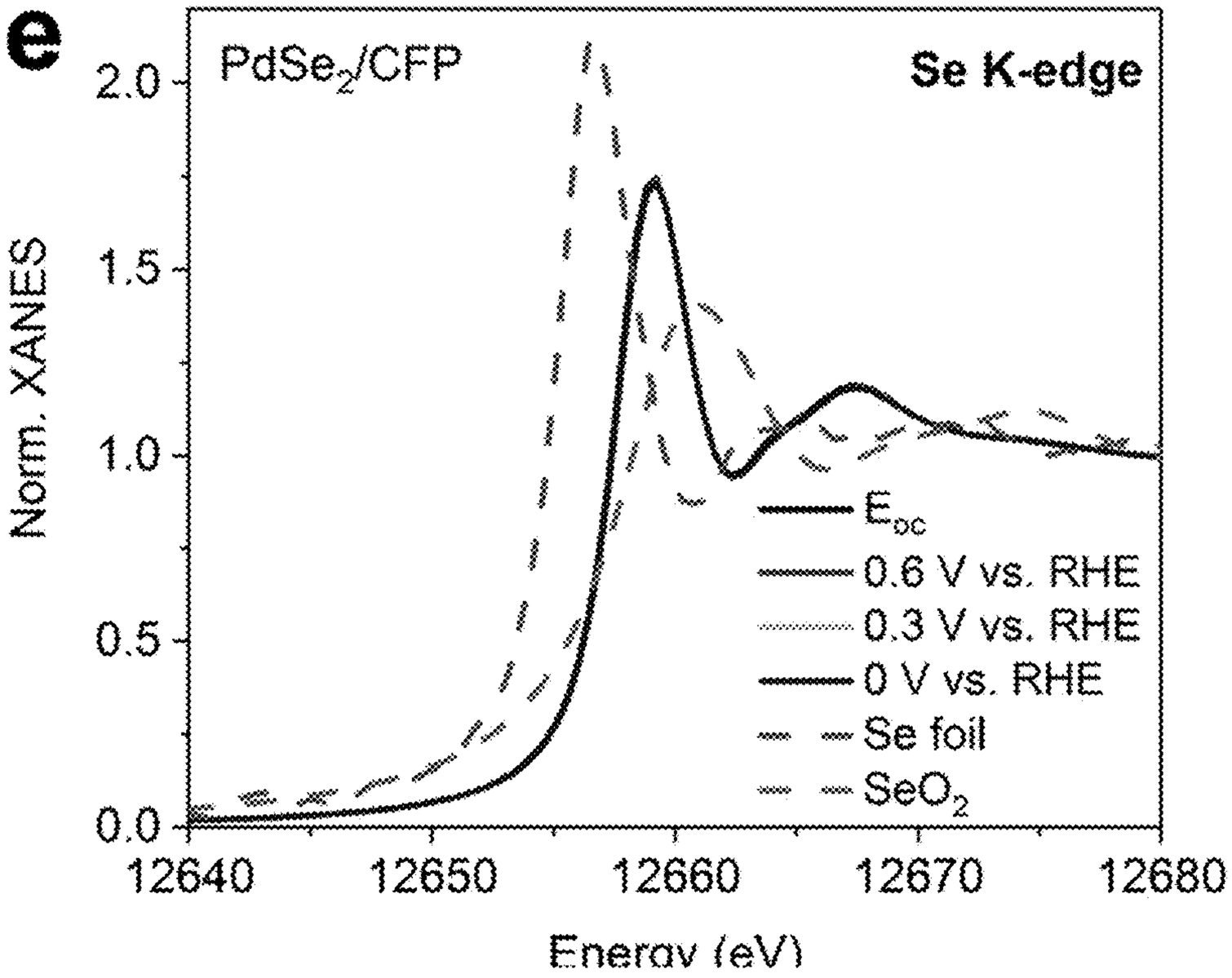

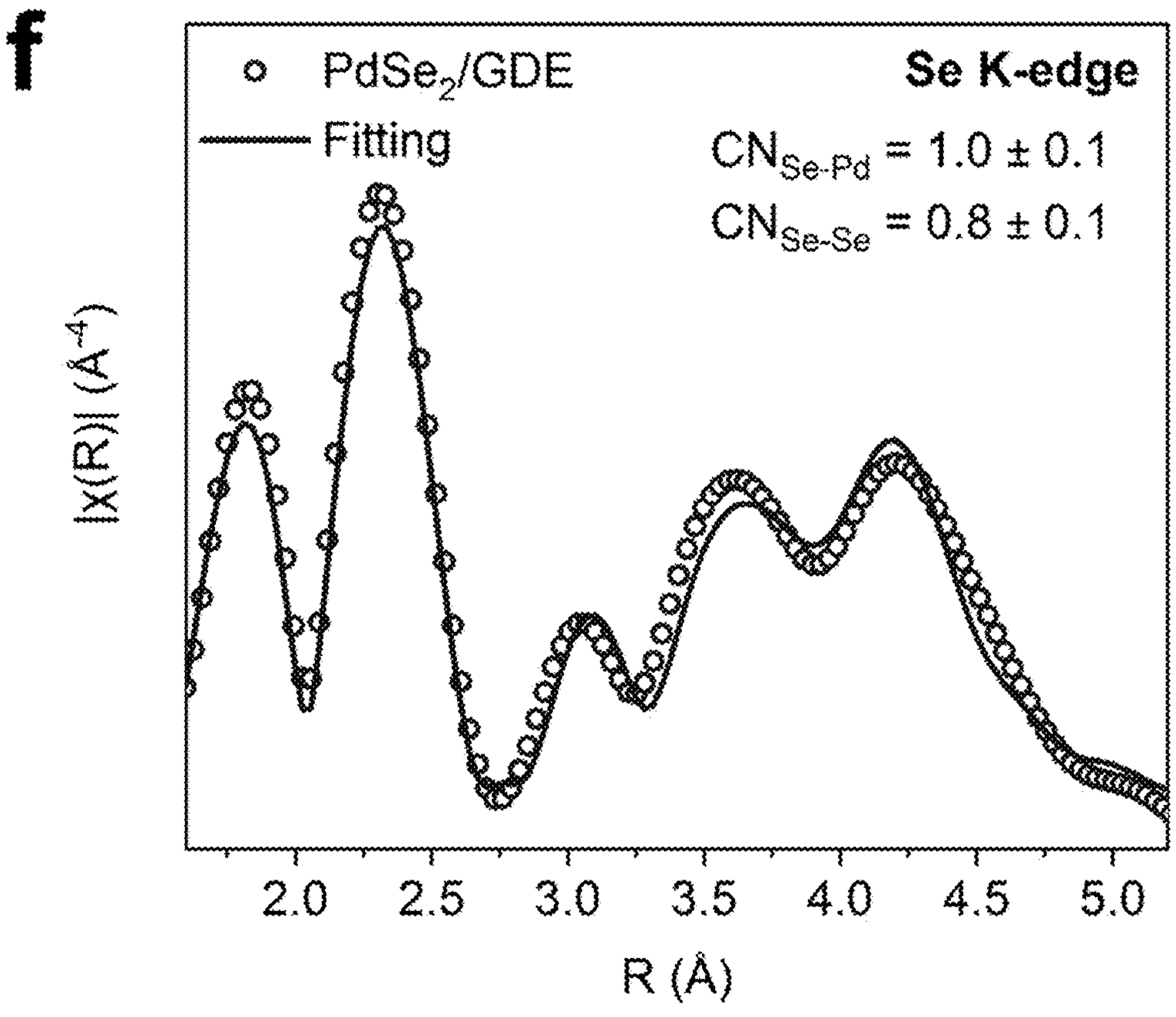

FIG. 36

(a) (001) facet

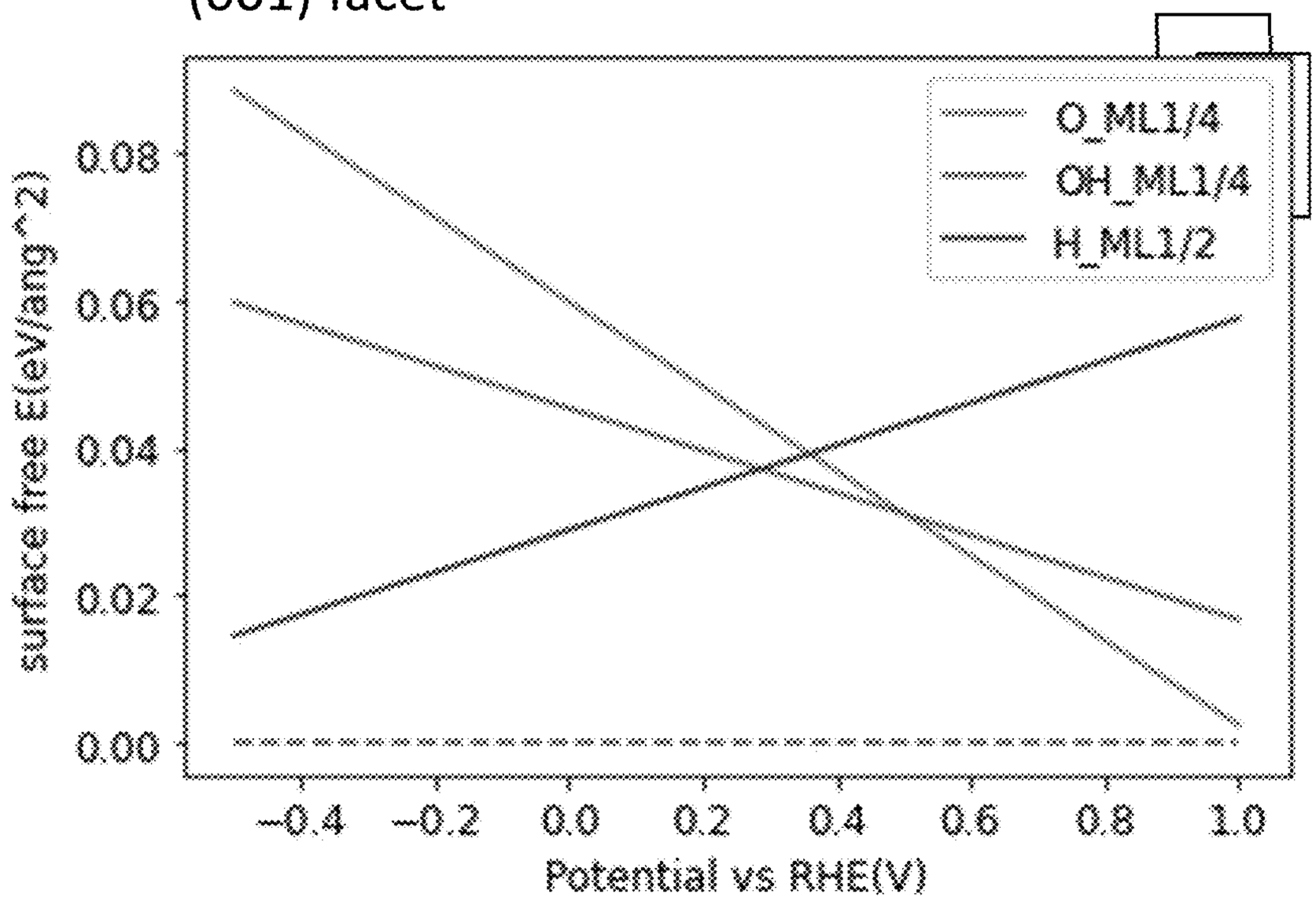

(b) (100) facet

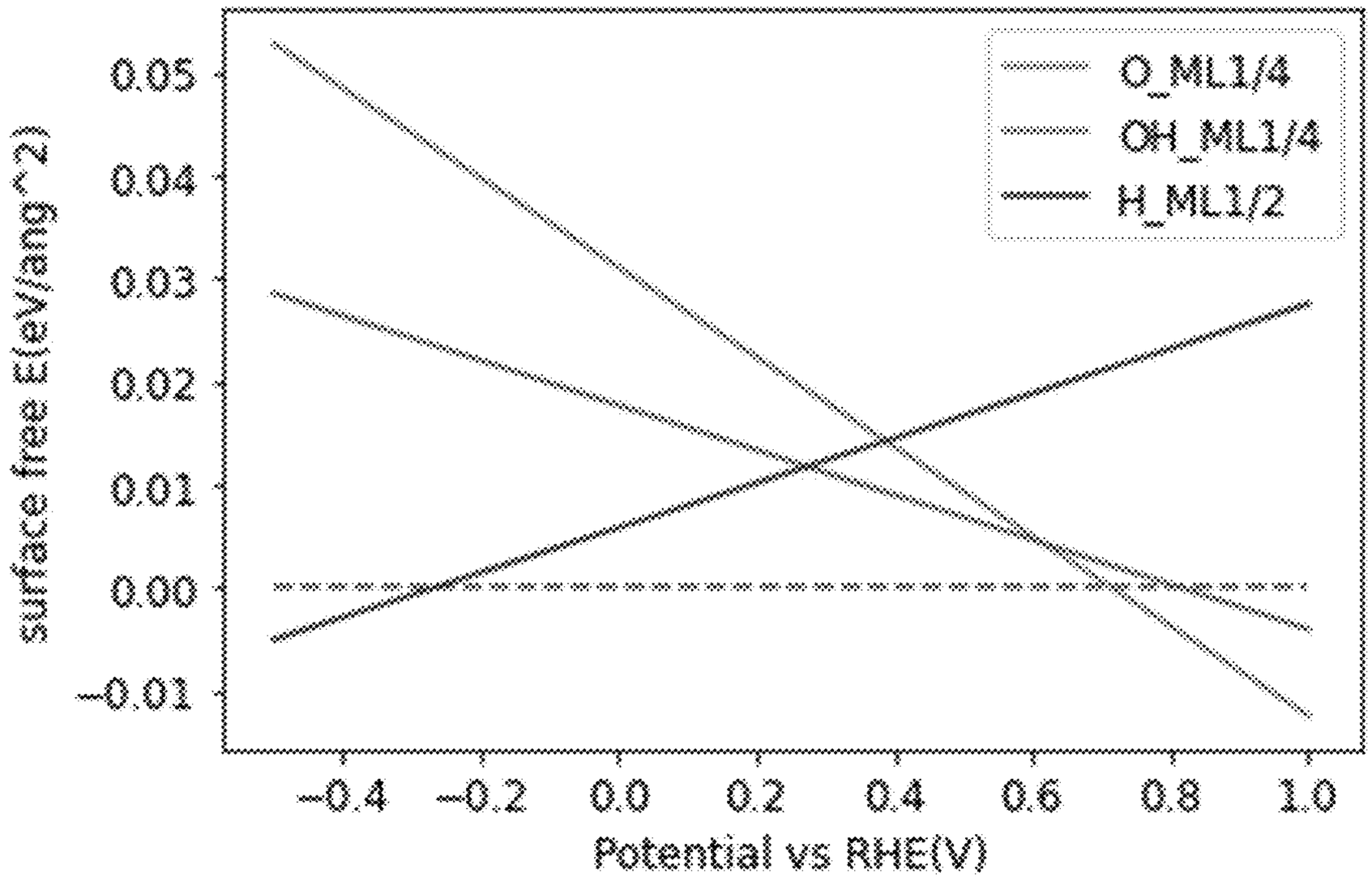

FIG. 37

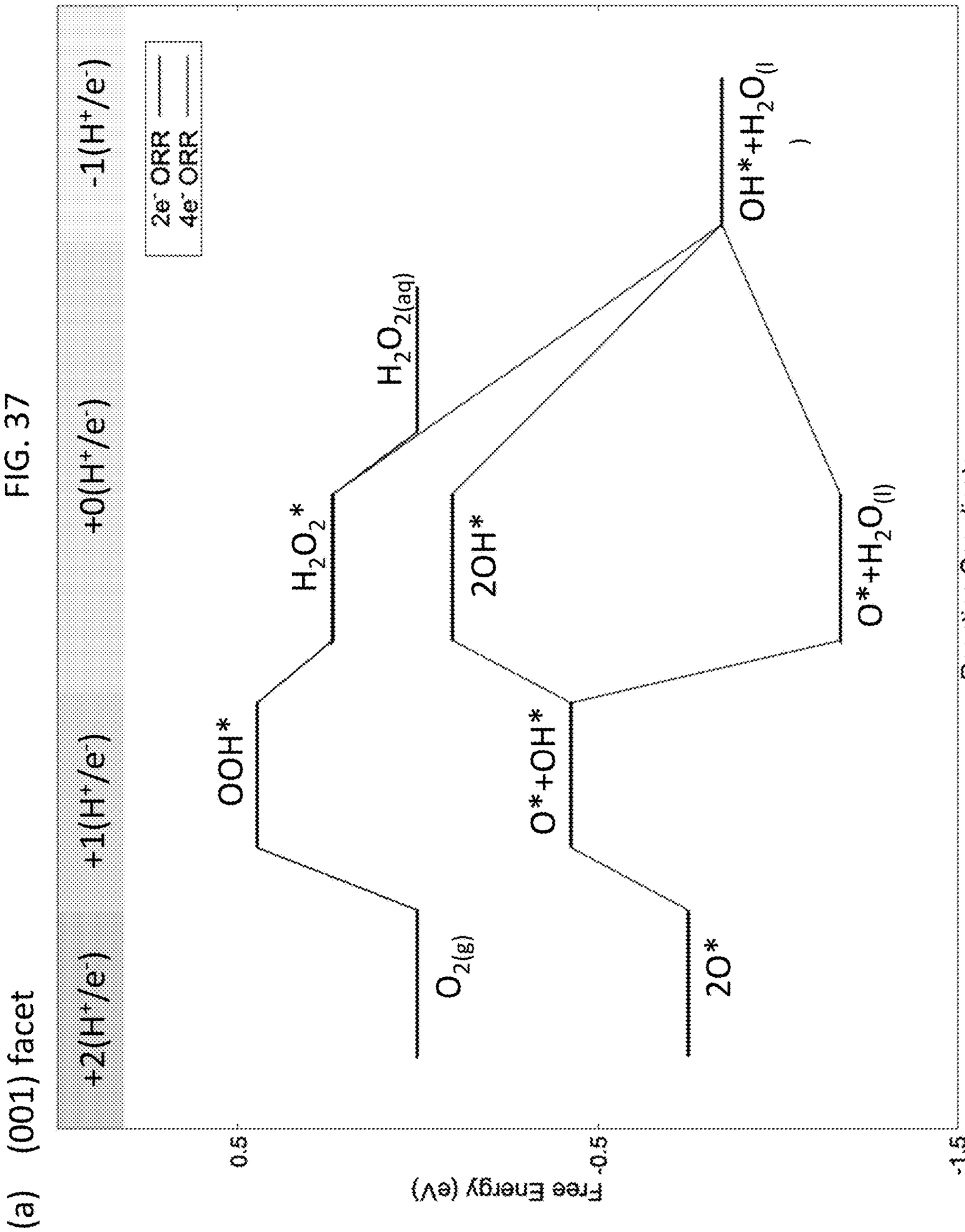
(a) (001) facet
-1(H+/e-)
+0(H+/e-)
+1(H+/e-)
+2(H+/e-)
2e- ORR
4e- ORR
OOH*
H2O2*
H2O2(aq)
2OH*
O*+OH*
O*+H2O(l)
OH*+H2O(l)
O2(g)
2O*
0.5
-0.5
-1.5
Free Energy (eV)
Reaction Coordinate

FIG. 37 continued

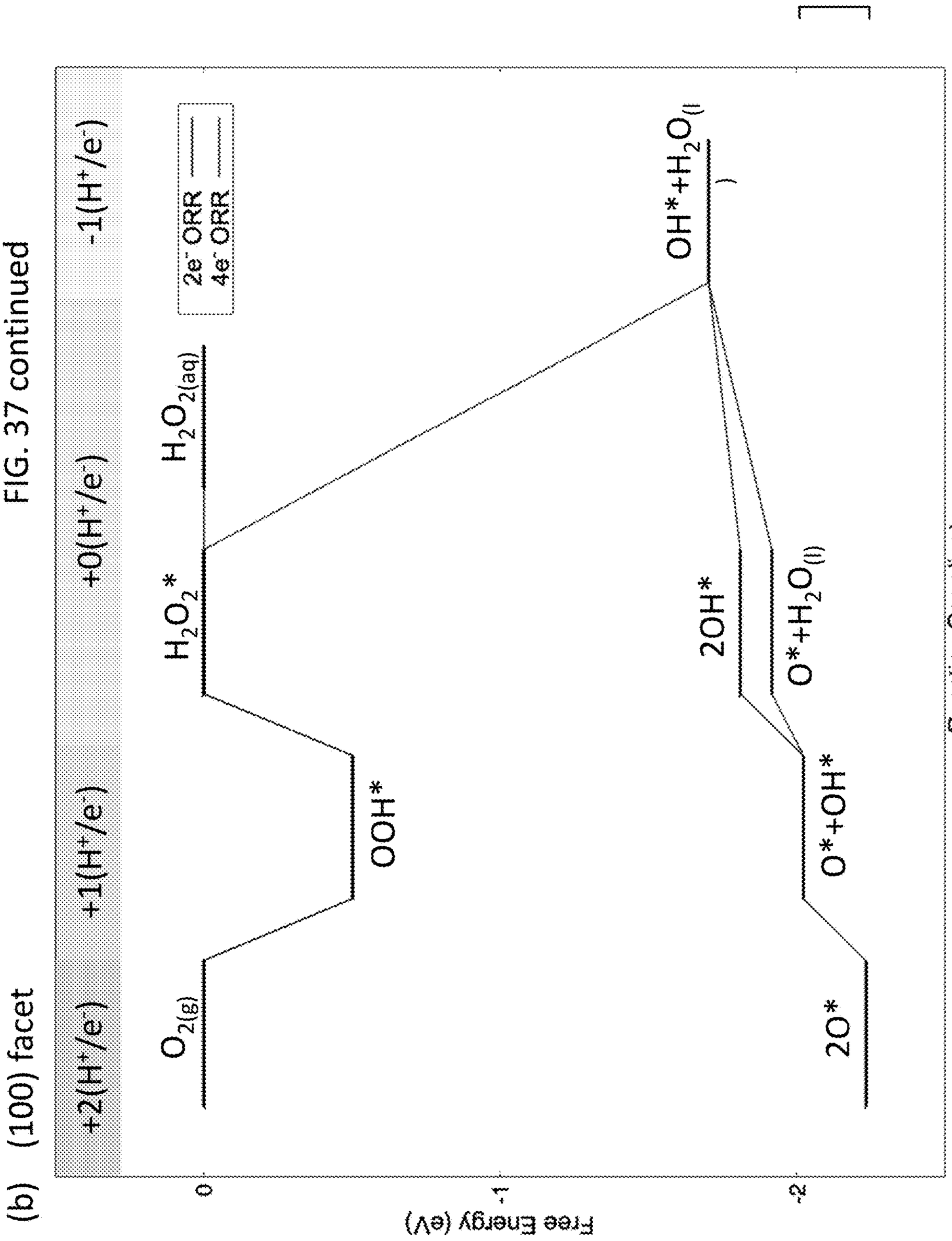

FIG. 38

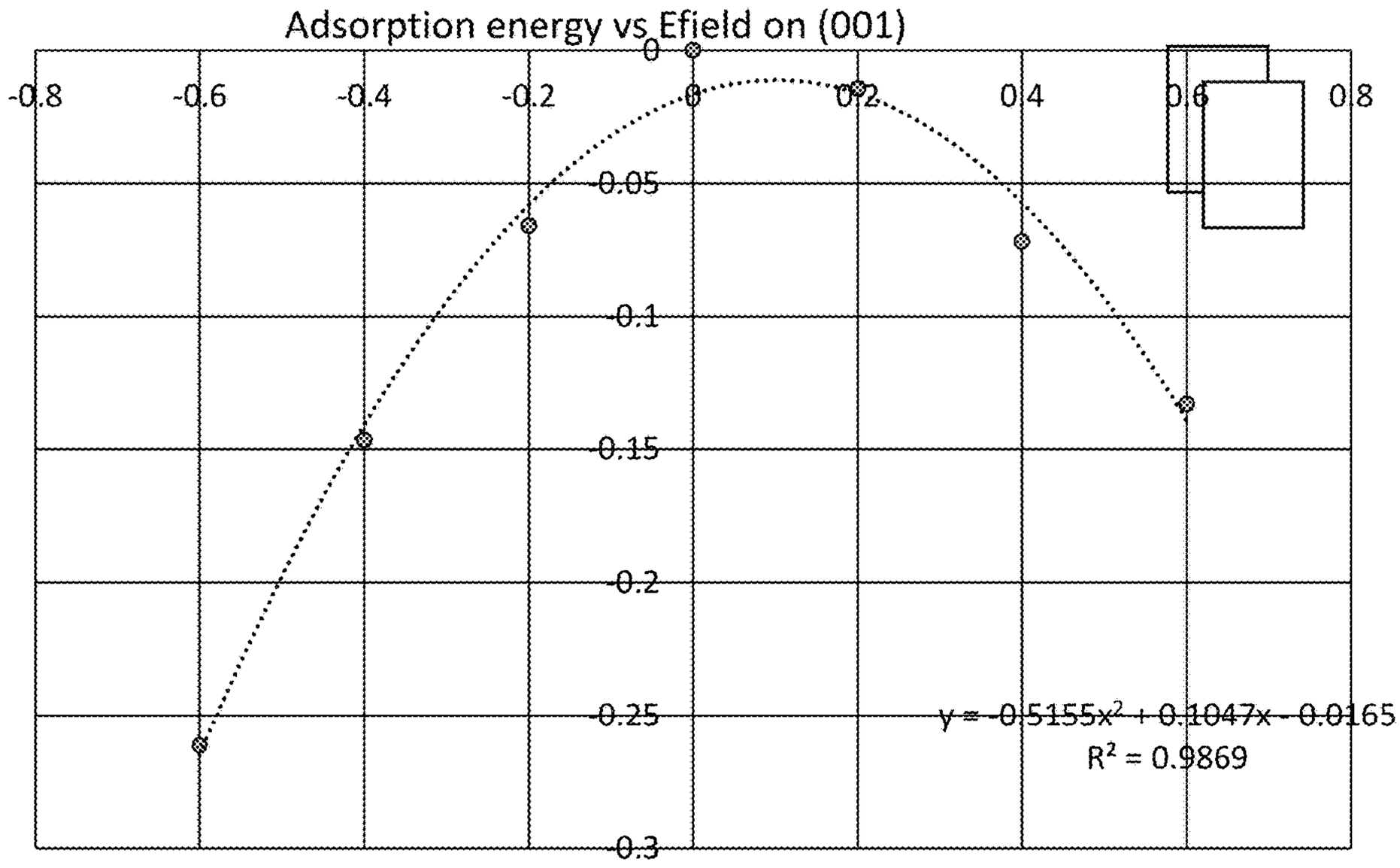
Adsorption energy vs Efield on (001)
0
-0.05
-0.1
-0.15
-0.2
-0.25
-0.3
-0.8
-0.6
-0.4
-0.2
0
0.2
0.4
0.6
0.8
y = -0.5155x² + 0.1047x - 0.0165
R² = 0.9869

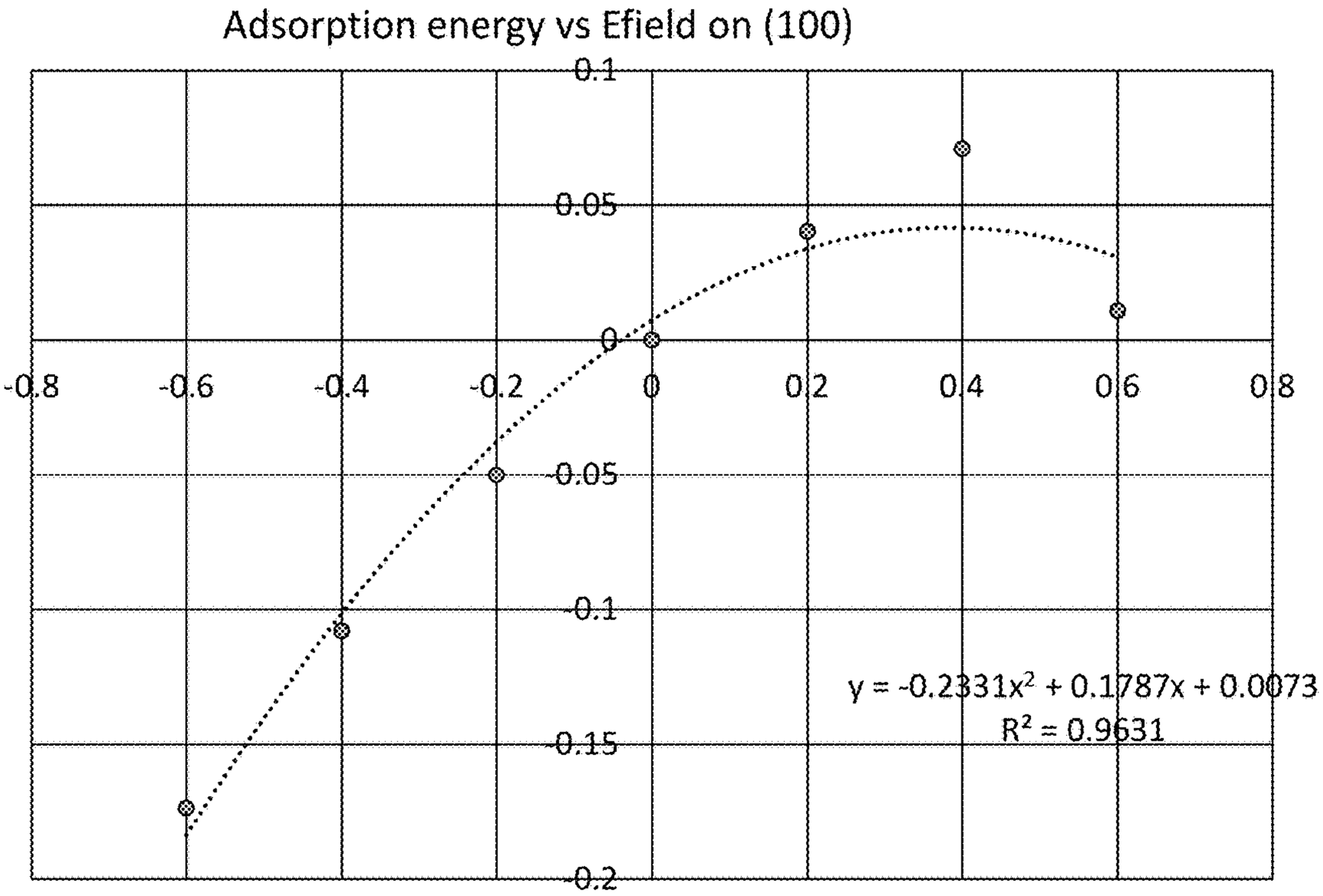
Adsorption energy vs Efield on (100)
0.1
0.05
0
-0.05
-0.1
-0.15
-0.2
-0.8
-0.6
-0.4
-0.2
0
0.2
0.4
0.6
0.8
y = -0.2331x² + 0.1787x + 0.0073
R² = 0.9631

FIG. 39

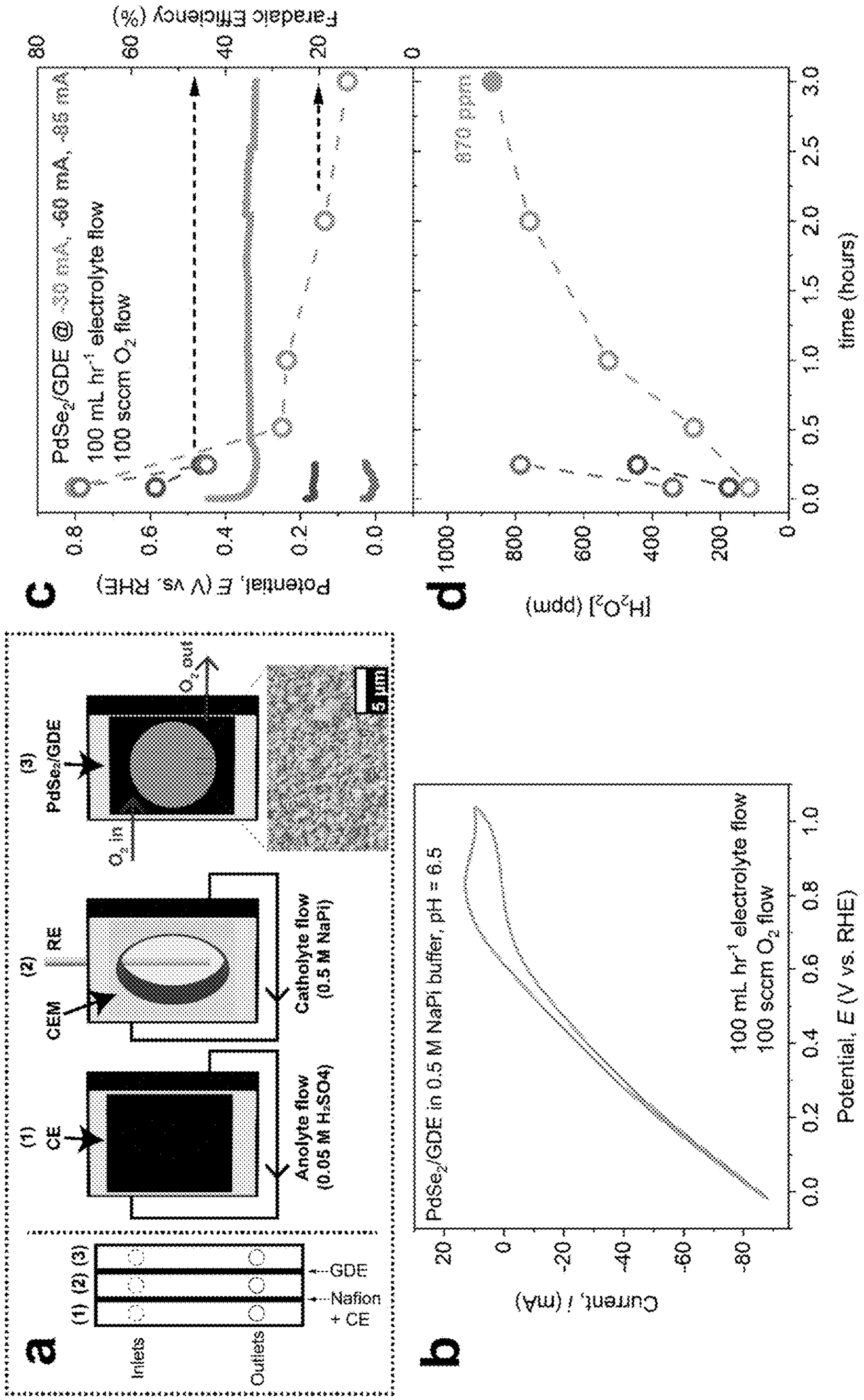
a
(1) (2) (3)
Inlets
Outlets
GDE
Nafion + CE
(1) CE
(2) CEM
RE
(3) PdSe2/GDE
O2 in
O2 out
5 μm
Anolyte flow (0.05 M H2SO4)
Catholyte flow (0.5 M NaPi)
b
PdSe2/GDE in 0.5 M NaPi buffer, pH = 6.5
100 mL hr-1 electrolyte flow
100 sccm O2 flow
Current, i (mA)
Potential, E (V vs. RHE)
c
PdSe2/GDE @ -80 mA, -60 mA, -85 mA
100 mL hr-1 electrolyte flow
100 sccm O2 flow
Faradaic Efficiency (%)
Potential, E (V vs. RHE)
d
870 ppm
[H2O2] (ppm)
time (hours)

FIG. 40

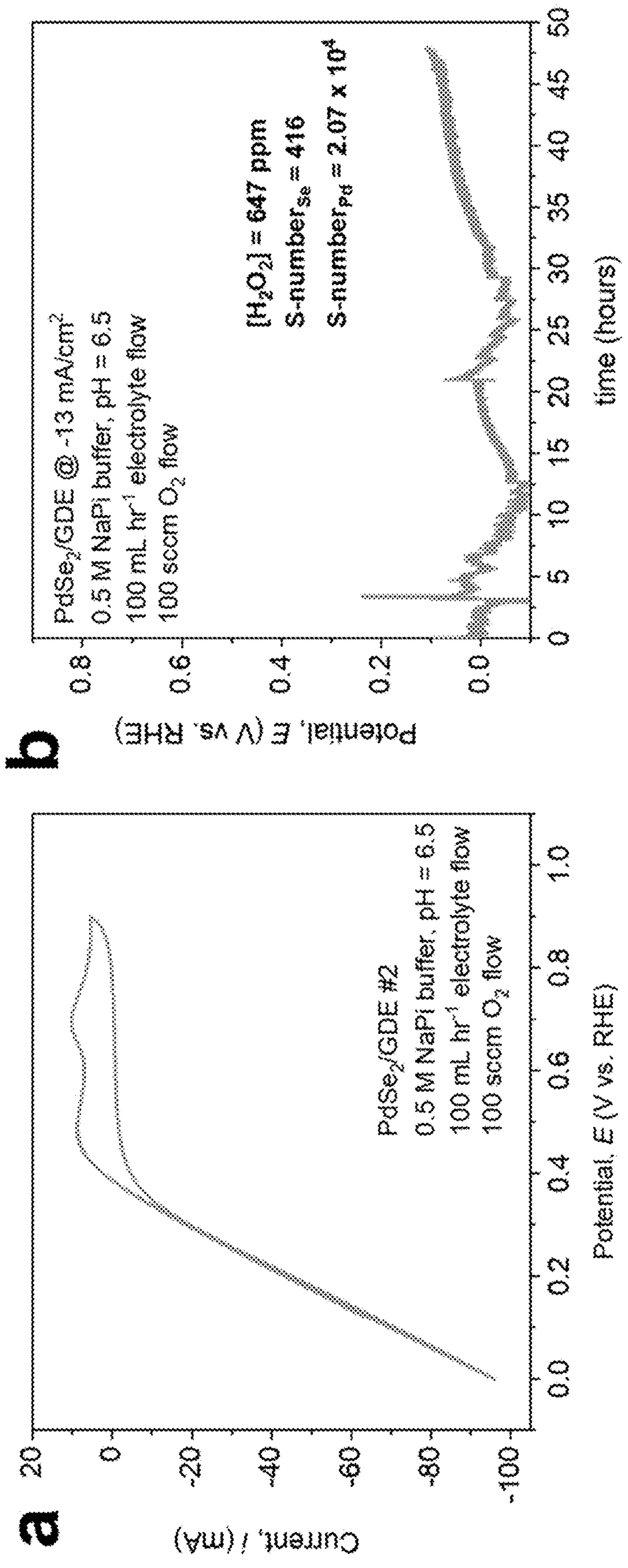
a
Current, i (mA)
20
0
-20
-40
-60
-80
-100
0.0
0.2
0.4
0.6
0.8
1.0
Potential, E (V vs. RHE)
PdSe2/GDE #2
0.5 M NaPi buffer, pH = 6.5
100 mL hr-1 electrolyte flow
100 sccm O2 flow
b
Potential, E (V vs. RHE)
0.8
0.6
0.4
0.2
0.0
0
5
10
15
20
25
30
35
40
45
50
time (hours)
PdSe2/GDE @ -13 mA/cm2
0.5 M NaPi buffer, pH = 6.5
100 mL hr-1 electrolyte flow
100 sccm O2 flow
[H2O2] = 647 ppm
S-numberSe = 416
S-numberPd = 2.07 x 10^4

METAL COMPOUND BASED CATALYSTS FOR ELECTROSYNTHESIS OF HYDROGEN PEROXIDE AND LINEAR PAIRED ELECTROCHEMICAL VALORIZATION OF BIOMASS-DERIVED FEEDSTOCKS

CROSS-REFERENCE TO RELATED APPLICATIONS

[0001] This application claims priority to U.S. Provisional Application No. 63/430,933 filed on Dec. 7, 2022, the content of which is incorporated by reference in its entirety.

STATEMENT REGARDING FEDERALLY SPONSORED RESEARCH

[0002] This invention was made with government support under 1955074 awarded by the National Science Foundation. The government has certain rights in the invention.

BACKGROUND OF THE INVENTION

[0003] Hydrogen peroxide (H_2O_2) is a powerful and green oxidant with diverse applications in chemical manufacturing, wastewater treatment, and the paper and pulp industry. The COVID-19 pandemic has also contributed to the recent growth of the global H_2O_2 market for use in disinfection. The traditional industrial production of H_2O_2 that proceeds chemically through the anthraquinone process consumes H_2 gas and is energy-intensive. It produces up to 70 wt % concentrated H_2O_2 at centralized plants and requires hazardous transportation to the point-of-use. Decentralized electrosynthesis of H_2O_2 via the two-electron oxygen reduction reaction ($2e^-$ ORR, $O_2+2\ H^++2\ e^- \rightarrow H_2O_2$) offers a more sustainable route because it can be driven by increasingly affordable renewable electricity, eliminate the need for H_2 gas, and produce dilute H_2O_2 directly at the point-of-use, which is advantageous for distributed applications such as water treatment that only requires dilute (<0.1 wt %) H_2O_2. The key challenge is to develop robust electrocatalysts with high activity, selectivity, and stability for the desired $2e^-$ reduction to H_2O_2 (vs. the competing $4e^-$ reduction to water).

[0004] Electrochemical valorization of surplus biomass-derived feedstocks, such as glycerol, into high-value chemicals offers a sustainable route for utilizing biomass resources and decarbonizing chemical manufacturing. Glycerol, for example, is typically valorized solely via anodic oxidation, with lower-value products such as hydrogen gas or water generated at cathode. However, there is a need to improve biomass utilization by valorizing biomass resources at both the anode and cathode.

BRIEF SUMMARY OF THE INVENTION

[0005] Disclosed herein are electrochemical cells and methods for using the same. One aspect of the invention provides for an electrochemical cell comprising an acidic or neutral electrolyte and a cathode immersed in the electrolyte, wherein the cathode comprises a two-electron oxygen reduction reaction (2e– ORR) electrocatalyst composed of a metal chalcogenide, wherein the metal is Ni or Pd. Another aspect of the technology provides for production of hydrogen peroxide or preparing an oxidation produce of a biomass-derived feedstock with the electrochemical cell.

[0006] Another aspect of the technology provides for an electrochemical cell comprising an acidic catholyte, a cathode immersed in the catholyte, an acidic anolyte, and an anode immersed in the anolyte, wherein the cathode comprises a two-electron oxygen reduction reaction ($2e^-$ ORR) electrocatalyst composed a metal chalcogenide and the catholyte comprises oxygen (O_2), hydrogen peroxide (H_2O_2), hydroxyl radical (·OH), a regenerable metal ion, and a biomass-derived feedstock, and wherein the anolyte comprises the biomass-derived feedstock. Another aspect of the technology provides for production of hydrogen peroxide or preparing an oxidation product of a biomass-derived feedstock with the electrochemical cell.

BRIEF DESCRIPTION OF THE DRAWINGS

[0007] Non-limiting embodiments of the present invention will be described by way of example with reference to the accompanying figures, which are schematic and are not intended to be drawn to scale. In the figures, each identical or nearly identical component illustrated is typically represented by a single numeral. For purposes of clarity, not every component is labeled in every figure, nor is every component of each embodiment of the invention shown where illustration is not necessary to allow those of ordinary skill in the art to understand the invention.

[0008] FIG. **1**: Linear pairing strategy for electrochemical valorization of glycerol. The schematic shows cathodic valorization of glycerol enabled by the electro-Fenton process at a stable cathode is further paired with anodic oxidation and integrated into a linear paired electrochemical process to concurrently produce the same glycerol-derived oxidation products at both cathode and anode.

[0009] FIG. **2**: Computational assessments of the ORR energetics and the surface stability of c-$NiSe_2$ (in comparison with c-$CoSe_2$). Panel (a) shows crystal structures of c-$NiSe_2$ and c-$CoSe_2$. Panel (b) shows calculated free energy diagrams of the $2e^-$ vs. $4e^-$ ORR pathway on the c-$NiSe_2$ vs. c-$CoSe_2$ (100) surface at U_{RHE}^{o}. Panel (c) shows different coverages of O* and/or OH* (top) and comparisons of their free energies (bottom) on the c-$NiSe_2$ vs. c-$CoSe_2$ (100) surface in equilibrium with water. The binding energies of O* and OH* on their preferential binding sites at U_{RHE}^{o} are shown as the bottom insets in panel c. The yellow shaded regions indicate the potential range where the adsorbate-free clean surface is lower in free energy compared to the O*- and/or OH*-adsorbed surfaces. The inset images show the co-adsorption of one O* and one OH* to their preferential binding sites on the surface unit cell including two metal sites and four Se sites. The Ni, Co, Se, O, and H atoms are displayed in green, magenta, orange, red, and white, respectively.

[0010] FIG. **3**: The electrocatalytic properties and stability of c-$NiSe_2$ (in comparison with c-$CoSe_2$) for acidic $2e^-$ ORR and bulk electrosynthesis of H_2O_2. Panel (a) shows RRDE voltammograms recorded at 1600 rpm and panel (b) shows the H_2O_2 selectivity profiles of drop-casted c-$NiSe_2$ (left) and c-$CoSe_2$ (right) catalysts with various catalyst loadings in O_2-saturated 0.05 M H_2SO_4 (pH~1.2). Panel (c) shows normalized metal and selenium leaching rates of drop-casted c-$NiSe_2$ and c-$CoSe_2$ catalysts during RRDE stability tests in O_2-saturated 0.05 M H_2SO_4 (pH~1.2, left) and 0.1 M $NaHSO_4/Na_2SO_4$ buffer (pH~2.8, right). For each catalyst, the error bars result from four RRDE stability tests at different catalyst loadings (Table 2). Panel (d) shows the cumulative H_2O_2 yield (left) and H_2O_2 selectivity (right) after 6 hours for four trials of H_2O_2 bulk electrosynthesis in

O_2-saturated 0.05 M H_2SO_4 (4 mL, stirred at 1200 rpm) using four $NiSe_2$/CFP electrodes (~1.06 mg_{Ni} $cm^{-2}{}_{geo}$, ~1 $cm^{-2}{}_{geo}$) operated at different fixed applied potentials (0.50, 0.55, 0.60, 0.65 V vs. RHE) (see details in FIG. **18**). Panel (e) show long-term (37 h) sustained bulk electrosynthesis of H_2O_2 in O_2-saturated 0.05 M H_2SO_4 at the optimum potential of 0.60 V vs. RHE using one $NiSe_2$/CFP electrode repeatedly for five consecutive runs (see details in FIG. **21**).

[0011] FIG. **4**: Glycerol valorization enabled by the electro-Fenton process on $NiSe_2$/CFP in the cathodic half-cell. Panel (a) shows balanced equation of cathodic glycerol valorization, which suggests proton consumption. Panel (b) shows possible reaction pathways of glycerol oxidation into various C_3, C_2, and C_1 products by the electro-Fenton process at $NiSe_2$/CFP cathode. The detected (or anticipated) and undetected products are labeled based on NMR analyses. Panel (c) shows glycerol conversion (left) and the selectivity toward all detected C_3 products (right) as a function of [Fe^{2+}] (0.1, 0.5, 1.0, or 2.5 mM) after passing a controlled amount of charge through $NiSe_2$/CFP cathode in O_2-saturated 0.1 M $NaHSO_4/Na_2SO_4$ buffer (pH~2.8) starting with ~50 mM glycerol under vigorous stirring. Panel (c) shows aqueous phase organic (C_3, C_2, and C_1) product selectivity, glycerol conversion percentage, and carbon balance of all detected aqueous phase organic products for cathodic valorization of glycerol (~50 mM) under the optimum [Fe^{2+}] of 0.5 mM.

[0012] FIG. **5**: Linear paired electrochemical valorization of glycerol via the electro-Fenton process at $NiSe_2$/CFP cathode and oxidation at Pt/C anode. Panel (a) shows the cathode current and external bias over time, which shows the steady operation of the linear paired system including a $NiSe_2$/CFP cathode (~1.24 mg_{Ni} $cm^{-2}{}_{geo}$, ~1 $cm^{-2}{}_{geo}$) operated at 0.60 V vs. RHE in O_2-saturated $NaHSO_4/Na_2SO_4$ buffer (pH~2.8, containing ~50 mM glycerol and 0.5 mM Fe^{2+}) and a Pt/C anode (~2 mg_{Pt} $cm^{-2}{}_{geo}$, ~1 $cm^{-2}{}_{geo}$) operated in Ar-saturated H_2SO_4 solution (containing ~50 mM glycerol). The current and bias are influenced by different supporting electrolyte concentrations (Condition I: 0.1 M $NaHSO_4/Na_2SO_4$ for catholyte, and 0.05 M H_2SO_4 for anolyte; Condition II: 0.5 M $NaHSO_4/Na_2SO_4$ for catholyte, and 0.5 M H_2SO_4 for anolyte). Panel (b) shows product selectivity, glycerol conversion percentage, and carbon balance of all detected aqueous phase organic (C_3, C_2, and C_1) products for linear paired electrochemical valorization of glycerol under different supporting electrolyte conditions (I and II, as described in panel a).

[0013] FIG. **6**: Calculated bulk Pourbaix diagrams. Panel (a) shows c-$NiSe_2$ and panel (b) shows c-$CoSe_2$ assuming an ionic concentration of 10^{-6} mol/kg for each element of interest (59 ppb Ni, 59 ppb Co, and 79 ppb Se, which are reasonably low concentrations that can fairly reflect the acidic electrolyte solutions used in our experiments). These diagrams are adapted from the Materials Project[S1]. The multicolor gradient indicates the Gibbs free energy of the compound at a given set of potential and pH conditions with respect to its Pourbaix stable phase (ΔG_{pbx}), reflecting the electrochemical stability window of the compound. It was surmised in a previous report[S2] that materials with ΔG_{pbx} up to high values as much as 0.5 eV/atom can persist in electrochemical environments because of the energy barriers for the dissociation reactions. The solid white frame defines the thermodynamic equilibrium stability window of the compound without considering the kinetics of the dissociation reactions. The yellow and orange color vertical bars indicate the potential and pH ranges of interest for the acidic $2e^-$ ORR (in 0.05 M H_2SO_4) and for the Fe^{2+}-mediated electro-Fenton process (at the optimum pH of 2.8 to 3.0), respectively.

[0014] FIG. **7**: Panel (a) shows SEM image of $Ni(OH)_2$ precursor. Panel (b) shows SEM image, panel (c) shows PXRD pattern, panel (d) shows Raman spectrum, panel (e) shows Ni 2p and panel (f) shows Se 3d XPS spectra of as-synthesized c-$NiSe_2$ sample. The standard PXRD pattern of c-$NiSe_2$ (PDF #88-1711) is adapted from the International Centre for Diffraction Data (ICDD) database. From the structural characterization results, the as-synthesized c-$NiSe_2$ sample is phase-pure and exhibits unoxidized surface.

[0015] FIG. **8**: Panel (a) shows SEM image of CHCH precursor. Panel (b) shows SEM image, Panel (c) shows PXRD pattern, panel (d) shows Raman spectrum, panel (e) shows Co 2p and panel (f) shows Se 3d XPS spectra of as-synthesized c-$CoSe_2$ sample. The standard PXRD pattern of c-$CoSe_2$ (PDF #88-1712) is adapted from the International Centre for Diffraction Data (ICDD) database. From the structural characterization results, the as-synthesized c-$CoSe_2$ sample is phase-pure and exhibits unoxidized surface.

[0016] FIG. **9**: Cyclic voltammograms of c-$NiSe_2$ in panels (a-d) and c-$CoSe_2$ in panels (e-h) catalysts with various catalyst loadings recorded in Ar-saturated 0.05 M H_2SO_4 solution (pH~1.2) at various scan rates. The corresponding C_{dl} values of (i) c-$NiSe_2$ and (j) c-$CoSe_2$ catalysts with various catalyst loadings at 0.35 V vs. RHE in Ar-saturated 0.05 M H_2SO_4 solution (pH~1.2). (k) Various catalyst loadings of c-$NiSe_2$ and c-$CoSe_2$ catalysts result in similar ranges of C_{dl} values between these two catalysts at 0.35 V vs. RHE in Ar-saturated 0.05 M H_2SO_4 solution.

[0017] FIG. **10**: Panel (a) shows RRDE voltammograms recorded at 1600 rpm and panel (b) shows the H_2O_2 selectivity profiles of drop-casted c-$NiSe_2$ (left) and c-$CoSe_2$ (right) catalyst with various catalyst loadings in O_2-saturated 0.1 M $NaHSO_4/Na_2SO_4$ buffer solution (pH~2.8, the optimal pH for the electro-Fenton process).

[0018] FIG. **11**: Cyclic voltammograms of c-$NiSe_2$ in panels (a-d) and c-$CoSe_2$ in panels (e-h) catalysts with various catalyst loadings recorded in Ar-saturated 0.1 M $NaHSO_4/Na_2SO_4$ buffer solution (pH~2.8) at various scan rates. The corresponding C_{dl} values of c-$NiSe_2$ in panel (i) and c-$CoSe_2$ in panel (j) catalysts with various catalyst loadings at 0.35 V vs. RHE in Ar-saturated 0.1 M $NaHSO_4/Na_2SO_4$ buffer solution (pH~2.8). Panel (k) shows various catalyst loadings of c-$NiSe_2$ and c-$CoSe_2$ catalysts result in similar ranges of C_{dl} values between these two catalysts at 0.35 V vs. RHE in Ar-saturated 0.1 M $NaHSO_4/Na_2SO_4$ buffer solution.

[0019] FIG. **12**: Protocols for the RRDE stability tests of c-$NiSe_2$ and c-$CoSe_2$ catalysts. Step 1 (red shaded region): In O_2-saturated electrolyte solution, the Pt ring electrode was electrochemically cleaned by running cyclic voltammetry between 0.05 V and 1.2 V vs. RHE (without iR-correction) at the scan rate of 100 mV s^{-1} and the rotation rate of 1600 rpm for 10 cycles, meanwhile holding the catalyst-coated disk electrode at 0.75 V vs. RHE. The purpose of this step is to remove PtO_x from the Pt ring electrode surface[S3, S4].

[0020] Step 2 (blue shaded region): In O_2-saturated electrolyte solution, the catalyst-coated disk electrode was linearly swept from 0.75 V to −0.025 vs. RHE (without iR-correction) at the scan rate of 50 mV s^{-1} and a constant rotation rate (400, 625, 900, 1225, 1600, or 2025 rpm) to drive the acidic $2e^-$ ORR, meanwhile holding the Pt ring electrode at 1.3 V vs. RHE to detect the H_2O_2 production. The rotation rate was sequentially changed between scans.

[0021] Overall procedure: Since holding the Pt ring electrode at 1.3 V vs. RHE for an extended period of time in Step 2 would result in the formation of the surface PtO_x [S3, S4], the Pt ring electrode was periodically cleaned during the RRDE stability tests using the protocol described in Step 1. Thus, the RRDE stability tests were performed by alternating between Step 1 and Step 2, leading to a total of 255 linear sweep voltammetry scans on the disk electrode over the entire course of ~-4.0 h. The catalyst stability was monitored by tracking the disk potential required at a certain disk current density (j_{disk}) or peroxide current density ($j_{peroxide}$) of 0.5 mA cm^{-2}_{disk} at 2025 rpm (FIGS. **13** and **14**).

[0022] FIG. **13**: The stability of c-$NiSe_2$ shown in in panel (a) and c-$CoSe_2$ shown in panel (b) catalysts with various catalyst loadings monitored by tracking the disk potential at a certain disk current density (j_{disk}, top) or peroxide current density ($j_{peroxide}$, bottom) of 0.5 mA cm^{-2}_{disk} at 2025 rpm during the RRDE stability tests in O_2-saturated 0.05 M H_2SO_4 solution (pH~1.2). The red shaded regions refer to the electrochemical cleaning of the Pt ring electrode, and the blue shaded regions refer to the linear sweep voltammetry of the catalyst-coated disk electrode (see details in FIG. **12**). The disk potential of c-$NiSe_2$ remained stable to reach the same magnitude of j_{disk} or $j_{peroxide}$ throughout the tests (panel a), whereas that of c-$CoSe_2$ cathodically shifted over the scans (panel b).

[0023] FIG. **14**: The stability of c-$NiSe_2$ shown in panel (a) and c-$CoSe_2$ shown in panel (b) catalysts with various catalyst loadings monitored by tracking the disk potential at a certain disk current density (j_{disk}, top) or peroxide current density ($j_{peroxide}$, bottom) of 0.5 mA cm^{-2}_{disk} at 2025 rpm during the RRDE stability tests in O_2-saturated 0.1 M $NaHSO_4/Na_2SO_4$ buffer solution (pH~2.8, optimal for the electro-Fenton process). The red shaded regions refer to the electrochemical cleaning of the Pt ring electrode, and the blue shaded regions refer to the linear sweep voltammetry of the catalyst-coated disk electrode (see details in FIG. **12**). The disk potential of c-$NiSe_2$ remained stable to reach the same magnitude of j_{disk} or $j_{peroxide}$ throughout the tests (panel a), whereas that of c-$CoSe_2$ cathodically shifted over the scans (panel b).

[0024] FIG. **15**: Panels (a,b) show Raman spectra of (a) c-$NiSe_2$ and (b) c-$CoSe_2$ catalysts before and after RRDE stability tests in O_2-saturated 0.05 M H_2SO_4 (pH~1.2) or 0.1 M $NaHSO_4/Na_2SO_4$ (pH~2.8), showing no change after electrochemical testing. (c,d) X-ray photoelectron spectra of (c) c-$NiSe_2$ and (d) c-$CoSe_2$ catalysts before and after RRDE stability tests in O_2-saturated 0.05 M H_2SO_4 (pH~1.2) or 0.1 M $NaHSO_4/Na_2SO_4$ (pH~2.8). The Ni 2p spectra of the spent c-$NiSe_2$ catalyst were interfered by the F KL2 Auger signal because of the presence of Nafion in the recovered catalyst (panel c, left). Since the Se 3d spectra of the spent c-$NiSe_2$ catalyst (panel c, right) and the Co 2p and Se 3d spectra of the spent c-$CoSe_2$ catalyst (panel d) showed no change after electrochemical testing, it can be concluded that the surface chemical states of the spent c-$NiSe_2$ and c-$CoSe_2$ catalysts remained the same as those of the pristine samples.

[0025] FIG. **16**: Panel (a) shows SEM image of $Ni(OH)_2$/CFP precursor. Panel (b) shows SEM image, panel (c) shows PXRD pattern, panel (d) shows Raman spectrum, panel (e) shows Ni 2p and panel (f) shows Se 3d XPS spectra of as-synthesized c-$NiSe_2$/CFP sample. The asterisks in (c) indicate the PXRD peaks of the CFP substrate. The standard PXRD pattern of c-$NiSe_2$ (PDF #88-1711) is adapted from the International Centre for Diffraction Data (ICDD) database. From the structural characterization results, the as-synthesized c-$NiSe_2$/CFP sample is phase-pure and exhibits unoxidized surface.

[0026] FIG. **17**: Shows a schematic of the two-compartment three-electrode setup for bulk electrosynthesis of H_2O_2 in acidic solution. Nafion 117 membrane was used to separate the two compartments to avoid the oxidation of H_2O_2 product on the anode. A minimal volume (4 mL) of catholyte was used and vigorously stirred at 1200 rpm to achieve higher H_2O_2 concentrations under facilitated mass transfer of O_2 gas. A blanket of O_2 gas was maintained over the surface of O_2-saturated catholyte during H_2O_2 electrosynthesis. A rubber septum punctured with a syringe needle served as the gas outlet, which was only removed when a small aliquot of catholyte was sampled for chemical detection of H_2O_2 product and was otherwise capped to minimize the evaporation of catholyte during H_2O_2 electrosynthesis.

[0027] FIG. **18**: Bulk electrosynthesis of H_2O_2 in O_2-saturated 0.05 M H_2SO_4 solution (pH~1.2, 4 mL, stirred at 1200 rpm) using four c-$NiSe_2$/CFP electrodes (~1.06 mg_{Ni} cm^{-2}_{geo}, ~1 cm^{-2}_{geo}) operated at four different fixed applied potentials (0.65 V, 0.60 V, 0.55 V, 0.50 V vs. RHE). Panel (a) shows chronoamperometry curves, cumulative H_2O_2 concentration, cumulative H_2O_2 yield, cumulative H_2O_2 selectivity and Faradaic efficiency as a function of time. Comparisons of the cumulative H_2O_2 yield and H_2O_2 selectivity at the 6 h mark of each trial are shown in FIG. **3***d*. Panel (b) shows cyclic voltammograms of the c-$NiSe_2$/CFP electrodes recorded before and after each trial of the H_2O_2 electrosynthesis in O_2-saturated 0.05 M H_2SO_4 solution (stirred at 1200 rpm).

[0028] FIG. **19**: Panel (a) shows RRDE voltammograms of c-$NiSe_2$ (left, 458 μg_{Ni} cm^{-2}_{disk}) and c-$CoSe_2$ (right, 229 μg_{Co} cm^{-2}_{disk}) catalysts recorded at 1600 rpm in O_2-saturated 0.05 M H_2SO_4 solution (pH~1.2) were performed to study the $2e^-$ ORR (j_{disk}: disk current density; j_{ring}: ring current density; $j_{peroxide}$: peroxide current density). C_{dl} values of c-$NiSe_2$ (304 μF cm^{-2}_{disk}) and c-$CoSe_2$ (365 μF cm^{-2}_{disk}) was evaluated at 0.35 V vs. RHE in the same solution under Ar saturation. Linear sweep voltammograms of the catalyst-coated disk electrode recorded at 1600 rpm in Ar-saturated 0.05 M H_2SO_4 solution (pH~1.2) containing 1 mM, 5 mM, 10 mM, or 20 mM H_2O_2 were performed to study the electroreduction of H_2O_2 (j_{PRR}: current density of the hydrogen peroxide reduction reaction). The shaded regions (green: c-$NiSe_2$; magenta: c-$CoSe_2$) define the potential range where the magnitude of $j_{peroxide}$ under O_2 saturation (~1 mM O_2) was greater than that of j_{PRR} under 20 mM H_2O_2. Panel (b) shows $j_{peroxide}-j_{PRR}$ plotted against potential under 0 mM H_2O_2 (dashed lines, where $j_{PRR}=0$) or 20 mM H_2O_2 (solid lines). The shaded regions in (b) have the same physical meanings as those in (a). Compared to c-$CoSe_2$, the H_2O_2 production on c-$NiSe_2$ was more affected by the H_2O_2 electroreduction, as reflected by the greater

decrease in the peak value of $j_{peroxide}-j_{PRR}$ when the H_2O_2 concentration increased from 0 mM to 20 mM.

[0029] FIG. **20**: Panel (a) shows RRDE voltammograms of c-$NiSe_2$ (left, 381 μg_{Ni} $cm^{-2}{}_{disk}$) and c-$CoSe_2$ (right, 229 μg_{Co} $cm^{-2}{}_{disk}$) catalysts recorded at 1600 rpm in O_2-saturated 0.1 M $NaHSO_4/Na_2SO_4$ solution (pH~2.8) were performed to study the $2e^-$ ORR (j_{disk}: disk current density; j_{ring}: ring current density; $j_{peroxide}$: peroxide current density). C_{dl} values of c-$NiSe_2$ (328 μF $cm^{-2}{}_{disk}$) and c-$CoSe_2$ (337 μF $cm^{-2}{}_{disk}$) was evaluated at 0.35 V vs. RHE in the same solution under Ar saturation. Linear sweep voltammograms of the catalyst-coated disk electrode recorded at 1600 rpm in Ar-saturated 0.1 M $NaHSO_4/Na_2SO_4$ solution (pH~2.8) containing 1 mM, 5 mM, 10 mM, or 20 mM H_2O_2 were performed to study the electroreduction of H_2O_2 (j_{PRR}: current density of the hydrogen peroxide reduction reaction). The shaded regions (green: c-$NiSe_2$; magenta: c-$CoSe_2$) define the potential range where the magnitude of $j_{peroxide}$ under O_2 saturation (~1 mM O_2) was greater than that of j_{PRR} under 20 mM H_2O_2. Panel (b) shows $j_{peroxide}-j_{PRR}$ plotted against potential under 0 mM H_2O_2 (where $j_{PRR}=0$, dashed lines) or 20 mM H_2O_2 (solid lines). The shaded regions in (b) have the same physical meanings as those in (a). Compared to c-$CoSe_2$, the H_2O_2 production on c-$NiSe_2$ was more affected by the H_2O_2 electroreduction, as reflected by the greater decrease in the peak value of $j_{peroxide}-j_{PRR}$ when the H_2O_2 concentration increased from 0 mM to 20 mM.

[0030] FIG. **21**: Bulk electrosynthesis of H_2O_2 in O_2-saturated 0.05 M H_2SO_4 solution (pH~1.2, 4 mL, stirred at 1200 rpm) at the optimum potential of 0.60 V vs. RHE using one c-$NiSe_2$/CFP electrode (~1.06 mg_{Ni} $cm^{-2}{}_{geo}$, ~1 $cm^{-2}{}_{geo}$) repeatedly for five consecutive runs and a total of 37 hours. Panel (a) shows chronoamperometry curve. Panel (b) shows cumulative H_2O_2 concentration, panel (c) shows cumulative H_2O_2 yield, panel (d) shows cumulative H_2O_2 selectivity and Faradaic efficiency as a function of time. Fresh H_2O_2-free electrolyte solution was replaced into the cathode compartment between runs. Comparisons of the cumulative H_2O_2 yield and H_2O_2 selectivity at the 2 h mark and the end of each run are shown in FIG. **3***e*.

[0031] FIG. **22**: Bulk electrosynthesis of H_2O_2 in O_2-saturated 0.1 M $NaHSO_4/Na_2SO_4$ solution (pH~2.8, 4 mL, stirred at 1200 rpm) using c-$NiSe_2$/CFP electrode (~1.06 mg_{Ni} $cm^{-2}{}_{geo}$, ~1 $cm^{-2}{}_{geo}$) operated at 0.60 vs. RHE. Shows chronoamperometry curve, cumulative H_2O_2 concentration, cumulative H_2O_2 yield, and cumulative H_2O_2 selectivity and Faradaic efficiency as a function of time.

[0032] FIG. **23**: Panel (a) shows Raman spectra and panel (b) shows X-ray photoelectron spectra of c-$NiSe_2$/CFP before and after H_2O_2 bulk electrosynthesis at 0.60 V vs. RHE in O_2-saturated 0.05 M H_2SO_4 or 0.1 M $NaHSO_4/Na_2SO_4$. Panel (c) shows Ni K-edge and Se K-edge X-ray absorption near edge structure (XANES, left) and extended X-ray absorption fine structure (EXAFS, right) spectra of c-$NiSe_2$/CFP before and after H_2O_2 bulk electrosynthesis at 0.60 V vs. RHE in O_2-saturated 0.05 M H_2SO_4, which are nearly identical. Panel (d) shows normalized nickel and selenium leaching rates of c-$NiSe_2$/CFP (~1.06 μg_{Ni} $cm^{-2}{}_{geo}$, ~1 $cm^{-2}{}_{geo}$) during H_2O_2 bulk electrosynthesis at 0.60 V vs. RHE in O_2-saturated 0.05 M H_2SO_4 or 0.1 M $NaHSO_4/Na_2SO_4$.

[0033] FIG. **24**: Shows schematic of the two-compartment three-electrode setup for half-cell studies of the electro-Fenton process for glycerol valorization at c-$NiSe_2$ cathode.

[0034] FIG. **25**: Panel (a) shows chronoamperometry curves when passing a controlled amount of charge (14.6 C, 29.2 C, or 43.9 C) through the c-$NiSe_2$ cathode (~1.06 mg_{Ni} $cm^{-2}{}_{geo}$, ~1 $cm^{-2}{}_{geo}$) at 0.60 V vs. RHE in 4 mL of O_2-saturated 0.1 M $NaHSO_4/Na_2SO_4$ solution (pH~2.8, stirred at 1200 rpm) containing ~50 mM glycerol and 0.5 mM Fe^{2+}. Panel (b) shows ^1H NMR spectra before and after passing a controlled amount of charge through the c-$NiSe_2$ cathode. Each NMR sample in (b) was made by mixing 25 μL of D_2O (containing the maleic acid internal standard) with 475 L of aqueous catholyte, and the final concentration of the maleic acid internal standard after mixing is ~5 mM. As the amount of passed charge increased, the solution volume in the cathode compartment decreased due to evaporation under the O_2 gas flow, the solution pH in the cathode compartment decreased due to proton permeation from the more acidic 0.05 M H_2SO_4 solution in the anode compartment (see FIG. **24**). Panel (c) shows aqueous phase organic (C_3, C_2, and C_1) product selectivity, glycerol conversion percentage, and carbon balance of all detected aqueous phase organic products determined by ^1H NMR results after passing a controlled amount of charge through the c-$NiSe_2$ cathode.

[0035] FIG. **26**: The impact of Fe^{2+} concentration on the glycerol valorization in the cathodic half-cell after passing a controlled amount of charge (14.6 C, 29.2 C, or 43.9 C) through the c-$NiSe_2$ cathode (~1.06 mg_{Ni} $cm^{-2}{}_{geo}$, ~1 $cm^{-2}{}_{geo}$) at 0.60 V vs. RHE in 4 mL of O_2-saturated 0.1 M $NaHSO_4/Na_2SO_4$ solution (pH~2.8, stirred at 1200 rpm) containing ~50 mM glycerol and various concentration of Fe^{2+} (0.1, 0.5, 1.0, or 2.5 mM). Aqueous phase organic (C_3, C_2, and C_1) product selectivity, glycerol conversion percentage, and carbon balance of all detected aqueous phase organic products were determined by ^1H NMR analyses. As high concentrations of paramagnetic Fe^{2+} ions could cause ^1H NMR peak broadening, the NMR samples were prepared differently depending on the [Fe^{2+}] in the aqueous catholyte. When [Fe^{2+}] was low (0.1 mM or 0.5 mM), the NMR sample was made by mixing 25 μL of D_2O (containing the maleic acid internal standard) with 475 μL of aqueous catholyte, and the final concentration of the maleic acid internal standard after mixing was ~5 mM. When [Fe^{2+}] was high (1.0 mM or 2.5 mM), the NMR sample was made by mixing 450 μL of D_2O (containing the maleic acid internal standard) with 50 μL of aqueous catholyte, and the final concentration of the maleic acid internal standard after mixing is ~0.5 mM.

[0036] FIG. **27**: Panel (a) shows Raman spectra and panel (b) shows X-ray photoelectron spectra of c-$NiSe_2$/CFP before and after half-cell studies of the cathodic valorization of glycerol via the electro-Fenton process at 0.60 V vs. RHE in O_2-saturated 0.1 M $NaHSO_4/Na_2SO_4$ (pH~2.8) containing ~50 mM glycerol and 0.5 mM Fe^{2+}.

[0037] FIG. **28**: Panel (a) shows a schematic of the two-compartment three-electrode setup for half-cell studies of the direct anodic oxidation of glycerol at Pt/C anode. Panel (b) shows cyclic voltammograms of Pt/C anode (2 mg_{Pt} $cm^{-2}{}_{geo}$, 1 $cm^{-2}{}_{geo}$) for glycerol oxidation. Panel (c) shows chronopotentiometry curves when passing a controlled amount of charge (14.8 C, 29.7 C, or 45.1 C) through the Pt/C anode at 1.7 mA in 4 mL of Ar-saturated 0.05 M H_2SO_4

solution (pH~1.2, stirred at 1200 rpm) containing ~50 mM glycerol. Panel (d) shows ^{1}H NMR spectra before and after passing a controlled amount of charge through the Pt/C anode. Each NMR sample in (d) was made by mixing 25 μL of D_2O (containing the maleic acid internal standard) with 475 μL of aqueous anolyte, and the final concentration of the maleic acid internal standard after mixing was ~5 mM. As the amount of passed charge increased, the solution volume in the anode compartment decreased due to evaporation under the Ar gas flow. Panel (e) shows aqueous phase organic (C_3, C_2, and C_1) product selectivity, glycerol conversion percentage, and carbon balance of all detected aqueous phase organic products determined by ^{1}H NMR results after passing a controlled amount of charge through the Pt/C anode.

[0038] FIG. **29**: Shows a schematic of the two-compartment three-electrode setup for linear paired electrochemical valorization of glycerol at c-$NiSe_2$ cathode and Pt/C anode. The electro-Fenton process for glycerol valorization takes place in the cathode compartment at the c-$NiSe_2$ cathode in O_2-saturated $NaHSO_4/Na_2SO_4$ buffer solution (pH~2.8) containing ~50 mM glycerol and 0.5 mM Fe^{2+}. The direct anodic oxidation of glycerol takes place in the anode compartment at the Pt/C anode in Ar-saturated H_2SO_4 solution containing ~50 mM glycerol. Protons are transported through the Nafion 117 membrane to stabilize the acidic pH of the cathode compartment.

[0039] FIG. **30**: The c-$NiSe_2$ cathode potential and the Pt/C anode potential during the linear paired electrochemical valorization of glycerol (catholyte: O_2-saturated $NaHSO_4/Na_2SO_4$ solution containing ~50 mM glycerol and 0.5 mM Fe^{2+}, pH~2.8; anolyte: Ar-saturated H_2SO_4 solution containing ~50 mM glycerol) under supporting electrolyte condition I (shown in panel A: 0.1 M $NaHSO_4/Na_2SO_4$ for catholyte, 0.05 M H_2SO_4 for anolyte) or condition II (shown in panel B: 0.5 M $NaHSO_4/Na_2SO_4$ for catholyte, 0.5 M H_2SO_4 for anolyte).

[0040] FIG. **31**: Computational pre-screening of stability, selectivity, and activity of metal compound-based $2e^-$ ORR catalysts. Panel (a) shows crystal structures of pyrite- and marcasite-type metal chalcogenides. Panel (b) shows energetics of O* and OH* adsorption to their preferential binding sites on the most stable facets of c-CoS_2, c-$CoSe_2$, o-$CoSe_2$, and c-$NiSe_2$. Panel (c) shows comparisons of free energies of different O* and/or OH* coverages on c-$NiSe_2$ (100) surface unit cell including two Ni and four Se sites. For 3 O* and 4 O* coverages, two O* bind to Ni, and the rest of O* bind to Se. For the other O* and/or OH* coverages, all adsorbates bind to Ni. (d) Free energy diagrams of the $2e^-$ and $4e^-$ ORR pathways.

[0041] FIG. **32**: Structural characterization of as-synthesized $PdSe_2$. Panel a) shows crystal structure of $PdSe_2$ viewed down the [200] and [002] directions. Panel b) shows powder x-ray diffraction pattern of $PdSe_2$ compared to the standard pattern. Panel c) shows SEM micrograph of $PdSe_2$ with overlaid SEM-EDS atomic ratios. Panel d) shows Raman spectrum of $PdSe_2$ with previously calculated Raman modes overlaid. Panel e) shows Pd L_3 edge XANES of $PdSe_2$ with Pd foil, PdO, and K_2PdCl_6 shown as oxidation state standards.

[0042] FIG. **33**: Rotating ring disk electrode (RRDE) results of $PdSe_2$. Panel a) shows $PdSe_2$ measured in O_2-saturated conditions in 0.05 M NaPi buffer (pH=6.5) and 0.05 H_2SO_4 (pH=1.2), and panel b) shows with a kinetic current comparison plot of $PdSe_2$ in neutral conditions compared to other $2e^-$ ORR catalysts measured in neutral conditions from the literature, and panel c) shows extended stability plot of $PdSe_2$ measured at a constant potential of 0 V vs. RHE for >6 hours (dashed lines indicate ring cleaning via CV).

[0043] FIG. **34**: Bulk electrolysis of $PdSe_2$ (compared to o-$CoSe_2$) measured in 0.5 M NaPi buffer. Panel a) shows current comparison, panel b) shows concentration of H_2O_2, panel c) shows total accumulation of H_2O_2, and panel d) shows H_2O_2 selectivity over time.

[0044] FIG. **35**: Evaluation of the stability of $PdSe_2$. Panel a) shows leached Pd and Se measured by ICP-OES after electrolysis at 0.2 V vs. RHE and 0.3 V vs. RHE, panel b) shows Raman spectra, panel c) shows XRD and panel d) shows XPS Se 2d peak of $PdSe_2$/CFP after 6 hours of ORR operation at the labeled potentials compared to the pristine sample, and panel e) shows operando XANES and panel f) shows EXAFS at E_{oc} (the open circuit potential) and at several applied potentials as labeled.

[0045] FIG. **36**: Surface Pourbaix diagrams of the (001) and (100) surfaces of $PdSe_2$. Each line represents the free energy of formation of each configuration. The clean surface, $H_2O_{(l)}$ and H^+/e^- are used as reference states.

[0046] FIG. **37**: Calculated free energy diagrams of $2e^-$ ORR pathways and their competing steps on the (001) and (100) $PdSe_2$ at the calculated equilibrium potential.

[0047] FIG. **38**: The interaction of OOH* with the external electric field on $PdSe_2$. X-axis is electric field in V/Å and y-axis is the interaction in eV.

[0048] FIG. **39**: Electrosynthesis of H_2O_2 in a flow cell on a $PdSe_2$/GDE electrode. A constant current of −30 mA (~5 mA cm^{-2}), −60 mA (~10 mA cm^{-2}), and −85 mA (~15 mA cm^{-2}) in a buffer solution of 0.25 M Na_2HPO_4/0.25 M NaH_2PO_4 (initial pH~6.5). Panel a) shows schematic of the 3-layer GDE/flow-cell assembly with each layer annotated and a representative SEM image of the $PdSe_2$ catalyst dispersed on GDE electrode. Panel b) shows cyclic voltammogram of the $PdSe_2$ loaded GDE before the electrosynthesis process, panel c) shows potential vs. time curve (continuous line, left-axis) and Faradaic efficiency (dots, right axis) of the $PdSe_2$/GDE during constant current electrosynthesis, and panel d) shows the corresponding H_2O_2 accumulation during the H_2O_2 electrosynthesis processes.

[0049] FIG. **40**: Long term stability of $PdSe_2$. Panel a) shows CV of $PdSe_2$/GDE electrode with high Nafion loading in the catalyst dispersion (~0.05 mg, or 1 mL of 5 wt. % solution), and panel b) shows galvanostatic test of $PdSe_2$ over 48 hours at −75 mA, stopped due to counter electrode overload.

DETAILED DESCRIPTION OF THE INVENTION

[0050] Disclosed herein is an electrochemical cell and a method of using the same. The present technology allows for harnessing electricity (which could be generated from solar and wind) for electrochemical synthesis of H_2O_2 and high-value chemicals from biomass feedstocks, which offers a sustainable alternative to conventional centralized chemical manufacturing. For example, glycerol is a byproduct of biodiesel production and has become a surplus biomass-derived chemical. Oxidative upgrading of glycerol is very attractive, because all C_3 and C_2 oxidation products have higher economic values than glycerol. Compared to thermal

oxidation that requires high temperature and oxygen pressure, electrochemical oxidation poses several advantages including near-ambient operation, less reagent waste, and distributed small-scale production.

[0051] Electrochemical oxidation of glycerol typically occurs at catalytic anodes made of noble metals or earth-abundant electrocatalysts, which is paired with either four-electron oxygen reduction reaction ($4e^-$ ORR) in a galvanic cell or hydrogen evolution reaction (HER) in an electrolytic cell (FIG. **1**). In either case, the chemicals generated at cathode have lower economic values (e.g., H_2 from steam methane reforming) than the glycerol-derived chemicals generated at anode [e.g., dihydroxyacetone (DHA)]. Anodic glycerol oxidation has been paired with CO_2 or CO reduction reaction (CO_2/CORR) that generates C_1 and/or C_{2+} products at the cathode, but the different cathode and anode feeds lead to different product portfolios between the two half-cells with additional system complexity and separation cost. Using glycerol as the sole feed in a so-called linear paired electrochemical process allows for production of value-added oxidation products at both cathode and anode simultaneously could be appealing.

[0052] An electrochemical cell is defined as a device that may produce an electrical current from a chemical reaction and/or use electrical energy to drive a chemical reaction. The electrochemical cell here includes a cathode immersed in an electrolyte and an anode immersed in an acidic electrolyte. In some embodiments of the disclosed technology, the electrochemical cell may contain two or three electrodes. The two-electrode configuration may contain a working electrode and a counter electrode. The three-electrode configuration may contain a working electrode, a reference electrode, and a counter electrode.

[0053] In one aspect, the electrochemical cell includes an electrolyte. An electrolyte is defined as a substance that conducts electric current. The catholyte is defined as an electrolyte used in the cathodic compartment of the electrochemical cell. An anolyte is defined as an electrolyte used in the anodic compartment of the electrochemical cell. The electrolyte, catholyte, and anolyte may be the same material or different material.

[0054] In one aspect of the technology, the electrochemical cell contains a cathode with an electrocatalyst that can perform the two-electron oxygen reduction reaction ($2e^-$ ORR). The oxygen reduction reaction (ORR) is the reduction half-reaction whereby oxygen is reduced to water via the four-electron pathway or hydrogen peroxide via the two-electron pathway. Hydrogen peroxide (H_2O_2) is a useful oxidant for a range of applications including the pulp and paper industry, chemical manufacturing, wastewater treatment, healthcare disinfection, and biomass valorization. Other chemical methods of hydrogen peroxide production, including via the anthraquinone process, are energy-intensive and unsafe as it produces concentrated H_2O_2 at centralized plants and requires hazardous transportation to end-users. Alternatively, decentralized electrosynthesis of H_2O_2 via $2e^-$ ORR offers a more sustainable route because it can be driven by increasingly affordable renewable electricity, eliminate the need for H_2 gas, and produce dilute H_2O_2 directly at the point of use, which is advantageous for distributed applications. A key challenge is to develop robust electrocatalysts with high activity, selectivity, and stability for the desired 2e (vs. the competing $4e^-$) ORR pathway.

[0055] The thermodynamics of $2e^-$ ORR ($O_2+2\ H^++2\ e^-\rightarrow H_2O_2$, standard equilibrium potential E^o=0.69 V vs. reversible hydrogen electrode, RHE) and $4e^-$ ORR ($O_2+4\ H^++4e^-\rightarrow 2\ H_2O$, E^o=1.23 V vs. RHE) are often described by the volcano relations between the thermodynamic limiting potential (UL) and the energetics of key reaction intermediates. $2e^-$ ORR proceeds via the adsorption of OOH* ($O_2+*+H^++e^-\rightarrow$OOH*, where * is an unoccupied surface binding site) followed by its desorption to form H_2O_2 (OOH*+$H^++e^-\rightarrow H_2O_2+*$); $4e^-$ ORR occurs via the O—O bond cleavage processes (thermal cleavage: $O_2+2*\rightarrow 2\ O*$, and OOH*+*$\rightarrow$O*+OH*; electrochemical reductive elimination: OOH*+$H^++e^-\rightarrow$O*+H_2O). The key intermediates of $2e^-$ ORR (OOH*) and $4e^-$ ORR (OH*) follow a linear scaling relationship (typically $\Delta G_{OOH}{}^*=\Delta G_{OH}{}^*+3.2$ eV), resulting in the $2e^-$ and $4e^-$ ORR volcanos. The $2e^-$ ORR activity, determined by the OOH* adsorption energy ($\Delta G_{OOH}{}^*$), is maximized at the peak of $2e^-$ ORR volcano. Moving leftwards from $2e^-$ ORR volcano peak, the catalyst surface binds OOH* (and OH*) more strongly, and UL of $4e^-$ ORR is always more positive than that of $2e^-$ ORR, indicating the 4e pathway will dominate because there is a greater driving force to form H_2O than H_2O_2. To the right of $2e^-$ ORR volcano peak, UL of the $2e^-$ and $4e^-$ pathways overlap and moving rightwards will increase the selectivity (but lowering the activity) for $2e^-$ ORR because the formation of OH* (and OOH*) becomes more difficult. Besides electronic effects described above, the $2e^-$ ORR selectivity can also be improved by controlling geometric (or ensemble) effects by rearranging catalyst surface atoms to change adsorption sites of reaction intermediates, so that O* can be destabilized relative to OOH*, deviating from the conventional scaling relationship.

[0056] Several classes of selective $2e^-$ ORR catalysts, including noble metal alloys, carbon nanomaterials, single-atom catalysts, and metal compounds, have been studied for H_2O_2 electrosynthesis under different pH conditions. Among these reports, $2e^-$ ORR catalysts in alkaline solution have been mostly extensively studied, but H_2O_2 is unstable in alkaline solution. In contrast, the less studied acidic and neutral conditions are attractive for several reasons besides the chemical stability of H_2O_2. Acidic H_2O_2 electrosynthesis can proceed in the technologically mature proton exchange membrane (PEM) devices. On-site water disinfection and environmental treatment can also benefit from acidic H_2O_2 electrosynthesis because the electro-Fenton process operates at the optimum pH of about 3 to convert the produced H_2O_2 into the more oxidizing hydroxyl radical (·OH) for the removal of persistent bacteria and organic pollutants. For direct applications, neutral solutions can avoid the need for neutralization. However, high-performance yet cost-effective $2e^-$ ORR electrocatalysts in acidic and neutral solutions are still being developed.

[0057] One class of selective $2e^-$ ORR electrocatalysts are metal chalcogenides. In one embodiment of the disclosed technology, the cathode includes an electrocatalyst composed of a metal chalcogenide. A chalcogenide is defined as a chemical compound with at least one chalcogen anion (any anionic form of elements in Group 16 of the periodic table) and at least one more electropositive element. In one embodiment, the chalcogen anion may be a sulfide, selenide, telluride, polonide, or, less commonly, oxide, or any combination thereof.

[0058] In one embodiment the electropositive element of the metal chalcogenide is at least one metal. In one embodiment the metal may be earth-abundant or noble metals, including transition metals, post-transition metals, or any combination thereof. In some embodiments, the metal may be Li, Be, Na, Mg, Al, K, Ca, Sc, Ti, V, Cr, Mn, Fe, Co, Ni, Cu, Zn, Ga, Rb, Sr, Y, Zr, Nb, Mo, Tc, Ru, Rh, Pd, Ag, Cd, In, Sn, Cs, Ba, Hf, Ta, W, Re, Os, Ir, Pt, Au, Hg, Tl, Pb, Bi, Po, Fr, Ra. In some embodiments the metal chalcogenide may be cubic pyrite-type c-CoS_2, c-$CoSe_2$, c-$NiSe_2$, orthorhombic marcasite-type o-$CoSe_2$, layered $PdSe_2$, layered $MoSe_2$, MoS_2, $MoSe_2$, WS_2, WSe_2, or any combination thereof. In other embodiments, the metal chalcogenide is a spinel such as $CuCO_{2-x}Ni_xS_4$.

[0059] Another aspect of $2e^-$ ORR metal chalcogenide electrocatalysts is the preferential binding of O* and OH* products to either the chalcogenide or the metal. Previously studied metal chalcogenide electrocatalysts, including CoS_2 and $CoSe_2$, demonstrate preferential binding of O* and OH* to the sulfide and selenide. This has implications for electrocatalyst stability. Surface oxidation is more likely in electrocatalysts where O* and OH* more strongly bind to the chalcogenide due to the formation of highly soluble anions, such as SO_4^{2-}, and is followed by metal leaching and electrocatalyst degradation. One embodiment of the disclosed technology includes the preferential binding of O* and OH* to the earth abundant metal of the metal chalcogenide. In one embodiment, the electrocatalyst demonstrates preferential binding of O* and OH* to Ni.

[0060] In another aspect of the disclosed technology, the electrochemical cell may additionally contain reagents for electrosynthesis purposes. Generally, this involves reagents needed to generate hydroxyl radicals (·OH) via the advanced oxidation processes, including hydrogen peroxide (H_2O_2), and a regenerable metal ion. In one embodiment, the advanced oxidation may be via the electro-Fenton process, wherein the regenerable metal ion is Fe^{2+}. In other embodiments, the advanced oxidation may be via a Fenton-like process wherein the regenerable metal ion is Co, Cu, or Mn. In some embodiments a regenerable metal ion is not required for the production of the hydroxyl radical. For reasons discussed above, the pH of the electrochemical cell is acidic. In some embodiments, the electrochemical cell has a pH no lower than 0 and no higher than 7. In one embodiment, the electrochemical cell has a pH no lower than 0 and no higher than 4. In another embodiment, the electrochemical cell has a pH between 4.0 and 7.0. In one embodiment where the regenerable metal ion is Fe^{2+}, the electrochemical cell has a pH no lower than 0 and no higher than 4. In some embodiments the pH of the electrochemical cell is adjusted by the addition of a mineral acid. In some embodiments the mineral acid is sulfuric acid, hydrochloric acid, or perchloric acid. In one embodiment where the regenerable metal ion is Fe^{2+}, the pH of the electrochemical cell may be about 3 to prevent the precipitation of iron oxides in more basic conditions. Other regenerable metals may have other ideal acidic, basic, or neutral conditions of the electrochemical cell.

[0061] In one embodiment, the electrochemical cell electrolyte further includes a biomass-derived feedstock. Biomass-derived feedstock is defined as sustainable feedstock derived from biomass for chemicals and energy products. In some embodiments, biomass-derived feedstock includes forest product wastes, agricultural residues, organic fractions of municipal solid wastes, paper, cardboard, plastic, food waste, green waste, and other waste. In other embodiments, the biomass-derived feedstock may be polyols such as glycerol, hydroxymethylfurfural (HMF), glucose, fructose, and other monosaccharide and disaccharide (sugar) molecules, lignin, hemicellulose, cellulose, or other oxygen-containing compounds including compounds with ether, alcohol, aldehyde, and ester functional groups.

[0062] In some embodiments, the oxidation products of the electrochemical half cell starting from glycerol include C_3, C_2, and C_1 products. In some embodiments the oxidation products include aldehyde and ketone functional groups. In some embodiments the oxidation product may include dihydroxyacetone (DHA), glyceraldehyde (GLAD), glyceric acid (GLA), hydroxypyruvic acid (HPA), glycolaldehyde (GAD), glycolic acid (GA), glyoxylic acid (GLOA), formic acid (FA), or any combination thereof.

[0063] Advanced oxidation products are typically only produced at one electrode of the electrochemical cell. In one embodiment, the anode produces oxidation products. One aspect of the disclosed technology is an electrochemical cell wherein electrochemical reactions at both the cathode and anode both produce oxidation products, sometimes referred to as linear paired electrochemical cell.

[0064] In another aspect of the technology, the electrochemical cell may contain one or more compartments. In one embodiment, the electrochemical cell is oriented in a two-compartment H-type electrochemical cell (denoted as H-cell), wherein the two compartments are separated by a proton-permeable membrane. In another embodiment, electrochemical flow cell configurations may be used. In electrochemical flow cells, liquid biomass-derived feedstocks, reagents, and electrolytes may be continuously or periodically flowed past electrodes. In one embodiment, the proton permeable membrane may be a Nafion, Fumasep, Fumapem, or Aquivion membrane. In one embodiment the cathode is isolated to one compartment and the anode is isolated to the second compartment. %

[0065] In one embodiment, the anode may include platinum, palladium, ruthenium, antimony, bismuth, tin, and bimetallic alloys of these metals, ruthenium oxide, iridium oxide, or boron doped diamond.

[0066] In one embodiment the biomass-derived feedstock could be the same in each of the electrochemical cell compartments, representing the linear paired electrochemical process starting with the same feedstock. In another embodiment the biomass-derived feedstock in the cathodic compartment may be different from the biomass-derived feedstock in the anodic compartment, representing the paired electrochemical process in general.

[0067] The anodic and cathodic reaction products may be mixed and further purified together but they need not be. Where the anodic and cathodic reaction products are expected to be similar, mixing and purifying the reaction products from both the anodic and cathodic reactions together may simplify processing or reduced costs. In some embodiments, where biomass-derived feedstock is the same in each of the electrochemical cell compartments for the linear paired electrochemical process, the anodic and cathodic reaction products may be mixed and further purified together.

[0068] A further aspect of the disclosed technology is a method of preparing oxidation product of biomass-derived feedstock. In one embodiment of the method, the applied

potential to the anode is between 0.00 and 1.50 V vs. RHE. In another embodiment, the applied potential to the cathode is between 0.00 and 0.70 V vs. RHE.

[0069] Another aspect of the disclosed technology is a method of preparing oxidation product of biomass-derived feedstock with externally applied bias to the two-compartment H-cell. In one embodiment the externally applied bias is less than 0.01 V, 0.02V, 0.03 V, 0.04V, 0.05 V, 0.06 V, 0.07 V, 0.08 V, 0.09 V, 0.10 V, 0.11 V, 0.12 V, 0.13 V, 0.14 V, 0.15 V, 0.16 V, 0.17 V, 0.18 V, 0.19 V, 0.20 V, 0.21 V, 0.22 V, 0.23 V, 0.24 V, 0.25 V, 0.26 V, 0.27 V, 0.28 V, 0.29 V, 0.30 V, 0.31 V, 0.32 V, 0.33 V, 0.34 V, 0.35 V, 0.36 V, 0.37 V, 0.38 V, 0.39 V, 0.40 V, 0.41 V, 0.42 V, 0.43 V, 0.44 V, 0.45 V, 0.46 V, 0.47 V, 0.48 V, 0.49 V, 0.50 V, 0.51 V, 0.52 V, 0.53 V, 0.54 V, 0.55 V, 0.56 V, 0.57 V, 0.58 V, 0.59 V, 0.60 V, 0.61 V, 0.62 V, 0.63 V, 0.64 V, 0.65 V, 0.66 V, 0.67 V, 0.68 V, 0.69 V, 0.70 V, 0.71 V, 0.72 V, 0.73 V, 0.74 V, 0.75 V, 0.76 V, 0.77 V, 0.78 V, 0.79V, 0.80V, 0.81 V, 0.82 V, 0.83 V, 0.84 V, 0.85 V, 0.86 V, 0.87 V, 0.88 V, 0.89 V, 0.90 V, 0.91 V, 0.92 V, 0.93 V, 0.94 V, 0.95 V, 0.76 V, 0.77 V, 0.78 V, 0.79 V, 0.80 V, 0.81 V, 0.82 V, 0.83 V, 0.84 V, 0.85 V, 0.86 V, 0.87 V, 0.88 V, 0.89 V, 0.90 V, 0.91 V, 0.92 V, 0.93 V, 0.94 V, 0.95 V, 0.96 V, 0.97 V, 0.98 V, 0.99 V, 1.00 V, 1.01 V, 1.02V, 1.03 V, 1.04V, 1.05 V, 1.06 V, 1.07 V, 1.08 V, 1.09 V, 1.10 V, 1.11 V, 1.12 V, 1.13 V, 1.14 V, 1.15 V, 1.16 V, 1.17 V, 1.18 V, 1.19 V, 1.20 V, 1.21 V, 1.22 V, 1.23 V, 1.24 V, 1.25 V, 1.26 V, 1.27 V, 1.28 V, 1.29 V, 1.30 V, 1.31 V, 1.32 V, 1.33 V, 1.34 V, 1.35 V, 1.36 V, 1.37 V, 1.38 V, 1.39 V, 1.40 V, 1.41 V, 1.42 V, 1.43 V, 1.44 V, 1.45 V, 1.46 V, 1.47 V, 1.48 V, 1.49 V, or 1.50 V.

[0070] By way of example, glycerol valorization in the cathodic half-cell via the electro-Fenton process was studied by applying a fixed potential of 0.60 V vs. RHE to c-$NiSe_2$ grown on carbon fiber paper (denoted as c-$NiSe_2$/CFP) cathode (~1.06 mg_{Ni} $cm^{-2}{}_{geo}$, ~1 $cm^{-2}{}_{geo}$) in O_2-saturated 0.1 M $NaHSO_4/Na_2SO_4$ (pH~2.8) containing ~50 mM glycerol and 0.5 mM Fe^{2+}, and the cathode current was ~1.7 mA. Direct oxidation of glycerol in the anodic half-cell was studied by applying a fixed current of 1.7 mA to nanoparticular Pt supported on carbon black (denoted as Pt/C) anode (2 mg_{Pt} $cm^{-2}{}_{geo}$, 1 $cm^{-2}{}_{geo}$) in Ar-saturated 0.05 M H_2SO_4 (pH~1.2) containing ~50 mM glycerol, and the anode potential was ~0.55 V vs. RHE at pH~1.2. If c-$NiSe_2$/CFP cathode (in O_2-saturated 0.1 M $NaHSO_4/Na_2SO_4$ containing ~50 mM glycerol and 0.5 mM Fe^{2+}, pH~2.8) and Pt/C anode (in Ar-saturated 0.05 M H_2SO_4 containing ~50 mM glycerol, pH~1.2) were coupled together and both operated at 1.7 mA for glycerol valorization in a linear paired electrochemical system (as shown in FIG. **29**), the cell potential (E_{cell}) in principle can be estimated by the cathode potential ($E_{cathode}$) and the anode potential (E_{anode}) from the respective half-cell studies. From the cathodic half-cell study:

[0071] $E_{cathode}$ (at ~1.7 mA)=0.60 V vs. RHE (at pH~2.8)=~0.435 V vs. standard hydrogen electrode (SHE)

From the anodic half-cell study:

[0072] E_{anode} (at 1.7 mA)=~-0.55 V vs. RHE (at pH~1.2)=~-0.479 V vs. SHE

[0073] Under the ideal assumption of no internal resistance (i.e., no ohmic overpotential) in the linear paired electrochemical system:

$$E_{cell}(\text{at}\sim 1.7\ \text{mA}) = E_{cathode}\ \text{vs. SHE} - E_{anode}\ \text{vs. SHE}$$

$$= \sim(0.435 - 0.479)\ V$$

$$= \sim -0.044\ V$$

[0074] This example shows that to deliver a current of ~1.7 mA for glycerol valorization at both c-$NiSe_2$/CFP cathode and Pt/C anode, the linear paired electrochemical system ideally can operate as an electrolytic cell at an external bias as low as <0.05 V with almost no external energy input needed if the internal resistance is negligible.

[0075] The thermodynamic basis of the linear paired glycerol valorization process is provided. Intuitively, the overall process is a controlled partial oxidation of glycerol by oxygen gas to produce mainly C_3 and C_2 oxidation products in an electrochemical cell, and such oxidation process should be thermodynamically spontaneous.

[0076] Considering an ideally simplified linear paired process where both the electro-Fenton process and the direct anodic oxidation process generate a single oxidation product of glyceraldehyde from glycerol, the respective electrochemical reactions at the cathode and the anode should be:

electrochemical reaction at the cathode: $O_{2\ (g)}+2H^+ + 2e^- \rightarrow H_2O_{2\ (aq)}$

electrochemical reaction at the anode: $\text{glycerol}_{(aq)} \rightarrow \text{glyceraldehyde}_{(aq)}+2H^+ + 2e^-$

The balanced net electrochemical reaction that determines the overall achievable cell potential of this simplified linear paired glycerol-to-glyceraldehyde valorization process should be:

net electrochemical reaction: $\text{glycerol}_{(aq)}+O_{2\ (g)} \rightarrow \text{glyceraldehyde}_{(aq)}+H_2O_{2\ (aq)}$

Because the standard Gibbs free energies of formation (ΔfG^o) of these organic compounds are not directly available, we consider the net electrochemical reaction as the combination of the following two reactions:

$$O_{2(g)} + H_{2(g)} \rightarrow H_2O_{2(aq)}$$

$$\Delta G^0 = \Delta G_f^0[H_2O_{2(g)}] + \Delta G_{solv}^0[H_2O_{2(g)}] = \Delta G_f^0[H_2O_{2(g)}] - R \cdot T \cdot \ln(k_H)$$

$$= -105.6\ \frac{\text{kJ}}{\text{mol}} \times 1\ \text{mol} - 8.314\ \frac{10^{-3}\ \text{kJ}}{\text{mol} \cdot K} \times 298\ K \times$$

$$\ln\left(99000\ \frac{\text{mol}}{\text{kg} \cdot \text{bar}}\right) \times 1\ \text{mol} = -134.1\ \text{kJ}$$

$$\text{glycerol}_{(aq)} \rightarrow \text{glyceraldehyde}_{(aq)} + H_{2(g)}$$

$$\Delta G^0 = 9.4\ \text{kcal mol}^{-1} \times 4.184\ \text{kJ kcal}^{-1} \times 1\ \text{mol} = 39.3\ \text{kJ}$$

where $\Delta G_f^o[H_2O_{2\ (g)}]$ may be sourced from a reference, such as the CRC Handbook of Chemistry and Physics, $\Delta G_{solv}{}^o[H_2O_{2\ (g)}]$ is the solvation free energy of $H_2O_{2\ (g)}$ based on the experimental Henry's law constant (k_H), and ΔG^o for $\text{glycerol}_{(aq)} \rightarrow \text{glyceraldehyde}_{(aq)}+H_{2\ (g)}$ may be sourced from a theoretical report and may be calculated with quantum chemistry software, such as the Gaussian 03 program, and includes both electrostatic and nonelectrostatic components of the solvation free energies.

[0077] As a result, the net electrochemical reaction is thermodynamically spontaneous and results in a galvanic cell with an overall achievable cell potential of 0.49 V:

$$\text{glycerol}_{(aq)}+O_{2\ (g)}\rightarrow\text{glyceraldehyde}_{(aq)}+H_2O_{2\ (aq)}$$

$$\Delta G^{o}=-134.1\ \text{kJ}+39.3\ \text{kJ}=-94.8\ \text{kJ}$$

$$\Delta G^{o}/(-n\times F)=-94.8\ \text{kJ}/(-2\ \text{mol}\times 96485\ \text{C mol}^{-1})=0.49\ \text{V}$$

where n is the number of electrons transferred, and F is the Faraday constant.

The linear paired glycerol valorization process is a hybrid of electrochemical and chemical steps. Besides the as-mentioned electrochemical reactions at the cathode and the anode, chemical reaction of glycerol oxidation using H_2O_2 as the oxygen source takes place in the catholyte solution:

chemical reaction in the catholyte: $\text{glycerol}_{(aq)}+H_2O_{2\ (aq)}\rightarrow\text{glyceraldehyde}_{(aq)}+2\ H_2O_{(l)}$

The ΔG^{o} (=−300.8 kJ) of this chemical reaction in the catholyte solution cannot be harnessed electrochemically, and thus the overall achievable cell potential for the linear paired glycerol valorization process is governed by the O_2/H_2O_2 redox couple but not the O_2/H_2O redox couple. Combining all steps together, the overall cell reaction of this simplified linear paired glycerol-to-glyceraldehyde valorization process should be:

$$2\ \text{glycerol}_{(aq)}+O_{2\ (g)}\rightarrow 2\ \text{glyceraldehyde}_{(aq)}+2\ H_2O_{(l)}$$

[0078] This overall cell reaction is thermodynamically spontaneous (ΔG^{o}=−395.6 kJ), but only part of the ΔG^{o} is harnessed electrochemically to result in a galvanic cell with an overall achievable cell potential of 0.49 V (as discussed above).

[0079] Similarly, it holds true for other oxidation products (dihydroxyacetone, glyceric acid, etc.) that the linear paired glycerol valorization process results in a galvanic cell that is thermodynamically spontaneous, which can be derived from the calculated thermochemical data found in ref.

[0080] Earlier in this description we estimated based on experimental half-cell studies that, to deliver a current of ~1.7 mA, our linear paired electrochemical system for glycerol valorization ideally can operate as an electrolytic cell at an external bias as low as <0.05 V if the internal resistance is negligible. In this estimate, the linear paired electrochemical system operates as an electrolytic cell rather than a galvanic cell, because both $2e^-$ ORR at the $NiSe_2$ cathode and glycerol oxidation at the Pt anode require kinetic overpotentials to deliver a catalytic current of ~1.7 mA. By designing more active cathode and anode electrocatalysts to further reduce the kinetic overpotentials and further optimizing the electrochemical device design, linear paired electrochemical systems for glycerol valorization that need no external bias and no external energy input could be realized.

[0081] The linear paired system ideally could operate at an external bias as low as <0.05 V if there was no internal resistance. In FIG. **30***a*, the measured external bias was higher than this estimated ideal value, mostly caused by the large solution IR drop (where IR refers to the product of current and resistance) at the anode as it situated on the opposite side of the Hg/Hg_2SO_4 reference electrode across the Nafion 117 membrane. The magnitude of the ohmic overpotential (solution IR drop) at the anode was almost identical to the measured external bias, suggesting that the ideal estimation in provided above is still valid. The large solution IR drop at the anode was mostly caused by the solution resistance rather than the membrane resistance, because it was almost unaffected by the membrane thickness when the catholyte and anolyte compositions remained the same (see comparisons between the 183 μm-thick Nafion 117 membrane and the 89 μm-thick Nafion NE1035 membrane in Table 4). As shown in FIG. **30***b*, by increasing the supporting electrolyte concentrations of both catholyte and anolyte, the measured external bias was reduced because of the decrease in the solution IR drop at the anode. To operate this linear paired system at an even lower (or zero) external bias in the future, the ohmic overpotential needs to be further reduced, and one possible optimization pathway is to employ zero-gap cell designs involving membrane electrode assemblies.

Miscellaneous

[0082] Unless otherwise specified or indicated by context, the terms "a", "an", and "the" mean "one or more". For example, "a molecule" should be interpreted to mean "one or more molecules."

[0083] As used herein, "about", "approximately," "substantially," and "significantly" will be understood by persons of ordinary skill in the art and will vary to some extent on the context in which they are used. If there are uses of the term which are not clear to persons of ordinary skill in the art given the context in which it is used, "about" and "approximately" will mean plus or minus ≤10% of the particular term and "substantially" and "significantly" will mean plus or minus >10% of the particular term.

[0084] As used herein, the terms "include" and "including" have the same meaning as the terms "comprise" and "comprising." The terms "comprise" and "comprising" should be interpreted as being "open" transitional terms that permit the inclusion of additional components further to those components recited in the claims. The terms "consist" and "consisting of" should be interpreted as being "closed" transitional terms that do not permit the inclusion additional components other than the components recited in the claims. The term "consisting essentially of" should be interpreted to be partially closed and allowing the inclusion only of additional components that do not fundamentally alter the nature of the claimed subject matter.

[0085] All methods described herein can be performed in any suitable order unless otherwise indicated herein or otherwise clearly contradicted by context. The use of any and all examples, or exemplary language (e.g., "such as") provided herein, is intended merely to better illuminate the invention and does not pose a limitation on the scope of the invention unless otherwise claimed. No language in the specification should be construed as indicating any non-claimed element as essential to the practice of the invention.

[0086] All references, including publications, patent applications, and patents, cited herein are hereby incorporated by reference to the same extent as if each reference were individually and specifically indicated to be incorporated by reference and were set forth in its entirety herein.

[0087] Preferred aspects of this invention are described herein, including the best mode known to the inventors for carrying out the invention. Variations of those preferred aspects may become apparent to those of ordinary skill in the art upon reading the foregoing description. The inventors expect a person having ordinary skill in the art to employ

such variations as appropriate, and the inventors intend for the invention to be practiced otherwise than as specifically described herein. Accordingly, this invention includes all modifications and equivalents of the subject matter recited in the claims appended hereto as permitted by applicable law. Moreover, any combination of the above-described elements in all possible variations thereof is encompassed by the invention unless otherwise indicated herein or otherwise clearly contradicted by context.

ILLUSTRATIVE EMBODIMENTS

[0088] Embodiment 1: An electrochemical cell including an electrolyte and a cathode immersed in the electrolyte,

[0089] wherein the cathode includes a two-electron oxygen reduction reaction ($2e^-$ ORR)

[0090] electrocatalyst composed of a metal chalcogenide,

[0091] wherein the metal is Ni or Pd.

[0092] Embodiment 2: The electrochemical cell of embodiment 1, wherein the metal is Ni.

[0093] Embodiment 3: The electrochemical cell of embodiment 2, wherein the metal chalcogenide includes c-$NiSe_2$.

[0094] Embodiment 4: The electrochemical cell of any one of embodiments 1-3, wherein the electrolyte has a pH below 4.0, optionally wherein the electrolyte has a pH between 0.0 and 4.0 pH or any pH therebetween.

[0095] Embodiment 5: The electrochemical cell of embodiment 1, wherein the metal is Pd.

[0096] Embodiment 6: The electrochemical cell of embodiment 5, wherein the metal chalcogenide includes layered $PdSe_2$.

[0097] Embodiment 7: The electrochemical cell of any one of embodiments 1 or 5-6, wherein the electrolyte has a pH above 4.0, optionally wherein the electrolyte has a pH between 4.0 and 8.0 pH or any pH therebetween.

[0098] Embodiment 8: The electrochemical cell of any one of embodiments 1-7, wherein the electrolyte includes oxygen (O_2), hydrogen peroxide (H_2O_2), hydroxyl radical (·OH), a regenerable metal ion, and a first biomass-derived feedstock.

[0099] Embodiment 9: The electrochemical cell of embodiment 8 further including an acidic anolyte and an anode immersed in the anolyte, wherein the anolyte includes a second biomass-derived feedstock.

[0100] Embodiment 10: A method for production of hydrogen peroxide, the method including introducing oxygen into the electrochemical cell according to any one of embodiments 1-9 under conditions sufficient for preparing the hydrogen peroxide.

[0101] Embodiment 11: The method of embodiment 10, wherein the conditions sufficient for preparing hydrogen peroxide include a potential between 0.00 and 0.70 V vs. RHE applied to the cathode.

[0102] Embodiment 12: An electrochemical cell including an acidic catholyte, a cathode immersed in the catholyte, an acidic anolyte, and an anode immersed in the anolyte,

[0103] wherein the cathode includes a two-electron oxygen reduction reaction ($2e^-$ ORR)

[0104] electrocatalyst having a metal chalcogenide and the catholyte having oxygen (O_2),

[0105] hydrogen peroxide (H_2O_2), hydroxyl radical (·OH), a regenerable metal ion, and a first biomass-derived feedstock, and wherein the anolyte includes a second biomass-derived feedstock.

[0106] Embodiment 13: The electrochemical cell of embodiment 12, wherein the two-electron oxygen reduction reaction ($2e^-$ ORR) electrocatalyst includes a metal chalcogenide.

[0107] Embodiment 14: The electrochemical cell of embodiment 13, wherein the metal chalcogenide includes c-$NiSe_2$.

[0108] Embodiment 15: The electrochemical cell of embodiment 13, wherein the metal chalcogenide includes layered $PdSe_2$.

[0109] Embodiment 16: The electrochemical cell of embodiment 13, wherein the metal chalcogenide includes pyrite or marcasite type $CoSe_2$, pyrite type CoS_2, or $CuCO_{2-x}Ni_xS_4$.

[0110] Embodiment 17: The electrochemical cell of embodiment 13, wherein the metal chalcogenide includes an earth-abundant metal or a noble metal.

[0111] Embodiment 18: The electrochemical cell of embodiment 13, wherein the earth abundant metal includes Ni, Co, Fe, Cu, Mn, or any combination thereof.

[0112] Embodiment 19: The electrochemical cell of embodiment 18, wherein the earth abundant metal includes Ni.

[0113] Embodiment 20: The electrochemical cell of embodiment 18, wherein the earth abundant metal includes Co.

[0114] Embodiment 21: The electrochemical cell of embodiment 17, wherein the noble metal includes Pd.

[0115] Embodiment 22: The electrochemical cell of any one of embodiments 12-21, wherein the acidic catholyte and/or the acidic anolyte has a pH between 0.0 and 4.0 pH.

[0116] Embodiment 23: The electrochemical cell of any one of embodiments 12-22, wherein the regenerable metal ion is Fe^{2+}.

[0117] Embodiment 24: The electrochemical cell of any one of embodiments 12-23, wherein the electrochemical cell includes a semipermeable barrier between the cathode from the anode.

[0118] Embodiment 25: The electrochemical cell of any one of embodiments 12-24, wherein the first biomass-derived feedstock or the second biomass-derived feedstock includes glycerol.

[0119] Embodiment 26: The electrochemical cell of any one of embodiments 12-25, wherein each of the catholyte and the anolyte further include oxidation products of the first biomass-derived feed stock and the second biomass derived feed stock.

[0120] Embodiment 27: The electrochemical cell of embodiment 26, wherein the oxidation products include dihydroxyacetone (DHA), glyceraldehyde (GLAD), glyceric acid (GLA), hydroxypyruvic acid (HPA), glycolaldehyde (GAD), glycolic acid (GA), glyoxylic acid (GLOA), formic acid (FA), or any combination thereof.

[0121] Embodiment 28: A method for preparing an oxidation product of a biomass-derived feedstock, the method including introducing the biomass-derived feedstock into the electrochemical cell according to any one of embodiments 1-9 under conditions sufficient for preparing the oxidation product.

[0122] Embodiment 29: The method of embodiment 28, wherein a potential is between 0.00 and 0.70 V vs. RHE is applied to the cathode.

[0123] Embodiment 30: The method of any one of embodiments 28-29, wherein the biomass-derived feedstock includes glycerol.

[0124] Embodiment 31: The method of any one of embodiments 28-30, wherein the electrolyte further includes an oxidation product of the biomass-derived feedstock.

[0125] Embodiment 32: The method of embodiment 31, wherein the oxidation product includes dihydroxyacetone (DHA), glyceraldehyde (GLAD), glyceric acid (GLA), hydroxypyruvic acid (HPA), glycolaldehyde (GAD), glycolic acid (GA), glyoxylic acid (GLOA), formic acid (FA), or any combination thereof.

[0126] Embodiment 33: A method for preparing an oxidation product of a biomass-derived feedstock, the method including introducing the biomass-derived feedstock into the electrochemical cell according to any one of embodiments 12-24 under conditions sufficient for preparing the oxidation product.

[0127] Embodiment 34: The method of embodiment 33, wherein less than 1.0 V of externally applied bias is applied.

[0128] Embodiment 35: The method of embodiment 33, wherein less than 0.2 V of externally applied bias is applied.

[0129] Embodiment 36: The method of any one of embodiments 33-35, wherein the biomass-derived feedstock includes glycerol.

[0130] Embodiment 37: The method of any one of embodiments 33-36, wherein the electrolyte further includes an oxidation product of the biomass-derived feedstock.

[0131] Embodiment 38: The method of embodiment 37, wherein the oxidation product includes dihydroxyacetone (DHA), glyceraldehyde (GLAD), glyceric acid (GLA), hydroxypyruvic acid (HPA), glycolaldehyde (GAD), glycolic acid (GA), glyoxylic acid (GLOA), formic acid (FA), or any combination thereof.

EXAMPLES

Example 1

[0132] Linear paired electrochemical valorization of glycerol requires a cathodic reaction that can generate oxidative species to oxidize glycerol. Hydrogen peroxide (H_2O_2) is an oxidant (E^o=1.76 V vs. SHE) that can be cathodically generated via the selective $2e^-$ ORR (O_2+2 H^++2 $e^-\rightarrow H_2O_2$), and be further converted into the even more oxidizing hydroxyl radical (·OH, E^o=2.80 V vs. SHE) by the Fe^{2+}-mediated electro-Fenton process in acidic solutions ($Fe^{2+}+H_2O_2+H^+\rightarrow Fe^{3+}+H_2O+\cdot OH$) where Fe^{2+} is regenerated at the H_2O_2-generating cathode ($Fe^{3+}+e^-\rightarrow Fe^{2+}$) The application of electro-Fenton process has been largely limited to environmental pollutant removal, but chemically generated ·OH from H_2O_2 has found use in biomass-to-chemical processes such as carbohydrate oxidation and lignin depolymerization.

[0133] Here, we present the cathodic valorization of glycerol via the electro-Fenton process, and the further linear pairing with the anodic oxidation to concurrently produce the same glycerol-derived oxidation products at both cathode and anode (FIG. **1**). This is made possible by robust and earth-abundant electrocatalyst, such as $NiSe_2$, for the selective $2e^-$ ORR and electro-Fenton process in acidic solutions. Building on the recent developments of transition metal compounds as selective $2e^-$ ORR catalysts that are more cost-effective than noble metals and more catalytically active than carbon-based materials in acidic solutions, we demonstrate through theory and experiment high selectivity toward acidic $2e^-$ ORR and excellent stability against surface oxidative leaching. Cathodes operated at the optimum potential for H_2O_2 electrosynthesis and electro-Fenton process enables the efficient glycerol oxidation in the cathodic half-cell, with a high glycerol conversion and high selectivity for valuable C_3 products. Finally, a new linear paired electrochemical system having valorization at both the cathode and anode for efficient concurrent glycerol valorization to C_3 products is demonstrated under a marginal external applied bias.

Identifying c-$NiSe_2$ Catalyst for the Electro-Fenton Process

[0134] The Fe^{2+}-mediated electro-Fenton process operates at an optimum pH of ~3 and poses more stringent requirements for catalyst stability than $2e^-$ ORR because OH is more oxidizing than H_2O_2. Therefore, an electrocatalyst that is not only selective for acidic $2e^-$ ORR but also stable in the presence of strong oxidants such as H_2O_2 and ·OH is needed. We utilized the calculated bulk Pourbaix diagrams available from the Materials Project to identify promising earth-abundant catalyst candidates with high aqueous electrochemical stability in the pH and potential ranges of interest for acidic $2e^-$ ORR. Similar to cubic pyrite-type $CoSe_2$ (c-$CoSe_2$, FIG. **2***a*), an acidic $2e^-$ ORR catalyst with demonstrated stability, cubic $NiSe_2$ (c-$NiSe_2$, FIG. **2***a*) exhibits a wide electrochemical stability window in the bulk Pourbaix diagram (FIG. **6**). Therefore, $NiSe_2$ could be a promising cathode catalyst for the electro-Fenton process.

[0135] The promise of c-$NiSe_2$ as an active and selective $2e^-$ ORR catalyst is revealed by the calculated free energy diagrams of the ORR energetics on the most thermodynamically stable (100) surface. The $2e^-$ ORR (FIG. **2***b*, solid traces) proceeds via the adsorption of OOH* ($O_{2\ (g)}+*+H^++e^-\rightarrow$OOH*, where * is the unoccupied surface binding site) followed by its desorption to form H_2O_2 (OOH*+H^++e^- $\rightarrow H_2O_{2\ (aq)}+*$). At the calculated standard equilibrium potential of $2e^-$ ORR (U_{RHE}^{o}), the preferential binding of OOH* to the Ni site on c-$NiSe_2$ is relatively weak (endothermic by 0.10 eV), whereas the Co site on c-$CoSe_2$ preferentially binds to OOH* more strongly (exothermic by 0.24 eV). Thus, c-$NiSe_2$ is expected to be not only active for $2e^-$ ORR as the OOH* adsorption is nearly thermoneutral at U_{RHE}^{o}, but also selective toward $2e^-$ (vs. $4e^-$) ORR because it is situated on the weak OOH* binding leg of the $2e^-$ ORR volcano. In contrast, c-$CoSe_2$ is situated on the strong OOH* binding leg. Furthermore, the $2e^-$ ORR selectivity is also kinetically governed by the resistance to the O—O bond cleavage in OOH*, which leads to the competing 4e-ORR (FIG. **2***b*, dashed traces). We reason that the OOH* dissociation on pyrite-type structures likely proceeds via a dinuclear pathway across two neighboring metal sites (OOH*+*→O*+OH*). But this pathway features a high activation barrier of 0.61 eV (0.63 eV) on c-$NiSe_2$ (c-$CoSe_2$) and is kinetically disfavored due to the large spacing between the neighboring metal sites separated by diselenide anions. Thus, computational assessments of ORR pathways suggest that c-$NiSe_2$ should be active and selective for $2e^-$ ORR.

[0136] The surface stability of c-$NiSe_2$ under aqueous electrochemical environments is evaluated by considering O* and/or OH* adsorbate formation when the surface is in equilibrium with water. Unlike c-$CoSe_2$ where O* and OH* preferentially bind to Se (Se—O*) and Co (Co—OH*), respectively, Ni on c-$NiSe_2$ is the preferential binding site for both O* (Ni—O*) and OH* (Ni—OH*). On a surface unit cell including two metal sites and four Se sites, should O* builds up on the c-$NiSe_2$ surface, a significant O* coverage would have to be reached (which is unlikely because O* binds to Ni endothermically by 0.08 eV at U_{RHE}°) before any O* would bind to Se; however, any presence of O* on c-$CoSe_2$ would bind to Se immediately (FIG. **2***c*). Since one possible degradation pathway of pyrite-type structures is the oxidation of dichalcogenide anions followed by the dissolution of metal cations (FIG. **6**), the low affinity of O* to Se on c-$NiSe_2$ suggests an increased resistance to surface oxidation. In addition, OH* binds to Ni more weakly (endothermic by 0.27 eV) than to Co (exothermic by 0.08 eV) at U_{RHE}°, which allows the c-$NiSe_2$ surface to stay clean and mostly free of adsorbate over a wider range of potentials compared to the c-$CoSe_2$ surface (FIG. **2***c*). Note that O* and OH* can also form during ORR if the O—O bond cleavage occurs (FIG. **2***b*). Therefore, these surface adsorbate analyses suggest c-$NiSe_2$ should be more resistant to surface oxidation and degradation under aqueous environments and ORR operating conditions.

Electrocatalytic Properties and Stability of c-$NiSe_2$ for Acidic $2e^-$ ORR

[0137] We synthesized nanostructured c-$NiSe_2$ (FIG. **7**) via a hydrothermal method, and examined the acidic $2e^-$ ORR catalytic properties of the powder sample by drop-casting on a rotating ring-disk electrode (RRDE). We also synthesized nanostructured c-$CoSe_2$ catalyst as a comparison (FIG. **8**). RRDE experiments were performed with various catalyst loadings that resulted in similar ranges of double-layer capacitances (C_{dl}) between these two catalysts (FIG. **9**) for fair comparisons. In O_2-saturated 0.05 M H_2SO_4 (pH~1.2), c-$NiSe_2$ exhibits high H_2O_2 selectivity (up to 95%) and relatively little dependence on overpotential and catalyst loading (FIGS. **3***a* and **3***b*). In contrast, although c-$CoSe_2$ is more catalytically active toward $2e^-$ ORR, the H_2O_2 selectivity decreases more dramatically with increasing overpotential and catalyst loading (FIGS. **3***a* and **3***b*). Such differences between the H_2O_2 selectivity profiles of c-$NiSe_2$ and c-$CoSe_2$ are also observed at pH~2.8 in O_2-saturated 0.1 M $NaHSO_4/Na_2SO_4$ buffer (FIGS. **10** and **11**), further showing that c-$NiSe_2$ is more selective toward acidic $2e^-$ ORR than c-$CoSe_2$.

[0138] The stability of c-$NiSe_2$ (vs. c-$CoSe_2$) catalyst for acidic $2e^-$ ORR was evaluated by long-term RRDE stability tests at various catalyst loadings. The catalyst stability is monitored by tracking the disk potential at a certain disk current density (j_{disk}) or peroxide current density ($j_{peroxide}$) (FIG. **12**). The stable disk potential throughout the tests shows that c-$NiSe_2$ exhibits a higher catalyst stability than c-$CoSe_2$ at both pH~1.2 (0.05 M H_2SO_4) and pH~2.8 (0.1 M $NaHSO_4/Na_2SO_4$) (FIGS. **13** and **14**). The spent catalysts show no obvious structural and compositional change (FIG. **15**). We further performed elemental analyses of the spent electrolytes to quantify the leaching rates of metal and selenium from the catalysts normalized by the catalyst masses ($\mu mol\ g_{catalyst}^{-1}\ h^{-1}$). The ratio between the Co and Se leaching rates of the less stable c-$CoSe_2$ is close to the 1:2 stoichiometry (FIG. **3***c* and Table 2). This suggests the leaching of c-$CoSe_2$ could be initiated by the surface oxidation of Se_2^{2-} to the soluble SeO_x due to the preferential affinity of O* to its Se site (FIG. **2***c*), followed by the near-stoichiometric dissolution of Co^{2+} from the surface. In contrast, the Se leaching from the more stable c-$NiSe_2$ is not only substantially suppressed compared to c-$CoSe_2$, but also slower than the Ni leaching (FIG. **3***c*). These suggest the leaching of c-$NiSe_2$ could mainly result from the preferential adsorption of both O* and OH* onto Ni (FIG. **2***c*) and the subsequent acid-base reaction with the electrolyte to dissolve Ni^{2+}. This hypothesis is supported by the slower leaching of c-$NiSe_2$ under the less acidic pH of ~2.8 (FIG. **3***c*), and future studies will be helpful for confirming the catalyst leaching mechanisms. These in-depth catalyst leaching studies further confirm the enhanced stability of c-$NiSe_2$ for acidic 2e ORR.

TABLE 1

Comparisons of the normalized Ni and Se leaching rates from RRDE stability tests of c-$NiSe_2$ (where H_2O_2 accumulation is negligible) vs. H_2O_2 bulk electrosynthesis of c-$NiSe_2$/CFP (with steady accumulation of H_2O_2), which are comparable and thus confirm that $NiSe_2$'s stability is maintained in the presence of dilute H_2O_2 oxidant.

Experiment	Catalyst	Electrolyte	Normalized Ni Leaching Rate ($\mu mol_{Ni}\ g_{catalyst}^{-1}\ h^{-1}$)	Normalized Se Leaching Rate ($\mu mol_{Se}\ g_{catalyst}^{-1}\ h^{-1}$)
RRDE Stability Test	c-$NiSe_2$	O_2-saturated 0.05M H_2SO_4 (pH ~1.2)	17.2 ± 5.6 [1]	5.77 ± 2.86 [1]
		O_2-saturated 0.1M $NaHSO_4/Na_2SO_4$ (pH ~2.8)	6.64 ± 0.68 [1]	4.54 ± 0.78 [1]
H_2O_2 Bulk Electro-synthesis	c-$NiSe_2$/CFP	O_2-saturated 0.05M H_2SO_4 (pH~1.2)	9.9 [2]	9.0 [2]
		O_2-saturated 0.1M $NaHSO_4/Na_2SO_4$ (pH ~2.8)	6.2 [2]	5.2 [2]

[1] These avg. ± std. dev. leaching rates come from four RRDE stability tests of c-$NiSe_2$ at different catalyst loadings in each electrolyte, as tabulated in Table 2.

[2] These leaching rates come from the initial H_2O_2 bulk electrosynthesis run of c-$NiSe_2$/CFP at 0.60 V vs. RHE in each electrolyte, as shown in FIG. 23d.

TABLE 2

ICP-MS analyses of the spent electrolytes after the RRDE stability tests of c-$NiSe_2$ and c-$CoSe_2$ catalysts at various catalyst loadings in 0.05M H_2SO_4 (PH ~1.2) and 0.1M $NaHSO_4/Na_2SO_4$ (PH~2.8) solutions (see FIG. 3c).

Electrolyte	Ex	Catalyst	Catalyst Loading ($\mu g_{metal}\ cm^{-2}{}_{disk}$)	Electrolyte Volume (mL)	Time (h)
O2-saturated 0.05M H_2SO_4 (pH ~1.2)	1	c-$NiSe_2$	229	41.0	4.0
	2		305	42.5	3.9
	3		381	41.0	4.0
	4		458	41.5	4.0
	5		—	—	—
	6	c-$CoSe_2$	76	45.0	4.1
	7		114	42.0	4.0
	8		152	43.0	4.2
	9		229	44.5	4.1
	10		—	—	—
O_2-saturated 0.1M $NaHSO_4$/ Na2SO4 (pH ~2.8)	11	c-$NiSe_2$	152	42.5	4.1
	12		229	41.5	4.0
	13		305	41.0	4.0
	14		381	43.0	4.0
	15		—	—	—
	16	c-$CoSe_2$	76	41.5	4.0
	17		114	40.0	4.0
	18		152	41.5	4.0
	19		229	41.5	4.0
	20		—	—	—

Electrolyte	Ex	Catalyst	[Metal] (ppb)	[Se] (ppb)	Normalized Metal Leaching Rate ($\mu mol_{metal}\ g_{catalyst}^{-1}\ h^{-1}$)	Normalized Se Leaching Rate ($\mu mol_{Se}\ g_{catalyst}^{-1}\ h^{-1}$)
O_2-saturated 0.05M H_2SO_4 (pH ~1.2)	1	c-$NiSe_2$	7.75	2.75	12.8	3.38
	2		10.6	3.74	13.8	3.62
	3		17.2	9.02	17.0	6.63
	4		30.5	15.4	25.2	9.45
	5		—	—	Avg. ± Std. Dev. = 17.2 ± 5.6	Avg. ± Std. Dev. = 5.77 ± 2.86
	6	c-$CoSe_2$	2.93	5.31	15.5	21.0
	7		5.69	11.0	19.0	27.6
	8		8.91	19.6	21.9	35.9
	9		13.6	27.8	23.5	35.9
	10		—	—	Avg. ± Std. Dev. = 20.0 ± 3.5	Avg. ± Std. Dev. = 30.1 ± 7.2
O2-saturated 0.1M $NaHSO_4$/ Na_2SO_4 (pH ~2.8)	11	c-$NiSe_2$	2.44	2.15	6.15	4.03
	12		3.62	3.06	6.06	3.82
	13		6.15	6.07	7.54	5.53
	14		6.55	6.22	6.79	4.79
	15		—	—	Avg. ± Std. Dev. = 6.64 ± 0.68	Avg. ± Std. Dev. = 4.54 ± 0.78
	16	c-$CoSe_2$	3.37	6.32	17.0	23.9
	17		4.98	8.42	16.1	20.4
	18		9.62	19.2	24.1	36.0
	19		22.8	53.6	38.5	67.6
	20		—	—	Avg. ± Std. Dev. = 23.9 ± 10.3	Avg. ± Std. Dev. = 37.0 ± 21.5

Bulk Electrosynthesis of H_2O_2 in Acidic Solution Using c-$NiSe_2$ Cathode

[0139] We further performed constant-potential bulk electrosynthesis using integrated electrodes of c-$NiSe_2$ nanosheets directly grown on carbon fiber paper ($NiSe_2$/CFP, FIG. **16**) to accumulate H_2O_2 in O_2-saturated 0.05 M H_2SO_4 in a two-compartment three-electrode H-cell (FIG. **17**) at various applied potentials ranging from 0.50 to 0.65 V vs. RHE (FIG. **3***d* and FIG. **18**). Both the cumulative H_2O_2 yield and selectivity after 6 hours of bulk electrosynthesis are potential-dependent, and peak at the optimum potential of 0.60 V vs. RHE (FIG. **3***d*). Cyclic voltammograms recorded before and after each electrosynthesis trial suggest additional cathodic current is generated on $NiSe_2$/CFP after the accumulation of H_2O_2 in the solution (FIG. **18**), likely due to the electroreduction of H_2O_2 to water as the Faradaic side reaction.

[0140] To understand this potential-dependent electrosynthesis of H_2O_2, we studied the side reaction of H_2O_2 electroreduction in competition with $2e^-$ ORR on c-$NiSe_2$ catalyst drop-casted on RRDE. In 0.05 M H_2SO_4, the catalytic onset potential of H_2O_2 electroreduction on c-$NiSe_2$ coincides with that of $2e^-$ ORR, and the rate of H_2O_2 electroreduction increases with higher overpotential and H_2O_2 concentration (FIG. **19***a*). Therefore, as H_2O_2 concentration builds up, the net rate of H_2O_2 production (i.e., the production rate minus the electroreduction rate of H_2O_2) on c-$NiSe_2$ is positive only in a certain potential range and displays a parabolic trend peaking at an optimum potential (FIG. **19***b*). Similarly, H_2O_2 electroreduction also occurs on c-$CoSe_2$ but it affects the net production rate less because c-$CoSe_2$ exhibits a more positive catalytic onset potential for $2e^-$ ORR (FIG. **19** and FIG. **3***a*). A similar parabolic trend in the net rate of H_2O_2 production on c-$NiSe_2$ is observed in 0.1 M $NaHSO_4/Na_2SO_4$ buffer at pH~2.8 (FIG. **20**). These results show the importance of considering H_2O_2 electroreduction and operating $NiSe_2$/CFP at the optimum applied potential for H_2O_2 electrosynthesis.

[0141] We demonstrated sustained bulk electrosynthesis of H_2O_2 in O_2-saturated 0.05 M H_2SO_4 at the optimum 0.60 V vs. RHE using one $NiSe_2$/CFP electrode repeatedly for five consecutive runs over 37 hours (FIG. **3***e*). Since the cathodic current on $NiSe_2$/CFP gradually increased over time because of the electroreduction of the accumulated H_2O_2, we replaced the catholyte with fresh H_2O_2-free electrolyte between runs to maintain the steady net production of H_2O_2 (FIG. **21**). Over the initial 2-hour period of each run, the $NiSe_2$/CFP electrode consistently accumulated 203±10 ppm H_2O_2 and produced 15.4±1.4 μmol H_2O_2 with a cumulative H_2O_2 selectivity of 51.8±1.8% with no obvious decay (FIG. **3***e* and FIG. **21**). A higher H_2O_2 yield of 34.8±2.8 μmol and a higher accumulated concentration of 661±53 ppm were achieved over a longer period of 7.4±0.5 hours at the end of each run, but with a lower H_2O_2 selectivity of 30.8±1.2% (FIG. **3***e* and FIG. **21**). $NiSe_2$/CFP shows a similar H_2O_2 electrosynthesis performance in O_2-saturated 0.1 M $NaHSO_4/Na_2SO_4$ buffer at pH~2.8 (FIG. **22**). The spent $NiSe_2$/CFP electrode is structurally and compositionally stable after H_2O_2 electrosynthesis (FIG. **23**), and catalyst leaching studies confirm that $NiSe_2$'s stability is maintained in the presence of dilute H_2O_2 oxidant (Table 1). These experiments suggest that the unavoidable electroreduction of H_2O_2 could limit the maximum accumulated concentration of H_2O_2 and the overall selectivity practically achievable using these new earth-abundant electrocatalysts, however, the electro-Fenton process of converting H_2O_2 to OH may allow us to utilize the produced H_2O_2 as an oxidant more efficiently by circumventing the undesired H_2O_2 electroreduction to water.

Glycerol Valorization Via the Electro-Fenton Process at c-$NiSe_2$ Cathode

[0142] To enable glycerol valorization by the electro-Fenton process, we operated $NiSe_2$/CFP cathode at the fixed potential of 0.60 V vs. RHE in O_2-saturated 0.1 M $NaHSO_4/Na_2SO_4$ buffer (pH~2.8) containing Fe^{2+} and glycerol. The balanced equation shows that cathodic glycerol conversion consumes protons (FIG. **4***a*). To maintain the proton balance and stabilize the acidic pH in the cathodic half-cell, it is critical to place 0.05 M H_2SO_4 in the anode compartment to transport protons through the Nafion membrane (FIG. **24**). We used proton and carbon-13 nuclear magnetic resonance (^1H and ^{13}C NMR) to identify and quantify the many possible C_3, C_2, and C_1 products that can be sequentially formed from the oxidation of glycerol (FIG. **4***b*). Control experiments show that the electrogenerated H_2O_2 itself is not capable of oxidizing glycerol without the presence of Fe^{2+}, which confirms that the electro-Fenton process is indeed responsible for glycerol valorization at the cathode.

[0143] We further studied the impact of Fe^{2+} concentration ([Fe^{2+}]) on the glycerol valorization via the electro-Fenton process. The rate of OH formation from the Fenton reaction should increase with higher [Fe^{2+}] based on the rate law, but too much Fe^{2+} would consume the formed OH and decrease the oxidizing power ($Fe^{2+}\cdot OH+H^+\rightarrow Fe^{3+}+H_2O$). After a controlled amount of charge is passed through $NiSe_2$/CFP cathode at 0.60 V vs. RHE, high glycerol conversion is achieved when [Fe^{2+}] is 0.5 mM or 1.0 mM, while too little Fe^{2+} (0.1 mM) results in low glycerol conversion likely due to the slow OH formation (FIG. **4***c*). On the other hand, the selectivity toward all detected C_3 products [glyceraldehyde (GLAD), dihydroxyacetone (DHA), glyceric acid (GLA)]remain relatively high when [Fe^{2+}] is 1.0 mM or below but decreases substantially when [Fe^{2+}] is increased to 2.5 mM (FIG. **4***c*). One possible explanation is that at high [Fe^{2+}], the high ·OH formation rate increases the relative concentration of ·OH to glycerol locally near the cathode, which might not be effectively dissipated even under vigorous stirring, driving the glycerol oxidation further to primarily C_2 [glycolaldehyde (GAD), glycolic acid (GA), glyoxylic acid (GLOA)] and C_1 [formic acid (FA)] products. This could also explain the relatively low glycerol conversion when [Fe^{2+}] is 2.5 mM despite the fast OH formation rate (FIG. **4***c*). Overall, we identified 0.5 mM as the optimum [Fe^{2+}] to concurrently achieve high glycerol conversion of up to ~55% and high C_3 product selectivity for cathodic valorization of glycerol (FIG. **4***d* and Table 3). As more charge is passed, the glycerol conversion steadily increases but the C_3 product selectivity decreases slightly due to the sequential oxidation of intermediate products. The gradual loss in the carbon balance of all detected aqueous phase organic products likely results from the eventual oxidation of FA to gaseous CO_2 undetectable by NMR (vide infra). The spent $NiSe_2$/CFP cathode was shown to be structurally and compositionally stable after the electro-Fenton process (FIG. **27**). These observations suggest that achieving an efficient electro-Fenton production of OH but maintaining a moderate concentration of this strongly oxidizing radical is the key to achieving high C_3 product selectivity and conversion from glycerol

TABLE 3

Summary of the aqueous phase organic (C_3, C_2, and C_1) product selectivity, glycerol conversion percentage, and carbon balance and Faradaic efficiency of all detected aqueous phase organic products for glycerol valorization in the cathodic half-cell via the electro-Fenton process at c-$NiSe_2$/CFP cathode and the direct anodic oxidation at Pt/C anode.

Half-Cell Studies	Example	Starting Volume (mL)	Starting [Glycerol] (mM)	Starting [Fe^{2+}] (mM)	Starting pH	Charge Passed (C)	Final Volume (mL)	Final [Glycerol] (mM)	Final pH	Glycerol Conversion (%)
Electro-Fenton Process at c-$NiSe_2$ Cathode	1	4	50.6	0.1	2.79	14.6	3.23	58.5	2.11	6.6
	2	4	50.6	0.1	2.79	29.3	2.66	63.3	2.06	16.9
	3	4	50.6	0.1	2.79	43.9	2.39	61.5	1.96	27.4
	4	4	50.5	0.5	2.85	14.6	3.27	52.2	2.19	15.6
	5	4	50.5	0.5	2.83	29.2	2.38	51.1	2.01	39.8
	6	4	50.5	0.5	2.85	43.9	2.05	44.4	1.95	54.9
	7	4	50.6	1.0	2.80	14.6	3.42	45.0	2.20	22.3
	8	4	50.6	1.0	2.80	29.3	2.87	41.6	2.08	39.8
	9	4	50.6	1.0	2.81	43.9	2.61	34.2	2.03	55.0
	10	4	50.5	2.5	2.84	14.6	3.14	53.7	2.16	13.8
	11	4	50.5	2.5	2.86	29.2	2.62	54.8	2.08	26.6
	12	4	50.5	2.5	2.85	43.9	2.08	59.5	1.94	36.8
Direct Anodic Oxidation at Pt/C Anode	13	4	51.1	—	1.21	14.8	3.49	45.6	1.15	22.2
	14	4	51.1	—	1.21	29.7	3.00	39.7	1.09	41.8
	15	4	51.9	—	1.21	45.1	2.20	36.9	0.95	60.9

		Aqueous Phase Organic Product Selectivity (%) [1]								Carbon	
Half-Cell		C_3				C_2			C_1	Balance	Efficiency
Studies	Example	GLAD	DHA	GLA	HPA	GAD	GA	GLOA	FA	(%)	(%) [2]
Electro-Fenton Process at c-$NiSe_2$ Cathode	1	37.7	17.1	1.3	—	7.4	2.7	0.7	5.4	98.2	16.8
	2	33.3	13.9	1.9	—	4.7	3.0	0.4	7.5	94.1	21.3
	3	27.0	12.3	2.3	—	4.6	3.7	0.3	9.3	88.9	23.4
	4	50.2	20.6	2.3	—	9.1	3.0	1.0	10.7	99.5	57.6
	5	34.5	13.8	2.0	—	6.6	2.6	1.6	8.0	87.7	55.3
	6	29.6	12.4	3.2	—	6.6	3.5	1.3	9.5	81.3	52.1
	7	38.3	15.1	1.3	—	7.5	2.6	0.4	10.4	94.6	67.6
	8	31.1	13.9	2.2	—	7.2	2.9	0.5	11.9	88.0	60.3
	9	28.1	12.7	2.9	—	7.0	3.2	1.5	12.4	82.3	57.3
	10	11.2	7.5	1.2	—	7.8	7.3	0.4	37.8	96.3	73.5
	11	9.0	6.3	1.1	—	6.4	7.6	0.3	36.7	91.3	67.6
	12	7.9	5.6	1.5	—	6.0	8.5	0.4	37.6	88.0	64.0
Direct Anodic Oxidation at Pt/C Anode	13	37.2	7.0	43.6	0.7	—	3.9	—	0.2	98.4	85.1
	14	29.1	5.1	37.6	0.6	—	4.5	—	0.3	90.4	68.6
	15	20.4	4.5	39.9	0.9	—	3.2	—	0.1	80.6	62.6

[1] GLAD = glyceraldehyde; DHA = dihydroxyacetone; GLA = glyceric acid; HPA = hydroxypyruvic acid; GAD = glycolaldehyde; GA = glycolic acid; GLOA = glyoxylic acid; FA = formic acid;
[2] See Examples for details in the Faradaic efficiency calculation.

Pairing the Electro-Fenton Process with Anodic Oxidation for Glycerol Valorization.

[0144] To valorize glycerol at both cathode and anode concurrently, anodic glycerol oxidation needs to operate in acidic solution to match the pH requirement of the electro-Fenton process. Therefore, anodic glycerol oxidation was performed in an Ar-saturated H_2SO_4 solution containing 50 mM glycerol on an anode made by drop-casting commercial Pt/C catalyst on carbon fiber paper. This paired system needs to operate in a two-compartment H-cell rather than in an undivided cell because the O_2 needed for the electro-Fenton process can undergo undesirable ORR on the Pt/C anode. Protons are transported through Nafion membrane and stabilize the pH of the catholyte (O_2-saturated $NaHSO_4$/Na_2SO_4 buffer containing 50 mM glycerol and 0.5 mM Fe^{2+}, pH~2.8) where the electro-Fenton process takes place.

[0145] Anodic glycerol oxidation at Pt/C anode in 0.05 M H_2SO_4 was first evaluated in the half-cell (FIG. **28**). To mimic the operation of the paired system, we applied a constant current of 1.7 mA (FIG. **28***c*) to approximately match with the current on $NiSe_2$/CFP cathode in the electro-Fenton half-cell studies. After a controlled amount of charge was passed, the applied potential of Pt/C anode was relatively stable around 0.55 V vs. RHE, and glycerol was selectively oxidized into C_3 products [GLAD, DHA, GLA, hydroxypyruvic acid (HPA)] with very small quantities of C_2 (GA) and C_1 (FA) products (FIG. **28***e* and Table 3). The anodic half-cell studies show the viability of valorizing glycerol in a linear paired electrochemical system that theoretically could operate at a negligible external bias (<0.05 V) with little external energy input needed if the internal resistance is negligible (discussion provided in the Detailed Description).

[0146] We then demonstrated the proof-of-concept linear paired electrochemical valorization of glycerol by feeding glycerol in both cathode and anode compartments of the H-cell where $NiSe_2$/CFP cathode was operated at 0.60 V vs. RHE and Pt/C anode matched the current (FIGS. **29** and **30**). With 0.1 M $NaHSO_4$/Na_2SO_4 catholyte and 0.05 M H_2SO_4 anolyte, the paired system operated steadily at an external bias around 1 V (FIG. **5***a*, Condition I), and the product distributions in the catholyte and anolyte (FIG. **5***b*, Condition I) closely resembled those found in the respective half-cell studies under similar conditions, i.e., high percent-

age of C_3 products. This external bias is higher than the theoretical value because there is a large solution IR drop between the anode and the reference electrode located on opposite sides of the membrane (FIG. **30***a*).

[0147] When a higher supporting electrolyte concentration of 0.5 M was applied for both catholyte and anolyte, the paired system operated at a much lower external bias below 0.2 V (FIG. **5***a*, Condition II) due to the greatly reduced solution IR drop at the anode (FIG. **30***b*). After a controlled amount of charge was passed, the product distributions in the anolyte were mostly unaffected (FIG. **5***b*, Condition II), whereas the detected aqueous phase organic products in the catholyte slightly decreased. The C_3 product selectivity in both catholyte and anolyte of the paired system decreased with increasing glycerol conversion up to ~53% (FIG. **5***b* and Table 5), due to the sequential oxidation of intermediate products, similar to the respective half-cell studies (vide supra). Since FA was detected as a late-stage oxidation product in both catholyte and anolyte (Table 5), control experiments suggested that both the electro-Fenton process and the anodic oxidation could further oxidize FA into gaseous CO_2, which may account for the loss in the carbon balance of all detected aqueous products in both catholyte and anolyte. Finally, we note that the residual excess external bias of 0.2 V for this paired system appears to be mostly caused by the internal resistance, and the overall paired process can be viewed as a controlled partial oxidation of glycerol by oxygen gas, which should be thermodynamically spontaneous. By employing zero-gap cell designs involving membrane electrode assemblies to lower the ohmic overpotential and by designing more active cathode and anode electrocatalysts to lower the kinetic overpotentials further, we believe that paired electrochemical systems for efficient glycerol valorization that need no external bias and no external energy input could be realized.

Summary

[0148] In summary, we demonstrated a linear paired electrochemical process for concurrent glycerol valorization by the electro-Fenton process at a stable and earth-abundant cathode together with direct oxidation at an anode. This process is enabled by the development of highly selective and stable $2e^-$ ORR catalyst for H_2O_2 production in acidic solution, which is elucidated by calculated free energy diagrams and surface adsorbate analyses and experimentally shown with RRDE and catalyst leaching studies together with sustained electrosynthesis of H_2O_2. The electro-Fenton process at the cathode at the demonstrated operation conditions leads to efficient cathodic glycerol valorization with a high selectivity toward valuable C_3 oxidation products and high glycerol conversion of 55%. The linear paired system achieves similarly high glycerol conversion and product selectivity and can operate at a very small external bias below 0.2 V, which could made into an unbiased system after further optimization in the future. The design principles for stable and selective electrocatalysts for acidic H_2O_2 production and the electro-Fenton process, and the conceptual strategy of linear pairing the electro-Fenton process with anodic oxidation presented here open up new opportunities for electrochemical valorization of a variety of biomass feedstocks with high atom efficiency and low energy cost.

Methods and Materials

Computational Method

[0149] Spin polarized electronic structure calculations were performed using the Vienna Ab initio Simulation package (VASP) interfaced with the Atomic Simulation Environment (ASE). Projector augmented wave (PAW) pseudopotentials with a cutoff of 450 eV were used to treat core electrons, and the Perdew-Burke-Ernzerhof (PBE) functional was used to treat exchange and correlation. Dispersion was treated using Grimme's D3(ABC) method. To better describe the Co 3d electrons in c-$CoSe_2$, a Hubbard U parameter, U_{eff}=2.0 eV, was taken from a previous report. A variety of Hubbard U parameters were tested for c-$NiSe_2$, and were found to have little to no effect on the geometries or energies; therefore, no Hubbard U parameter was used for this catalyst. Solvation effects were treated using the continuum solvent method VASPsol. The Brillouin zone was sampled using a (10, 10, 10) and (10, 10, 1) Γ-centered Monkhorst-Pack mesh for bulk and surface calculations, respectively. Lattice constants were determined by fitting to an equation of state (EOS).

[0150] For both c-$NiSe_2$ and c-$CoSe_2$, their respective (100) surface exhibits the lowest surface energy compared to other crystal surfaces, and thus is the most thermodynamically stable surface [0.044 vs. 0.064 vs. 0.069 eV $Å^{-2}$ for c-$CoSe_2$ (100) vs. (110) vs. (111) surface; 0.036 vs. 0.053 vs. 0.058 eV $Å^{-2}$ for c-$NiSe_2$ (100) vs. (110) vs. (111) surface]. The (100) surfaces of c-$NiSe_2$ and c-$CoSe_2$ were modelled as a 1×1 unit cell slab with two repeats in the z-direction, leading to a total of 8 metal atoms and 16 Se atoms and a vacuum gap of at least 15 Å. The top half of the slabs was allowed to relax while the bottom half was frozen to simulate the bulk. For each ionic configuration, the electronic energy was converged below 10^{-6} eV. Both the clean slab and adsorbates were allowed to relax until the forces were converged below 0.005 eV $Å^{-2}$. Transition states were located using the nudged elastic band (NEB) method and were refined using the dimer method. All transition states were confirmed saddle points with one imaginary frequency corresponding to bond breaking.

[0151] Binding energies were calculated with respect to $O_{2\ (g)}$ and $H^+_{(aq)}$ and e^-. The energy of $H^+_{(aq)}$ and e was calculated using the computational hydrogen electrode (CHE) method, where $H^+_{(aq)}$ is assumed to be in thermodynamic equilibrium with $H_{2\ (g)}$. The use of the CHE method for our calculation is validated by the fact that the difference in the OOH* binding energy on the c-$NiSe_2$ (100) surface calculated by the CHE method vs. the grand-canonical density functional theory (GC-DFT) method, accounting for the change in surface charge density upon adsorption, is <0.1 eV and can be safely neglected. In order to avoid well-known errors in the DFT treatment of $O_{2\ (g)}$, the free energy of $O_{2\ (g)}$ was determined by matching the experimental standard equilibrium potential (1.229 V) of the reaction $½\ O_{2\ (g)}+2\ H^+_{(aq)}+2\ e^- \rightarrow H_2O_{(l)}$. The adsorption of O_2, forming O_2* from $O_{2\ (g)}$, is excluded from our calculation because DFT does not treat $O_{2\ (g)}$ accurately, and the estimated free energy difference between $O_{2\ (g)}$ and O_2* on the c-$NiSe_2$ (100) surface is <0.1 eV and can be safely neglected. The free energies of species were calculated using G=H−T·S, where H is the enthalpy including zero-point energy (ZPE) and thermal corrections, and S is either the total experimental entropy at 298 K and 1 bar (for gas phase

species) or calculated under the harmonic approximation taking into account both vibrational contributions and hindered translations/rotations (for surface bound species). The free energy of $H_2O_{(l)}$ was calculated using the experimental free energy of formation for $H_2O_{(l)}$ and $H_2O_{(g)}$. The solvation free energy of $H_2O_{2\ (aq)}$ was calculated using the experimental Henry's law constant. The calculated standard equilibrium potential (U_{RHE}°) of the $2e^-$ ORR reaction $O_{2\ (g)}+2\ H^+_{(aq)}+2\ e^-\rightarrow H_2O_{2\ (aq)}$ is 0.81 V, slightly higher than the experimental standard equilibrium potential of 0.69 V.

[0152] Free energies of different surface adsorbate coverages were calculated to predict the most thermodynamically stable surface termination of each catalyst for a given set of potential and pH conditions under the assumption that the surfaces can be approximated in equilibrium with $H_2O_{(l)}$. The equilibrated proton-coupled electron transfer reaction for a general surface intermediate can then be written as:

$$X—O_mH_n^*+(2m-n)(H^++e^-)\leftrightarrows X^*+mH_2O$$

where X is the surface binding site, m is the number of oxygen atoms, and n is the number of hydrogen atoms. The free energy of this reaction can be written as:

$$\Delta G(U,pH)=G_{X^*}+mG_{H_2O}-G_{X\text{-}O_mH_n^*}-(2m-n)(G_{e^-}+G_{H^+})$$

[0153] Using the computational hydrogen electrode (CHE) method ($G_{e^-}+G_{H^+}=\frac{1}{2}G_{H_2}-U_{SHE}-2.303\ k_B\cdot T\cdot pH$) and converting the standard hydrogen electrode (SHE) to the reversible hydrogen electrode (RHE) ($U_{RHE}=U_{SHE}+2.303\ k_B\cdot T\cdot pH$), the free energy can be rewritten as a function of U_{RHE}:

$$\Delta G(U_{RHE})=G_{X^*}+mG_{H_2O}-G_{X\text{-}O_mH_n^*}-(2m-n)(\tfrac{1}{2}G_{e^-}-U_{RHE})$$

[0154] A 1×1 unit cell slab of the (100) surface of each catalyst that has two metal binding sites and four Se binding sites was used to model intermediate surface coverages as a function of potential. For c-$NiSe_2$, the Ni site is the preferential binding site for both OH* and O*. For c-$CoSe_2$, the Co site is the preferential binding site for OH*, and the Se site is the preferential binding site for O*. A wide variety of surface coverages were examined on various combinations of binding sites. For the sake of clarity, only the most thermodynamically stable surface coverages (in the U_{RHE} range of 0 V to 0.95 V) on the most preferential combination of binding sites were shown in FIG. **2***c*.

Chemicals

[0155] All chemicals were purchased from Sigma-Aldrich and used as received without further purification, unless noted otherwise. Deionized nanopure water (18.2 MΩ·cm) from Thermo Scientific Barnstead water purification systems was used for all experiments.

Materials Synthesis

[0156] c-$NiSe_2$ powder sample was prepared by a hydrothermal method. Following a procedure modified from a previous report, nickel hydroxide [$Ni(OH)_2$] precursor was first synthesized by dissolving 451.3 mg of $NiSO_4\cdot 6H_2O$ (Acros Organics, 98+%) in 58.3 mL of water and 8.75 mL of 2 M ammonia aqueous solution (diluted from ammonium hydroxide solution, 28.0-30.0% NH_3 basis), and heating the solution at 180° C. for 24 h in a sealed 100-mL Teflon-lined stainless-steel autoclave. The resulting $Ni(OH)_2$ precursor was hydrothermally converted into c-$NiSe_2$ as follows: 4.29 g of NaOH (≥97.0%) and 571 mg of Se powder (≥99.5%) were suspended in 50 mL of water via sonication and heated at 220° C. for 24 h in a sealed 80-mL autoclave; upon cooling to room temperature, 35 mg of $Ni(OH)_2$ precursor was suspended in 10 mL of water and added dropwise into the Se-containing solution under vigorous stirring, and then heated at 180° C. for additional 24 h in the same autoclave. The as-converted c-$NiSe_2$ product was successively washed with water, 1.25 M aqueous solution of Na_2S (nonahydrate, ≥98.0%) (to dissolve the elemental Se impurity), and water four times for each washing step, and dried under vacuum at 50° C.

[0157] To prepare $Ni(OH)_2$ precursor on carbon fiber paper ($Ni(OH)_2$/CFP), Teflon-coated carbon fiber paper (Fuel Cell Earth, TGP-H-060) was first treated with oxygen plasma at 150 W power for 5 min for each side and annealed in air at 700° C. for 5 min. A 3 cm×6 cm piece of annealed CFP was placed in the solution made of 2.1 mmol of $Ni(NO_3)_2\cdot 6H_2O$ (≥97.0%), 4.2 mmol of NH_4F (≥98.0%), and 10.5 mmol of urea (99.0-100.5%) in 80 mL of water, and heated at 110° C. for 5 h in a sealed 100-mL autoclave. $NiSe_2$/CFP was prepared by the same hydrothermal selenization method described above, except for using a 1.5 cm×6 cm piece of $Ni(OH)_2$/CFP as the precursor. The as-converted $NiSe_2$/CFP was immersed in 1.25 M aqueous solution of Na_2S three times to remove any excess elemental Se, rinsed with water and ethanol, and dried under N_2 gas flow. The areal loading of c-$NiSe_2$ grown on CFP was determined by the mass change of CFP after the materials growth. The c-$CoSe_2$ samples were prepared following the published procedures. All catalyst samples were stored in an argon-filled glove box to minimize the exposure to air.

Materials Characterization

[0158] Powder X-ray diffraction (PXRD) patterns were collected on a Bruker D8 ADVANCE powder X-ray diffractometer using Cu Kα radiation. Scanning electron microscopy (SEM) was performed on a Zeiss SUPRA 55VP field emission scanning electron microscope at an accelerating voltage of 1 kV. For SEM imaging, powder samples were drop-casted onto silicon wafer substrates. X-ray photoelectron spectroscopy (XPS) was performed on a Thermo Scientific K-Alpha XPS system with an Al Kα X-ray source. Raman spectroscopy was performed on a Thermo Fisher Scientific DXR3xi Raman Imaging Microscope using a 50 m confocal pinhole aperture and a 532 nm laser source and with a low laser power of 0.1 mW and an exposure time of 1.0 second to avoid sample degradation. For XPS and Raman experiments, powder samples were drop-casted onto graphite substrates, which were made by cutting thin slices of graphite rod (Graphite Store, low wear EDM rod), abrading with 600 grit silicon carbide paper (Allied High Tech Products), and sonicating in water and ethanol until clean. X-ray absorption spectroscopy (XAS) of $NiSe_2$/CFP before and after electrochemical testing was performed in transmission mode at the Advanced Photon Source (APS) Beamline 10-BM-B, and analyzed using ATHENA and ARTEMIS software.

Electrode Preparation

[0159] Drop-casted catalysts were prepared on a rotating ring-disk electrode (RRDE-3A, ALS Co., Ltd) made of a glassy carbon disk (with a geometric area of 0.126 cm^2_{disk}) surrounded by a Pt ring. The collection efficiency of the bare RRDE was 0.43, determined experimentally using the ferri-/ferrocyanide redox couple. The RRDE was successively polished with 1, 0.3, and 0.05 m alumina suspensions (Allied High Tech Products) on a polishing cloth (Buehler, MicroCloth), thoroughly rinsed with water and methanol, briefly sonicated in methanol for <20 s, and dried under ambient conditions before use. The catalyst inks were prepared by suspending pre-weighed catalyst powders in desired volumes of a 9:1 (v/v) mixture of water and 5 wt % Nafion solution by sonication for 1 h. A fixed volume (10 μL) of catalyst ink was then drop-casted on the disk electrode and dried under ambient conditions at a rotation rate of 700 rpm to form a uniform catalyst film where the Nafion loading was identical (0.4 mg_{Nafion} cm^{-2}_{disk}) whereas the catalyst loading was varied (FIGS. **3***a* and **3***b*). $NiSe_2$/CFP cathode was fabricated from as-synthesized $NiSe_2$/CFP sample (vide supra) by using 5-min epoxy (Devcon) to define the exposed geometric area as ~1 cm×~1 cm. The Pt/C anode was prepared by on drop-casting 200 μL of the catalyst ink (50 mg of 20 wt % Pt/C suspended in 900 μL of isopropanol and 100 μL of 5 wt % Nafion solution by sonication for 1.5 h) on both sides (100 μL on each side) of the pre-fabricated bare CFP electrode (~1 cm×~1 cm), resulting in a catalyst loading of ~2 mg_{Pt} cm^{-2}_{geo}.

Rotating Ring-Disk Electrode Measurement

[0160] RRDE measurements were conducted in an undivided three-electrode cell with a graphite rod counter electrode and a Hg/Hg_2SO_4 (saturated K_2SO_4) reference electrode (calibrated against a saturated calomel electrode) connected to a Bio-Logic VMP-300 multichannel potentiostat. All potentials were reported versus RHE (E vs. RHE=E vs. SHE+0.059×pH). Prior to RRDE measurements, the electrolyte solution (40-45 mL) of either 0.05 M H_2SO_4 (pH~1.2) or 0.1 M $NaHSO_4/Na_2SO_4$ buffer solution (pH~2.8) was purged with O_2 gas for >10 min, and a blanket of O_2 gas was maintained above the electrolyte solution during the measurements. Under O_2-saturated condition, the catalyst-coated disk was first conditioned by running cyclic voltammetry (CV) between −0.025 V and 0.75 V vs. RHE at 100 mV s^{-1} and 1600 rpm for 10 cycles, while holding the Pt ring at 1.3 V vs. RHE. The Pt ring was then conditioned by running CV between 0.05 V and 1.20 V vs. RHE at 100 mV s^{-1} and 1600 rpm for 10 cycles while holding the disk at 0.75 V vs. RHE to remove the surface PtO_x. The $2e^-$ ORR catalytic properties were evaluated by performing linear sweep voltammetry of the catalyst-coated disk from 0.75 to −0.025 V vs. RHE at 50 mV s^{-1} and various rotation rates, meanwhile holding the Pt ring at 1.3 V vs. RHE. Finally, the background current, double-layer capacitance (C_{dl}, determined by CV of the disk between −0.025 V and 0.75 V vs. RHE at various scan rates and 0 rpm), and uncompensated resistance (Ru, determined by electrochemical impedance spectroscopy of the disk at 0.75 V vs. RHE) were measured under Ar-saturated conditions. By manually conducting background current and iR corrections, the H_2O_2 selectivity (P_{RRDE}) is calculated as follows:

$$p_{RRDE}(\%) = \frac{2 \times \frac{i_{ring}}{N}}{i_{disk} + \frac{i_{ring}}{N}} \times 100\%$$

where i_{disk} and i_{ring} are the respective disk and ring current, and N is the collection efficiency. For the ease of visualizing the H_2O_2 selectivity from RRDE voltammograms (FIG. **3***a*), both disk and ring current densities (j_{disk} and j_{ring}) are normalized to the geometric area of the disk electrode (A_{disk}), and the ring current density is further adjusted by the collection efficiency:

$$j_{disk} = \frac{i_{disk}}{A_{disk}}$$

$$j_{ring} = \frac{i_{ring}}{A_{disk} \times N} = j_{peroxide}$$

where $j_{peroxide}$ is the partial current density for H_2O_2 production.

[0161] The protocols for long-term RRDE stability tests were described in FIG. **12**. After these stability tests, the spent catalysts were recovered from the disk electrode by sonicating in water and ultracentrifuging at 13200 rpm for 1 min, followed by re-dispersing in minimal amount of water and drop-casting onto graphite substrates for XPS and Raman characterization (vide supra). To monitor the catalyst leaching during these stability tests, the spent electrolyte solutions were filtered with 0.22-μm syringe filters (Restek) and then analyzed with inductively coupled plasma mass spectrometry (ICP-MS) measurements on an Agilent 8900 Triple Quadrupole ICP-MS spectrometer. ICP-MS standard solutions were prepared by dissolving $NiSO_4 \cdot 6H_2O$ (≥98%), or $CoSO_4 \cdot 7H_2O$ (≥99%), or SeO_2 (≥99.9%) in a matrix solution of 0.05 M H_2SO_4 (pH~1.2) or 0.1 M $NaHSO_4/Na_2SO_4$ (pH~2.8).

Bulk Electrosynthesis of H_2O_2

[0162] $NiSe_2$/CFP cathode (vide supra) was used for constant-potential bulk electrosynthesis of H_2O_2 in O_2-saturated 0.05 M H_2SO_4 (pH~1.2) or 0.1 M $NaHSO_4/Na_2SO_4$ (pH~2.8) solution (4 mL, stirred at 1200 rpm) placed in the cathode compartment of a two-compartment three-electrode H-cell (see FIG. **17**). Nafion 117 membrane (Fuel Cell Store) was cleaned by successively immersing in 3 wt % H_2O_2, water, 1 M H_2SO_4, and water at 80° C. for 1 h for each cleaning step and stored in 0.05 M H_2SO_4 at room temperature before use. $NiSe_2$/CFP cathode was conditioned by running CV between −0.025 V and 0.75 V vs. RHE at 100 mV s^{-1} for 5 cycles to reach the steady state before use. Chronoamperometry was then performed to produce H_2O_2 at $NiSe_2$/CFP cathode, and the optimum operating potential was found to

be 0.60 V vs. RHE (see FIG. **3***d*). A small aliquot (25 μL) of catholyte was periodically sampled during chronoamperometry and mixed with 8 mL of $Ce(SO_4)_2$ stock solution (~0.4 mM Ce^{4+} in 0.5 M H_2SO_4 matrix solution) to chemically detect the produced H_2O_2 by UV-Vis spectrophotometry at 318 nm ($2\ Ce^{4+}+H_2O_2 \rightarrow 2\ Ce^{3+}+O_2+2\ H^+$). The concentration of the produced H_2O_2 can be calculated as follows:

$$[H_2O_2] = \frac{8\ \text{mL} \times [Ce^{4+}]_{before} - 8.025\ \text{mL} \times [Ce^{4+}]_{after}}{2 \times 0.025\ \text{mL}}$$

where $[H_2O_2]$ is the cumulative H_2O_2 concentration, $[Ce^{4+}]_{before}$ and $[Ce^{4+}]_{after}$ are the $[Ce^{4+}]$ in the stock solution (determined by fitting to the standard curve) before and after mixing with the catholyte aliquot. The cumulative H_2O_2 yield ($n_{H_2O_2}$), H_2O_2 selectivity ($P_{H_2O_2}$), and Faradaic efficiency ($FE_{H_2O_2}$) are calculated based on $[H_2O_2]$, the catholyte volume (taking into account the evaporation), and the total amount of charge passed (Q_{total}) (see detailed methodology for these calculations described in our previous report):

$$P_{H_2O_2}(\%) = \frac{n_{H_2O_2}(\text{mol})}{n_{H_2O_2}(\text{mol}) + \frac{Q_{total}(C) - 2 \times n_{H_2O_2}(\text{mol}) \times F}{4 \times F}} \times 100\%$$

$$FE_{H_2O_2}(\%) = \frac{2 \times n_{H_2O_2}(\text{mol}) \times F}{Q_{total}(C)} \times 100\%$$

where F is the Faraday constant (96485 C mol^{-1}). To monitor the catalyst leaching during H_2O_2 bulk electrosynthesis, the spent catholytes were filtered with 0.22-μm syringe filters (Restek) and diluted by 15 times with a matrix solution of 0.05 M H_2SO_4 for ICP-MS analysis (vide supra).

Glycerol Valorization and Product Analysis

[0163] All experiments of glycerol valorization were performed in the two-compartment three-electrode H-cell described above. Half-cell studies of glycerol valorization via the electro-Fenton process at $NiSe_2$ cathode were performed by chronoamperometry with controlled amounts of charge passed at 0.60 V vs. RHE in O_2-saturated 0.1 M $NaHSO_4/Na_2SO_4$ solution (pH~2.8) containing glycerol (~50 mM) and Fe^{2+} (0.1, 0.5, 1.0, or 2.5 mM, prepared from $FeSO_4 \cdot 7H_2O$, ≥99.0%) (see schematic in FIG. **24**). Half-cell studies of direct oxidation of glycerol at Pt/C anode were performed by chronopotentiometry with controlled amounts of charge passed at 1.7 mA in Ar-saturated 0.05 M H_2SO_4 solution (pH~1.2) containing glycerol (~50 mM) (see schematic in FIG. **28**). Linear paired glycerol valorization at the $NiSe_2$ cathode (in O_2-saturated 0.1 M or 0.5 M $NaHSO_4/Na_2SO_4$ solution containing ~50 mM glycerol and 0.5 mM Fe^{2+}, pH~2.8) and Pt/C anode (in Ar-saturated H_2SO_4 solution containing ~50 mM glycerol) was performed by operating the cathode via chronoamperometry at 0.60 V vs. RHE while recording the applied potential of the anode (see schematic in FIG. **29**). The analysis of the products from glycerol valorization was performed by ^1H and ^{13}C NMR spectroscopy on a Bruker AVANCE III 600 MHz NMR spectrometer. Glycerol (≥99.0%), DL-glyceraldehyde (≥90%), dihydroxyacetone (Pharmaceutical Secondary Standard; Certified Reference Material), DL-glyceric acid (TCI America, 20% in water, ca. 2 mol/L), β-hydroxypyruvic acid (≥95.0%), tartronic acid (Alfa Aesar, 98%), sodium mesoxalate monohydrate (≥98.0%), glycolaldehyde dimer (crystalline, mixture of stereoisomers), glycolic acid (99%), glyoxylic acid monohydrate (98%), oxalic acid (99.999%), and formic acid (≥98%) were individually prepared into NMR standard samples (500 μL) in Norell® Sample Vault Series™ NMR tubes (diam.×L 5 mm×178 mm) using D_2O (99.9 atom % D) as the solvent and maleic acid (Standard for quantitative NMR, TraceCERT®) as the internal standard. To achieve quantitative ^1H NMR results, the relaxation delay was set to 20 seconds (longer than 5 times of the T1 relaxation times of all compounds of interest determined by inversion recovery experiments). UW pulse sequence was used for the solvent suppression, and 4 scans were collected. For ^{13}C NMR results, the relaxation delay was set to 2 seconds, and 256 scans were collected. After the half-cell or linear paired glycerol valorization experiments, the catholytes and/or anolytes of interest were filtered with 0.22-μm syringe filters (Restek) and prepared into NMR samples accordingly. The quantifications of $[glycerol]_i$, $[glycerol]_f$, and $[C_n\ product]_f$ are based on the selected ^1H NMR peak integration ratios relative to the maleic acid internal standard. The glycerol conversion, C_n product selectivity (n=1, 2, 3), and carbon balance of all detected aqueous phase organic products are calculated as follows:

$$\text{glycerol conversion}\ (\%) = \frac{[\text{glycerol}]_i \times V_i - [\text{glycerol}]_f \times V_f}{[\text{glycerol}]_i \times V_i} \times 100\%$$

$$C_n\ \text{product selectivity}\ (\%) = \frac{n}{3} \times \frac{[C_n\ \text{product}]_f \times V_f}{[\text{glycerol}]_i \times V_i - [\text{glycerol}]_f \times V_f} \times 100\%$$

$$\text{carbon balance}\ (\%) = \frac{3 \times [\text{glycerol}]_f \times V_f + \sum_{n=1}^{3} \{n \times [C_n\ \text{product}]_f \times V_f\}}{3 \times [\text{glycerol}]_i \times V_i} \times 100\%$$

where V_i and V_f are the initial and final electrolyte volume, $[glycerol]_i$ and $[glycerol]_f$ are the initial and final concentration of glycerol, $[C_n\ product]_f$ is the final concentration of C_n product (n=1, 2, 3), all of which are listed in Table 3 and 5. The Faradaic efficiency of all detected aqueous phase organic products at the anode (FE_{anode}) and the cathode ($FE_{cathode}$) are calculated and estimated, respectively, based on the methods described in below and these calculated FE_{anode} and estimated $FE_{cathode}$ values are also listed in Table 3 and 5.

TABLE 4

Comparisons between the 183 μm-thick Nafion 117 membrane and the 89 μm-thick Nafion NE1035 membrane.

Membrane	Thickness	Catholyte	Anolyte	R at Cathode	R at Anode
Nafion 117	183 μm	0.1M $NaHSO_4/Na_2SO_4$ (pH ~2.8) + ~50 mM Glycerol + 0.5 mM Fe^{2+}	0.05M H_2SO_4 + ~50 mM Glycerol	1.4 Ω (Run 1) [1]	713 Ω (Run 1) [1]
				1.3 Ω (Run 2) [1]	726 Ω (Run 1) [1]
				1.3 Ω (Run 3) [1]	722 Ω (Run 1) [1]
		0.5M $NaHSO_4/Na_2SO_4$ (pH ~2.8) + ~50 mM Glycerol + 0.5 mM Fe^{2+}	0.5M H_2SO_4 + ~50 mM Glycerol	0.8 Ω (Run 4) [2]	159 Ω (Run 4) [2]
				0.8 Ω (Run 5) [2]	166 Ω (Run 5) [2]
Nafion NE1035	89 μm	0.1M $NaHSO_4/Na_2SO_4$ (pH ~2.8)	0.05M H_2SO_4	2.2 Ω	685 Ω
		0.5M $NaHSO_4/Na_2SO_4$ (pH ~2.8)	0.5M H_2SO_4	1.8 Ω	173 Ω

[1] See FIG. 30a.

[2] See FIG. 30b.

TABLE 5

Summary of the aqueous phase organic (C_3, C_2, and C_1) product selectivity, glycerol conversion percentage, and carbon balance and Faradaic efficiency of all detected aqueous phase organic products for linear paired electrochemical valorization of glycerol at c-$NiSe_2$/CFP cathode and Pt/C anode.

Supporting Electrolyte Condition (I or II)			Starting Volume (mL)	Starting [Glycerol] (mM)	Starting [Fe^{2+}] (mM)	Starting pH	Charge Passed (C)	Final Volume (mL)	Final [Glycerol] (mM)	Final pH
I	Run 1	Catholyte	4	50.4	0.5	2.91	15.0	3.24	50.6	1.95
		Anolyte	4	53.1	—	1.21	15.0	3.58	48.1	1.29
	Run 2	Catholyte	4	50.4	0.5	2.89	30.0	2.80	44.7	1.85
		Anolyte	4	53.1	—	1.21	30.0	3.33	39.6	1.29
	Run 3	Catholyte	4	50.4	0.5	2.89	44.9	2.35	40.1	1.66
		Anolyte	4	53.1	—	1.21	44.9	3.20	32.1	1.34
II	Run 4	Catholyte	4	50.4	0.5	2.91	14.9	2.65	58.4	1.13
		Anolyte	4	52.9	—	0.38	14.9	3.41	50.8	0.43
	Run 5	Catholyte	4	50.4	0.5	2.88	29.9	2.20	55.6	0.97
		Anolyte	4	52.9	—	0.38	29.9	3.12	43.4	0.43

Supporting Electrolyte Condition (I or II)			Glycerol Conversion (%)	Aqueous Phase Organic Product Selectivity (%) [1]								Carbon Balance (%)	Faradaic Efficiency (%)
				C_3				C_2			C_1		
				GLAD	DHA	GLA	HPA	GAD	GA	GLOA	FA		
I	Run 1	Catholyte	18.8	47.8	19.1	2.6	—	10.1	3.7	0.5	12.0	99.2	69.1
		Anolyte	18.9	43.1	6.6	37.9	0.7	—	3.6	—	0.3	98.5	71.2
	Run 2	Catholyte	38.0	37.1	15.9	4.0	—	7.9	4.1	0.7	11.9	93.0	63.8
		Anolyte	37.8	32.3	5.2	35.4	1.0	—	3.7	—	0.4	91.7	63.1
	Run 3	Catholyte	53.3	29.5	13.9	4.7	—	8.4	5.9	2.1	15.9	89.5	68.4
		Anolyte	51.6	29.4	5.8	40.9	1.4	—	4.7	—	0.4	91.0	63.3
II	Run 4	Catholyte	23.2	33.2	10.3	1.8	0.3	7.5	2.5	1.0	9.1	92.0	61.7
		Anolyte	18.1	44.3	8.3	38.1	0.4	—	3.9	—	0.3	99.2	70.0
	Run 5	Catholyte	39.3	25.4	9.4	2.9	1.4	7.2	4.3	1.5	14.1	86.7	64.0
		Anolyte	35.9	32.7	5.7	40.0	0.5	—	5.0	—	0.3	94.3	65.4

[1] GLAD = glyceraldehyde; DHA = dihydroxyacetone; GLA = glyceric acid; HPA = hydroxypyruvic acid; GAD = glycolaldehyde; GA = glycolic acid; GLOA = glyoxylic acid; FA = formic acid.

[0164] Here we provide the details in the Faradaic efficiency (FE) calculation for glycerol valorization at the $NiSe_2$ cathode and the Pt anode.

[0165] The FE of all detected aqueous phase organic products (i.e., not including the potential product of CO_2, which is not detectable by ^1H NMR) from glycerol oxidation at the Pt anode (FE_{anode}) can be calculated using the following equation:

$$FE_{anode}(\%) = \frac{\sum_{n-1}^{3}\left\{\frac{n}{3}\times[C_n\ \text{product}]_f \times V_f \times x \times F\right\}}{Q_{total}} \times 100\%$$

where V_f is the final electrolyte volume, $[C_n\ \text{product}]_f$ is the final concentration of C_n product (n=1, 2, 3), x is the theoretical number of electrons transferred for oxidizing 1 molecule of glycerol to 3/n molecule(s) of a specific C_n product at anode (x=2 for glyceraldehyde, dihydroxyacetone, or glycolaldehyde; x=4 for glyceric acid; x=5 for glycolic acid; x=6 for hydroxypyruvic acid; x=8 for glyoxylic acid, or formic acid) based on the balanced anodic half-cell reactions below (see FIG. **4***b*), F is the Faraday constant (96485 C mol^{-1}), Q_{total} is the total amount of charge passed.

$$\text{glycerol} \rightarrow \text{glyceraldehyde} + 2H^+ + 2e^-$$

$$\text{glycerol} \rightarrow \text{dihydroxyacetone} + 2H^+ + 2e^-$$

$$\text{glycerol} + H_2O \rightarrow \text{glyceric acid} + 4H^+ + 4e^-$$

$$\text{glycerol} + H_2O \rightarrow \text{hydroxypyruvic acid} + 6H^+ + 6e^-$$

glycerol→3/2 glycolaldehyde+2H^++2e^-

glycerol+3/2H_2O→3/2 glycolic acid+5H^++5e^-

glycerol+3/2H_2O→3/2 glyoxylic acid+8H^++8e^-

glycerol+3H_2O→3 formic acid+8H^++8e^-

[0166] The calculated FE_{anode} values for the anodic half-cell studies (63-85%) and the linear paired experiments (63-71%) are listed in Table 3 and 5, respectively. These calculated FE_{anode} values are less than unity due to the oxidation of formic acid into CO_2 at the Pt anode. An earlier literature also showed the possible formation of CO_2 from glycerol oxidation at Pt anode under similar applied potential and pH conditions.

[0167] On the other hand, the estimate of the FE for the cathodic electro-Fenton process is complicated by the multi-step process. We assume that cathodic valorization of glycerol theoretically proceeds via electrogeneration of H_2O_2 from O_2 (O_2+2 H^++2 e^-→H_2O_2), followed by using H_2O_2 as the oxygen source that is using the ·OH and Fe^{3+} pair generated from the Fenton reaction (Fe^{2+}+H_2O_2→Fe^{3+}+·OH+OH^-) as the oxidants to oxidize glycerol in the solution.

[0168] The balanced cathodic half-cell reactions should theoretically be (see FIG. **4***a*):

glycerol+O_2+2H^++2e^-→glyceraldehyde+2H_2O

glycerol+O_2+2H^++2e^-→dihydroxyacetone+2H_2O

glycerol+2O_2+4 H^++4e^-→glyceric acid+3H_2O

glycerol+3O_2+6 H^++6e^-→hydroxypyruvic acid+5H_2O

glycerol+O_2+2H^++2e^-→3/2 glycolaldehyde+2H_2O

glycerol+5/2O_2+5 H^++5e^-→3/2 glycolic acid+7/2 H_2O

glycerol+4O_2+8 H^++8e^-→3/2 glyoxylic acid+13/2 H_2O

glycerol+4O_2+8 H^++8e^-→3 formic acid+5H_2O

[0169] The FE of all detected aqueous phase organic products from glycerol valorization at the $NiSe_2$ cathode ($FE_{cathode}$) can be estimated using the following equation:

$$FE_{cathode}(\%) = \frac{\sum_{n=1}^{3}\left\{\frac{n}{3}\times[C_n\ \text{product}]_f \times V_f \times y \times F\right\}}{Q_{total}} \times 100\%$$

where y is the theoretical number of electrons transferred for oxidizing 1 molecule of glycerol to 3/n molecule(s) of a specific C_n product (n=1, 2, 3) at cathode as shown in the balanced cathodic half-cell reactions above (y=2 for glyceraldehyde, dihydroxyacetone, or glycolaldehyde; y=4 for glyceric acid; y=5 for glycolic acid; y=6 for hydroxypyruvic acid; y=8 for glyoxylic acid, or formic acid). Note that this would be a conservative lower bound estimate of the $FE_{cathode}$, because any non-ideal electro-Fenton process will lead to larger y values and thus larger $FE_{cathode}$ values. The estimated $FE_{cathode}$ values for the cathodic half-cell studies (52-58% when [Fe^{2+}]=0.5 mM) and the linear paired experiments (62-69% when [Fe^{2+}]=0.5 mM) are listed in Table 3 and 5, respectively. These estimated $FE_{cathode}$ values are less than unity due to the oxidation of formic acid into CO_2 at the $NiSe_2$ cathode.

Example 2

[0170] Synthesis and Characterization of $PdSe_2$ Nanoplates. We synthesized layered $PdSe_2$ (FIG. **32***a*) using a facile hydrothermal reaction by reacting palladium chloride and selenourea in near-stoichiometric amounts. $PdSe_2$ nanoplates with similar morphology (and variable thickness/size) could also be prepared by liquid exfoliation from bulk $PdSe_2$ crystals. The powder X-ray diffraction pattern (PXRD) of as-synthesized $PdSe_2$ matched the standard pattern (FIG. **32***b*) without detectable impurities from other known Pd—Se phases. Scanning electron microscopy (SEM) images show that the resulting $PdSe_2$ has a nanoplate-like morphology, with enriched surface area in the (200) basal plane compared to the (002) edges (FIG. **32***c*). The Raman spectra (FIG. **32***d*) matched the previously reported spectrum for bulk $PdSe_2$, suggesting the as-prepared $PdSe_2$ nanoplates do not approach few-layer thicknesses. To elucidate the electronic structure of $PdSe_2$, we then conducted X-ray absorption near edge spectroscopy (XANES) at the Pd L_3-edge (FIG. **32***e*), wherein the position of the white line and the white line intensity were most similar to that of PdO (Pd^{2+}), falling between the intensities/edge positions of Pd foil (Pd^0) and K_2PdCl_6 (Pd^{4+}), suggesting that the Pd sites in $PdSe_2$ have a near 2+ oxidation state. Se K-edge XANES showed similarity in XANES peak shapes to Se_2^{2-} compounds, such as $CoSe_2$, which has similar Se—Se dumbbells. Pd L_1 and L_2 edge XANES further supported a Pd^{2+} oxidation state.

[0171] Evaluation of the 2e^- ORR Activity, Selectivity and Operational Stability of $PdSe_2$. To evaluate the 2e^- ORR activity, selectivity, and stability of $PdSe_2$, electrochemical tests using a rotating ring disk electrode (RRDE) in acidic (0.05 M H_2SO_4, pH=1.2) and neutral (0.05 M NaPi buffer=0.025 M Na_2HPO_4/0.025 M NaH_2PO_4, pH=6.5) conditions (FIG. **33***a*) were conducted. In contrast to other metal compound electrocatalysts, the activity of $PdSe_2$ in buffered neutral conditions is higher than its activity in acidic conditions, while high selectivity (≥80%) is maintained in both pH conditions at potentials up to 0.05 V vs. RHE. The RRDE results for $PdSe_2$ suggest that $PdSe_2$ can produce large amounts of H_2O_2 while operating at higher overpotentials, compared to other electrocatalysts measured in neutral solution (FIG. **33***b*) which primarily have large partial kinetic current towards H_2O_2 production ($j_{k,peroxide}$) at lower overpotentials, but decrease in current at higher overpotentials (more cathodic). Furthermore, the RRDE measurements of Pd^4Se and $Pd_{17}Se_{15}$ further highlight the unique behavior of $PdSe_2$ in the family of Pd—Se phases, with only $PdSe_2$ exhibiting high selectivity and activity for H_2O_2 production. The stability of the $PdSe_2$ phase was further evaluated at a fixed potential of 0 V vs. RHE over >6 hours while continually monitoring the ring current and consequent H_2O_2 selectivity (FIG. **33***c*). The ring current remained >1 mA/cm^2_{disk} for the duration of the measurement, indicating that >80% selectivity can be continuously maintained. However, some decrease in the disk current was observed over time, which could indicate some changes occurring at the catalyst that even further increase the barrier to the 4e^- pathway.

[0172] Bulk Electrosynthesis of H_2O_2 on $PdSe_2$. To evaluate the practical performance of $PdSe_2$ for electrosynthesis

of H_2O_2, Inventors prepared a gas diffusion electrode (GDE) loaded with $PdSe_2$ catalyst (FIG. **39***a*) and applied a pulsed electrolysis procedure in a two-compartment flow cell to rapidly accumulate H_2O_2 (see Methods). Inventors initially measured CV on the $PdSe_2$/GDE electrode and observed a cathodic current onset of ~0.6 V vs. RHE, and a large increasing current up to almost −90 mA (or −16 mA cm^{-2}) at 0 V vs. RHE (FIG. **39***b*).

[0173] Based on the CV, Inventors performed an extended electrosynthesis test at a fixed current of −30 mA (FIG. **39***c*). After an initial onset curve, the potential remained fairly constant at ~0.3 V vs. RHE over a 3-hour electrolysis, and yielded an accumulated H_2O_2 concentration of 870 ppm (FIG. **39***d*). Rapid accumulation of H_2O_2 was also achieved over the $PdSe_2$/GDE electrode at constant currents of −85 mA and −60 mA (FIG. **39***c,d*) allowing for accumulation of a similar amount of H_2O_2 (785 ppm) in just 15 minutes with a Faradaic efficiency of >50% and a potential of ~0 V vs. RHE. After the electrosynthesis, the final pH remained near neutral for all measurements.

[0174] The drops in Faradaic efficiency over the duration of bulk electrolysis are similar to that observed for cubic $NiSe_2$. To understand this, Inventors comprehensively considered both the production and decomposition of the H_2O_2 and also computationally compare the expected catalytic properties of 2D pentagonal $PdSe_2$ against those of pyrite phase $NiSe_2$ with a cubic symmetry and identical (100) and (001) surfaces (FIG. **1***b*). $NiSe_2$ is predicted to be more active than the $PdSe_2$ based on the stability of OOH*. The $PdSe_2$ (100), $PdSe_2$ (001), and $NiSe_2$ surfaces each have large barriers for the thermal bond dissociation of OOH* [reaction (7)], which is beneficial for $2e^-$ ORR. Since both $PdSe_2$ (100)/(001) and $NiSe_2$ show barrierless PCET steps for $2e^-$ ORR with larger barriers for reaction (4), both should favor 2e-ORR over 4e-ORR. However, the barrier for the further reduction of H_2O_2[reaction (5)] over $NiSe_2$ lies between those of $PdSe_2$ (100) and $PdSe_2$ (001) surfaces, which can be explained by the trend of the relative stability of OH* to H_2O_2* (or the Brønsted-Evans-Polanyi (BEP) principle). Therefore, the $PdSe_2$ (001) surface is expected to demonstrate better selectivity and accumulation of H_2O_2, and the kinetic behavior of $NiSe_2$ and $PdSe_2$ (100) edges may dictate the overall Faradaic efficiency of electrosynthesis over these surfaces.

[0175] Notably, the $PdSe_2$/GDE electrosynthesis performance is dependent on the loading and morphology of the deposited catalyst film—a $PdSe_2$ film with higher loading on the GDE limited the Faradaic efficiency and accumulation of H_2O_2 during electrolysis. This was most likely due to inhibited O_2 transport to the triple phase boundary. Despite this, all GDE flow cell electrosyntheses resulted in significantly more H_2O_2 accumulation in a much shorter time than a traditional H-cell electrosynthesis, which highlights the importance of cell design in evaluating the performance of $2e^-$ ORR catalysts. The high H_2O_2 production rate (7933 mmol $g_{catalyst}^{-1}$ h^{-1}) at 0 V vs. RHE is notably among the highest to reach practically useful concentrations of H_2O_2 in a conventional flow cell device.

[0176] Post-Electrolysis and Operando Stability of $PdSe_2$. In order to confirm the predicted stability of $PdSe_2$ experimentally, several post-electrolysis experiments were conducted. First, in order to evaluate $PdSe_2$'s viability for direct applications where only small amounts of Pd and Se leaching into solution can be tolerated (i.e. wastewater treatment, semiconductor cleaning), we measured the amount of Pd and Se leached during electrolysis at 0.2 V vs. RHE and 0.3 V vs. RHE using inductively coupled plasma optical emission spectroscopy (ICP-OES) and found that Pd leaching was near-zero at the more active operating potential of 0.2 V vs. RHE, while Se leaching increased at the more active $2e^-$ ORR potential (FIG. **35***a*). The effective amount of Se in the low-volume (<5 mL) H-cell is slightly higher than the allowed amount in drinking water, this problem could likely be solved by operating $2e^-$ ORR on $PdSe_2$ in high volume flow-cell devices. Despite this small amount of metal leaching, there was very little change observed in the Raman spectrum (FIG. **35***b*) and the XRD pattern (FIG. **35***c*) of the catalyst after the electrolysis, indicating that the bulk structure of $PdSe_2$ is maintained after the electrolysis. Similarly, X-ray photoelectron spectroscopy (XPS) indicated that the electronic environment of Se changed little before and after the electrolysis (FIG. **35***d*), indicating that the O* adsorption, which prefers the Se site, did not permanently modify the Se on the surface after operation. However, the Se/Pd ratio increased post-operation, suggesting that the leaching could trigger some surface rearrangement.

[0177] After confirming ex-situ that the $PdSe_2$ maintained its bulk structure and surface electronic environment before and after electrolysis, we sought to probe the dynamic electronic and local structure environments during the true operating conditions of $PdSe_2$ during $2e^-$ ORR using operando XAS. Interestingly, the Se K-edge XANES peak shape and edge position were unchanged from E_{OC} up to potentials of 0 V vs. RHE (FIG. **35***e*). The lack of changes in the intensity of the while line or edge position indicates that there is no substantial adsorption of oxygenates on the Se sites. Similarly, the extended Se K-edge X-ray absorption fine structure (EXAFS) spectra at the same set of potentials are completely overlapped (FIG. **35***f*). Thus, the average local environment around the Se must remain unchanged, further indicating no substantial absorption oxygenates are generated during the $2e^-$ ORR process. In contrast, the Pd K-edge spectrum does show small shifts in the XANES as well as minor coordination changes in the EXAFS, which is a result of oxygenate adsorption slightly changing the electronic environment and local structure around the Pd sites.

[0178] Surface Pourbaix Diagrams. To understand the electrochemical stability of $PdSe_2$, we calculated the surface Pourbaix diagrams of the (001) and (100) surfaces under the assumption that the surfaces are in equilibrium with bulk water. The proton-coupled electron transfer (PCET) reaction of a general adsorbate can be written as:

$$O_mH_n^*+(2m-n)(H^++e^-)\rightarrow^*+mH_2O_{(l)} \quad (1)$$

The electrochemical potentials of a proton and an electron pair were calculated by using the computational hydrogen electrode (CHE) method (Equation 2).

$$\widetilde{\mu_{H^+}}+\widetilde{\mu_{e^-}}=0.5\mu_{H_2}-U_{RHE} \quad (2)$$

where $\widetilde{\mu_{H^+}}$ and $\widetilde{\mu_{e^-}}$ are electrochemical potentials of a proton and an electron, and μ_{H_2} is a chemical potential of hydrogen gas at the standard state, and U_{RHE} refers to the applied potential vs RHE. The preferential binding sites for H, O, OH and OOH on two surfaces are shown in Table 6.

TABLE 6

The preferential binding sites for O*/OH*/OOH* on (001) and (100) surfaces of $PdSe_2$. Note that OOH is assumed to have no preferential binding site on (001) because the difference in adsorption energy is less than 0.05 eV.

	(001)	(100)
H*	Se	Pd
O*	Se	Se
OH*	Se	Pd
OOH*	—	Pd

[0179] Clean surface is predicted for the (001) surface over a wide range of potential, which is unsurprising considering its small surface energy, indicating that this surface is much more stable than the (100) surface. Likewise, (100) surface is predicted to be bare at the applied potential although the potential window where the clean surface is predicted is narrower. Note that bond breaking is not required to generate the (001) surface because the interaction between layers is through the van der Waals interaction. Pd atoms on the (001) surface have the same coordinate number as that of bulk Pd atoms. Although the coordination number of Se atoms does not change, Se atoms of bulk $PdSe_2$ will interact with the atoms in a neighboring layer. This will make Pd atoms on the (001) surface less active. On the other hand, Pd—Se bonds need to be broken to generate the (100) surface, which makes this surface more reactive. Because the implicit solvation model, such as VASPsol, cannot describe the competitive water adsorption, the interaction of water with $PdSe_2$ should be taken into account, considering water adsorption energy on the (100) surface is strong and the preferential binding sites for H_2O and OOH are the same. To investigate if all the Pd atoms are covered by specifically adsorbed water or not, ab-initio molecular dynamics (AIMD) was performed over 10 picoseconds by putting 30 water molecules in the 2×1 supercell of the $PdSe_2$ (100) slab and we found that the specifically adsorbed water will occupy half of Pd atoms of the (100) surface and this can affect the adsorption energies of adsorbates, such as O*, OH*, OOH* and H*. After equilibration steps, 2 Pd atoms out of 4 Pd atoms are always covered, and desorption did not occur during AIMD. This AIMD result is consistent with the calculations along with VASPsol, which shows that the adsorption free energy of 0.5 ML (monolayer) gives −0.54 eV while that of 1.0 ML is −0.58 eV, i.e., the differential adsorption free energy from 0.5 ML to 1.0 ML is small enough (~0.04 eV) that the thermal fluctuation can overcome. Therefore, for the (100) surface, we put 1 specifically adsorbed water molecule on Pd for all configurations. Note that both give the clean surface at the applied potential although the presence of a specifically adsorbed water molecule makes the surface more stable.

[0180] Free energy diagrams. We further calculated the free energy diagrams of $2e^-$ ORR to investigate the activity and selectivity of the $PdSe_2$ catalyst. Likewise, two surfaces, (001) and (100), were considered, and the CHE method was utilized to treat the electrochemical potential of a proton/electron pair. Note that there is one specifically adsorbed H_2O, which corresponds to 0.5 ML, for the (100) surface. At the calculated equilibrium potential of $2e^-$ ORR, the first PCET step is uphill by 0.45 eV and downhill by 0.34 eV on (001) and (100) surfaces, respectively, which is unsurprising considering that the (001) surface is more stable than the (100) surface, which will lead to making the OOH* state unstable. Note that the corresponding coverage used for the free energy is 0.5 ML and the stability of the OOH* state also depends on its coverage (Table 7).

TABLE 7

The adsorption free energy (in eV) of OOH* on the (001) and (100) surface of $PdSe_2$ at various coverages at calculated equilibrium potential. The coverage used in the free energy diagrams corresponds to 0.500 ML.

OOH* Coverage (ML)	(001)	(100)
0.125	0.47	
0.250	—	
0.500	0.45	−0.34
1.00	0.48	−0.34

TABLE 8

Activation barriers of thermal bond dissociation steps (eV).

	(100) facet	(001) facet
O—O	1.04	0.77
O—OH	0.66	0.74
HO—OH	0.58	0.24

[0181] Considering that the standard reduction potential of $4e^-$ ORR (1.23 V) is higher than that of $2e^-$ ORR (0.69 V), kinetics should be taken into account to explain the selectivity. Because the adsorbates are likely to result in $4e^-$ ORR once the O—O bond is broken, we considered three thermal bond dissociation processes:

$$O_2(g) \rightarrow 2O^* \quad (3)$$

$$OOH^* \rightarrow O^* + OH^* \quad (4)$$

$$H_2O_2^* \rightarrow 2OH^* \quad (5)$$

Although all these steps are thermodynamically favorable, all the activation barriers are much higher than that of the O—OH bond breaking on Pd metal (0.06 eV), suggesting that the high activation barriers can stem from the spatial separation of active sites, which will result in the high selectivity for $2e^-$ ORR. Note that the activation free energy of the bond dissociation of hydrogen peroxide on the (100) surface is relatively small (0.24 eV), but this activation energy can be high considering the competing step is desorption from the surface, which is assumed to be barrierless.

[0182] Kinetics of PCET. In addition to thermal bond dissociation steps, we considered relevant PCET processes to investigate the selectivity for $2e^-$ ORR:

$$O_2(g) + (H^+ + e^-) \rightarrow OOH^* \quad (6)$$

$$OOH^* + (H^+ + e^-) \rightarrow H_2O_2^* \quad (7)$$

$$OOH^* + (H^+ + e^-) \rightarrow O^* + H_2O_{(l)} \quad (8)$$

$$H_2O_2^* + (H^+ + e^-) \rightarrow OH^* + H_2O_{(l)} \quad (9)$$

To obtain activation energy for an electrochemical process, a solvated proton should be treated explicitly unlike the CHE method. Among several models for a solvated proton, such as a Zundel ion ($H_5O_2^+$), the Eigen ion ($H_9O_4^+$) and the water bilayer model, we used the Eigen ion as a proton donor

because the use of the Eigen ion was validated for HER on Pt. Furthermore, because the purpose of this calculation lies in the comparison of activation energy, we believe it is safe to rely on the static minimum energy path and ignore the entropic effects and solvent fluctuations. In addition, we believe the trend remains the same even if the proton donor changes from a solvated proton to water. To obtain constant-potential activation barriers, the number of electrons varied so that the work function, which is related to electrode potential, is fixed. The details about this methodology can be found in *J. Phys. Chem. C* 2019, 123, 4116-4124, incorporated by reference, for any purpose, herein.

[0183] By using the nudged elastic band (NEB) method and the dimer method, we calculated the "raw" activation energy. The raw activation energy means the work function varies across the reaction. First, the most important step to determine the selectivity for $2e^-$ ORR is the second PCET step (Equations 7 or 8). On the (100) surface, the step of reducing OOH to H_2O_2 is a barrierless step (the raw activation barrier is zero), while the step of reducing OOH to $H_2O_{(l)}$+O* gives a barrier of 0.44 eV. By varying the number of electrons to set the electrode potential to be −0.21 V vs SHE, which corresponds to 0.2 V vs RHE at pH 7 and constant, the potential constant activation barrier becomes 0.37 eV, i.e., the potential-constant correction term is small. This is because the change in work function is small enough and the work function is already close to the target potential. Thus, it is sufficient to consider just the "raw" activation energy to compare competing reaction steps. Similarly, others have shown that the constant potential correction term is sufficiently small, they used the average value of the potential at the initial and final states. This is particularly important for the (001) surface because there are some issues, such as a non-zero band gap and dependence of the potential of zero charge (PZC) on the interlayer distance, that make it tricky to convert raw activation barriers into potential-constant activation barriers.

[0184] Similarly, on the (001) surface, the step of reducing OOH to H_2O_2 becomes barrierless, while that of reducing OOH to $H_2O_{(l)}$+O* has a barrier of 0.23 eV. Therefore, the high selectivity for $2e^-$ ORR can be explained by kinetics.

[0185] Additionally, we calculated the activation barrier for other steps (Equations 6 and 9). Because the further reduction of H_2O_2 shows a larger activation barrier than that of the first PCET step, this can explain the selectivity of H_2O_2 production.

[0186] pH dependence of the activity. The pH dependence of the activity of electrochemical processes like ORR has been explained by the stabilization of the OOH* state, which arises from the interaction with the electric field formed at the interface when the applied potential deviates from the PZC. Note that the OOH* state is calculated at PZC in the CHE method and the potential dependence is added as a posteriori correction via the RHE scale, where the applied potential is coupled with pH. Therefore, to decouple the electrode potential and pH, we calculated the binding energy of OOH* including the interaction of OOH with the electric field formed at the interface because the electric field formed at the interface is related to the shift in potential from the PZC (Equation 1). Others calculated the dipole moment and polarizability of each adsorbate by fitting a second-order polynomial (Equation 2) to calculations across the range of external electric fields and concluded that OOH* becomes stable as pH decreases.

$$\vec{E} = \frac{C_{dl}(U_{SHE} - U_{PZC})}{\epsilon\epsilon_0} \tag{10}$$

$$G_{ads} = G_{ads}^{PZC} + \mu\vec{E} - \frac{1}{2}\alpha\vec{E}^2 \tag{11}$$

[0187] In the same manner, we calculated the dipole moment and polarizability of OOH* by applying the external electric field from −0.6 V/Å to 0.6 V/Å. (FIG. **38**) The PZC (0.2 V vs SHE) and the double layer capacitance (13.6 μF/cm^2) of the $PdSe_2$ catalyst was calculated by adding/removing electrons and measuring the work functions. As mentioned above, because the PZC of (001) surface is highly sensitive to the distance between slabs and few-layers slab has a non-zero band gap, we used the values from (100) surface for both surfaces. The absolute electrode potential deviates more from its PZC as pH increases by 0.06*pH, leading to an increase in the magnitude of the electric field formed at the interface, which helps stabilize the OOH* by 0.1 eV at pH 6.5 on the (001) surface. The stability of the OOH* shows a different trend depending on the facet; the OOH* state on the (001) facet is uphill at the calculated equilibrium potential, while it is downhill on the (100) surface. Stabilization will lead to an increase in the activity for $2e^-$ ORR.

[0188] Regarding the (100) surface, the presence of specifically adsorbed water and the adsorption decrease as pH increases, i.e., it is more likely that O_2 can replace the adsorbed water at high pH.

[0189] Ex-situ and In-situ Studies on the Stability of $PdSe_2$. To confirm the predicted stability of $PdSe_2$, Inventors conducted several post-electrolysis characterization experiments. First, in order to evaluate the viability for direct applications of the produced H_2O_2 where the amounts of metal and Se leaching must be low (i.e. wastewater treatment, semiconductor cleaning), Inventors used inductively coupled plasma optical emission spectroscopy (ICP-OES) to measure the amount of Pd and Se leached into the electrolytes during GDE electrosynthesis conducted with applied constant currents of −30 mA, and −60 mA, and −85 mA (FIG. **35***a*). The leaching of Pd into the solution from the $PdSe_2$ catalyst was negligible at all measured operating currents, but the leaching rate increased with increasing current density from 0.05±0.05 μg g_{cat}^{-1} h^{-1} at −30 mA to 0.5±0.5 μg g_{cat}^{-1} h^{-1} at −85 mA. The Se leaching rate at an operating current of −30 mA (12.4±0.5 μg g_{cat}^{-1} h^{-1}) was higher than that of Pd and was only slightly higher than the leaching rate of Se from $NiSe_2$ measured in an H-cell (9.9 μg g_{cat}^{-1} h^{-1}).[4] Additionally, Inventors compared several other metrics of stability under different operating currents across metal chalcogenide catalysts. One such stability metric is an adaption of the "stability number" (S-number) previously defined for OER catalysts, which we define as the molar ratio of the produced H_2O_2 to leached metal or Se. Inventors find that $PdSe_2$ has a higher metal S-number than $NiSe_2$ (~105 vs. ~103) and $PdSe_2$ and $NiSe_2$ have Se S-numbers on the same order of magnitude (~600 to ~900 depending on conditions).

[0190] Inventors then investigated the chemical stability of the $PdSe_2$ catalyst. Very little change was observed in the post-electrolysis Raman spectrum (FIG. **35***b*), showing that the catalyst surface structure is largely maintained. Given the previously observed dependence of the Raman spectrum on $PdSe_2$ layer number, this also suggests that $PdSe_2$ does

not significantly delaminate. The XRD pattern of the $PdSe_2$/GDE after the electrolysis and rinsing with nanopure water closely matched a combination of the XRD patterns of $PdSe_2$ and the bare GDE (FIG. **35***c*). X-ray photoelectron spectroscopy (XPS) indicated that the valence states of Pd (FIG. **35***d*) remained unchanged, suggesting that the Pd^{2+} active sites maintained their surface electronic environment. While there were minor changes to the Se XPS, these changes did not suggest formation of SeO_2, which was observed for other metal chalcogenides. Furthermore, the peak shifts of the Pd 3d and Se 3d XPS due to partial oxidization of $PdSe_2$ were not observed. Similarly, the Pd—O bond was not observed in the extended Raman spectrum for both pristine $PdSe_2$ powder and the post-electrosynthesis $PdSe_2$/GDE electrode. The XPS measurements revealed the Se:Pd ratio decreased post-electrolysis, but was still in excess of a 2:1 ratio, thus precluding the formation of $Pd_{17}Se_{15}$ triggered by Se leaching. These results confirm that the active site for $2e^-$ ORR is indeed the square planar Pd^{2+} motif, rather than the higher valent Pd or Pd—O bonds formed due to oxidation, as observed for other $2e^-$ ORR catalysts.

[0191] To further investigate the changes to the electronic structure of Se, Inventors conducted ex-situ X-ray absorption spectroscopy (XANES) at the Se K-edge. The similar ratio between the main white line peak and the post-white line peak (at ~12660 eV and ~12770 eV) confirms that Se remains anionic in character and precludes the formation of bulk Se oxides. Namely, the peak near 12770 eV was still clearly present, unlike in Se(0) powder, and cationic Se compounds (such as SeO_2) which show a clearly blue shifted white line peak. Additionally, the Se K-edge extended X-ray absorption fine structure (EXAFS) spectroscopy of post-electrosynthesis $PdSe_2$/GDE showed little change in the first two major peaks (FIG. **35***f*). Fitting the EXAFS data suggested a minimal decrease in Se—Se coordination (from 1 to 0.8±0.1) but larger decreases in direct Se—Pd coordination (from 2 to 1.0±0.1) and Se—Pd interlayer coordination (from 1 to 0.3±0.1). Similar results were achieved with a simplified fitting model. Given the Se-rich samples and the lack of significant Pd leaching, these changes in Se—Pd paths could be indicative of some subtle local restructuring of the Pd sites that does not disrupt the overall layered motif of the $PdSe_2$ catalyst.

[0192] To confirm these stability trends on a longer timescale, we fabricated an electrode with a high loading of Nafion to prevent flooding (FIG. **40***a*). By tuning the microenvironment, the $PdSe_2$/GDE electrode was able to operate for 48 hours at −75 mA (FIG. **40***b*). Additionally, despite the long operation time, the $PdSe_2$/GDE retained high S-numbers of 416 for Se and 2.07×10^4 for Pd. The lack of significant decrease in stability at high operating times suggests that H_2O_2 concentration buildup is likely the primary mechanism of Se leaching for $PdSe_2$. Although the H_2O_2 saturation saturates, the stability is promising for the repeated use of the $PdSe_2$ catalysts in separate solutions or in a single pass flow cell configuration. After several tests, this electrode was digested for measurement by ICP-OES, which showed a slight decrease from 1.98:1 Se:Pd ratio (as measured in the pristine electrode) to 1.30:1. Taken with the more surface sensitive XPS/EDS results and the bulk sensitive EXAFS, this further suggests differences between the active phase surface and the bulk triggered by Se loss.

Methods and Materials

[0193] Computational Methods. The Vienna Ab initio Simulation Package (VASP) interfaced with the Atomic Simulation Environment (ASE) was used for energies and geometries for all adsorbates. The core electrons are described by projector augmented wave (PAW) pseudopotentials and the Perdue-Burke-Ernzerhof (PBE) functional was used to treat exchange and correlation. Because PBE-TS (Tkatchenko-Scheffler) method gives reasonable lattice constants of bulk $PdSe_2$, the Tkatchenko-Scheffler method was utilized to treat dispersion. Solvation effects are described by using the implicit solvation model, VASPsol. For numerical stability, the effective surface tension is set to zero, which is validated by the fact that the difference in adsorption energy between the default value (0.025 meV/Å^2) and 0 meV/Å^2 is less than 0.01 eV.

[0194] The Brillouin zone was sampled using 10×10×10, 10×10×1, and 10×8×1 Γ-centered Monkhorst-Pack mesh for bulk, (001), and (100) facets calculations, respectively. When larger supercells were used, the corresponding Brillouin zones were sampled.

[0195] The (001) surface of $PdSe_2$ was modeled as a 3-layer 1×1 unit cell slab with two bottom layers fixed, which corresponds to 6 Pd atoms and 12 Se atoms. The (100) surface was modeled as 5-layer 1×1 unit cell slab with two bottom layers fixed, which corresponds to 20 Pd atoms and 40 Se atoms. For the electrochemical activation barrier calculations, 4-layer (100) surface was used for efficiency.

[0196] Each electronic self-consistent field (SCF) calculation was converged below 10^{-5} eV and the surface adsorbates were allowed to relax until forces became below 0.01 eV/Å. Transition states for thermal bond dissociation were searched using the nudged elastic band (NEB) method and the dimer method. Additionally, all transition states were confirmed first-order saddle points with one imaginary frequency. The free energy of $H_2O_{(l)}$ was calculated using the experimental free energy difference between $H_2O_{(l)}$ and $H_2O_{(g)}$. The free energy of O_2 was determined by setting it to give the experimental standard reduction potential (1.229 V) of the reaction, $0.5\ O_{2\ (g)}+H_2\rightarrow H_2O_{(l)}$. The free energies of adsorbates were calculated using $G=E_{DFT}+U_{thermal}+ZPE-TS$, where E_{DFT} is the energy obtained from DFT calculation, $U_{thermal}$, ZPE and S are the contribution from thermal internal energy, the zero-point energy, and entropy, which are calculated under the harmonic approximation. The free energies of gas-phase/aqueous species, such as H_2, H_2O, and H_2O_2 are calculated by using Gaussian 16 with the SMD continuum solvation model. The calculated standard reduction potential of $2e^-$ ORR is 0.83 V, which is slightly higher than the experimental value (0.69 V) and close to other computed values.

[0197] For potential-constant electrochemical barrier calculations, we included the correction term QV_{ref}, which comes from using the finite height of the system, where Q is the net charge of the DFT subsystem and V_{ref} is the negative of the electrochemical potential of the bulk electrolyte. Note that specifically adsorbed water is not considered for the calculations of transition states. Chemicals and materials. Palladium chloride (≥99.9%) was obtained from Sigma-Aldrich. Selenourea (98+%) was obtained from Acros Organics. Carbon fiber paper (CFP, Toray: 5% wet proofing) was obtained from Fuel Cell Earth and plasma treated and briefly heated at 700° C. for 5 minutes prior to

use. Sigracet 28 BC gas diffusion electrodes (GDE) were used for all GDE electrosynthesis measurements.

[0198] Materials synthesis. The $PdSe_2$ nanoplates were synthesized by a hydrothermal method. Briefly, 1.0 mmol of $PdCl_2$ (0.18 g) and 2.0 mmol selenourea (0.25 g) were dissolved in 9 mL of nanopure water and added to a Teflon lined 20 mL stainless steel autoclave. A piece of CFP (~1.8 cm×~2.2 cm) was also added to the autoclave. The autoclave was sealed and heated at 220° C. for 12 hours, and then cooled naturally in air. The resulting powder was washed with nanopure water and ethanol before being dried under vacuum at 60° C., and the CFP piece was similarly rinsed with nanopure water and ethanol and then dried in air. Nanoparticles of Pd_4Se and $Pd_{17}Se_{15}$ were synthesized by similar methods with appropriate stoichiometric amounts of $PdCl_2$ and selenourea.

[0199] Materials characterization. Powder X-ray diffraction (PXRD) patterns were collected on a Bruker D8 ADVANCE powder X-ray diffractometer using Cu Kα radiation with a 0.6 mm slit. Scanning electron microscopy (SEM) images were collected on a Zeiss SUPRA 55VP field emission scanning electron microscope at an accelerating voltage of 1-3 kV for imaging, and electron dispersive spectroscopy (EDS) spectra were collected on the same microscope using an accelerating voltage of 22 kV and a Thermo Scientific UltraDry EDS Detector. X-ray photoelectron spectroscopy (XPS) was performed on a Thermo Scientific K-Alpha XPS system with an Al Kα X-ray source. Raman spectra were collected on a Thermo Fisher Scientific DXR3xi Raman Imaging Microscope using a 532 nm laser with a 10 mW laser power. X-ray absorption spectroscopy (XAS) was collected at beamlines 10-ID (Pd K-edge data) and beamline 9-BM (Se K-edge data, Pd L-edge data) of the Advanced Photon Source at Argonne National laboratories in fluorescence mode with an ion chamber detector for the Pd K-edge, a Vortex silicon drift detector for the Pd L-edge, and a Passivated Implanted Planar Silicon (PIPS) detector for the Se K-edge. Pd L-edge spectra were collected in a He-purged sample chamber.

[0200] Rotating ring disk Electrode Preparation. Catalysts were drop-casted onto a rotating ring-disk electrode (RRDE, Gaoss Union, 4 mm disk diameter) which was polished successively with 1, 0.3, and 0.05 μm alumina suspensions (Allied High Tech Products) on polishing pads (Buehler, MicroCloth), and subsequently rinsed with nanopure water before brief (~20 seconds) sonication in ethanol then quickly blown dry with N_2. Catalyst dispersions typically used a 1:9 v:v mixture of Nafion solution and water with an effective catalyst loading of ~12 μg/μL.

[0201] Rotating ring-disk electrode measurement. RRDE measurements were conducted in an undivided cell using a Bio-Logic VMP3 potentiostat. A graphite rod was used as the counter electrode and a Hg/Hg_2SO_4 reference electrode (CH Instruments Inc., CHI151) that was calibrated against a saturated calomel electrode (CH Instruments Inc., CHI150). The cell contained approximately 45 mL of electrolyte, which was pre-purged with Ar or O_2 gas before measurement, and then the corresponding gas was kept in the headspace of the solution for the duration of the measurement. During RRDE measurements, the ring was typically held at 1.3 V vs. RHE (pre iR correction) where H_2O_2 reduction is diffusion limited. The H_2O_2 selectivity was then calculated according to the follow equation:

$$H_2O_2\ \text{Selectivity}\ (\%) = \frac{200\left(\frac{I_{ring}}{N}\right)}{\frac{I_{ring}}{N} + I_{disk}}$$

where N is the collection efficiency of the ring, which was calculated using a ferri-/ferrocyanide redox couple.

[0202] Bulk electrolysis measurements. Bulk electrolysis experiments were conducted in a glass H-cell with an Hg/Hg_2SO_4 reference electrode. The working electrode consists of the as-synthesized $PdSe_2$ catalyst directly grown onto carbon fiber paper (CFP) cut into a 1×2 cm area, where the area exposed to electrolyte was ~1 cm^2 with the electrode contacted via a Teflon clip with a platinum contact. The other chamber, separated by a Nafion-117 membrane, contained a graphite rod which served as the counter electrode. The working chamber was pre-purged with O_2 and then kept under a continuous flow of O_2 gas during the measurement. Aliquots were continuously taken during the measurement and added to solutions of ~0.4 mM $Ce(SO_4)_2$, which were then measured shortly thereafter by UV-Vis on a JASCO V-570 UV/Vis/NIR spectrophotometer, which were converted to the corresponding concentration of H_2O_2 via the following equation:

$$\text{Cumulative Faradaic Efficiency} = \frac{Q_{H_2O_2}}{Q_{tot}} = \frac{2 * F * [H_2O_2] * V_{tot}}{Q_{tot} * 10^6}$$

where F corresponds to Faraday's constant (in C/mol e^-), $[H_2O_2]$ is the H_2O_2 concentration (in mM) calculated from the previous equation, V_{tot} corresponds the total solution volume (in mL), and Q_{tot} is the total charge passed through the measurement (in C).

$$\text{Cumulative } H_2O_2\ \text{Selectivity} = \frac{200}{1 + \left(\frac{100}{\text{Cumulative Faradaic Efficiency}}\right)}$$

[0203] Operando X-ray absorption spectroscopy measurements. Operando XAS measurements performed at the Advanced Photon Source were collected using a custom-built fluorescence detection H-cell where the working electrode was mounted on the front using an acrylic or aluminum face plate, with the catalyst side facing inward to the electrolyte and the bare side facing back towards the incident X-rays and the fluorescence detector. To contact the working electrode under the faceplate, a small piece of copper foil was used. A leakless Ag/AgCl reference electrode was used (and secured in the front chamber with the working electrode) and a graphite rod was used as the counter electrode in the back chamber, which was separated from the front chamber by a Nafion-117 membrane to avoid H_2O_2 crossover and decomposition. 2.5 mL of electrolyte was added to the front chamber for each measurement, and was kept under a continuous stream of O_2 gas throughout the duration of the measurement via a port in the top of the cell. XAS spectra were continuously collected for the duration of the measurement, with each displayed spectrum representing the average of at least three raw spectra.

1. An electrochemical cell comprising an electrolyte and a cathode immersed in the electrolyte,

wherein the cathode comprises a two-electron oxygen reduction reaction ($2e^-$ ORR) electrocatalyst composed of a metal chalcogenide,

wherein the metal is Ni or Pd.

2. The electrochemical cell of claim **1**, wherein the metal chalcogenide comprises c-$NiSe_2$.

3. The electrochemical cell of claim **1**, wherein the electrolyte has a pH below 4.0, optionally wherein the electrolyte has a pH between 0.0 and 4.0 pH or any pH therebetween.

4. The electrochemical cell of claim **1**, wherein the metal chalcogenide comprises layered $PdSe_2$.

5. The electrochemical cell of claim **1**, wherein the electrolyte has a pH above 4.0, optionally wherein the electrolyte has a pH between 4.0 and 8.0 pH or any pH therebetween.

6. The electrochemical cell of claim **1**, wherein the electrolyte comprises oxygen (O_2), hydrogen peroxide (H_2O_2), hydroxyl radical (·OH), a regenerable metal ion, and a first biomass-derived feedstock.

7. The electrochemical cell of claim **6** further comprising an acidic anolyte and an anode immersed in the anolyte, wherein the anolyte comprises a second biomass-derived feedstock.

8. A method for production of hydrogen peroxide, the method comprising introducing oxygen into the electrochemical cell according to any one of claim **1** under conditions sufficient for preparing the hydrogen peroxide.

9. An electrochemical cell comprising an acidic catholyte, a cathode immersed in the catholyte, an acidic anolyte, and an anode immersed in the anolyte,

wherein the cathode comprises a two-electron oxygen reduction reaction ($2e^-$ ORR) electrocatalyst comprised of a metal chalcogenide and the catholyte comprises oxygen (O_2), hydrogen peroxide (H_2O_2), hydroxyl radical (·OH), a regenerable metal ion, and a first biomass-derived feedstock, and wherein the anolyte comprises a second biomass-derived feedstock.

10. The electrochemical cell of claim **9**, wherein the two-electron oxygen reduction reaction ($2e^-$ ORR) electrocatalyst comprises a metal chalcogenide.

11. The electrochemical cell of claim **10**, wherein the metal chalcogenide comprises an earth-abundant metal or a noble metal.

12. The electrochemical cell of claim **10**, wherein the metal chalcogenide comprises Ni, Co, Fe, Cu, Mn, Pd, or any combination thereof.

13. The electrochemical cell of claim **10**, wherein the metal chalcogenide comprises c-$NiSe_2$, $PdSe_2$, pyrite or marcasite type $CoSe_2$, pyrite type CoS_2, or $CuCO_{2-x}Ni_xS_4$.

14. The electrochemical cell of claim **9**, wherein the acidic catholyte and/or the acidic anolyte has a pH between 0.0 and 4.0 pH.

15. The electrochemical cell of claim **9**, wherein the regenerable metal ion is Fe^{2+}.

16. The electrochemical cell of claim **9**, wherein each of the catholyte and the anolyte further comprise oxidation products of the first biomass-derived feed stock and the second biomass derived feed stock.

17. A method for preparing an oxidation product of a biomass-derived feedstock, the method comprising introducing the biomass-derived feedstock into the electrochemical cell according to claim **1** under conditions sufficient for preparing the oxidation product.

18. The method of claim **16**, wherein a potential between 0.00 and 0.70 V vs. RHE is applied to the cathode.

19. A method for preparing an oxidation product of a biomass-derived feedstock, the method comprising introducing the biomass-derived feedstock into the electrochemical cell according to claim **9** under conditions sufficient for preparing the oxidation product.

20. The method of claim **18**, wherein less than 1.0 V of externally applied bias is applied.

* * * * *